Development of Time Projection Chambers with Micromegas for Rare Event Searches.

memoria presentada por
Alfredo Tomás Alquézar
para optar al grado de doctor
en Física

Laboratorio de Física Nuclear y Astropartículas
Área de Física Atómica, Molecular y Nuclear
Departamento de Física Teórica

Universidad de Zaragoza

May 2013

A mis padres

Acknowledgments.

En primer lugar quiero agradecer al profesor José Ángel Villar que me diera la oportundad de trabajar con el Grupo de Física Nuclear y Astropartículas. También me gustaría tener un recuerdo para el profesor Julio Morales, cuya combinación de experiencia y jovialidad hacía su persona inolvidable.

Si me remonto hasta un poquito antes del principio, he de dar las gracias —casi habría de pedir perdón— a Sebastián Jarabo, quien me introdujo en la investigación. Me impresionaron tanto su capacidad como su integridad, y quiero hacer constar sus dotes pedagógicas. Esta experiencia me decidió a intentar el doctorado..., pero supongo que me pasé al lado oscuro —seguro que hubiese sido una muy buena experiencia de haber continuado. Parte de la culpa la tiene Susana Cebrián, quien me ha servido de apoyo en muchas ocasiones, de principio a fin de esta etapa.

Igor G. Irastorza ha sido inspiración y ejemplo. Todas las líneas de trabajo reunidas en esta memoria comenzaron y terminaron —si es que alguna se completó finalmente— en una conversación con él. Destacaré la ambición de su pensamiento —transmite que trabajas en algo realmente imporante— y el equilibrio de sus posturas. Le agradezco profundamente su confianza. En todo este tiempo jamás me mostró ni el palo ni la zanahoria. Y no menos diría de Theopisti Dafni. Ya que Igor y Theopisti..., pues Theopisti e Igor. Si una espina me queda, es no haber visto más pelis griegas y haber aprendido a bailar el *sirtaki*. Que no se me acabe este párrafo sin nombrar a Esther Ferrer, sólo más brillante como física que como anfitriona. Su salón es el punto de encuentro de la crème de la crème parisina (a cinco minutos del centro). Si no te han invitado a cenar Esther y Fred, no eres nadie.

En este periodo, ciertamente un poco largo, he tenido ocasión de trabajar muy estrechamente con varias personas. Al principio —cuando eramos jóvenes— con Francisco José Iguaz, ambos compartimos la experiencia de partir de cero. Los primeros programas, viajes, la experiencia de París, el trabajo de laboratorio, los meetings. No sé si fuimos los auténticos, pero sí los primeros *micromachines* — creo que formamos un buen tandem, Paco. Después Javier Galán, antiguo amigo que regresó del CERN convertido ya en un viejo zorro. Su incorporación fue como vitaminas para el grupo —*Bless the beatiful hide wherever you may be*, Javi. Y en tramo final Juan Antonio García y Javier G. Garza, cuya capacidad y entrega posibilitaron que yo pudiera escribir esta memoria, imprescindibles. Ha sido un placer ver de cerca como os convertíais en dos físicos expectaculares —y no me refiero al tipín que lucís. El trabajo que se relatará aquí les pertenece a todos en gran medida.

Lo mejor de esta experiencia, sin duda la gente que conoces en cuanto asomas la cabeza fuera del despacho —y si no, acaba llegando a tu despacho. El espectro es tan variado como positivo. Yo incluiría al menos media docena más de personajes principales en *The Big Bang Theory*. No he dejado de sorprenderme de la calidad

humana en este último trámite, en el que he generado bastantes más molestias que trabajo productivo.

Como es muy español valorar primero lo de fuera, I aknowledge the support from all the people I met at CEA/Saclay: Arnaud, Jean Philippe, Begoña —sí, con un acento terrible de Cádiz, pero parisina a tu pesar—, Fabien, Julien, Stephan. Happening to meet with Ioannis Ioamataris in a lab is a encouraging experience. It was hard to believe such a genuine entusiasm from a person with his experience for the little things a young researcher was doing. He is the living proof that passion and an endless imagination (and surely another two hundred things) are the key to success. Thomas Papaevangelou is rated number one in the Forbes list of most experience people in micromegas —thanks for a lot of stimulating and useful discussions. I also want to thank people from CAST: Konstantin, Martyn, Mike, Theodoros, Jaime, Julia, Biljana, particularly the tireless CAST grand holders, Cenk, Theodoros, Antonis, Madalin and many others.

Mi sincero agradecimiento a todo la gente del pasillo en Zaragoza, los que están y que estaron. Sólo podré nombrar a aquellos con los que he compartido más alegrías y penurias, kilómetros y cafés: Ysrael, Diana, Asun, Héctor, Fran, Laura, Alicia, Gloria, José Manuel. Voy a destacar a los técnicos, porque se enfrentan a la tarea de entender qué pasa por nuestras cabecitas —y a menudo lo hacen realidad—, comparten nuestro destino aunque no comprendan nuestras motivaciones y nunca son suficientemente reconocidos: Fredi, Ángel, David, Silvia y Álvaro. Mención aparte para Juan F. Castel —un mago de paciencia infinita— y Alfonso Ortiz de Solórzano, de los Ortiz de Solórzano de toda la vida, verdadero comandante en jefe de los becarios a los que introduce en muchos aspectos fundamentales. No en vano, bautizó a *la patera*. Gracias también al personal del Laboratorio Subterráneo de Canfranc.

Fuera del ámbito científico dicen que hay más vida. Muchas gracias a mis padres por su apoyo más allá de lo razonable, me habéis tratado como a un verdadero hijo. Gracias Laurica, hace tiempo que te convertiste en la hermana mayor. Gracias a los amigos que, no por haber estado yo inaccessible y embrutecido durante meses, dejaron de pasar de mí. Sirvan estás bromas a su costa —las últimas— como ejemplo de lo que han tenido que soportar. Y sobre todo, gracias a tí, mi novia, que aún esperas, doncella, aburrida, en tu torre de marfil a que vaya a conocerte. Bueno..., tendrás que esperar un poco más.

Para acabar me dirijo a tí, becario que aún no conozco y utilizas este ladrillo de tesis para sujetar la ventana de la patera. Muéstrate feliz porque estás donde has de estar, donde la física bulle, en el centro creativo más fecundo desde la sala de guionistas de *Friends*.

Scope of the thesis.

This thesis reports diverse research efforts developed in the frame of the T-REX project which intends the application of gaseous Time Projection Chambers (TPCs) to Rare Event Searches. The activities include pure R&D together with specific research lines for the experiments CAST (CERN Axion Solar Telescope) and NEXT (Neutrinoless double beta decay Experiment with a Xenon TPC).

The Laboratorio de Física Nuclear y Astropartículas (LFNA) of the University of Zaragoza brings an exceptional opportunity to undertake this work because of its near three decades of experience in Rare Event Searches and a close relationship with the development of the Canfranc Underground Lab (LSC); besides its collaboration with the IRFU (Institut de Recherche sur les lois Fondamentales de l'Univers) at CEA/Saclay, which is the main authority on micromegas, one of the prominent Micro-Pattern Gaseous Detectors (MPGDs).

Some of the Rare Event Searches that motivate the work are briefly reviewed in chapter 1, remarking how TPCs can contribute to the different scenarios. The main concepts required to follow the rest of the work are concisely introduced in chapter 2.

The development of micromegas is quite recent, specially for the last micromegas types, bulk and microbulk. Therefore the exploration and characterization of their properties, even those that were already well known for classical layouts, is a first, basic but essential, stage of the research. Chapters 3 and 4 were aimed to be a practical reference (manual-like) about customary TPC features, despite focussing in micromegas particular issues. Part of the R&D original work on basic micromegas operation was inserted among these chapters. Chapter 5 can be seen as an appendix on TPCs and micromegas features of direct interest for particular applications to Rare Event Searches.

A software package for simulation of TPCs and micromegas was developed for T-REX and is generically described in chapter 6. Chapter 7 contains two particular examples of applications of the software to dark matter and to double beta decay TPCs.

The second part of the thesis naturally focusses on the CAST experiment, as the unique running Rare Event Search experiment that uses the state of the art micromegas. The experiment, that has a remarkable relation with the evolution of micromegas detectors, is presented in chapter 8. Chapters 9 and 10 report R&D on CAST micromegas background based on, respectively, simulations and experimental tests; and in chapter 11 their common conclusions are summarized as well as some reflections on the prospects of further background improvements.

Contents

Chapter 1

Rare Event Searches and TPCs.

Contents

1.1 Introduction.

The *Rare Event Searches* category is defined by a purely experimental feature: the identification of very unlikely phenomena for which very low (most of times unknown) detection rate is expected. Theoretically it is a heterogeneous field containing experiments with diverse goals from high energy physics and astroparticle physics to nuclear physics. Nevertheless, all of them require very low background, what makes the development of the detector a capital issue. Furthermore *experiment* and *detector* are often synonymous in Rare Event Searches. The detector will surely need shielding (active and/or passive), event discrimination capabilities, careful material selection for assuring an ultra-low radioactivity and (unavoidably in many cases) operation in underground labs.

They are finally these ultra-low background techniques which compose the common *know-how* that defines the field. Thus it often happens that an experiment initially designed for a particular purpose, delivers a result for a different physical issue as a by-product. That is the reason why generally talking about development for Rare Event Searches has sense for an R&D program, like the T-REX[1] (TPCs for Rare Events eXperiments) project, in which the present work is framed.

T-REX aims the application of a particular detector type, the Gaseous Time Projection Chamber (TPC)[1] in Rare Event Searches. The feasibility of that goal relies on the enhanced capabilities of TPCs thanks to the use of micromegas readout planes (section 2.2). The TPCs are outstanding in event discrimination thanks to

[1] Unless the contrary is specified, we will always refer to gaseous TPCs, though nowadays liquid TPCs are dominant in Rare Event Searches. A schematic revision of the TPC concept is done in section 2.1.

the topological information they can provide. Just the improvement of the discrimination based on gathering more variate and detailed event information, together with the availability for scaling the detector size, have been the keys of the impressive evolution of Rare Event Searches experiments along the last decade.

Perhaps the discovery of the neutrino by Reines and Cowan in 1956 marks the birth of the Rare Event Searches field. In fact the detection of atmospheric neutrinos in the 60's was pioneer of Underground Physics, and the (still not concluded) solution of the neutrino oscillations puzzle is probably its most important achievement until now. However, in this chapter, we will briefly describe the motivation for other three searches which are certainly more demanding, from the background point of view, as they aim to detect particles which are even more elusive than neutrinos: WIMPs (section 1.2.2) and WISPs (section 1.2.3); and the very rare neutrinoless double beta decay (section 1.2.1). Therefore these are the issues that boost the detectors evolution. The present tendency in current experiments will be mentioned and the contribution TPCs could bring to the each particular issue.

1.2 Physical issues.

1.2.1 Neutrinoless double beta decay.

The neutrinoless double beta decay ($\beta\beta0\nu$) is an hypothetical version of the standard (though very rare) double beta decay process ($\beta\beta2\nu$):

$$(A, Z) \rightarrow (A, Z + 2) + 2e^- \tag{1.1}$$

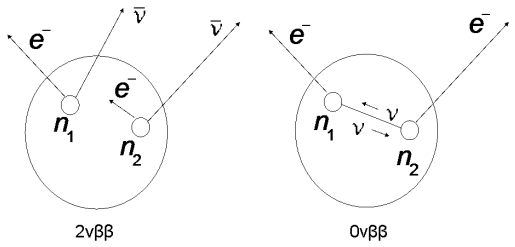

Figure 1.1: Schemes of $\beta\beta2\nu$ (left) and $\beta\beta0\nu$ (right) decays.

Note that lack of the pair of antineutrinos implies violation of the lepton number conservation; therefore we deal with physics beyond the Standard Model and of primary interest for Cosmology[2]. Moreover, the process requires neutrino and antineutrino to be the same particle (see figure 1.1 right), i.e. neutrino has to be a Majorana particle, instead of a Dirac particle; hence the observation of $\beta\beta0\nu$ would

[2]The violation of the lepton number during the leptogenesis could be a via for the matter-antimatter asymmetry generated during the bariogenesis.

solve a fundamental doubt that is pending since the 30's[2]. Furthermore, the determination of the $\beta\beta0\nu$ decay rate, $T^{0\nu}_{1/2}$, can be related with the absolute scale of the neutrino mass; thus complementing the neutrino oscillations experiments results, which are only sensible to mass differences. The accessible parameter, the *effective neutrino mass* is

$$\langle m_\nu \rangle = \frac{m_e}{\sqrt{F_N T^{0\nu}_{1/2}}} \tag{1.2}$$

where m_e is the electron mass and F_N is factor that depends on the nuclear matrix elements and so comes from Nuclear Physics[3]. $\langle m_\nu \rangle$ is a combination of the eigenvalues of the neutrino's mass states; however it would mean a hint for figuring out their hierarchy, i.e. the pattern the three neutrino masses are arranged in (see figure 1.2).

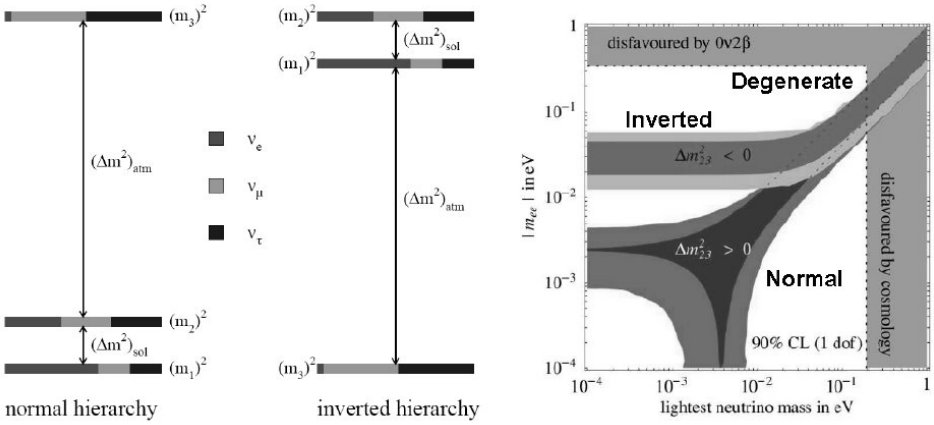

Figure 1.2: Left: schemes of the neutrino mass hierarchy models which are consistent with the observation of neutrino oscillations[4]. Right: representation of the schemes according to theory and observations regarding the effective neutrino mass, that is related with the experiment's sensitivity through (1.2)[5]. The *normal* and *inverted* schemes are practically coincident if the lightest neutrino mass is much higher than the differences (*degenerate* scheme). The most restrictive limit from germanium detectors (IGEX, see next section) set $\langle m_\nu \rangle < 0.33$–$1.5$, what needed $T^{0\nu}_{1/2} > 1.57 \times 10^{25}$ yr. Present generation of $\beta\beta0\nu$ decay experiments aim to rule out the degenerate region and enter, for the first time, in the inverse hierarchy region.

1.2.1.1 $\beta\beta0\nu$: Experimental approaches.

Most of the experiments are based on the reconstruction of the double beta decay spectrum (see figure 1.3). If there are no antineutrinos, the spectrum should be simply a peak at Q value. It would appear at the end of the continuum spectrum of

$\beta\beta 2\nu$ decay. The ratio between both decay modes and the detector's efficiency and energy resolution are crucial to identify the $\beta\beta 0\nu$ peak.

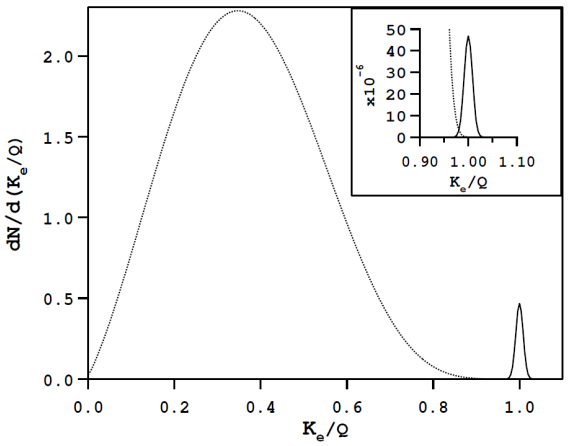

Figure 1.3: Spectrum showing $\beta\beta 2\nu$ and $\beta\beta 0\nu$ modes assuming 2% resolution for the detector, $K_e = T_1 + T_1$ the sum of electron energies. The energy resolution becomes critical if the $\beta\beta 0\nu$ is highly suppressed respect to $\beta\beta 2\nu$, as is indeed the case. The big picture is produced for a ratio of 10^2, the detail in the corner shows the situation for 10^6. The figure is extracted from [6].

Since the beginning the usage of germanium detectors has been a successful strategy. Germanium detectors had been used in γ spectroscopy because of its outstanding energy resolution and high efficiency, in addition they were a well established technology. Fortunately there is an isotope, ^{76}Ge, that is a $\beta\beta 0\nu$ decay candidate and the crystals can be enriched in this isotope. The concept of target and detector being the same entity is highly convenient since the efficiency is optimized and no physical frontiers affect the energy resolution.

During two decades this kind of experiments pioneered the evolution of all the basic techniques of Rare Event Searches: modifying the spectroscopy germanium detectors to become radiopure, building complex shieldings, using pulse-shape analysis for discrimination, etc. At the early 2000's the state-of-the-art seemed to reach its maxima with the IGEX[7] and Heidelberg-Moscow[8] experiments. They provided the (still now) best limit for $T^{0\nu}_{1/2}$ in ^{76}Ge and a controversial claim[9].

The next step in the evolution, unavoidable for scaling the mass up, is the development of a matrix of germanium detectors, each of them completely operational. In consequence the scaling requires huge efforts for gathering the ^{76}Ge crystals, implying the fusion of collaborations. But the challenge is also technical and in cost, since essentially the basic set-up (a single germanium detector) is multiplied n times for getting a n scaling factor of the mass. The MAJORANA[10] and GERDA[11] collaborations have undertook the challenge, nevertheless, and aim to instrumentalise about 1 ton of active germanium. The same consideration can be applied to experiment based on bolometers, like CUORE[12].

When the source/detector is a fluid contained in a vessel, the scaling is more natural. The complexity of the detector is essentially related with the readout, which grows slowly than the mass (typically the mass-readout ratio would go as $n^{2/3}$ with n the scaling factor). So a liquid xenon TPC can be an interesting option since ^{136}Xe is a good $\beta\beta0\nu$ candidate, with a high $Q_{\beta\beta}$, relatively abundant and with a not very intense $\beta\beta2\nu$ mode. The latter is so much so that only recently the EXO (Enriched Xenon Observatory)[13] collaboration, with 200 kg of xenon enriched 80% in ^{136}Xe, has reported the first observation of the $\beta\beta2\nu$ decay of this isotope[14]. The observation has been confirmed more recently by the KamLAND-Z en (KamLAND Zero-Neutrino Double-Beta Decay) experiment[15]. That is a 300 kg xenon (enriched in ^{136}Xe) calorimeter with capability to reconstruct the vertex and strong active shielding.

The liquid TPC has modest energy resolution compared with germanium detectors and bolometers ($\sigma/E < 2\%$ is showed in [13]) and limited topological capabilities, compared with a gaseous TPC, for discrimination. However both features are enhanced by the operation in hybrid mode that allows the measurement of light and charge and the self-shielding is excellent. In conclusion the liquid Xe TPC seems very appealing because of being a very balanced solution.

1.2.1.2 Gaseous TPCs for $\beta\beta0\nu$ decay.

The double beta decay has a clear topological signature: that of two electron tracks with a common vertex (see section 7.2). That suggests that a gaseous TPC would be powerful for event discrimination. The NEMO (Neutrino Ettore Majorana Observatory)[16] collaboration already exploits that by introducing the target foils in a kind of narrow gaseous chambers. However, because of leaving the source/detector identification, the efficiency and energy resolution are degraded. Moreover the scaling possibilities of this approach are linear in the same sense as in the germanium and bolometer arrays.

A gaseous enriched ^{136}Xe TPC is highly appealing. In principle most of the benefits of the liquid TPC approach are kept or enhanced, the drift is easier, no cryogenics is needed, the energy resolution is better and the mass can scale just by increasing the pressure. The Gotthard TPC[17], with 3.3 kg of gas at 5.5 atm, was an encouraging attempt, pioneer of the application of TPCs to Rare Event Searches in the 90's. Its main limitation was the energy resolution, which is the final requirement for all the detectors, since both neutrino and neutrinoless modes cannot be distinguished by topological means.

However, the introduction of MPGDs (Micro-Pattern Gaseous Detectors, see section 2.2) makes modern TPCs overcome the Gotthard TPC's limitations and they could exploit the promising results it actually showed. However a big enough high pressure gaseous xenon (HPGXe) TPC has still to be demonstrated (see some hints in chapter 5), and also that the discrimination capabilities (see section 7.2) would be powerful enough so as to compensate the total mass disadvantage (a first

deep study about that is done in a Ph.D. work inside T-REX[18], which is extended in [19]). NEXT (Neutrinoless double beta decay Experiment with a Xenon TPC)[20] is expected to operate 100 kg of enriched xenon in the Canfranc Underground Laboratory. The NEXT project's highlight is a full three dimensional reconstruction of the event topology, including its absolute position thanks to the combination of light and charge signals. NEXT has a R&D program dedicated to micromegas. The EXO project also supports a collateral R&D program for a HPGXe TPC[21].

1.2.2 Dark matter

The observational evidences that support the presence of Dark Matter (DM), accumulated since the 30's, are quite numerous and variate (see a review in [22]). It is particularly significant that they appear at very different scales, from galaxies to clusters up to the largest observed astronomical structures.

However the most valuable support comes from Cosmology; the last decade saw the birth of the *Cosmology's precision era*, whose results[23, 24, 25] crystallised in the ΛCDM model. That means a new paradigm for the Universe's History where its composition is quantified and rather constrained, giving an important role for DM. According to the customary notation in Cosmology the different contributions to the density of energy ρ are denoted as

$$\Omega_i \equiv \frac{\rho_i}{\rho_c} \tag{1.3}$$

where ρ_c is the critical density that corresponds with a flat, i.e. with Euclidean metric, Universe. Today, the two relevant contributions are Ω_M, the matter density, and Ω_Λ, which is the *Dark Energy (DE)* that causes the accelerated expansion of the universe. Figure 1.4 shows eloquently how the three independent observations were coincident in a scenario dominated by DE, with an also very important contribution from matter that requires most of it to be DM, and probably a flat universe.

Nevertheless the deductions taken from the Cosmic Microwave Background (CMB) registered by WMAP put the most precise constrains by far. Therefore the ΛCDM model suitability to fit the observational data has been recently confirmed and its accuracy be improved by the results of WMAP's successor, the PLANCK[26] in March 2013[27]. The new 68% limits are[28]:

$$\Omega_M = \quad 0.314 \pm 0.020 \tag{1.4}$$

$$\Omega_\Lambda = \quad 0.686 \pm 0.020 \tag{1.5}$$

From the 31.4% of matter density only the 4.2% corresponds to baryonic matter, constrained by the Big Bang Nucleosynthesis (only $\simeq 0.3\%$ is luminous); so 27.2% is non-baryonic DM and 68.6% is DE. The nature of the latter is even less known than that of DM, being the theoretical proposals rather diverse, from the Einstein's

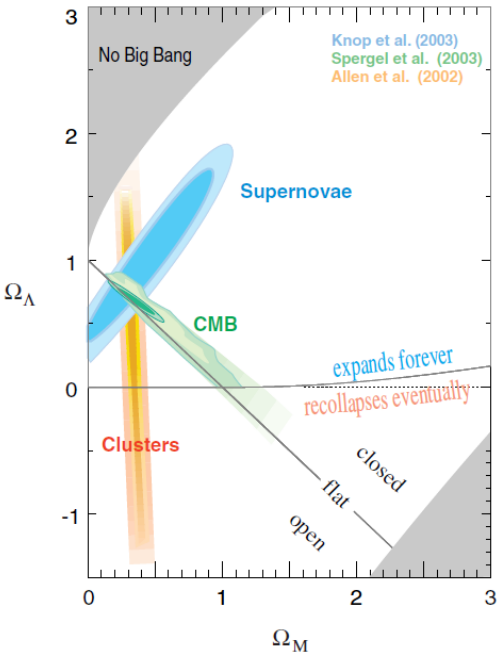

Figure 1.4: Three independent sets of observations: high-redshift supernovae, galaxy cluster inventories, and the CMB, converge nicely. The dark grey corner (down right) corresponds to a too recent Big Bang. Figure extracted from [24].

cosmological constant to *quintessence* fields. Its study is, in principle, out of the scope of this work[3]. The PLANCK's result for the *Curvature Parameter* today, that accounts for departures from spatial flatness, is $\Omega_K \equiv 1 - \sum \Omega_i = -0.0096^{+0.010}_{0.0082}$ (68% CL), what means a great hint towards a Universe with zero curvature.

The observations that allow to reconstruct the DM distribution show it to be relatively disperse in big halos that surpass the galaxy and cluster luminous dimensions[29]. The collision at the Bullet cluster[30] evidences the nature of DM dynamics: very weak interactions with itself and the other types of matter involved in the collision (gas and galaxies). That observation confirms DM to be very weakly interacting, but also atomized, likely composed of simple particles.

In ΛCDM, CDM stands for Cold DM, i.e. composed of non relativistic particles. A too large contribution of hot DM does not allow the structure formation as it is known to happen, from smaller to bigger structures. That rules out neutrinos as the only explanation (neither the main contribution, by far), and also *axions* that would had been generated thermically in the primordial plasma. However, a different mechanism can produce non relativistic axions, see section 1.2.3 about axions and axion-like particles.

Therefore the DM candidates must be looked for beyond the Standard Model. If they are relatively heavy, more likely to be non relativistic, they are generically called WIMPs (Weakly Interacting Massive Particles). Also WISPs (Weakly Interacting Slim Particles), like axions, are candidates if produced so as not to be relativistic (see section 1.2.3). It was decided to talk only about WIMPs in this DM section because

[3]There could be a link, nevertheless, regarding *chamaleons*, see section 1.2.3.

they are the traditional DM candidate, searched in most of DM experiments, and the experimental approaches of WIMP searches are usually very different from those searching WISPs. But WISPs are as good DM candidates as WIMPs; and WIMPs are as well motivated theoretically (independently on the DM problem) as WISPs. There is no lack of WIMPs in the Standard Model proposed extensions, like SUSY (Supersymmetry). Reviews on the zoo can be found in [22, 31].

1.2.2.1 Direct detection of WIMPs.

WIMPs direct detection inherits the requirements and techniques from $\beta\beta0\nu$ decay experiments, in fact many of the first limits where given as by-products of $\beta\beta0\nu$ decay experiments[32]. The challenge becomes even more exigent because of the detection at low energies and the absence of a peak in the expected spectrum (see figure 1.5). In principle, no event rejection based on topology (like simple PSA) is powerful with low energy events beyond the rejection of multi-interaction events. The energy resolution cannot help to focus the search in a narrow range of interest. The discrimination of γ/β and α by other means is mandatory.

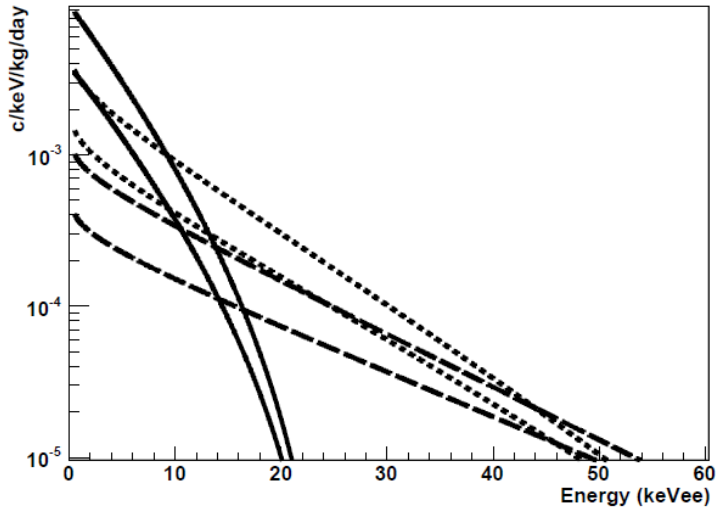

Figure 1.5: Examples of WIMP-induced nuclear recoil expected rates and spectra for a spin-independent nucleon cross section of 10^{-42} cm^2 and both 100 GeV and 500 GeV WIMP masses for three example target materials: germanium (dot), xenon (solid) and argon (dashed). Energy deposits are given in electron equivalent energy (see section 3.1.5.1). The figure is extracted from [33].

The use of hybrid bolometers has been specially successfully since the comparison of different energy measurements depends on the interaction type. Thus the capability of registering both heat and light (CRESST II[34], ROSEBUD[35]) or heat and charge (CDMS II[36], EDELWEISS II[37]) brings the possibility of selecting the nuclear recoils that might be caused by a WIMP scattering. The way DM

experiments are evolving is similar than that of the $\beta\beta0\nu$ decay ones. Therefore an increase of the available information (for discrimination) is procured. As well as scaling masses up, but also segmentation (for self-shielding).

The liquid TPCs have advantage in this sense since only their readout must be segmented, they guarantee the best self-shielding and the energy resolution limitations are not so critical in the DM context. They can be competitive because hybrid Liquid TPCs, reading both charge and light, have been developed (ZEPLIN III[38], XENON[39], LUX[40]) thanks to the combination of a liquid phase (which is the target itself) with a gaseous phase for charge amplification. For further scaling up, the use of argon, though apparently with worse scintillation/ionization properties, can be preferred because of its much lower cost. An argon-based liquid TPC, the ArDM project[41], will be soon operational at the Canfranc Underground Laboratory.

1.2.2.2 DM signatures and WIMP searches with TPCs.

The kind of spectra plotted in figure 1.5, with pseudo-exponential shape and a energy range depending on the WIMP's mass, makes very challenging the claim of a positive signal. To identify an excess of counts the background must be completely explained. The nuclear recoils caused by neutrons are practically not distinguishable from WIMP-induced ones. Underground sites usually have relatively high neutrons flux from fission in the rocks, which, in addition, is difficult to be characterized with accuracy. The recognition of an unambiguous extraterrestrial signature in the background signal could be indispensable to convince the DM community.

The most famous and significant case is that of the DAMA experiment. DAMA was based in NaI(Tl) scintillators and claims to have found the *annual modulation of the DM signal* in its background evolution. The WIMPs interaction rate is expected to be modulated by the changing relative velocity of the Earth with respect to the galaxy (and so with respect to the DM halo) along its translational movement around the Sun. Currently DAMA/LIBRA (experiment upgrade to 250 kg of NaI) has accumulated 0.87 ton $\times$ year along 6 complete annual cycles founding a positive signal with 8.9σ[42]. However the DM community has not accepted the result as a WIMPs direct detection evidence. It is also true that the claimed WIMP has been largely rejected by other experiments with, in principle, much better sensitivities (see figure 1.6). But the theoretical uncertainties still may have degrees of freedom to make compatible the DAMA positive results with the rest of negatives (see the next point about light WIMPs). The Canfranc Underground Laboratory will host the ANAIS[43] experiment that will try to confirm the DAMA result by means of the same basic technique, despite producing an independent result.

Another DM signature would require the use of a gaseous TPC: *the directional signature*, which is actually related with the annual and *daily* modulations. In galactic coordinates the WIMPs *wind* always comes from a fixed direction, approximately from the Cygnus constellation in the Earth's night sky view. Thanks to the correlation between the incident expected WIMP direction and the initial recoil's one, a

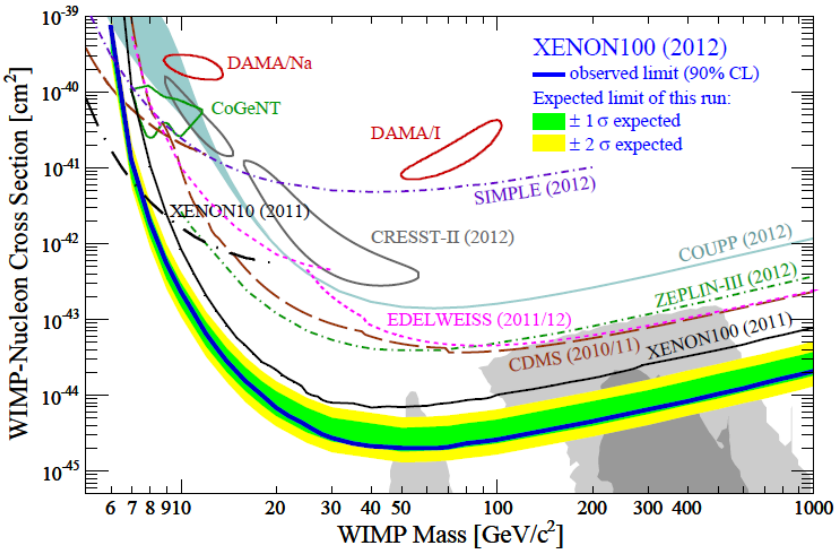

Figure 1.6: WIMPs exclusion plot summary for spin-independent WIMP-nucleon scattering and standard DM galactic halo[45] as published by XENON100[44], currently the most sensitive DM experiment. The remarked regions correspond to DAMA and other WIMP claims (by CoGeNT and CRESST), in principle excluded by XENON100. The XENON100 prospects are exploring the SUSY favoured region (grey $1\sigma/2\sigma$ contours). The plot shows the amazing improvement in experiments sensitivity, about 4 orders of magnitude, in the last decade, since in the early 2000's the DAMA region was not covered.

peak, that cannot be found in the energy spectra, should be identified in the direction distribution (see figure 1.7). In fact this method avoid the essential problem of neutron-induced background[4].

The experimental challenge is impressive: the reconstruction of low energy nuclear recoil tracks. It requires not only a gaseous TPC, but one working at low pressure, so decreasing the target mass. However, directionality allows a claim of a positive signal with less accumulation of statistics[46] which would be reinforced by an unmistakable galactic signature.

A correct reconstruction of the recoil track is challenging even before considering the practical details. The ionization theory of the recoils in the range of energies of interest is situated in the knowledge frontier (see section 3.1.5). A fully confident Monte Carlo simulation that demonstrates potential for a high efficiency direction and sense recognition is not available. The performance of the TPC must be outstanding from all the points of view: high gain (so as to assure a low energy threshold), and accurate imaging capabilities after the drift leaning on a highly granulated readout, in addition, a big chamber size (so as to procure a big target mass at low pressure).

[4] Another possibility the comparison of positive signals in different materials based on a different dependency on A, the atomic mass, of WIMPs and neutron cross sections.

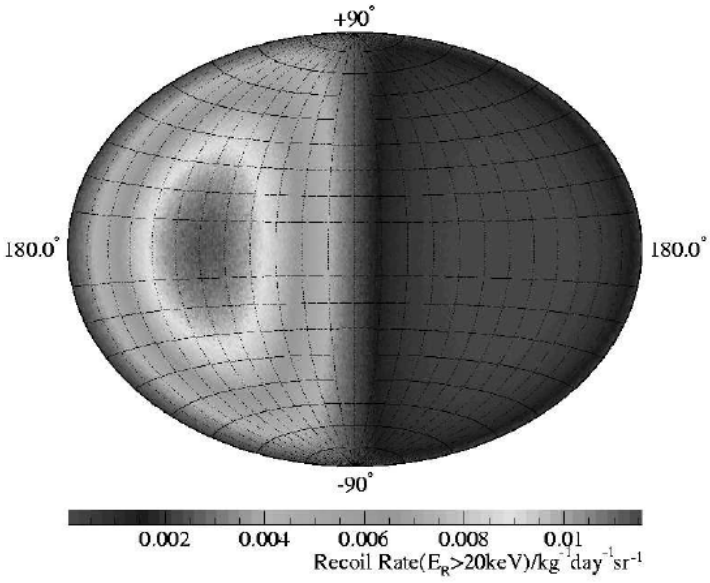

Figure 1.7: 100 GeV WIMPs induced nuclear recoils rate for cross section of 10^{-6} pb and standard DM halo model, as they would be registered by an ideal directional detector in galactic (l, b) coordintates. Extracted from [46].

Nevertheless there are several projects that undertook the design and operation of prototypes. The DRIFT[47] collaboration has pioneered the field, proposing and proving non conventional TPCs (see section 4.2.2.1). However DRIFT prototypes' performance has been limited in part due to the use of traditional wire planes readouts. The outstanding readout features demanded by the physical challenge make the present DM TPC projects opt for MPGDs: microdot in NEWAGE[48], GEM and micromegas in DMTPC[49] and micromegas in MIMAC[50].

These projects currently use fluorine as the target, instead of the classic option of argon or xenon. The reason is that only in the case of a WIMP cross section that were enhanced for non-zero spin nuclei, like fluorine, their discovery potential would be competitive. Furthermore the usage of a light nucleus brings practical advantages since the recoils are longer[5]. The community is growing, achieving milestones and generating expectations and gave birth to an international forum aiming to share R&D progress and also boost theoretical and simulation studies: CYGNUS (Cosmology with Nuclear Recoils)[51].

1.2.2.3 Low mass WIMPs and TPCs.

SUSY models prefer WIMP masses of ∼100 GeV; it is also true that sensitivity of common direct detection experiments sharply decreases for masses lower than ∼ 10 GeV because of the threshold of the discrimination techniques (see figure

[5]Unfortunately the use of ^{3}He is practically forbidden at present because of its shortage.

1.6). Therefore the window of masses < 10 GeV is not strongly constrained, though not theoretically forbidden. A low threshold, at the sub-keV level, is the main requirement to be competitive, even with a raw counting detector and low target masses.

The case for light WIMPs has been recently reinforced by the claim of an excess of counts in a novel low-noise germanium, CoGeNT[52], and analysis that proposes that a light neutralino could bring conciliation of CoGeNT excess and DAMA signal while the rest of experiments would be no sensitive to it[53, 54].

TPCs could have a contribution to this question. First, simple recoil versus γ/β event discrimination based on event topology (track length) could be powerful. Even operating at atmospheric pressure, it could lead to relatively low discrimination thresholds ~ 10 keV. A preliminary study on that possibility is presented in section 7.1. Second, TPCs equipped with micromegas readout have shown excellent discrimination capabilities as X-rays detectors below 10 keV. X-rays and nuclear recoils are not distinguished in this approach, but the discrimination for β, α, muons and noise rejection is efficient. The case is largely discussed in chapters 8 and 9. The same detector type has been already operated underground producing encouraging results (see chapter 10). These detectors, thanks to the micromegas readout, seem to be already able of threshold below the keV. Moreover, when operating in optimum conditions, there is no sign of an increase of the background level at low energies (present software threshold = 2 keV) while software efficiency from analysis discrimination criteria remains high.

The DM line of the T-REX project is oriented to this approach as a first goal. The detector mass of the prototypes already tried underground is easily scalable. The T-REX research summarized in section 5.1 even points to the possibility of increasing the gas pressure up to several bars without worsening the detector performance.

1.2.3 Axions, ALPs and WISPs.

Axions are consequence of one of the most traditional and best motivated extensions of the Standard Model (SM). The Quantum Chromodynamics (QCD) lagrangian naturally accepts a term with the following form[6]:

$$\mathcal{L}_{\bar{\theta}} = \bar{\theta}\frac{\alpha_s}{8\pi}G^{\mu\nu a}\tilde{G}_{\mu\nu a} \tag{1.6}$$

where G is the gluon field and $\tilde{G}$ its dual, α_s the strong coupling constant and $\bar{\theta}$ just parametrizes the term's strength. Such a term violates charge-parity (CP) symmetry, as electro-weak interactions actually do, and has observational consequences, like the prediction of an electric dipole moment for the neutron (nEDM). However

[6] It is not only the possibility, but the therm had been invoked[55] to bypass another SM deficiency, the $U_A(1)$ problem[56].

experimental tests on nEDM constrain $\bar{\theta} \lesssim 10^{-10}$[57]. This extreme fine-tuning which has to be assumed by the SM is known as the *strong CP problem*[58].

The Peccei-Quinn (PQ) mechanism[59, 60] proposes to see (1.6) as $\sim aG^{\mu\nu a}\tilde{G}_{\mu\nu a}$, where a is a new field associated with a new $U(1)$ global symmetry (the PQ symmetry), instead of a fixed parameter. The PQ symmetry is spontaneously broken at scale f_a, which is not fixed by theory, then $\mathcal{L}_{QCD}$ is CP-conserving as result of the dynamic relaxation to a minimum where $\mathcal{L}_{\bar{\theta}}$ vanishes. The field a would manifest itself as a pseudo-Nambu-Goldstone boson[61, 62]: the *axion*.

Since f_a is higher than 10^5 GeV, otherwise the axion would have been discovered in accelerators, its mass is small because is acquired by mixing with pions

$$m_a \sim m_\pi \frac{f_\pi}{f_a} \simeq 0.60\,\text{eV}\,\frac{10^7\,\text{GeV}}{f_a} \tag{1.7}$$

with $m_\pi = 135$ MeV and $f_\pi \approx 92$ MeV. The axion has a coupling with photons

$$\mathcal{L}_{a\gamma} \equiv g_{a\gamma}\vec{E}\cdot\vec{B}a, \quad g_{a\gamma} \sim 1/f_a \tag{1.8}$$

that leads to photon-axion oscillations in the presence of external magnetic fields[63]: the Primakoff[7] conversion of photons into axions (in the core of stars) and the inverse Primakoff conversion of axions into photons (in helioscopes, see later on). From (1.7) and (1.8)

$$m_a \sim g_{a\gamma} \tag{1.9}$$

and the three equations summarize the properties of the generic axion. Depending on the model an extra coupling with SM fermions can be postulated and the proportionality factors are varied[64].

They are called *axion-like particles (ALPs)* those that are light and share the axion phenomenology, i.e. the axion-like coupling with two photons (Primakoff effect), but are nor motivated by the strong CP problem neither linked with the PQ symmetry. In contrast to original QCD axions, for ALPs m_a and $g_{a\gamma}$ are independent parameters. They are typically consequence of new symmetries by SM extensions that are broken at high energy scales (like axions themselves), but also appear in string theory. They are an important key in the context of the low energy frontier of Particle Physics[65].

Several astrophysical and astronomical observations have been interpreted as hints for ALPs. To address the problem of the excessive transparency of the intergalactic medium to very high energy γ ($\gtrsim 100$ GeV), ALP-photon oscillations have been suggested. For instance as explanation for the observation of high energy γ from active galactic nuclei[66, 67, 68] and for the detection of ultra high energy cosmic rays ($\gtrsim 10^{18}$ GeV) correlated with very distant blazars[69]. The anomalies

[7] Named Primakoff by analogy with the Primakoff effects of pions.

observed in the white-dwarf (WD) stars' evolution could be a hint for an additional cooling mechanism via ALP emission[70, 71, 72].

A more generic category, that includes ALPs, is named *WISPs (Weakly Interacting Slim Particles)*, because of the role they can play in DM problem as an alternative to WIMPs (see just later on). Examples of WISPs are paraphotons[73], minicharged particles[74] and chameleons[75]. The latter are related with *quintessence* field theories to explain the Dark Energy and, inside particular contexts still in early stages of development, could be classified as ALPs; thus an experiment aiming detection of ALP might carry out a first Particle Physics tests of Dark Energy theories[76].

1.2.3.1 ALPs and DM.

Due to its small mass the present relic from the thermally produced axions in the primordial plasma would contribute to the hot dark matter, so they cannot account for the contribution required by the ΛC(old)DM model. In fact the astronomical constrains to the hot DM contributions impose an upper bound for the axion mass $m_a < 0.72$ eV[77], since the thermal production mechanism is more efficient for larger masses.

However, another two related mechanisms could produce non-relativistic axions[78, 79]. The *vacuum realignment* relies in the oscillation of the a field around the CP-conserving minimum. At the same time domains with different populations can be created, together with the corresponding borders or topological defects, which can relax producing a new axions population. The impact on the present axion's density depends on whether the inflation happens before or later than the PQ symmetry breaking[80].

In the second case the a field is homogenized by the inflation and no domains are left, only the particular primordial domain affects to the calculations. The bound imposed for m_a by the realignment mechanism, this time for accounting the whole DM contribution of the universe, is lower than the bound previously mentioned by the total amount of hot DM. Naturally a prediction for masses higher than μeV is deduced[80]. Smaller masses are not strictly forbidden, but must be argued by anthropic reasons. In the first case the calculation is much more complex, in principle a higher mass would be required, but for both cases axions could account for the cold DM.

These mechanisms are even more interesting since could be generic for ALPs from similar broken symmetries. Thus they became potential solutions of the DM problem in a wider range of the $g_{a\gamma}$ vs m_a space of parameters[81]. The, up to now, negative observation of WIMPs at LHC might favour the WISPy solution for the DM problem. The idea is also reinforced by the discovery of the Higgs, as a confirmation of the breaking symmetry mechanisms, and because its actual mass, relatively light, is not comfortable for SUSY expectations.

1.2.3.2 Direct axions detection. Helioscopes.

The experimental strategies for axions direct detection, all of them based in the Primakoff effect[8], can be classified according to the source of axions. *Haloscopes*[63] aim at direct detection of relic axions. The significance of such a discovery would be maximum as would imply a direct confirmation of axions as DM components. However the theoretical uncertainties are the biggest compared with other strategies. From the practical point of view the relic axions energies require the detection of microwave photons in resonant cavities. The resonant cavities are very sensitive for a given axion mass, but extending their sensitivity to wider mass ranges is painful (see figure 1.10). The opposite strategy is the use of laboratory axions from lasers in photon regeneration, also known as *light-shinning-through-wall* (LSW), experiments[82]. The theoretical uncertainties are minimized, but sensitivity is also smaller, basically because two consecutive Primakoff conversions are needed.

The *helioscope*[63] gets a nice balance between both strategies. The detection of solar actions provides an intense flux of relatively high energy axions (X-rays range, see figure 1.8) whose calculation[83, 84] relies in the rather robust Solar Physics. Its principle is the detection of X-rays from axion inverse-Primakoff conversion, in a transverse mangetic field, in correlation with the Sun (see figure 1.9).

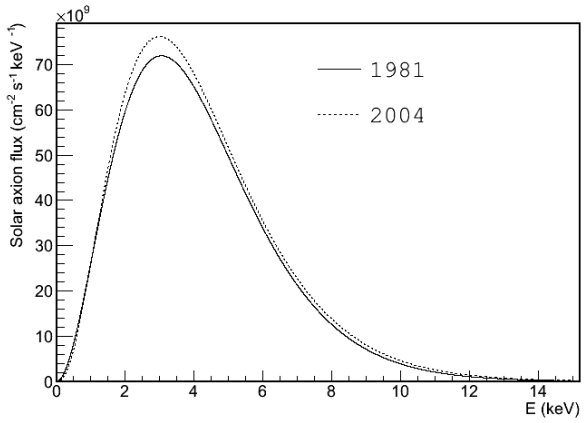

Figure 1.8: Solar axions flux spectrum. An early calculation[83] is compared with a 23 years newer one[84].

[8] therefore also susceptible to detect ALPs.

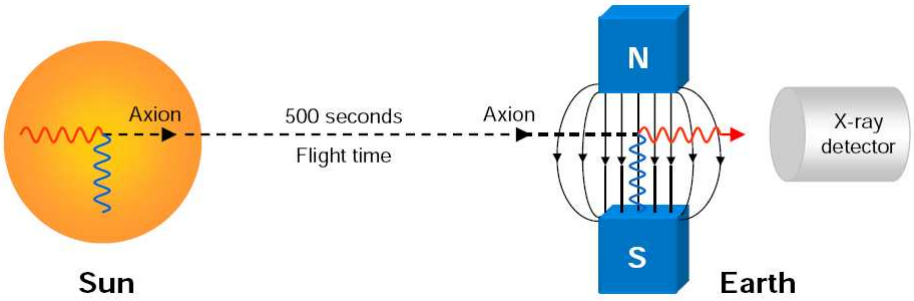

Figure 1.9: Illustration of the helioscope concept. Due to Primakoff effect in the core of the Sun, the virtual photon (vertical blue) comes from e ,Ze (solar plasma); while for the inverse conversion in the helioscope the source of the virtual photons is $\vec{B}$, the magnet field.

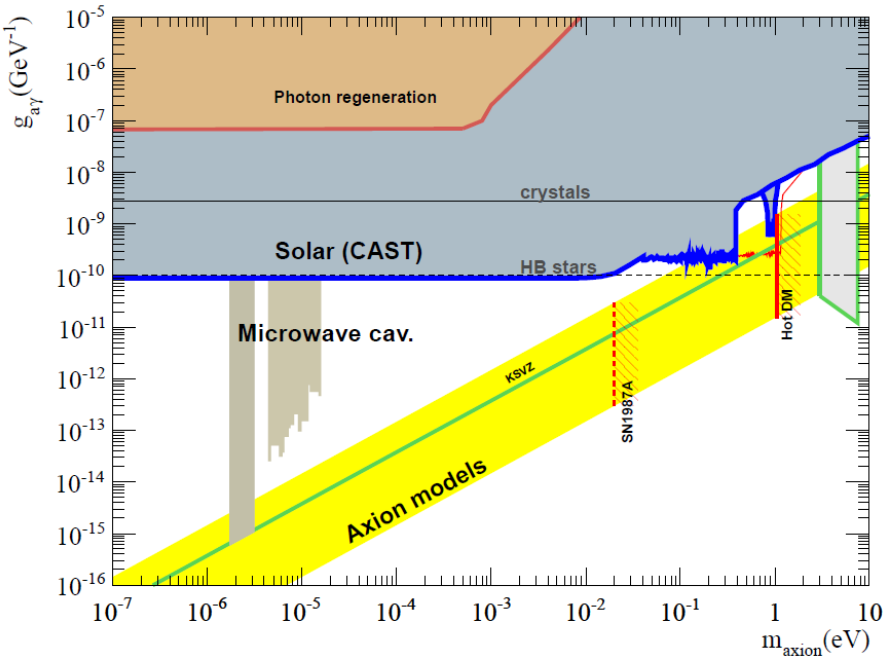

Figure 1.10: ALPs summary exclusion plot, taken from [86]. The yellow band represents the true axion models, with linked m_a and $g_{a\gamma}$. Helioscopes (blue line) are covering the biggest area of the parameters space, with better sensibility than LSW experiments and more versatile that MW cavities. Particularly CAST, the red thin line is an expectation for the 2012 campaign, touching the axions KSVZ line up to the Hot DM limit. The regular region corresponds to vacuum runs, while the bound is more irregular during the buffer gas scan. The axions preferred window for DM, $10^{-6} < m_a < 10^{-3}$ eV, could be explored beyond the bounds imposed by HB stars[87] if CAST's vacuum results were superseded (see section 8.1.1 and particularly the 2013 expectation plot in figure 8.4).

The conversion probability for a magnet with a transverse magnetic field B along a length L is[63]

$$P_{a\gamma} = 2.6 \times 10^{-17} \left(\frac{B}{10\mathrm{T}}\right)^2 \left(\frac{L}{10\mathrm{m}}\right)^2 (g_{a\gamma} \times 10^{10}\mathrm{GeV})^2 \mathcal{F} \tag{1.10}$$

where

$$\mathcal{F} = \frac{2[1-\cos(qL)]}{(qL)^2} \tag{1.11}$$

accounts for the coherence of the process, being q the momentum transfer. For a magnet length about 10 m the coherence is preserved up to $m_a \sim 10^{-2}$ eV, behind this axion mass the sensitivity of the experiment is constant and then drops (see figure 1.10). However it can be extended to higher masses by the technique of introducing a buffer gas in the magnet beam pipes[85], then scanning m_a in a similar way resonant cavities do in haloscopes.

1.2.3.3 TPCs and ALPs searches.

The interest in TPCs for ALPs searches is motivated by their merits as low background X-rays detectors for complementing a magnet in the implementation of a helioscope. In the study [86] the expression (1.10) is further developed to include the detection of the X-rays and the different aspects that influence a helioscope's discovery potential are quantified in a factorized figure of merits: $f_H = f_M f_O f_D f_T$ (Helioscope, Magnet, Optics, Detectors and Tracking, respectively):

$$f_M = B^2 L^2 A, \quad f_O = \frac{\varepsilon_o}{\sqrt{a}}, \quad f_D = \frac{\varepsilon_d}{\sqrt{b}}, \quad f_T = \sqrt{\varepsilon_t t} \tag{1.12}$$

Inside f_M, B, L and A are the magnet field, length and cross sectional area. f_O represents the possibility of a focussing device which concentrates the signal in a spot with area a and efficiency ε_o; if such a device is not used, $f_O = A^{-1/2}$ (in both cases the whole area A is assumed to be covered). The importance of detectors is manifested in f_D through its efficiency ε_d and background b, expressed in counts per unit area and time. The exposure f_T is related with the time extension of the experiment t and the fraction of time the helioscope is able to track the Sun ε_t.

The arguments for the proposal of a TPC as a suitable low background X-ray detector for a helioscope, specially TPCs equipped with micromegas, rely on its operation in the CAST experiment (the present state-of-the-art helioscope) during 10 years, which is reviewed in chapter 8 and discussed in detail in the followings chapters 9, 10 and 11. Although the impact of f_D in f_H seems to be modest, its improvement has been relevant enough so as to motivate new data taking campaigns in CAST (see section 8.1.1). Moreover the prospects to achieve ultra-low background micromegas detectors at surface is one of the ingredients of CAST's proposed successor: the International AXion Observatory (IAXO)[193].

Chapter 2

TPCs and Micromegas.

Contents

2.1 The TPC concept.

The *Time Projection Chamber* (TPC) idea was possible thanks to the development of *the Multi-Wire Proportional Chamber* (MWPC). The use of gaseous detectors in Particle Physics is as old as the field itself[89] since it was seen that ionizing radiation produces discharges in gases if a strong electric field is applied. The technical solution of amplifying the charges by means of the electric field created in a wire plane, but producing a signal proportional to energy, really meant a revolution in Particle Physics instrumentation. The invention of the MWPC by Georges Charpak in 1968[90] provided the physicists with a powerful tool for particle identification and tracking: not only energy measurement but also the energy loss rate (stopping power $\mathrm{d}E/\mathrm{d}x$, see section 3.1) was available, good spatial and time resolution, scalability, low material budget, high trigger rate capabilities. Two perpendicular wire planes can be superposed in order to complete the spatial information. A series of planes can be piled up to register slices of the ionization path.

The structure can be simplified if a single MWPC (or any other type of readout structure) is installed at the end of a gaseous chamber where a constant electric field is applied. That is a *drift chamber* whose working principle is sketched in figure 2.1. The electric *drift field* has to be not so strong as to produce charge amplification, but intense enough so as to safely drive the primary charges produced by ionizing particles through the chamber to the wires. Such a device is able to register the ionization path projection on its readout plane.

If the front-end electronics connected to the wires are fast enough, time differences between signals at wires can be quantified. These relative delays are generated

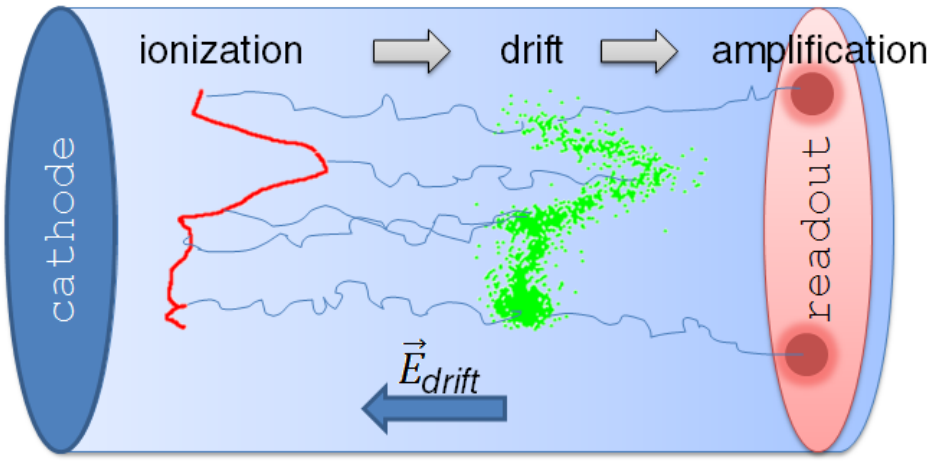

Figure 2.1: The drift chamber working principle, which is composed of three basic processes. First, *ionization*: a charged particle release electrons (primary charges) along its path in an amount that is proportional to the energy deposited in the gas. Second, *the drift*: the application of an electric field is able to drive the primary charges to the readout plane. Third, *the amplification*: the generation of good quality electronic signals requires the amplification of charge or light by means of any specialized structure. That has been classically a MWPC, despite nowadays MPGDs (see next section) are replacing them. When the readout can record the time differences between the several signals generated for the same event, the drift chamber evolves to a TPC.

during the drift of the primary charges to the wire, hence they are ideally proportional to the relative distances between the particular positions where ionization was produced projected on the drift field axis. The correct interpretation of these time differences allows the full three dimensional reconstruction of the track. That was the TPC proposal by David Nygren in 1974[91, 92], only six years after the MWPC.

2.2 New generation: MPGDs and micromegas.

Micro-Pattern Gas Detectors (MPGD) replace the MWPC with a readout implemented by means of printed-circuit-board (PCB) techniques, thus the typical anode's segments dimensions are $\sim$100 μm . That enhances some of the MWPC features: the spatial resolution can become $\sim$10 μm [93], faster signals $\sim$10-100 ns (see section 4.5, particularly figure 4.32) and higher counting rates $\sim 10^6$ counts/mm^2[94].

The first MPGD was the Micro Strip Gas Counter (MSGC) conceived by Oed in 1986[95]. In the MSGC, basically the MWPC was printed as metallic strips in a glass base (see figure 2.2). New MPGD designs multiplied in the 90's: we will remark the *microdot* gas avalanche chamber[96] (1995), the *MICROMEGAS (MI-CRO-MEsh-GAseous Structure)*[94] (1996), the *GEM (Gas Electron Multiplier)*[97] (1996), the *WELL* detector[98] (1999) and the *Micro PIxel Chamber (μ-PIC)*[99] (2004).

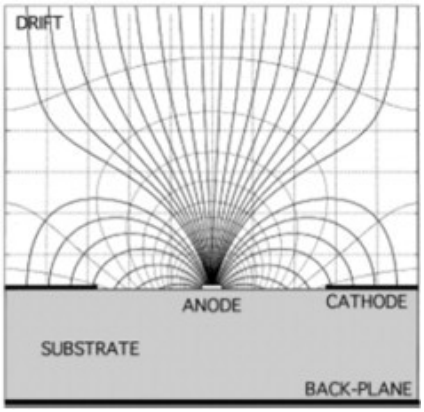

Figure 2.2: Field configuration in a MSGC. The field lines are distorted from the chamber drift region and the readout pattern design makes them condensate towards the anode. There is a clear dependence of the field on the position.

The introduction of micromegas by Ioannis Giomataris meant another stage in the readout evolution because the basic electric field layout is changed. The introduction of a flat electrode over the printed strips (gap $\sim 25-130$ μm) changes the typical shape of the amplification field produced by wires, with cylindrical symmetry, to a much simpler near parallel planes geometry. While for the former the field intensity depends on the distance r to the wire as $E \sim 1/r$, for the latter a constant amplification field E_{amp} is produced in all the amplification region (see figure 2.3 and compare with 2.2). That disposition, where a high E_{amp} acts since the beginning of the avalanche process, reports benefits for the amplification statistics (see section 4.4.2).

Another essential advantage is the fact that drift and amplification regions are practically decoupled. Thus there is E_{drift} that can be optimized regarding the drift properties of the gas while E_{amp} can be independently chosen so as to get a desired gain during the amplification process. The amplification does not depend on E_{drift}. It is needed, of course, that the drifted electrons enter the amplification region, so the flat electrode over the anode must be actually a grid, *the mesh*. The sharp increase of the electric field lines density below the mesh (see figure 2.3) can assure, in most of the situations, the electrons passage through the mesh not to be a practical limitation (see section 4.3).

The main technological challenge is the suspension of the thin mesh, typically $\sim$3–5 μm thick, assuring it to be parallel along all the area. Inhomogeneities of the gap would produce gain spatial dependence (though the problem is not so severe as it seems, see section 4.4.1.1), or even sparks in particulary bended zones; the quality of the mesh manufacturing is essential for the same reason. The solution adopted by all micromegas versions is the presence of periodic insulator spacers, *the pillars*, between the mesh and the anode. In early micromegas the pillars were glued to the anode and electroformed meshes were suspended on them. The electrostatical forces were mainly responsible of the mesh planarity, though peripheral tensors were also needed (as well as considerable skill and expertise). Latter developments[100] found ways to attach the pillars to the mesh.

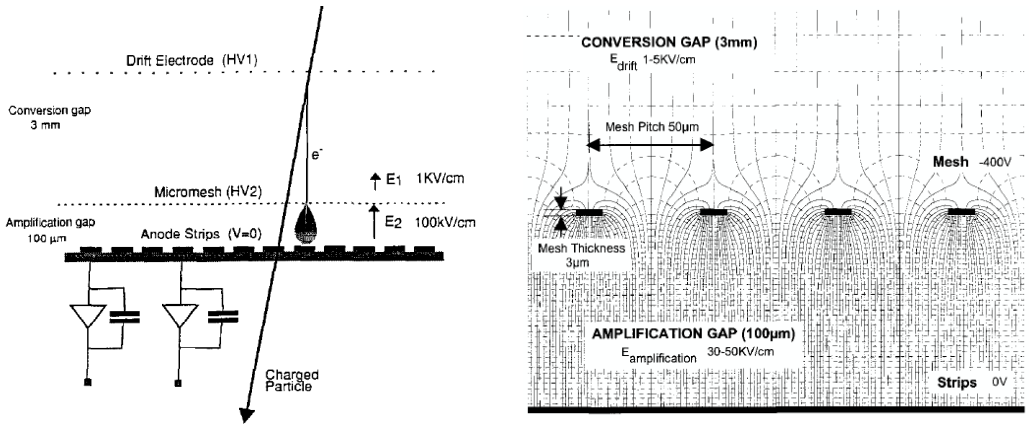

Figure 2.3: Left: the TPC concept with a micromegas readout as it was first presented[94]. The mesh divides the chamber into *drift-conversion volume* and *amplification volume*. The primary electrons released by ionization by charged particles are driven to the mesh by a constant electric field, E_{drift}; the drift velocity is also constant (see section 4.2.1). Once in the amplification gap, where there is an also constant E_{amp}, the avalanche process occurs. Fast front-end electronics connected to the anode strips register signals which are ideally proportional to the projection of the ionization yield path. The mesh signal can provide a common trigger while the time differences between mesh and anodes signals allow the reconstruction of the drift coordinate. Right: electric field layout in a drift chamber with micromegas. Note both main regions have constant electric field, with only a fast transition in between. The ration between both fields strength, typically $E_{amp} \sim 100 E_{drift}$, produces a condensation of the electric field lines that makes the mesh near fully transparent.

More recent micromegas manufacturing techniques build the complete micromegas amplification structure, anode-gap-mesh, as a unit, so as there is no freedom allowed for the mesh misalignment which relies in the manufacturing process accuracy. The robustness and homogeneity of these new micromegas, *bulk* and *microbulk* types (see next sections), have really boosted their applications, in particular allowing a feasible scaling to larger surfaces. After *classical* micromegas, bulk and microbulk have been tested in the CAST experiment; a summary of CAST experience with them is reported in section 8.2.1.

2.2.1 Bulk micromegas.

The *bulk* type of micromegas is the most similar one to a commercial micromegas thanks to the use of an actually commercial woven wired mesh (available in several materials: copper, iron, nickel) and a fast, and inexpensive as well, manufacturing process (see figure 2.4 left). Such a mesh (see figure 2.4 right) is stretched and then encapsulated in an isolator material, named vacrel, to lately remove part of the vacrel, remaining the pillars together with additional protection structures as

border reinforcements or contact protections. The mesh is attached between the pillars, so they emerge over the mesh giving additional protection. This structure, together with the hard woven mesh of 30 μm thickness wires, result in a remarkably robust and flexible micromegas, that is not easily damaged by touching or by sparks, which can be glued to a conventional PCB readout.

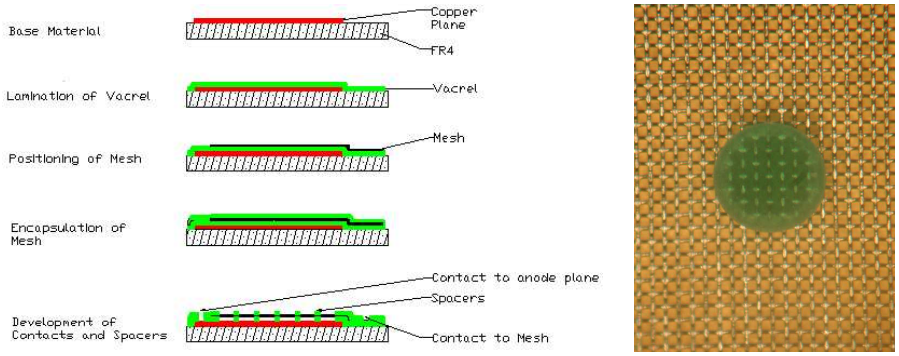

Figure 2.4: Left: sketch of the bulk manufacturing process[101]. Right: detail of the iron woven mesh showing one of the vacrel pillars.

However the bulks performance is limited by the nature of their mesh, which is relatively thick and irregular (presenting nodes). To assure the geometrical desirable condition of the amplification gap being much longer than the mesh thickness, bulks typical gap is 128 μm . That relatively long gap limits the velocity of their signals and they operate at lower amplification fields than other micromegas types. Nevertheless they are able of very high gain and acceptable energy resolution. Bulks performance is shown and compared with microbulks (the other recent micromegas version, see next section) in chapter 4. The fact that they are used together with PCB readouts makes them non convenient from the radiopurity point of view. However it may exist the possibility of using readout bases of a different nature.

The pillars, about 300 μm diameter, are relatively spaced, around 2 mm. Therefore the insulator amount of material between electrodes is minimized and bulks have low capacitance per unit area, what helps to build large areas without a limiting noise and there is no need to segment the mesh. Thus large areas are possible, like projected in MAMA (Muon Atlas Micromegas Activity) for the ATLAS detector upgrade for sLHC (LHC with enhanced luminosity)[102]. Bulks are the most popular micromegas type, in application to several experiments including the Rare Event Searches T2K[103] and MIMAC[50].

2.2.2 Microbulk micromegas.

The *microbulk* type of micromegas[105] was added the prefix *micro* to emphasize the better accuracy of their manufacture with respect to bulks and the return to very thin meshes, 5 μm , and narrower amplification gaps: 50, 25 μm . However they could be said to be really *bulk* micromegas because the mesh is not separately built and attached, like in bulks; in contrast, in microbulks, the raw material is a double clad kapton[1] foil (copper-kapton-copper) from which the mesh, gap pillars and anode are built as an unit.

The amplification structure is produced thanks to the state-of-the-art lithography techniques, particularly the etching of the kapton through the mesh holes to create the amplification volume. Thus the homogeneity of the gap has $\sim 1\,\mu$m accuracy, so the energy resolution is outstanding even for a MPGD (see proofs of their performance in 4, particularly figure 4.22 right) and the whole detector is a robust block (see figure 2.5 left). Microbulks are more fragile than bulks to handling and sparks due to their delicate mesh, however more robust against continuous vibrations and tensions, and generally more stable.

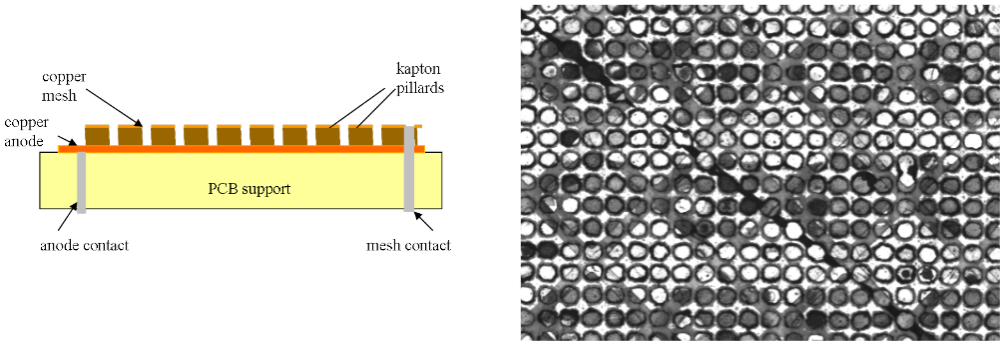

Figure 2.5: Left: sketch of the typical microbulk prototype (see a photo in figure 4.22 left). Right: microscope view of a CAST microbulk with a pixel-like anode's pattern. The circles delimit the areas where the kapton has been removed by etching.

Because the kapton etching is activated from the mesh printed holes, the amplification volume consists of a series of separated cells below the holes, rather than a common volume with pillars in between (see figure 2.5 right). That increases the capacity per unit area, with respect to bulks, what might mean a limitation for microbulks scaling to larger areas (they can be segmented, nevertheless). However a first experience with a relatively big microbulk is encouraging, see section 5.5.3, particularly figure 5.10. Moreover the manufacturing techniques are still progressing and new microbulk versions with true pillars are currently developed. On the other hand, there could be advantages for the isolated amplifications cells sketch related with *geometrical quenching* (see section 4.4.1.2).

[1] Kapton: flexible polyamide with very good insulating properties.

The microbulk basic structure can be glued to a complex readout plane. One advantage is that the readout layout can be also built by means of the lithography techniques using the same raw materials, therefore the whole microbulk is radiopure (see section 5.4). Readouts as complex as those used for pixel-like 2D CAST microbulk micromegas have been built in this way; the process, from the basic manufacturing of the mesh to the complete detector, is sketched in figure 8.14.

Microbulks are the most recent micromegas approach (ca. 2007), their manufacturing is exclusive at CERN and they still need to be better known by the Rare Event Searches community. However microbulk may have the best potential applicability to the field. They are gathering merits in the running CAST experiment (three of its four detectors are microbuks at present, see chapter 8) and also tested by the NEXT-micromegas R&D line[107].

2.2.3 InGrid.

InGrid[108, 109] are micromegas-like structures integrated in silicon chips. Thus a charge amplification stage and a high granularity readout are practically undistinguishable. They are descendants of the development line of high granularity pixel readouts based in CMOS technology that were commonly used as complement for MPGDs (usually GEM and micromegas) in small gaseous chambers. The MediPix chip[110] (whose name evidences the fact it was proposed for medical applications), was a matrix of photon counters. But the more recent TimePix[111] has the capability of measuring the arrival time of the avalanches, since it was already conceived to instrument a TPC.

In InGrid, wafer post-processing based in SU8 photo-resistor allows the creation of a micromegas-like mesh and pillars over the chip. That technique produces an outstanding accuracy of mesh manufacturing and a very good alignment between the mesh and readout patterns (see photo in figure 2.6). The InGrid fabrication process and performance are studied in detail in [112].

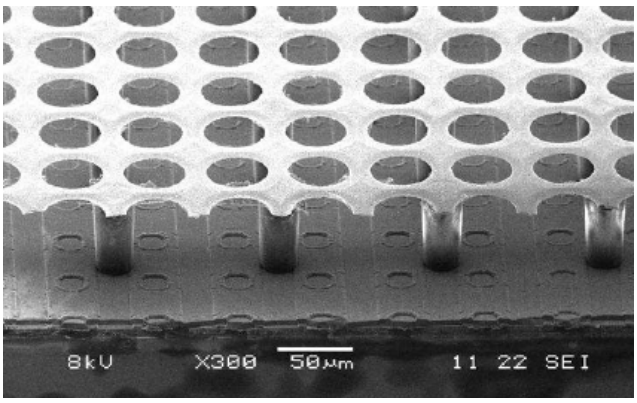

Figure 2.6: Microscopic photograph of a InGrid integrated on a TimePix chip, extracted from [112].

In spite of their impressing tracking capabilities, InGriD detectors still have to demonstrate they can fulfil some of the requirements to be competitive in Rare Event Searches: essentially scaling up and radiopurity. In principle, the fact they are based on Silicon technology is an advantage for any technical challenge and silicon chips are known to be radiopure, hence InGrids may be radiopure themselves by means of an optimized wafer post-processing. The upcoming installation of an InGrid detector in one of the CAST experiment's detection lines will be a significant step towards the confirmation of InGrids as low-background detectors.

2.2.4 GEMs

It is worth to comment on GEMs since they are, perhaps, the most known MPGD. At first sight, they can seem to be very similar to microbulks, since both are built from a double copper-clad kapton foil (50 μm thick) which is made holes in by etching. However, in the case for a GEM, the foil is completely perforated from face to face (see figure 2.7 right). The two copper faces are used as electrodes to produce an intense electric field whose lines concentrate through the holes that work as amplification regions.

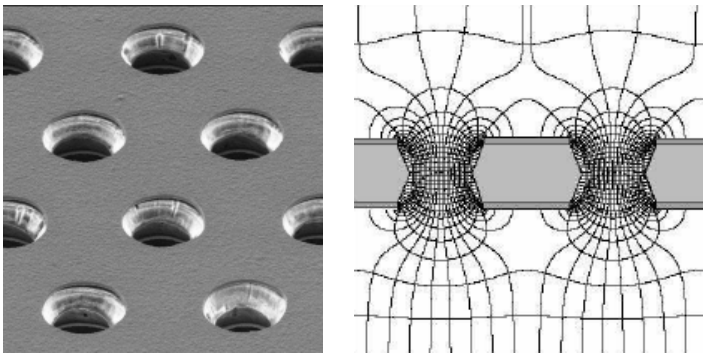

Figure 2.7: Left: microscope view of a GEM. Right: electric field configuration of a GEM.

The main difference with micromegas is the fact that there is no a clearly defined anode, therefore, despite about 50% of the avalanche electrons being collected by the electrodes, the induced signal is more bipolar (see section 4.5). The electric field configuration is a bit less regular, since they are two transition zones. One advantage of micromegas is how they are naturally integrated with a readout, as a single and robust unit, with correlation between mesh and anode designs, in particular in the case for the microbulks.

However the usage of GEMs as a floating pre-amplification stage over an independent readout brings a versatility that has made them very successful. They can work together with PCB readouts, CCDs or other MPGDs, typically MSGCs and micromegas. The idea can be generalized by the implementation of double or triple GEM (see figure 2.8) for higher amplification gains.

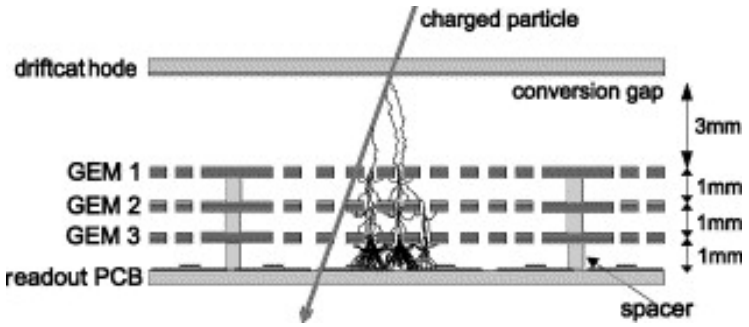

Figure 2.8: Sketch of a drift chamber operating a triple GEM[113].

The usage of a GEM cascade degrades the spatial resolution and implies construction difficulties; an alternative to avoid these problems can be the introduction of a thicker GEM (THGEM[114]) with 400 μm gap.

Chapter 3

Interactions of particles in the micromegas chamber.

Contents

This chapter, and the next one, aim to be a brief report on the processes involved in the detection of particles by gaseous chambers equipped with micromegas. It is not a Physics lesson, not complete nor deep, but only focused in the good understanding of this kind of detectors' phenomenology; the cases, always of direct interest for Rare Event Searches, are discussed in the context of a micromegas detector. The processes are described in chronological order, from the interaction of the particle to the amplification in the micromegas. Own research results are included, sometimes for illustration because the familiarization with this phenomenology, the creation of references, has been a goal of this work; others because our R&D lines were devoted to processes which are specific of micromegas or some particular cases interesting towards Rare Event Searches applications.

This chapter treats the physical absorption of energy from particles and radiation by the gas which triggers the detection mechanism when they interact in the chamber's sensitive volume. We will also pay some attention to processes which occur in the detector neighborhood, but can produce a secondary response of the detector. All the signal generated in the micromegas readout is finally due to the production of free charges by ionization by a charged particle (with exception of chambers equipped with light sensors); therefore this is the fundamental process we are going to start with and study in more detail.

3.1 Ionization by charged particles.

3.1.1 Coulomb scattering.

The ionization differential cross section is a previous result to obtain the ionization yield, however it is interesting by itself. It is important to define the physical picture and assumptions. The electron, the target which is susceptible to be hit resulting in ionization of the medium, is supposed to be free and at rest; thus no dependence on the medium can be expected from this scope. The interaction between the ionizing particle and the electron is purely Coulombian and the mass of the former makes the electron's one negligible (therefore the particle mass will not appear explicitly in the result). That is practically the famous Rutherford's problem, with just opposite projectile and target, and its deduction can be found in text books (semi-classical calculation by Bohr in [115] or by means of Fermi and Yukawa theories in [116]). When related with T, the energy lost by the particle and transferred to the electron in an individual Coulomb collision, it looks like

$$\frac{\mathrm{d}\sigma}{\mathrm{d}T} = \frac{2\pi z^2 \alpha^2}{m_e c^2 \beta^2} \frac{1}{T^2} \tag{3.1}$$

with z the net charge of the particle and $\beta = v/c$ its relative velocity; being $\alpha = \frac{e^2}{4\pi\varepsilon_0 \hbar} \approx \frac{1}{137}$ the fine-structure constant and m_e the electron mass. The expression (3.1) is valid while the ionizing particle, much heavier than an electron, is fast enough so as the electron can be considered to be at rest, and the energy transfer high enough to consider the electron to be free. The relevant remark is that $\frac{\mathrm{d}\sigma}{\mathrm{d}T} \propto 1/T^2$ what means a large tail in the dependence which assures that relatively high energy transfers are not so unlikely.

3.1.2 Mean energy loss. Bethe-Bloch formula.

The mean energy lost in ionization when the particle passes through a volume element of material, named *electronic stopping power*, is computed from (3.1) by weighting all the possible energy transfers:

$$\frac{\mathrm{d}E}{\mathrm{d}x} = \frac{\mathrm{d}N}{\mathrm{d}x} \int_I^{T_{max}} \frac{\mathrm{d}\sigma}{\mathrm{d}T}\, T\, \mathrm{d}T \tag{3.2}$$

where the medium, with atomic and mass numbers Z and A and mass density ρ is described as a homogeneous density of free electrons at rest

$$\mathrm{d}N/\,\mathrm{d}x = N_A (Z/A)\rho \tag{3.3}$$

being N_A the Avogadro's number; and the integral is extended from I, a sort of *mean ionization potential*, and, T_{max}, the maximum energy transfer allowed by the collision kinematics. Applying that the ionizing particle mass $M \gg m_e$:

$$T_{max} \simeq 2m_e c^2(\beta\gamma)^2; \quad \gamma = \left(\sqrt{1-\beta^2}\right)^{-1} \tag{3.4}$$

The final realization of this calculation for the electronic stopping power is the notorious Bethe-Bloch formula

$$-\frac{\mathrm{d}E}{\mathrm{d}x} = N_A\,\rho\frac{Z}{A}\,\frac{2\pi z^2\alpha^2}{m_e c^2\beta^2}\,2\left[\ln\left(\frac{2m_e c^2}{I}\beta^2\gamma^2\right)-\beta^2\right] \tag{3.5}$$

Although the final expression (3.5) has been obtained using higher order corrections, the simple description of the medium by (3.3) can still be recognized as well as the integration of (3.1) made in (3.2) using (3.4), which directly brings the two main terms that dominate the formula's character: $1/\beta^2$ at low velocities and the logarithm at high velocities (see figure 3.5). The former is responsible of the typical increase of the ionization yield experimented by charged particles at the end of their trajectory, usually called *blob* (see figure 3.1 right).

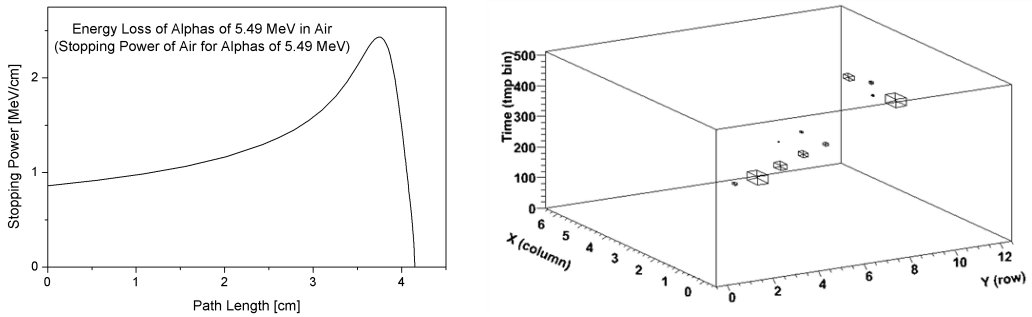

Figure 3.1: Left: Bragg curve for 5.5 MeV ^{241}Am α in air, extracted from [117]. Right: two of these alphas tracks in Ar as were registered by the Zaragoza's lab high pressure chamber (see section 5.5.3). The pixel size (X and Y) is 8.3 mm. It is clear from the Bragg curve that the typical *blob* corresponds to the end of the path.

The logarithmic term causes the apparition of a minimum followed by a soft rise, named the *relativistic rise*. An additional correction is needed at high velocities to take into account the *density effect*, the polarization of the medium by the particle's field which screens its ionization capabilities. Therefore the relativistic rise is attenuated and becomes the *Fermi plateau*; thus very fast particles electronic stopping power does not increase much more than 50% of the minimum value. For a parametrization to include this effect in (3.5) see [118]. Then, while particles are fast enough, $\mathrm{d}E/\mathrm{d}x$ is roughly independent on the velocity and relatively weak. Particles in this situation are called *minimum ionizing particles, MIPs*. This point of view of computing the stopping power along a particle trajectory is known as *Bragg curve* (see figure 3.1 left).

The main virtue of (3.5) resides in the fact that it provides an almost universal (under the assumptions explained above) curve that describes the stopping power of heavy particles [1] as function of its charge and β, or, if preferred, to the ratio between the kinetic energy and its mass since $\gamma(\beta)-1 = E_k/Mc^2$. This advantage is usually emphasized by using an alternative form of (3.5) that expresses the stopping power in terms of the mass thickness $\mathrm{d}(\rho x)$:

$$-\frac{\mathrm{d}E}{\rho\,\mathrm{d}x} = 0.3017\left(\frac{\mathrm{MeV}}{\mathrm{g/cm^2}}\right)\frac{Z}{A}z^2\frac{1}{\beta^2}\left[\ln\left(\frac{2m_ec^2}{I}\beta^2\gamma^2\right)-\beta^2\right] \quad (3.6)$$

$$= \frac{Z}{A}z^2 f(\beta, I) \quad (3.7)$$

The fact of requiring a minimum energy transfer to release the electron is somehow rectifying the free electrons picture and, indeed, its introduction means the only qualitative dependency on the medium. In addition, the selection of a *mean* or *effective* ionization potential (which in practice is deduced by fitting experimental data using (3.5)) is assuming that most of the energy transfers should be bigger than it. The respective values for Ar and Xe are 188 and 482 eV (see figure 3.2), useful values for gas of interest for TPCs can be found in table 1.5 of [116]). In practice, the dependence is weak, as for Z/A, and it can be generally said that the minimum, associated with the change of regime, is situated around $\beta \approx 0.96$ or $\gamma \simeq \gamma\beta \approx 3.2$; and MIPs lose $\sim$ 2 MeV g^{-1} cm^{-2}.

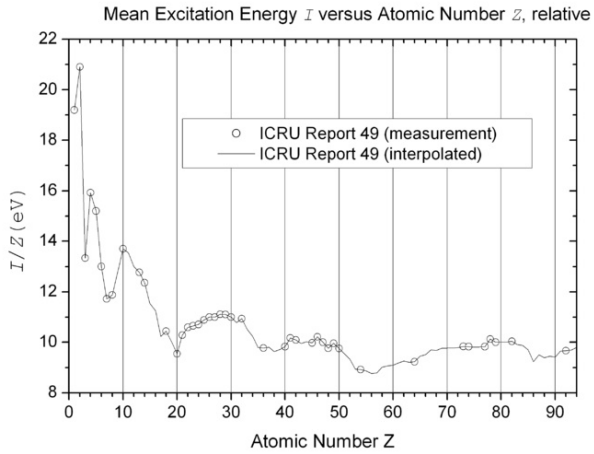

Figure 3.2: Mean Ionization Potential for several elements, extracted from [119]. $I \simeq 10\,\mathrm{eV}\cdot Z$ is a reasonable approximation for $Z > 18$ (from Ar on).

[1] Moreover, it can be extended, up to certain point, to electrons, see section 3.1.4.

3.1.3 Applicability of the Bethe-Bloch formula and thin absorbers.

The adjective *mean* preceding the previous result is a drastic limit for its usefulness, specially in the case of TPCs. Using a cross section so disperse as (3.1), the long tail has a big impact in the calculation of the mean as in (3.2). In reality, the cross section acts a limited number of times (following Poisson Statistics) while crossing an absorber material. The realization, or not, of a high energy transfer produces big deviations from the mean. The situation is even worse in the case of electrons[2] which can completely share its kinetic energy in a single collision ($T_{max} = E_k/2$), then suddenly changing all the event's story.

The mean energy loss will be reflected only after accumulating statistics or if the material is dense or thick enough to average many collisions; and, in both cases, if the absorber was also a detector, if it would be able to register all the energy loss (see next section 3.1.4). That can be achieved, for instance, by plastic scintillator detectors (and even there the energy loss distribution is not Gaussian); but, it is not the case for gaseous detectors equipped with a granular readout.

Landau developed an analytic approach for thin absorbers which assumes all the previous requirements to obtain the distribution of energy losses, Δ, which is described with a Landau distribution. Landau's *thin* absorbers are still too thick for most of TPC detectors because the calculation's assumptions (including $\Delta \gg$ electron binding energies) need for a thickness around 170 cm/bar in argon gas[120]. The Landau distribution becomes wider as ρx, the absorber thickness in g/cm^2, decreases; indeed, real energy fluctuations tend to be wider than Landau's theory prediction and its shape becomes irregular as the binding energies start being relevant[118].

However, for *really thin* absorbers, the most probable energy loss, Δ_p, from Landau's theory, is the best guess we can make for the passing of a single particle:

$$\Delta_p = \xi \left[\ln\left(\frac{2mc^2\gamma^2\beta^2\xi}{I^2} \right) - \beta^2 + 0.423 \right]; \quad \xi = \frac{0.1536\ Z\rho x}{A\beta^2}\ \text{keV} \tag{3.8}$$

which is situated far from the Bethe-Bloch $\langle \mathrm{d}E/\rho\,\mathrm{d}x \rangle$ (see figure 3.3).

3.1.4 δ-rays and restricted energy loss.

The strongest electronic collisions make electrons of the medium energetic enough so as to ionize the gas as well, and their tracks can be seen by a detector with high space resolution, like a TPC. These secondary electrons are called δ-rays and their contribution to the total strength of the signal *secondary ionization*[3]. As they are

[2] The previous calculus can be re-made for electrons, with correct kinematics, (see for, example, [115]), but it is even less useful for the reasons explained here. It is more practical to use the restricted energy loss formula (3.9).

[3] There are other phenomena which are said to contribute to the secondary ionization as the Auger electrons, see section 3.2.1.

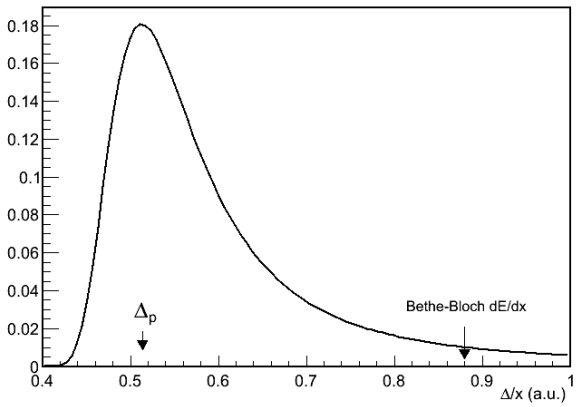

Figure 3.3: Example of the typical Landau distribution for MIP particles crossing a moderate thin absorber. The Landau FWHM is aproximately 4ξ. The most probable value divided the absorber thickness is compared with the Bethe-Bloch $\langle \mathrm{d}E/\mathrm{d}x \rangle$. The example is only for guidance and based in reference [118].

more energetic, these collisions fit better the assumptions of the calculus, and that is the reason why it is often said than secondary ionization follows the $\frac{\mathrm{d}\sigma}{\mathrm{d}T} \propto 1/T^2$ statistics rule described by Rutherford scattering (3.1).

Due to the shape of (3.5), δ-ray tracks can be much more intense than the main particle's, specially if that is a MIP. Working with an small TPC, the situation could be rather confusing for pattern recognition. Besides this additional problem, that is closely related with the discussion of the previous section because δ-rays can extract energy out of the chamber. Regarding the stopping power, as suffered by the incident particle, it is clear that the secondary ionization, even actually produced by the δ-rays, is contemplated in (3.5). On the other hand, if we are interested in the ionization density along the track, for particle recognition or by adjusting the chamber gain for selecting a practical dynamic range, the fact than δ-rays can significantly disperse the ionization is relevant.

The electrons' range dependency on energy and the readout pitch naturally introduce a maximum for the strength of the signal that can be registered by a readout unity (wire, pixel or strip) which can be used as a practical cut, E_{max}, in the calculation (3.2). In addition, the introduction of the cut minimized some of the disadvantages of the original Bethe-Bloch formula that were exposed in the previous section. In particular, the new cut disables the kinetic maximum ($E_{max} < T_{max}$) that meant an important difference between heavy particles and electrons. Therefore the *restricted energy loss formula*[121] inherits and reinforces the Bethe-Bloch formula's universality and can be trusted also for electrons:

$$-\frac{\mathrm{d}E}{\rho\,\mathrm{d}x} = 0.3017 \left(\frac{\mathrm{MeV}}{\mathrm{g/cm^2}}\right) \frac{Z}{A} z^2 \frac{1}{\beta^2} \left[\ln\left(\frac{\sqrt{2m_e c^2 E_{max}}}{I}\beta\gamma\right) - \beta^2\right] \tag{3.9}$$

Given a readout, the electrons' range is the other piece of information needed to define E_{max}. A customary parametrization [122] valid up to few hundreds of keV (while $\mathrm{d}E/\mathrm{d}x \propto 1/\beta^2$) is:

$$R\,[\mathrm{g/cm^2}] = 0.71\ E\,[\mathrm{MeV}]^{1.72} \tag{3.10}$$

In figure 3.4 we compare it with the results from a Monte Carlo simulation (realized with the GEANT4 application presented in chapter 6) for electrons in argon at 1 bar, the results can be scaled with $1/P$. Two different range definitions are considered: the *track length* is the complete length of the electron trajectory; the *projected range* is the maximum distance from the starting point to any point along its trajectory, projected on the initial direction, i.e. the depth it can penetrate in the medium.

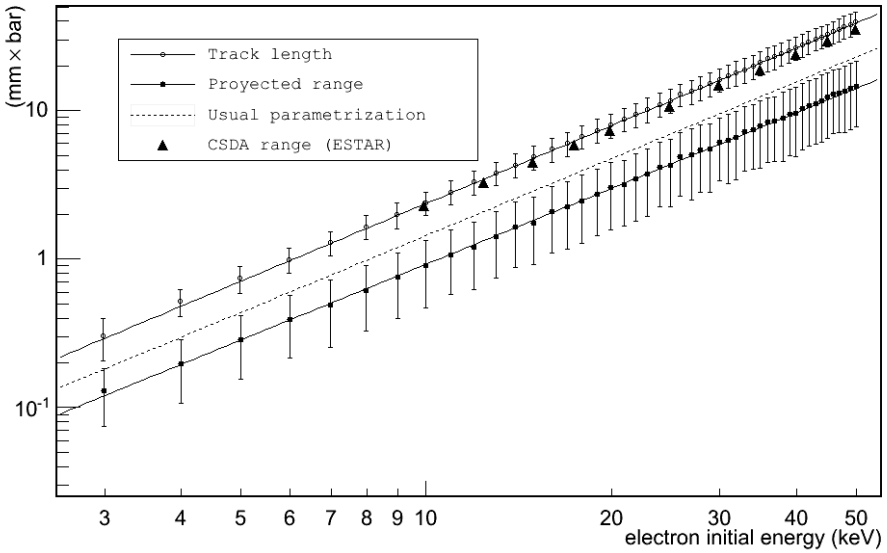

Figure 3.4: Electrons' range in argon at 1 bar. Computed by Monte Carlo and compared with parametrization (3.10) and NIST ESTAR database.

Because the low energy electron trajectories are rather chaotic (in fact, the selection of the initial direction or any other one would give practically the same result) both ranges are very different and the distributions quite wide (the bars in the plot represent the RMS of the obtained distribution). The application of (3.10) lies just between both series which have been fitted to:

$$\texttt{track length:}\quad (4.3 \pm 0.6)\cdot 10^{-2}\,\mathrm{mm}\ \cdot E\,[\mathrm{keV}]^{1.74\pm0.04} \tag{3.11}$$

$$\texttt{projected range:}\quad (1.9 \pm 0.5)\cdot 10^{-2}\,\mathrm{mm}\ \cdot E\,[\mathrm{keV}]^{1.69\pm0.09} \tag{3.12}$$

It is desirable to have a single and understandable expression, however there are parametrizations for the stopping power and related quantities available, like the

Stopping Power and Ranges for Electrons, ESTAR, database[123] from the National Institute of Standards and Technology (NIST). From ESTAR we have extracted the *CSDA (continuous-slowing-down approximation) range* for argon an plotted it in figure 3.4. In this approximation the rate of energy loss at every point along the track is assumed to be equal to the mean stopping power, that is to say, like drawing the Bragg curve, and we obtain something very similar to the mean value of the track length of the Monte Carlo. It must be noted that the stopping power curve used by ESTAR is already very different in strength than the Bethe-Bloch formula (3.5), see figure 3.5. We deduce that for ESTAR's CSDA calculation the fluctuations have been neglected, but not all the possible values were considered, i.e. a E_{max} cut was applied.

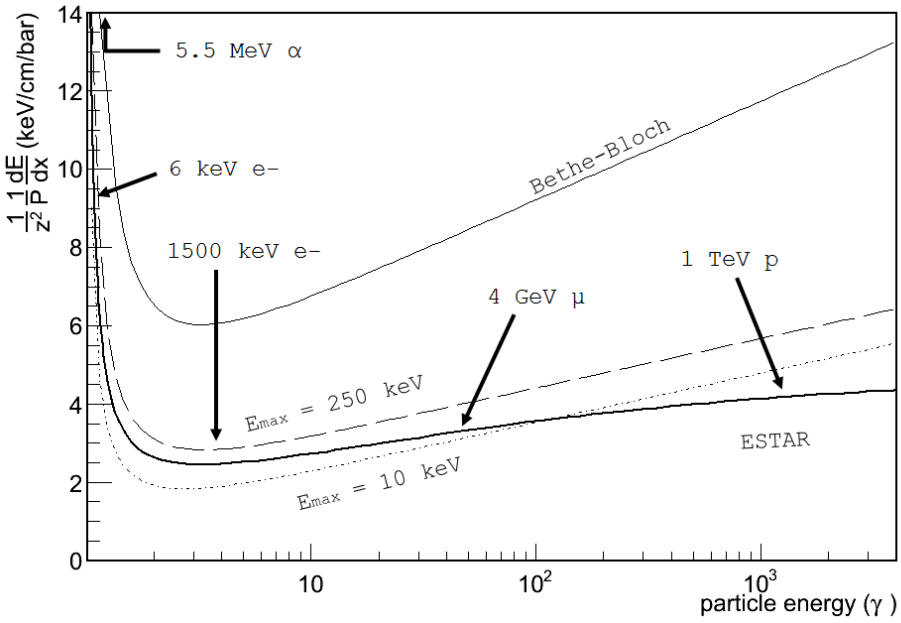

Figure 3.5: Several calculations for the stopping power in Ar. The original Bethe-Bloch formula is compared with the restricted energy loss modification for two different cuts (justified in the text) and the NIST ESTAR database. Note that ESTAR is a parametrization for electrons. Some usual incident particles are located in the plot to give a graphical idea of their Physics case: the ^{241}Am α ($\beta = 0.05$), the ^{55}Fe photoelectrons ($\beta = 0.15$), 1500 keV electrons ($\beta = 0.97$) as those involved in ^{136}Xe $\beta\beta$ decay, mean energy cosmic muons ($\beta = 0.9997$) and LHC protons ($\beta = 0.9999996$).

In order to define the cut, E_{max}, to be introduced in (3.9), we rely in the projected range to have an estimation of the maximum reasonable amount of energy expected in a readout unity. We choose, for instance, $E_{max} = 10$ keV for a highly granular readout, like a CAST detector (see section 8.2.2), with a pitch below 1 mm. For a second example, we think of a high pressure chamber, around 10 bar, with a pixel side of 0.5 cm like in NEXT micromegas prototypes (see section 5.5.4),

but we consider 2 cm projected range to estimate the case of xenon, were the track is shorter, therefore $E_{max} = 250$ keV is chosen using (3.12).

It is shown in figure 3.5 how the implementation of a practical cut has a dramatic effect on the stopping power relative to the Bethe-Bloch formula, however the behavior is soft with E_{max}. In particular the relativistic rise is strongly moderated. The parametrization by ESTAR is in between our two examples of restricted energy, and the difference at high energies is due to the implementation of the density effect. In any case the increase is below the 50% compared to the minimum along a very wide range.

The modified Bethe-Bloch formula with restricted energy loss by application of a custom-made E_{max} (3.9) seems to be a simple and understandable formula that allows a good description of the signal origin in the ionization chamber along a wide range of energies in most of the cases of interest for us. Even though it still has the disadvantages discussed in the previous section which are related with the *mean* adjective.

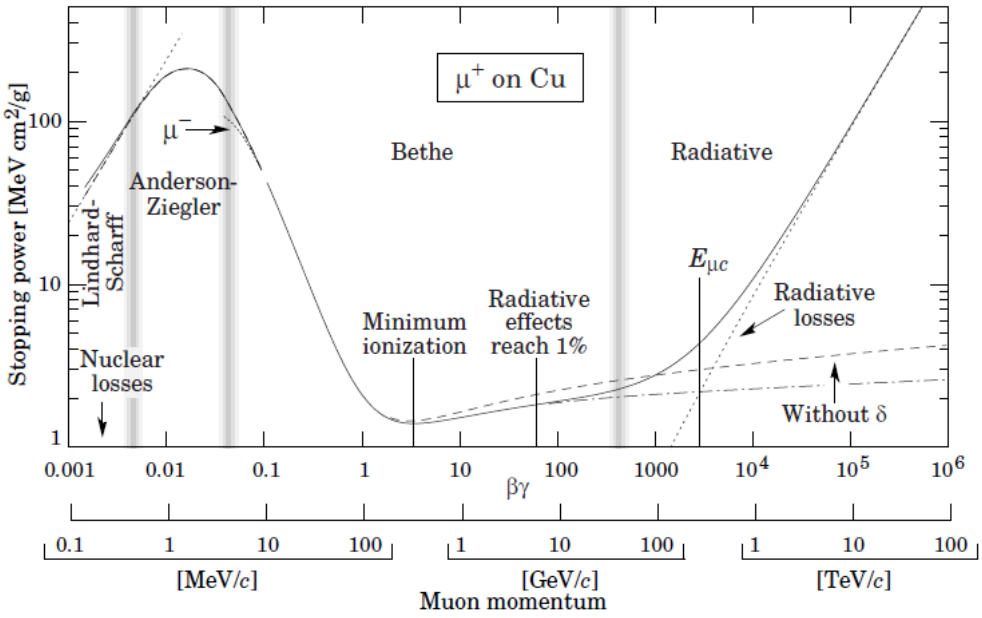

Figure 3.6: Stopping power of positive muons on copper along 12 orders of magnitude in energy. Vertical bands indicate boundaries between different approximations. Extracted from [118].

The complete picture is of course more complicated (see figure 3.6). At higher energies specially the lightest particles like electrons lose energy mainly by radiation yield, which in principle has no effect on the chamber, but can generate indirectly signals (see section 3.2.3). On the other hand, shell-corrections must be included to attend to atomic binding energies to assure good accuracy in the low energy region.

In addition, it is clear that when the energy is very low the ionization should also decrease. Although the Bethe-Bloch formula produces a fall at very low β, the actual effects that produce the decrease have not been contemplated and a new approach must be developed. The Bethe-Bloch based formulas explained here are valid only down to $\beta > 0.05$. The low energy ions which are of interest for dark matter searches are deeply below this threshold, and therefore their stopping power must be discussed in a specific section.

Regarding the distribution of energy depositions, The Landau's approach can be a good estimator of the most probable value, but fails in the distribution shape description in a TPC, especially at energies of few keV, comparable with medium binding energies. A Monte Carlo simulation should be carried out, what is even more necessary if we are interested in the distribution of charge along the particle path.

3.1.5 Stopping Power of non relativistic ions.

The boundary $\beta \approx 0.05$, pointed out as the condition for usage of Bethe-Bloch-based stopping power expressions, can be expressed as ~ 1 MeV/nucleon for ions, what is far from the typical nuclear recoil energies involved in dark matter searches. Two factors make the stopping power more complicated below this mark: the loss of efficiency in ionizing the medium and the inclusion of a new component to the stopping power related with strong interactions with the medium nuclei of increasing contribution as the energy decreases

$$\frac{\mathrm{d}E}{\mathrm{d}x} = \left[\frac{\mathrm{d}E}{\mathrm{d}x}\right]_{electronic} + \left[\frac{\mathrm{d}E}{\mathrm{d}x}\right]_{nuclear} \tag{3.13}$$

The energy lost in nuclear interactions is not directly involved in the ionization of the gas, but these elastic atom-atom collisions can produce secondary ions able to ionize by themselves (analogue to δ-electrons). The classical approach [125] is again Rutherford scattering in the screening field of the atoms, therefore the obtained stopping power looks very similar to a re-escaled Bethe-Bloch curve (see, for example, figure 3.8 left).

The electronic contribution is well characterized by the non relativistic approach developed by Lindhard *et al.* (LSS-Theory) [125, 126] where the media is described as a free electron gas whose interactions with the incident ion can be considered as small perturbations. Then, as a projectile moving in a viscous medium[4], in the LSS-Theory the energy loss is found to be proportional to the velocity:

$$\left[\frac{\mathrm{d}E}{\mathrm{d}x}\right]_{LSS} \propto vz^2 \tag{3.14}$$

[4] This is why ballistic jargon is very extended in this issue.

Besides the dependency on the medium to be much more complicated than the typical Z/A in Bethe-Bloch approach, the major difficulty here is how to define an effective ion charge z for nuclei which are moving with velocities similar to those of the orbiting electrons. As the atom kinetic energy is increased it is stripped of its orbital electrons but, at the same time, the medium is polarized resulting in a screening of the ion charge[5]; both effects are reciprocally influenced and the result is a complicate dependency on the ion, the medium and the velocity.

The LSS-theory is valid below $\beta \approx 0.01 \approx 50$ keV/nucleon (see figure 3.6 and 3.7 right). For the range $0.01 \lesssim \beta \lesssim 0.05$ there is not an accepted comprehensible statistical theory. The use of more complicated models for atoms (both as incident particle and as medium) forced the use of computers (or, alternatively, computers brought the opportunity to try them) in the late 70's[126]. The approach by Ziegler *et al.*[127] implemented in the free accessed, but not open source, SRIM (Stopping Range of Ions in Matter) software[128] has became the most similar to a paradigm.

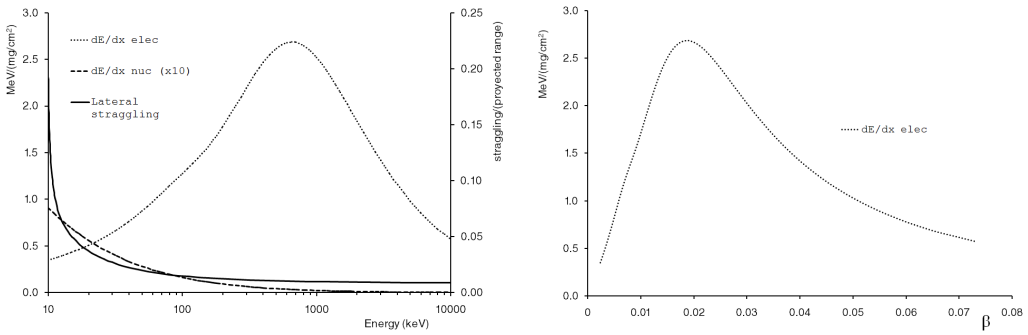

Figure 3.7: Left: Stopping power for He ions in He gas from SRIM tables. The nuclear stopping power has been amplified ten times. The lateral straggling is also represented for ions with this initial energy. Right: electronic stopping power as function of velocity for the same energy range. Note the linear regime around $0.01 \lesssim \beta$ predicted by LSS-theories.

Although SRIM was initially thought for ion transport in solids (for the study of ion implantation and similar applications), in our energy range of interest the atoms can be considered as free an SRIM is widely used by the gaseous TPC community (however, there is less experimental verification). Present version of SRIM produces tables for mean values of electronic and nuclear stopping ranges, also the projected range of the ion path and their longitudinal and lateral straggling. SRIM can also generate individual ion paths using Monte Carlo based on these tables, including cascades of secondary recoils caused by ion-atom collision, though only the primary path is described with detail registering, step by step, all the partial energy losses. The plots in figures 3.7 and 3.8, from SRIM tables, are used to illustrate the nature

[5]This is not exclusive of low energy ions, at higher energies difference between antiparticles stopping powers is known as the *Barkas effect*. An example of that is represented for μ^+ and μ^- in figure 3.6

of the stopping power in this context. Similar plots can be found in [129] for C, F and S recoils in CF_4 and CS_2 gases, but here we will focuses in noble gases.

In figure 3.7 α particles (He ions in this context) are used to show the electronic stopping range at low energies. For such light ions moving in light media the electronic contributions dominates during practically all the energy range. It is shown how the stopping power has a transition from the Bethe-Bloch application range to the LSS regime known as the *Bragg peak* which explains totally the shape of the curve if figure 3.1. We can detect that SRIM adds some small corrections to Lindhard simple model at very low energies which are more evident for heavier ions. The *straggling* is strongly related with the nuclear stopping power (hence for He ions is always small), as collisions with particle of the same, or similar, masses can sharply change the ion-projectile momentum. In particular, the lateral straggling (final deviation orthogonal to the initial direction) means a fundamental difficulty for directional detectors.

Plots for argon and xenon in figure 3.8 show that for medium and high ion masses the electric stopping power is always inside the LSS range and how the nuclear contribution enhances as the ion and the medium atoms masses increase. While for argon we can distinguish two stages where each contribution dominates, for xenon the nuclear stopping power is always the main effect. Like in the helium case, the straggling is more important where nuclear stopping power is higher and peaks up when electronic stopping power losses influence.

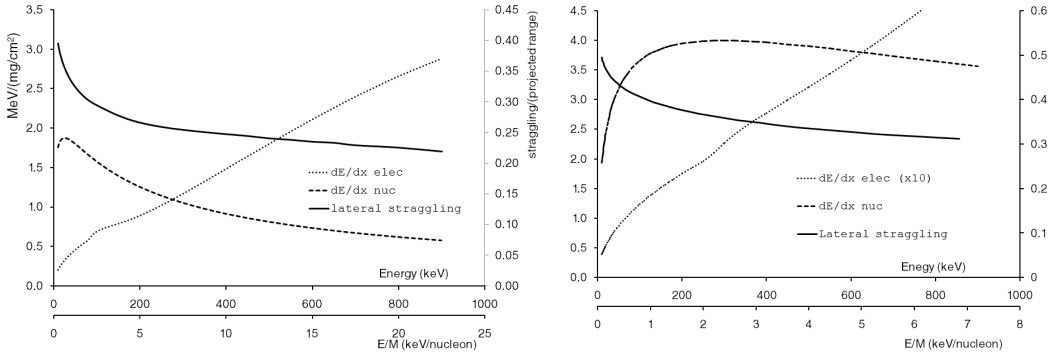

Figure 3.8: Left: Stopping power and lateral straggling for argon ions in argon gas from SRIM tables. Right: the same for Xe ions in Xe gas. The electronic stopping power has been amplified ten times.

In contrast to electrons, the projected range of low energy ions is approximately linear with energy. In figure 3.9, it is shown that this assertion is more accurate for medium size masses and fails at very low energies ($\lesssim$20 keV). In general, the lighter the ion and the medium atomic masses, the longer the range. The range scales with the inverse of the gas pressure and can also be stretched by addition of lighter atoms (figure 3.10), which also improves the straggling, but very softly.

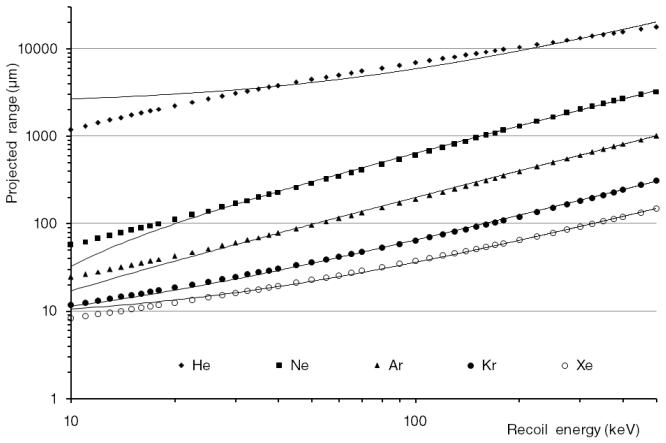

Figure 3.9: Projected range in noble gases as function of the initial ion recoil energies, from SRIM tables. The line is a linear fit attempt.

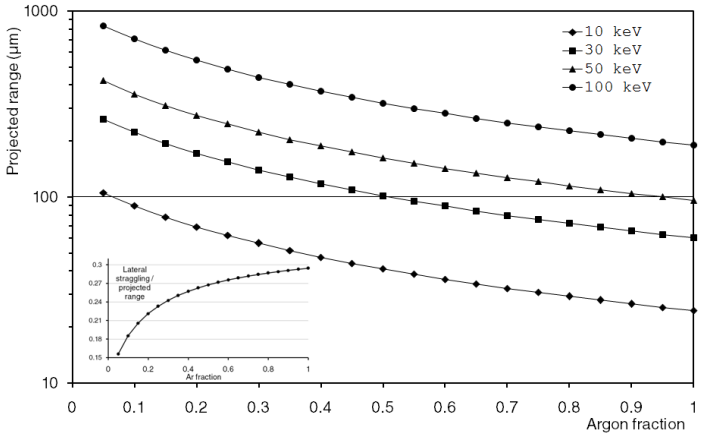

Figure 3.10: The line is a linear fit attempt. Right: projected range for Ar-He mixtures for several initial energies, from SRIM tables. The line is a linear fit attempt. The detail corresponds to the lateral straggling for 100 keV ions paths.

3.1.5.1 Quenching factor.

As a result of the effect of a non negligible nuclear stopping power, low energy ions are not as efficient in ionizing the medium as electrons. The heavy ion can keep a significant amount of energy, though being unable to ionize the medium [130]. The primary ion produces a certain number of secondary recoils in a cascade process, each one leads to a loss of an appreciable amount of residual energy.

Theoretically the *quenching factor*, Q, as it was introduced by Lindhard, is the ratio between the energy given to the electronic excitation and the total energy. This is an experimental key parameter that is usually to be defined as

$$Q \equiv \frac{E_r}{E_e}; \quad E_{ee} \equiv Q E_r \tag{3.15}$$

where E_r and E_e are the measurements of the energy done by the detector for a nuclear recoil and an electron of the same energy, since for electrons practically all the energy is lost in ionization[6]. Since electrons (basically photoelectrons from X-ray or γ sources) are commonly used to calibrate the detectors the *electron equivalent energy*, E_{ee}, is defined for nuclear recoils as the energy of an electron that would give the same measurement of the energy. As Q $<$ 1, this is a compromising parameter for Dark Matter detectors sensibility, because the recoils energy range of interest is invaded by lower energy (and so, surely, much many) γ.

Lindhard *et al.*[125] already gave a parametrization for the case of recoils of medium own atoms[7]:

$$Q = \frac{g(E)}{1 + g(E)} \tag{3.16}$$

and $g(E)$ is approximated in the range from 10 keV to 1 MeV by:

$$g(E) = 0.66 \frac{Z^{5/18}}{A^{1/2}} E(\text{keV})^{1/6} \tag{3.17}$$

F.J. Iguaz wrote a method to get a detailed description of the ion cascade built from individual nuclear recoils simulated with SRIM for the RESTSoft framework[133] (see chapter 6). An energy threshold is defined to decide when the energy loss by nuclear stopping power yielded by a simulation step motivates the simulation of a secondary recoil. This threshold also defines the residual energy lost per recoil. We will try a validation of the method by a direct comparison between the simulation results and 3.16 and 3.17. Figure 3.11 shows the simulation of 200 argon recoils in argon per initial energy using 100 eV as residual-threshold energy. The primary charge is generated only from electronic energy losses, using NIPs = E_{elec}/26.4 eV in average (see chapter 6). The comparison with the NIPs expected from the initial ion energy gives the simulated quenching factor.

The results for Ar ions in Ar gas are plotted in figure 3.12 where it is shown how the simulation approaches Lindhard calculation only if secondary ions are added to the simulation. Secondary recoils are responsible of at least one half of the charge yield, so they should be taken into account for a detailed study of charge generation along the recoil path. Regarding the theory-simulation comparison, we do not have a detailed study on energy residual-threshold dependency (which is

[6] Here, we refer in general to the measurement of energy instead of talking about primary charge yield because the same concept applies for detectors based on light collection or semiconductors. Therefore, E_r is the *visible* energy.

[7] The case of different ion and medium is discussed in [131] for directional detector purposes, and experimental data can be found in [132].

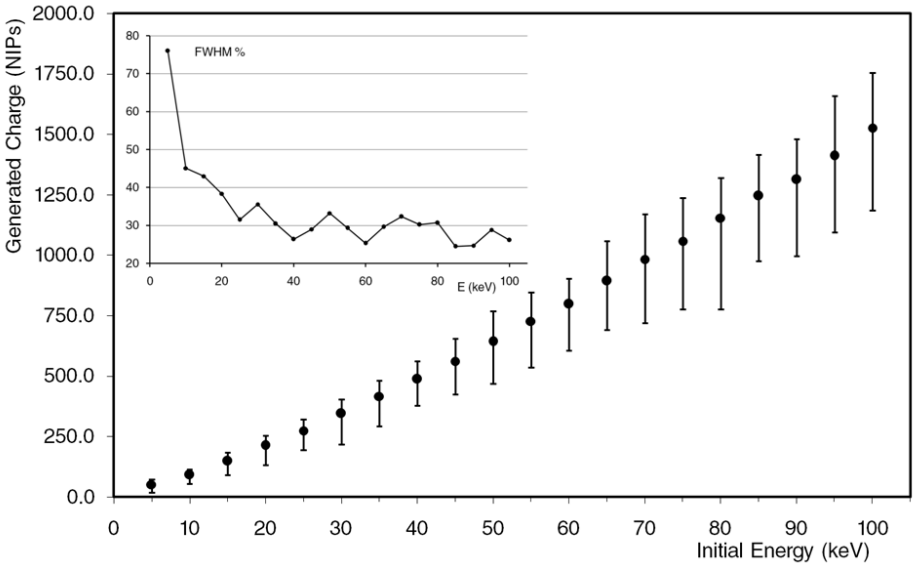

Figure 3.11: Charge yield for argon ions in argon obtained from SRIM plus RESTSoft ion cascade builder. The bars represent the distribution as FWHM. The little plot summarized the energy resolution as FWHM/E.

not a well understood parameter[130]). On the other hand an obvious limitation of our cascade reconstruction method is that all the partial energy loss by nuclear stopping power does not have to be interpreted as produced by a single collision, and so, invested in only one secondary recoil.

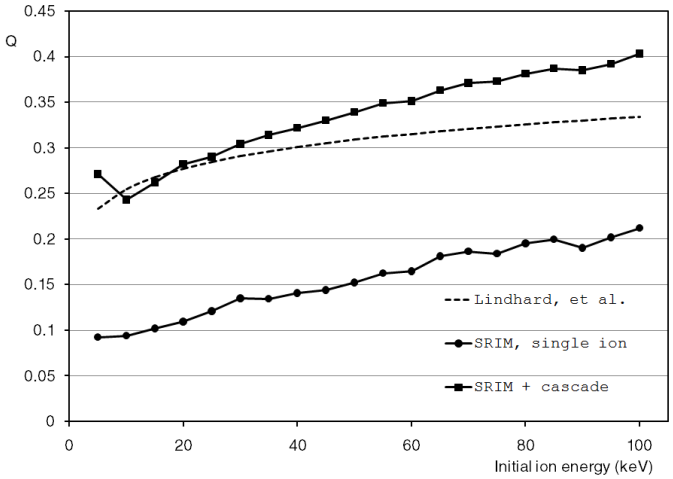

Figure 3.12: Quenching factor for Ar in Ar obtained from SRIM simulations, with and without addition of secondary recoils contribution, compared with 3.16.

Another remarkable point from these simulations is the very poor energy resolution visible in figure 3.11 which is consequence of the dispersion in the partition of

the energy losses between recoils residual energy and electronic excitation. With the 100 eV residual energy-threshold up to 200 secondary recoils are simulated for each primary ion of 100 keV, with very big variations on this number. The asymptotic value of $\sim$ 30% FWHM is in agreement with results from [134] for F ions in CF_4, even though secondary recoils are not used in those simulations. These results point to another fundamental difficulty for Dark Matter searches, despite it is not easy to be experimentally proven.

3.1.5.2 Head-tail effect.

The *head-tail effect* is a common way of speaking that makes reference to the possibility of an asymmetry in the Bragg curve, like the one clearly shown by α-particles in figure 3.1, which would allow to distinguish the *head* (end of the track) from the *tail* (beginning of the track). In the case of α-particles and electrons, the head has much more intense ionization since these particles move on the right side of the Bragg peak (see figures 3.5 and 3.7). In contrast, for low energy ions we would expect the tail to dominate over the head, as they are situated on the left side of the Bragg peak. Note this consideration has not taken into account the effect of nuclear stopping power, however more deep discussion [131] leads to the same conclusion (only from mean values). Moreover the effect has been observed by the DMTPC collaboration using 14.1 MeV neutrons from a deuteron-triton generator[135] and also with a ^{252}Cf source[136] for F recoils in the range from 200 to 800 keV.

In [129], stopping power curves using SRIM for C, F and S in CF_4 and CS_2 are plotted. The most interesting, F and S, as medium size atoms are basically very similar to Ar (figure 3.8 left); there is a low energy stage, dominated by the nuclear stopping power. While a high energy stage, where Lindhard model for electronic stopping power is a good approximation, can be distinguished. In the high energy stage a tail dominance is expected. The DMTPC would have seen the effect because their F recoils have a long part of their paths along which the electronic stopping power is clearly dominant.

In our preliminary study on argon recoils below 100 keV at 1 bar[8], we proposed[133] the volumetric density of the charge as discriminator because simple Bragg-like curves often give non conclusive results. We detected that limitation is due to the straggling of the main path plus the presence of secondary recoils; since both are more common near the head, a higher charge yield around the end of the path can be produced. However, this additional charge is expected to be more disperse. The algorithm is illustrated in figure 3.13 for a complete simulation (including secondary recoils) of an argon recoil. Even though the success rate was promising, such a method would need for a really powerful topological capabilities of the chamber.

[8] The simulated path is scalable with the inverse of the pressure and so conclusions based on the path features should be universal, with the exception of drift diffusion effects.

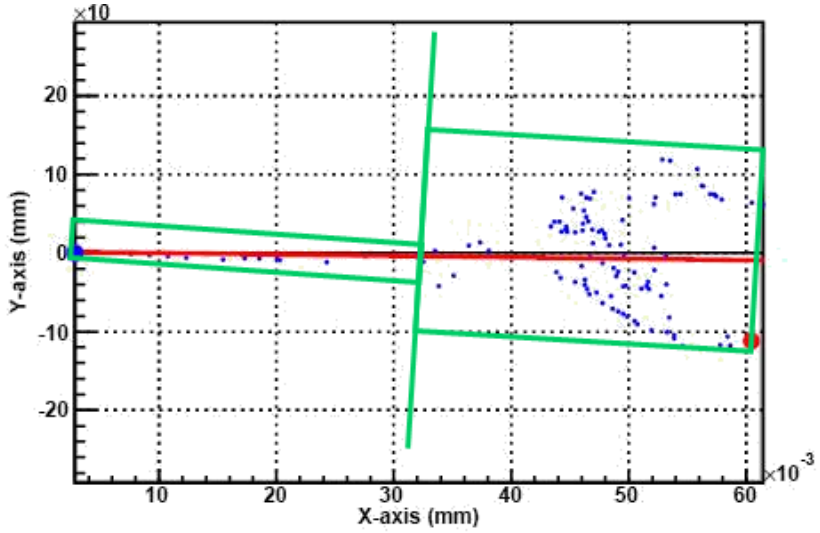

Figure 3.13: Illustration of a sense recognition algorithm over a 40 keV Ar ion cascade simulated with RESTSoft (based on individual SRIM recoil simulations). After the determination of the recoil direction, two volumetric regions (only readout projection is plot) are defined assuming that the head corresponds with the lowest density of charge.

In the paper previously mentioned [129], following a simulation extension of SRIM very similar to the RESTSoft approach (see section 6.3.3) the DRIFT researchers admit the importance of the straggling caused by the nuclear collisions (despite neglecting secondary recoils). The straggling together with the necessity to project the ionization yield onto the readout axes, means a factor that competes with the pure Bragg curve to enhance the strength of the head respect to the tail. Depending on the ion and its initial energy the Bragg-like curves (projected onto the readout axes) can be basically flat or inclined to the head or to the tail (in agreement with our studies[133]). After studying simulations of the same nature[134], researchers from the MIMAC collaboration suggest not to consider the head-tail effect for Dark Matter searches with recoils below 100 keV.

3.2 Other indirect mechanisms to generate ionization

Fast charged particles will always be the source of the signal readable in the micromegas chamber. Therefeore, at the end of every of the following subsections, we will be addressed to the previous section. However the following physical processes will enable the TPC to detect other kind of particles.

3.2.1 Interactions of photons.

In contrast to the ionizing particles (at least macroscopically), the photons interact with matter in a discrete way that suddenly changes the photon state and can even

be completely absorbed. The stopping power concept is replaced by the differential cross section which describes the possibility of such a process to happen.

The following expression illustrates the way that applies for a beam of photons with initial intensity I_0 crossing a thickness x of material with N molecules per unit volume, and it will be useful to show several common definitions related with the same concept:

$$I(x) = I_0\, e^{-\sigma N x} = I_0\, e^{-\mu X} = I_0\, e^{-x/\lambda} \tag{3.18}$$

where $X = \rho x$ is the mass thickness with ρ the mass density and $\mu = \sigma N/\rho$ is the (frequently tabled) *mass attenuation coefficient*, and $\lambda = 1/(\rho\mu)$ is the *mean free path* of the photons in the material.

The mass attenuation coefficient is probably the most useful construction because it is just summed for different processes or simply composed for a material mixture:

$$\mu_{\text{mix: }1,2\ldots,n} = p_1\mu_1 + p_2\mu_2 + \ldots + p_n\mu_n \tag{3.19}$$

with p_1, $p_2\mu_2\ldots$, p_n the percentages, in weigth, of the 1,2, ..., n compounds of the mixture.

Photons can interact with matter through four processes:

- *photo-electric effect*: absorption of the photon by the atom.
- *Compton effect*: scattering of the photon by one shell electron. Also called *Thompson scattering* at very low energies.
- *pair creation*: creation of an electron-positron pair.
- *Rayleigh scattering*, or *coherent scattering*: scattering of the photon by the whole atom.

All these effects are exposed in reference books as [115, 137] and here only the ideas of direct interest will be remarked. Pair creation, as a typical process in High Energy Physics (see figure 3.14) will not be discussed. Tables for mass attenuation coefficients can be found in the XCOM database[138] from NIST.

3.2.1.1 Photo-electric effect (Fluorescence, escape peaks and Auger electrons).

The photo-electric effect is the process that determines the quantum efficiency of the chamber for X-rays since is the one which can easily produce ionization yield proportional to the photon energy. The photo-electron is released with the energy of the absorbed photon E_γ with the payment of the electron binding energy, E_{shell}:

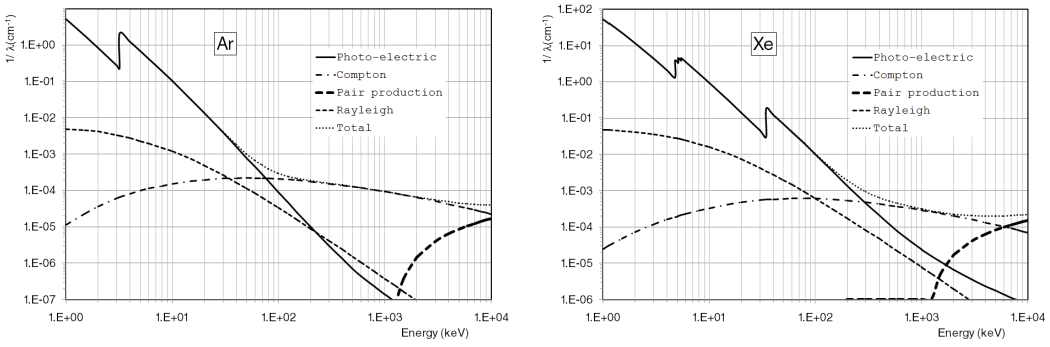

Figure 3.14: Cross sections obtained from [138], expressed as $1/\lambda$, for Ar (left) and Xe (right) gases at standard conditions ($1/\lambda \propto P$, with P the gas pressure).

$$E_e = E_\gamma - E_{shell} \tag{3.20}$$

However, many times E_{shell} is relatively small or can be finally delivered as secondary ionization (see below).

The photo-electric cross section is the sum of all the atom shells' contribution. When one shell becomes accessible to the photon energy a sharp increase is observed in the cross section (called K-edge, L-edge, M-edge, ...), and this new shell tends to dominate the cross section. In figure 3.14 left, it can be seen how, once the K shell is available, above 3.19 keV its contribution is $\sim 90\%$ of the total cross section. Something similar happens to Xe at 33 keV (in the same figure at right), and for L shells around 5 keV. Fast access to atomic shells data can be done through [139].

The dependency of the photo-electric cross section goes with the 4th or 5th power of the energy and is highly dependent on Z, the atomic number of the material. Therefore, the small fractions of organic gases usually added to noble gases in TPCs do not have an appreciable impact on the detector quantum efficiency since their molecules are usually composed of low-Z atoms.

Because the photo-electron has been rejected from an atomic shell, a vacancy has been created in the electronic structure (in fact, deeper vacancies are more likely when possible, as we saw just before) and the atom have two possibilities to relax which can result in *secondary ionization*:

- *fluorescence*, by radiative transition from an outer shell. If the fluorescence photons are absorbed by the gas, the detector can recover the initial energy of the X-ray (although in two separate *clusters*, or point-like energy depositions). While if the secondary photon is not absorbed the energy measurement will be shifted from the X-ray energy by an energy characteristic of the detector gas; this is the origin of the *escape peaks*.

- emission of an *Auger electron*, a non radiative transition where electrons with characteristic energies of the detector gas are rejected. Therefore the excitation energy is released as ionization and this kind of event is most of times indistinguishable from a single electron carrying the whole energy.

Several of these transitions can happen in cascade.

Fluorescence can have a big impact in the detector registered spectra, sometimes making difficult (others giving hints to) their interpretation (a practical example of that can be found in section 6.2.7.2). Generally speaking, for a gaseous detector where a big ratio of the chamber is an active volume (i.e. the ionization generated inside is susceptible to generate a signal in the micromegas) the fluorescences of the detector gas are reflected in the spectra as escape peaks. To see a gas fluorescence it would be needed an absorption in the dead volume of the detector and then the capture of the fluorescence photon. In contrast, fluorescence peaks are often due to solid parts of the detector, especially metallic pieces with medium Z elements (read-out, cathode, field-shaper, etc.), what could mean a limitation for the detector background at low energies. For illustration of that see figure 3.15.

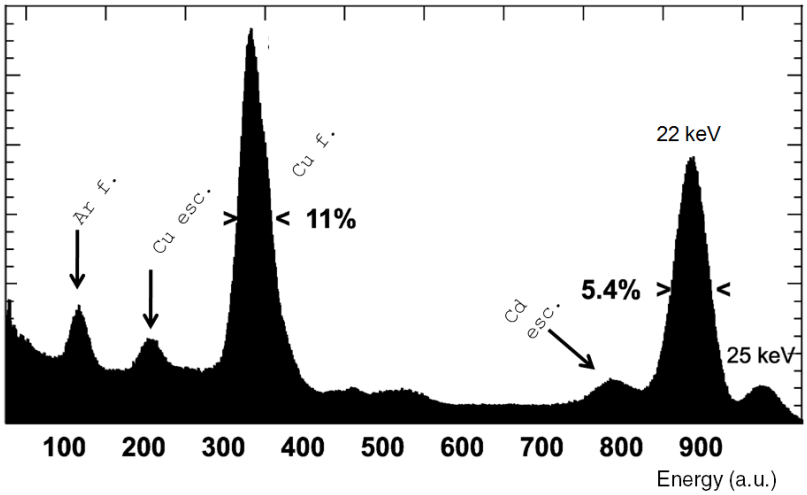

Figure 3.15: An already classic spectrum taken with a micromegas published in [100] for a ^{109}Cd calibration with γ-rays of 25 and 22 keV. Two argon escape peaks related with intense peaks can be observed as well as the 8 keV fluorescence of copper from the micromegas mesh and 3 keV from the argon itself. The percentages make reference to the energy resolution as FWHM.

A few words about the X-rays photo-electric effect in the particular case of Ar, as the most widely gas used to fill TPCs. We saw how for energies of few keVs the absorption cross section is dominated by the presence of the K-edge at 3.19 keV. A vacancy in the K-edge is followed ∼15% of times by a 3.19 keV photon and ∼85% of times by an Auger electron about the same energy. That means and advantage

for Ar chambers' X-rays efficiency. The ^{55}Fe 5.9 keV X-rays are commonly used to calibrate at low energies. They have only ∼10% possibilities to interact with an electron in a shell other than K, in these cases the result is fundamentally a photo-electron with the whole X-ray energy. If interacting with a K-electron and a fluorescence photon was emitted with energy ∼5.9–3.2, below the K-edge, we see from figure 3.14 left how its mean free path would be very similar to the 5.9 keV original X-ray's and it may have higher possibilities to escape than expected. Actually the relative strength of the Ar escape peak will strongly depend on the chamber geometry. A study on the ^{55}Fe 5.9 keV X-rays spectrum in Ar is done in [112].

3.2.1.2 Compton effect.

When interacting by Compton effect the photons are not absorbed but scattered by the medium electrons, the initial photon energy E_γ cannot be measured. Compton interactions are responsible of most of the counts in the chamber by medium-high energy γ-rays (see figure 3.14). At the energies where te Compton effect is dominant, the atomic binding energies are relatively small. When the electrons are considered to be free, conservation of energy and momentum lead to these relationship between the energy change and the dispersion angle θ of the photon:

$$\frac{1}{E'_\gamma} - \frac{1}{E_\gamma} = \frac{1}{m_e c^2}(1 - \cos\theta) \tag{3.21}$$

independent on the medium. Note that, from the kinematics of the collision, there is a maximum energy transfer to the Compton electron $T = E'_\gamma - E_\gamma$:

$$T_{max} = E_\gamma \left(\frac{2E_\gamma/(m_e c^2)}{1 + 2E_\gamma/(m_e c^2)} \right) \tag{3.22}$$

but there is not a minimum. In fact, the low energy depositions are favored, as can be seen from the differential cross section of the process $\mathrm{d}\sigma/\mathrm{d}\Omega$, deduced by Klein and Nishina in 1929. But it is more useful for us to substitute 3.21 in the Klein-Nishina formula to obtain the energy distribution of the Compton electrons:

$$\frac{\mathrm{d}\sigma}{\mathrm{d}T} = \pi r_e^2 m_e c^2 \frac{1}{E_\gamma^2} \left[2 + \frac{2(m_e c^2)^2 s^2}{E_\gamma^2 (1-s)^2} + \frac{s}{1-s} \left(s - \frac{2m_e c^2}{E_\gamma} \right) \right] \tag{3.23}$$

where $s = T/E_\gamma$ and $r_e = e^2/(4\pi\varepsilon_0 \hbar c)$ is the classical electron radius. The distribution, which is plotted for several E_γ values in figure 3.16, must be truncated in $T = T_{max}$, what leads to a sharp rise, known as *Compton-edge*, and the consequent peak, the *back-scattering peak*. In the same figure can be appreciated that, even though they do not form a peak, low energy transfers are relatively more frequent than big angle dispersions, specially for medium energy γ-rays, which is a threat for low energy background.

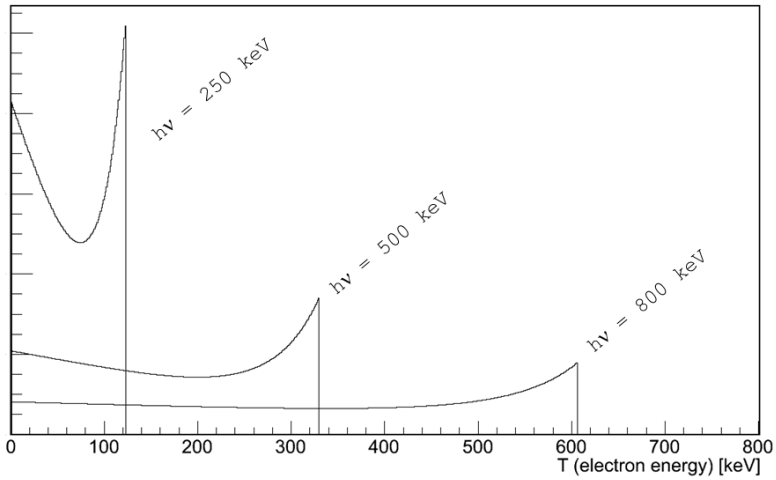

Figure 3.16: Compton electron energy distributions drawn using (3.23) for $E_\gamma = 250, 500$ and 800 keV.

In the classical limit the cross section becomes independent of the energy and equal to the *Thompson cross section* and no energy is transferred, photons are just dispersed.

3.2.1.3 Rayleigh scattering.

This is the classical radiation dispersion by the atoms which do not transfer energy to the medium. Here we just make a warning about the fact that the Rayleigh cross section can be non negligible at low energies (see figure 3.14). Then, in principle forbidden trajectories could be allowed for the X-rays thanks to Rayleigh dispersion, what might become an unexpected background origin.

3.2.2 Interactions of neutrons and WIMPs.

Neutrons and WIMPs can experiment elastic scattering with the detector gas nuclei. Although the nature of the processes are different (and depending on the WIMP type and model), both mechanisms are fundamentally elastic collisions that share the same kinematics and reject a nuclear recoil which ionizes the medium and can be registered by the micromegas (from this point on, the event description is addressed to section 3.1.5). Therefore it is clear why neutrons are the most dangerous background for direct Dark Matter searches which look for WIMP-induced recoils; in addition, neutron-induced recoils can also mimic the signal from low energy X-rays.

The conservation of energy and momentum leads to the following energy share-out for a collision in which the incoming neutron, or WIMP, with energy E and mass m is scattered and angle θ from its incident direction by a nucleus of mass M:

$$T = \frac{2mM}{(m+M)^2} E(1-\cos\theta) \tag{3.24}$$

where T is the energy transferred to the nucleus, which can be as high as E only if $m = M$. If the nucleus could be considered as a point-like particle, such a collision would be isotropic; then, since from (3.24) $\mathrm{d}T \propto \sin\theta\,\mathrm{d}\theta$ like $\mathrm{d}\Omega$, the differential cross section $\frac{\mathrm{d}\sigma}{\mathrm{d}T}$ is not dependent on the recoil energy and can be expressed as

$$\left.\frac{\mathrm{d}\sigma}{\mathrm{d}T}\right|_{point-like}(E) = \frac{\sigma^0}{T_{max}} \tag{3.25}$$

where σ^0 is the cross section at zero momentum transfer and T_{max} is the maximum energy transferred when $\theta = \pi$ in (3.24) In (3.25) has been emphasized that $\mathrm{d}\sigma/\,\mathrm{d}T$ is dependent on E, but not on T.

Because the nuclei are actually not point-like (at least it cannot be considered to be when the momentum transfer $q = \sqrt{2MT}$ related wavelength q/h is not large compared with the nucleus effective radius) the previous expression must be corrected by the nucleus form factor $F\left((T(\theta)\right)$

$$\frac{\mathrm{d}\sigma}{\mathrm{d}T} = \left.\frac{\mathrm{d}\sigma}{\mathrm{d}T}\right|_{point-like} |F(T)|^2 \tag{3.26}$$

When the scattering is *coherent*, i.e. the nucleus acts as a whole, the *nuclear form factor* is computed as the Fourier transform of the nuclear mass density distribution $\rho(r)$:

$$F(q) = \iiint \mathrm{e}^{ipr}\rho(r)\,\mathrm{d}^3r = \frac{4\pi}{p}\int_0^\infty \sin(qr) r\rho r\,\mathrm{d}r \tag{3.27}$$

hence it depends on the description of $\rho(r)$ for which there are several classic and widely used parametrizations (see [130] and references there in).

In the *incoherent scattering* the particle is absorbed by the nucleus and then rejected, but the same kinematics described above are valid. Neutron cross section curves are dominated by the resonances due to incoherent scattering (see figure 3.17) and so they change dramatically even to similar nuclei. WIMPs cross sections have a different signature that can be used by Dark Matter Searches to differentiate from neutron's background by comparison of the results of several target materials. They depend, of course, on the WIMP's nature and model, but can be divided in two basic groups which can coexist:

- *Spin Independent* (SI) interactions, as supposed for most of standard WIMP Dark Matter candidates as MSSM neutralino [140]. If the scattering is coherent $\sigma \propto [Zg_p + (A-Z)g_n]^2$, i.e. the contributions from the Z protons and the $A-Z$ neutrons of the nucleus, with their respective coupling WIMP-proton (g_p) and WIMP-neutron (g_n), are just summed. In the easiest case $g_p \approx g_n$ and $\sigma \propto A^2$.

- *Spin Dependent* (SD) interactions are sensitive to the nuclear spin, J, then they are subject to more uncertainity from both WIMP and nuclear models (besides, the form factor for SD cannot be calculated only on basis to 3.27). However, for some nuclei, they can enhance the cross section what motivates Dark Matter searchers with TPCs based in CF_4 (^{19}F) or ^3He.

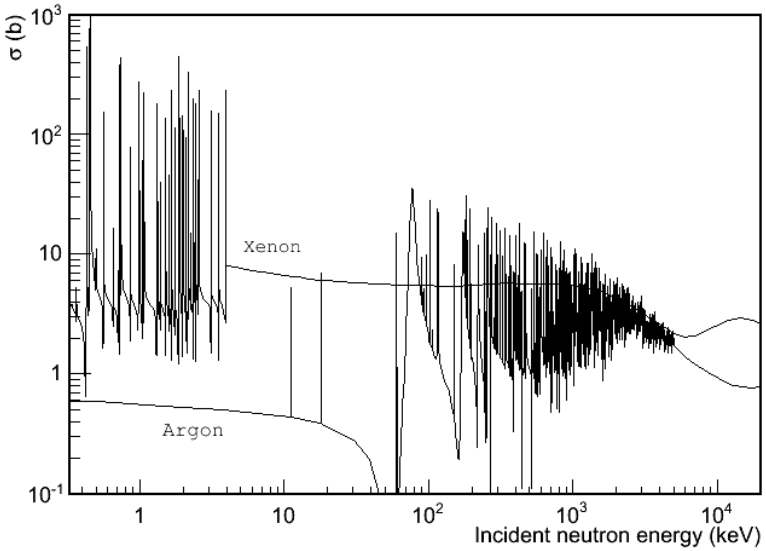

Figure 3.17: Elastic cross sections for ^{40}Ar and ^{131}Xe obtained using [141].

Much more detailed explanation on WIMPs cross sections and how to use it to estimate the detection rate in a Dark Matter experiment can be found in other Ph. D. theses by colleagues of my group as [142, 143, 144] and the references there in.

In the case of *inelastic scattering* (the nucleus is excited) a nuclear recoil is also produced, but 3.24 is not valid here. The collision can be followed by a γ-decay that can help to identify the process, however gaseous TPCs detection efficiency is poor for γ. Neutrons can also trigger a variety of nuclear reactions (spallation, fission, etc.) which are typical of High Energy and Nuclear Physics and are beyond the scope of this text.

3.2.3 Bremsstrahlung.

The last section of this chapter is devoted to a process that does not generate immediately ionization in the medium, on the contrary, it can mean a loss of the deposited energy by a charged particle. On the other hand, it can produce secondary ionization in the chamber, even when the interaction itself has happen out of the chamber. The *Bremsstrahlung* (braking radiation) is experimented by charged particles when they are scattered by the electric field of the medium nuclei. That mechanism of radiative energy loss is in competition with the ionization produced by scattering with

the electrons of the medium that was studied in the first sections of this chapter.

$$\frac{\mathrm{d}E}{\mathrm{d}x} = \left[\frac{\mathrm{d}E}{\mathrm{d}x}\right]_{ion} + \left[\frac{\mathrm{d}E}{\mathrm{d}x}\right]_{rad} \tag{3.28}$$

The radiative stopping power is proportional to the particle energy (see, for example sections 11.5.2 and 11.5.3 of [145])

$$\left[\frac{\mathrm{d}E}{\mathrm{d}x}\right]_{rad} \approx -\frac{E}{X_0} \tag{3.29}$$

The last equation justifies the name of *radiation length* given to X_0 since, in average, $E = E_0 \exp(-x/X_0)$. The radiation length dependency with medium (Z, A) and particle mass, m, is approximately (calculus and tables can be found in [146])

$$\frac{1}{X_0} \approx \frac{Z^2}{A}\frac{1}{m^2} \tag{3.30}$$

Then bremsstrahlung is more efficient for light particles that can suffer strong decelerations which act as photon *shots*. Since it is proportional to the particle energy, while ionization tends to saturate, it becomes dominant at high energies (see figure 3.6) and finally the energy loss by bremsstrahlung rises over the ionization stopping power at the *critical energy*, E_c (see figure 3.6). For our purposes, bremsstrahlung is only relevant for cosmic (high energy) muons or for electrons around the MeV. The following approximations (see [118] and references there in) are valid *only for electrons*:

$$E_c = \frac{610\,\mathrm{MeV}}{Z + 1.24} \quad \text{(solids and liquids)}; \tag{3.31}$$

$$E_c = \frac{700\,\mathrm{MeV}}{Z + 0.92} \quad \text{(gases)}; \tag{3.32}$$

$$X_0 = \frac{716\mathrm{g/cm}^2 \cdot A}{Z(Z+1)\ln 287/\sqrt{Z}} \tag{3.33}$$

Even still far from their critical energy, electron's radiation length in a xenon TPC at 10 bars is $\sim$ 1.5 m and so, along the few tens of cm paths of electrons between 1 or 2 MeV, it is not rare that some photons are shoe. They can generate secondary clusters or escape from the chamber with consequent danger for calorimetric detectors. On the other hand, the possibility is higher in metals, in particular in lead, and therefore relatively high energy electrons originated by natural radioactivity or cosmic muons can induce low energy events in the chamber by bremsstrahlung experimented in the detector's shielding.

Chapter 4

Working principles of the TPC-micromegas.

Contents

This chapter is devoted to the chain of processes that happen in the detector, which are triggered by the physical interactions described in the previous chapter and yield an electronic signal, and how they transform the original information.

Since there exist several manuals that explains the working of a TPC, we will focus in micromegas particularities, and the discussion will be more detailed about the features that are being directly studied by the T-REX project. The next chapter is an special extension in this sense, dealing with no essential aspects, but which are critical for most or some applications of TPCs to rare event searches.

4.1 Primary Charge generation.

The creation of free electrons by the interaction of the gas atoms or molecules with the ionizing particles is the essential process that allows the working of the gaseous detectors. This process has, in principle, several dependences: on the type of gas molecule, on the type of the ionizing particle, on the strength of the particular energy deposition. The relationship between these issues brings diverse possibilities for the process end which, in principle, produce big statistical fluctuations. Fortunately the nature moderates these dependences and limits the fluctuations for the benefit of the gaseous detectors' potential as proportional counters. There are two main parameters, empirically defined, that quantify the generation of the primary charge, which are the scope of this section.

4.1.1 W, averaged energy per ion pair.

The original interactions that trigger the detection process are the inelastic collisions produced by an ionizing particle that were studied in section 3.1. These discrete energy deposits can ionize the gas molecules, but also excite higher energy electronic states (radiative excitations) or vibrational or rotational states[1]. Sometimes the energy invested in excitation can be reconverted into ionization (see section 3.2.1.1). Besides, even if the collision produces effective ionization, the free electron can retain a certain amount of energy and being unable to ionize again the gas.

The ionization yield must be characterized by an empirical parameter that relates the total production of primary charges, n_e, with the energy deposited in the active volume of the chamber E_0[2]

$$W \equiv E_0/n_e \tag{4.1}$$

W is the average energy required to produce an electron-ion pair, often referred simply as the W-value. As a rule: E_{exc} (first energy of excitation) $< E_i$ (first energy of ionization) $< W$. Recompilations of these values can be found in [147] and [115]. Roughly speaking W is about 1.5–2 times E_i for noble gases, and 2–3 times E_i for more complex molecules. We will just remark $W_{Ar} = 26.3$ eV and $W_{Xe} = 21.9$ eV.

A crucial result for the operation of gaseous detectors is the fact that W is only slightly decreasing with the energy of the ionizing particle. Only when energies are of the same order than the ionization and excitation potentials W rises[148].

[1] Precisely the kind of gases used in the gaseous chambers usually belong to one of the two extreme cases: the simplest molecules, noble gases, unable of vibrational or rotational modes; or complex organic molecules with numerous and energetic excitation modes. In most of cases a mixture of both types is used because of reasons that will be shown along the chapter.

[2] The absolutely empirical character of the W-value causes some confusion about its exact definition. For practical reasons E_0 is often the initial total energy of the ionizing particle, what can produce a small overestimation of W because of its rise at very low energies.

The dependence is also weak with the radiation type. In figure 4.1 the charge yield obtained in a chamber with micromegas is directly compared for 13.9 keV X-rays and 5.4 MeV α. Although the micromegas gain is plotted, it has been extracted from a comparison of the signal strength which already assumes $W_\alpha = W_{Xray}$ (see 4.4). These measurements were conceived to study other processes as well, and they would be revisited and discussed with more detail later; for the moment it is clear that the calculated gains could not match unless $W_\alpha \simeq W_{Xray}$, even though $< \mathrm{d}E/\mathrm{d}x >$ is more than one order of magnitude higher for the α.

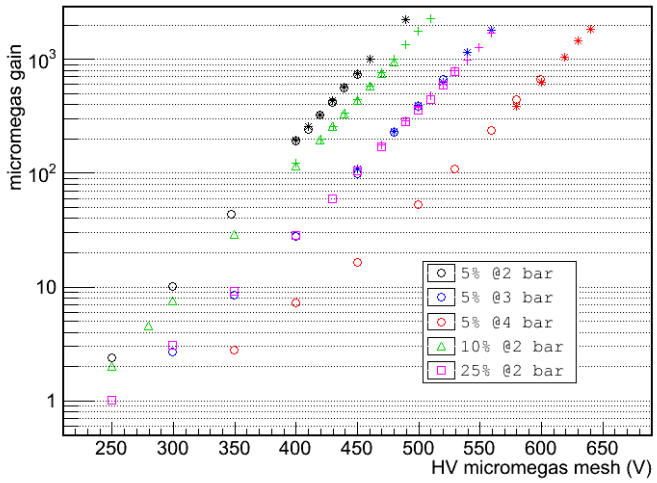

Figure 4.1: Gains deduced for a micromegas in Ar with CH_4 for several CH_4 concentrations and pressures, using the set-up described in section 5.1. The closed markers (circle, squares and triangles) are calculated from ^{241}Am 5.4 α while asterisks and crosses from ^{241}Am 13.9 keV X-rays at the same time, i.e. during an only measurement run, using exactly the same gas and set-up conditions. The highest point of the series is the last one before the micromegas starts continuously sparking.

The W-value for a gas mixture is given by a simple weighted average

$$W = \left(\prod_k W_k\right) / \sum_k \left(C_k \sigma_k \prod_{i \neq k} W_i\right) \tag{4.2}$$

with C_k the concentration of each component and σ_k the relative cross sections ($\sum \sigma_k = 1$). Therefore no spectacular effect is expected from the addition of a new component in small concentrations. The rule 4.2 is not valid when there is an interplay between two components (see the case of Penning mixtures in section 5.3).

4.1.2 F, the Fano factor.

If the generation of primary charges followed Poisson Statistics, the variance of the charge yield for events that average n_e would be $\sigma^2 = n_e$. Then that would imply an essential limitation for the energy resolution of the detector because of the variation of the primary ionization, which would be expressed as full width at half maximum (FWHM):

$$R(\text{FWHM})|_{pi} = 2.35\sigma\frac{1}{n_e} = 2.35\sqrt{\frac{1}{n_e}} = 2.35\sqrt{\frac{W}{E_0}} \tag{4.3}$$

that produces $R|_{pi@Ar} \simeq 15.6\%$ FWHM for 6 keV X-rays in argon. Microbulk micromegas actually achieve 11% FWHM for the ^{55}Fe peak[3] (see figure 4.22 right), an experimental value certainly affected by other additional variance sources (see section 4.4.2).

Facing the evidence that the process is not purely Poissonian (besides the ionizing particle has a finite energy that imposes a maximum n_e, the excitation and ionization possibilities are not independent) the actual variance is corrected using the $Fanofactor$, whose empirical definition could be: the F so as to fit

$$\sigma^2 = Fn_e \tag{4.4}$$

thus

$$R(\text{FWHM})|_{pi} = 2.35\sqrt{\frac{FW}{E_0}} \tag{4.5}$$

what is known as the *Fano's limit* and yields $R|_{pi@Ar} \simeq 7\%$ and $R|_{pi@Xe} \simeq 5\%$ FWHM for argon ($F = 0.17$) and xenon ($F = 0.13$) respectively at 6 keV. A good compilation of F values is done in [112]. It seems that F follows a composing rule equivalent to (4.2), and so small amounts of additives cannot bring impressive improvements, again with the possible exception of the Penning mixtures (section 5.3).

4.2 Drift, diffusion and attachment.

The drift of the electrons along the chamber to the readout plane is obviously a crucial process for a TPC. The deviation suffered by the electrons from the projection of its initial position to the readout plane and the expected arrival time produces a diffusion of the topological information that affects the TPC imaging capabilities.

[3] That has been obtained with argon plus an small amount (2–5%) of isobutane, however the primary charge generation is a process where atoms basically can be considered independent (see equation (4.2), but keeping in mind the exception of the Penning mixtures), then the primary charge generation statistics are dominated by the interaction with the argon atoms.

The drift time limits its application to high rates scenarios and a slow drift velocity can produce undesired secondary effects.

In spite of being continuously accelerated by the action of the drift field $\vec{E}$, the electrons get an steady drift velocity $\vec{v_d}$, which manifests macroscopically. That reminds the classical case of the motion with friction proportional to the velocity

$$m_e \frac{\mathrm{d}\vec{v_d}}{\mathrm{d}t} = e\vec{E} - K\vec{v_d} \tag{4.6}$$

with m_e and e the electron mass and charge[4]. Note that the equation (4.6) suggests the definition of a characteristic time $\tau = m/K$ for reaching the steady state. From a microscopic point of view, from which the electrons have an instantaneous velocity $\vec{v_i}$ different than $\vec{v_d}$, the macroscopic characteristic time is justified by the average time between collisions of the electrons with the gas molecules, $1/\tau = \sigma N v_i$, with N the molecules density of the gas and σ the cross section for interactions producing an effective momentum transfer between electrons and molecules.

The following qualitative picture may help to construct comprehensive explanations for most of the formulas and plots recompiled in the section, though some of them can seem to go against intuition. Firstly, it must be noticed that the direction of $\vec{v_i}$ can change completely after a collision (in simple models the scattering is isotropic), due to the mass ratio between electrons and molecules. Besides, for elastic collisions the fraction of energy loss per collision, Λ, is of the order of 10^{-4}. So, if only elastic collisions are frequent, we have basically a random walk affected by a continuously interrupted tendency to drift in the direction of $\vec{E}$.

Under these circumstances it is understandable that the possibility of $\vec{v_i}$ being eventually reduced by a big energy loss could bring a benefit, since it would work like a kind of *reset* of the instantaneous velocity. Thus the deviations caused by the scattering are minimized and the electric field energy is invested in driving the charges only in the drift direction. The inelastic collisions causing high Λ can partially materialize such a *reset*.

However, an excessive shortening of the electron's mean free path is also negative for the drift velocity. In addition, each collision means a possibility of the electron being attached by the molecule. The interplay between both effects together with the cross sections that define the interactions between electrons and molecules explain the drift properties of the gases.

There are two extreme cases for gases regarding the way they interact with free electrons[5], both are often chosen for gaseous chambers. On one hand there are the noble gases, with the simplest molecular structures, inelastic collisions at low energies with electrons are not possible and they are very unlikely to absorb

[4] Equation (4.6), was first introduced for electrons transport by P. Langevin. With the addition of a magnetic force is known as the *Langevin formula*.

[5] Molecules with high electron affinity that tend to attach the electron are not considered here.

an electron and have low cross sections allowing long mean free paths. On the other hand there are molecules with complex structures, like organic vapours, whose rotational or vibrational modes can be activated at energies much lower than the electronic excitation energies, what requires a relatively high energy loss for the electron. Those possibilities also increase the cross section.

The most common choice is a gas mixture based in a noble gas with addition of a, usually not too big, amount of a gas of the second group, called *the quencher*[6]. The mixture's drift properties can be optimized depending on the composition and the applied drift field.

There is a rigorous theory of the electrons transport in gases, which can calculate the velocities' distribution, etc; it was just revised during the development of the first TPCs[149]. Usually the Monte Carlo approach is more popular, being the Magboltz code[150] the most common. We will just comment general tendencies and cases of particular interest.

4.2.1 Drift velocity.

If the thermal energy is negligible, i.e. $(1/2)mv_i^2 \gg (3/2)kT$, as in the case of the operational TPCs, the drift velocity as well as the mean instantaneous velocity can be accounted from the energy balance along the drift. The manifestation of a steady (macro picture) or a well defined mean (micro picture) drift velocity entails taht the energy won from the drift field equals the energy lost from collision to collision in average. The resulting velocities are function of the collision properties. The following expressions are due to Townsend[151] from a simple approach which can be also found in [116]:

$$v_d^2 = \frac{eE}{m_e N\sigma(\varepsilon)}\sqrt{\frac{\Lambda(\varepsilon)}{2}} \tag{4.7}$$

$$v_i^2 = \frac{eE}{m_e N\sigma(\varepsilon)}\sqrt{\frac{2}{\Lambda(\varepsilon)}} \tag{4.8}$$

The shape of the velocities' functions have been basically transferred to the dependence of $\Lambda(\varepsilon)$ and $\sigma(\varepsilon)$ with $\varepsilon = (1/2)mv_i^2$; N being the atomic density. As actually $\varepsilon \simeq E\lambda \sim v_i^2$, with $\lambda \sim N^{-1}$ the average path drifted between collisions, both velocities are function of the ratio E/N, or E/P (P the gas pressure), called the *reduced field*, which is conveniently used to parametrize the drift properties. Note the opposite dependence in equations (4.7) and (4.8) on Λ; that is the manifestation of the *reset effect* of the collisions with big losses we referred to in the section's introduction.

[6] This denomination more exactly comes from the role the *quencher* plays in the amplification process (see section 4.4), however in a TPC the gas must be selected regarding as much to the gain as to the drift properties.

From the drift velocity point of view, the optimum case is a gas that allows a long mean free path but causes very inelastic collisions. Thus the electrons are able to reach high velocities and are only driven by the drift field with small deviations.

These are often conflicting features for a simple gas, and that is the reason why mixtures are frequently used. The average time between collisions (or the effective cross section) and the mean fraction of energy loss per collision can be constructed from the components following direct composing rules. The huge differences in the cross sections and the impact of a single inelastic collision implies that, in contrast to the W-value, impressive effects are produced by addition of small fractions of quencher gases. How it works is illustrated in figure 4.2 for argon gas and two typical quenchers. The shape of the drift curves can be justified in basis to the collision properties for the involved gases plotted in figure 4.3.

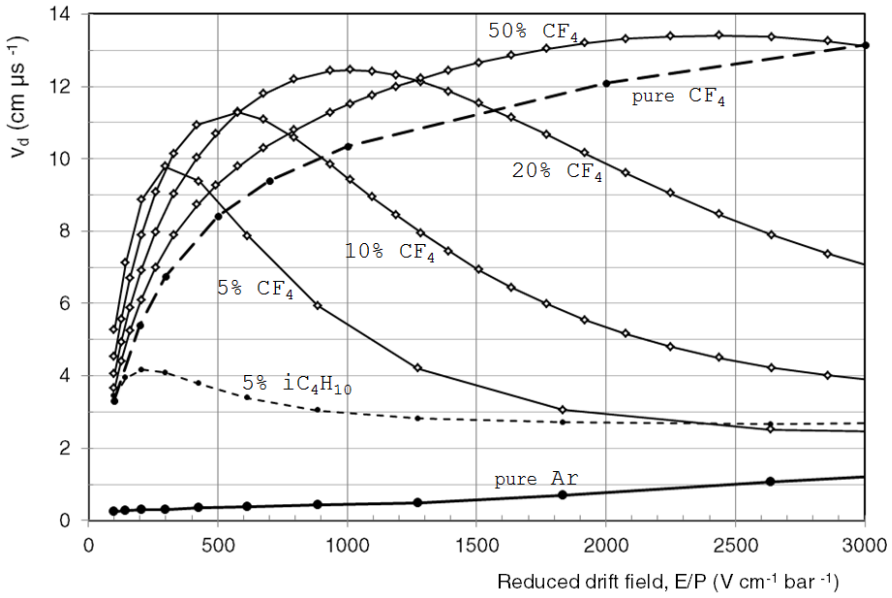

Figure 4.2: Drift velocities calculated with Magboltz. Note the dependence on the E/P ratio, explicitly written in the axis; it was exactly reproduced in the Monte Carlo results.

Although the pure argon gas has the lowest cross sections, the strategy of having only elastic collisions does not work satisfactorily because of the reason advanced in the section's introduction: the dispersion of the direction of the electron's velocity in each collision. The cross section has a dip due to a quantum interaction between the electron and the gas molecules wave lengths named *Ramsauer effect*, that is related with a maximum in the drift velocity, but it is placed at very low drift fields. The opposite strategy, that of the quencher here represented by the CF_4 gas[7], certainly yields higher drift velocities, however a high E is needed to compensate the short mean free path.

[7]Many times called *freon*.

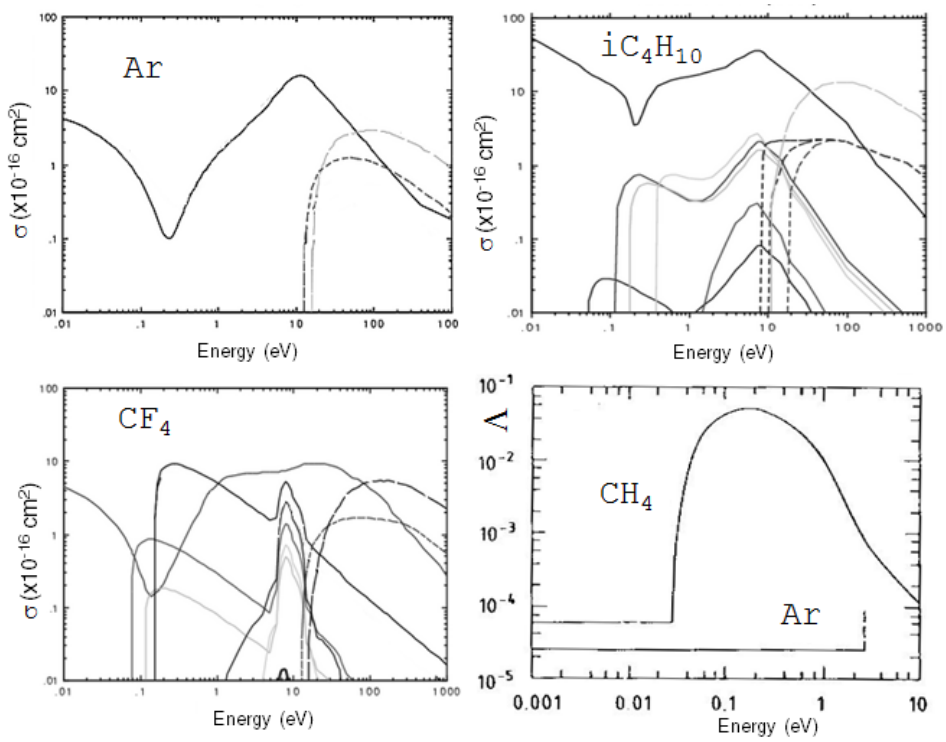

Figure 4.3: Cross sections for effective momentum transfer of electron with Ar, isobutane and CF_4, extracted from [150]. The solid line, which is continuous along the energy range and shows the Ramsauer dip around 0.1 eV, corresponds to the elastic cross section. The rest of solid lines are vibrational modes. The short dashed lines curves, which raise about 10 eV, are excitation cross sections. The long dashed ones, which are activated only with slightly higher energies, corresponds to the ionization cross sections. The last plot, taken from [116] shows a comparison of the *inelasticity* of the collisions of Ar and methane.

When a mixture of gases that follow the opposite strategies is tried, the interplay between the mean free path and the efficiency of the *reset* mechanism makes the drift velocity curve develop a peak whose strength and position depends on the mixture composition: the higher the quencher fraction, the faster the gas can become, but stronger drift fields are needed.

The effect of isobutane, iC_4H_{10}, in the drift properties is also plotted and compared with CF_4. The isobutane is more appreciated for its benefits of the amplification properties, but its addition produces also an important improvement of the pure noble gases drift features. However, figure 4.3 shows that, in contrast to CF_4, any amount of isobutane cannot make the inelastic collisions dominant, since the elastic cross section is also very high for this organic molecule. As a consequence, even with higher fractions of isobutane, drift velocities higher than $\simeq 5$ cm/ μs cannot be surpassed in argon-isobutane mixtues. The butane, C_4H_{10}, whose $\Lambda(\varepsilon)$ is plotted in figure 4.3 to illustrate generically the difference between a noble gas and

a quencher, is another usual quencher whose effects in the drift are intermediate between CF_4 and isobutane.

4.2.2 Diffusion.

The particular history of collisions suffered by the electrons during the drift to the readout cathode accumulate individual deviations of the positions of the electrons respect to the *center of charge* motion described by the drift velocity. For an electron starting at the origin and drifted by the field $\vec{E} = -E\hat{z}$, the density of probability of the electron's position after drifting a time t is

$$n(x,y,z,t) = \frac{1}{\sqrt{4\pi D_L t}}\left(\frac{1}{\sqrt{4\pi D_T t}}\right)^2 \exp\left[-\frac{x^2+y^2}{4D_T t} - \frac{(z-v_d t)^2}{4D_L t}\right] \tag{4.9}$$

where D_L and D_T are the diffusion constants in the direction of the drift field and perpendicular to it, respectively. Many times it is more convenient to re-parametrize (4.9) using

$$\sqrt{2D_x t} = \sqrt{\frac{2D_x l}{v_i}} \equiv \sigma_x \cdot \sqrt{l} \tag{4.10}$$

where l is the drifted distance. The D's and σ's are called equally *diffusion constants* and *coefficients* in the literature, they will be distinguished by their dimensions.

The Gaussian shape of the diffusion is suggested as solution of a transport equation for a conserved current of density, and can also be justified in a simple microscopic picture considering random collisions and isotropic scattering. Note that the particular expression (4.9) considers the electric anisotropy of the media, as it is experimentally observed (see details in [116]). The microscopic treatment brings some interesting results, however they have implicit, but essential, dependences on the gas electronic properties. For instance, it is found that $D_L < D_T$, the ratio being given by

$$\frac{D_L}{D_T} = \frac{1+\gamma}{1+2\gamma}; \quad \gamma \equiv \frac{\varepsilon}{\nu}\frac{\partial \nu}{\partial \varepsilon} \tag{4.11}$$

with $\nu = 1/\tau$ and the derivative evaluated in the balance point.

We will comment particular examples produced with Magoltz. Equivalent figures to 4.2 for diffusion σ's are 4.4 and 4.5. The conclusions and reasonings that can be extracted from them are practically equivalent to those of the drift velocity dependences. The first remarkable fact is the impressive improvement got with the addition of even an small amount of quencher, which is more moderated in the case of the isobutane than in the case of CF_4.

Regarding the diffusion, it seems more clear than in the case of the velocity that inelastic collisions, even being frequent, are useful since a short mean free path also

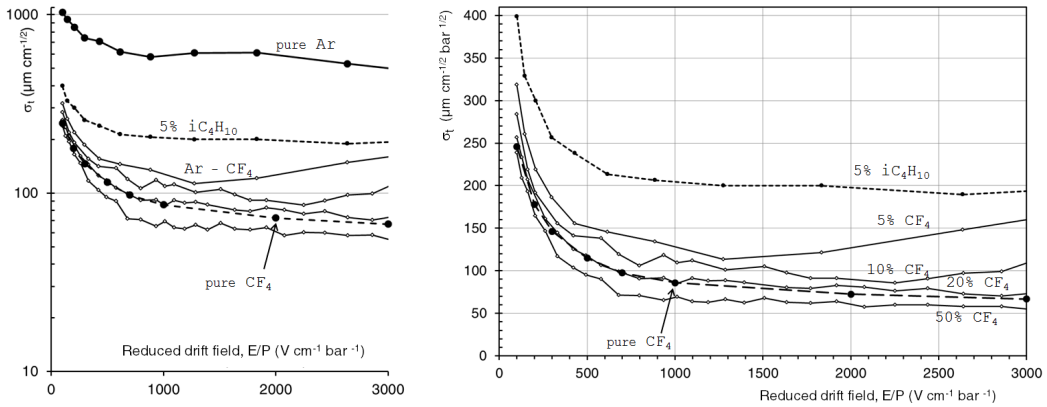

Figure 4.4: Transversal σ calculated with Magboltz (same mixtures and notations of figure 4.2. In the right a detail in linear scale for the mixtures. Notice the scaling factors E/P and $P^{1/2}$.

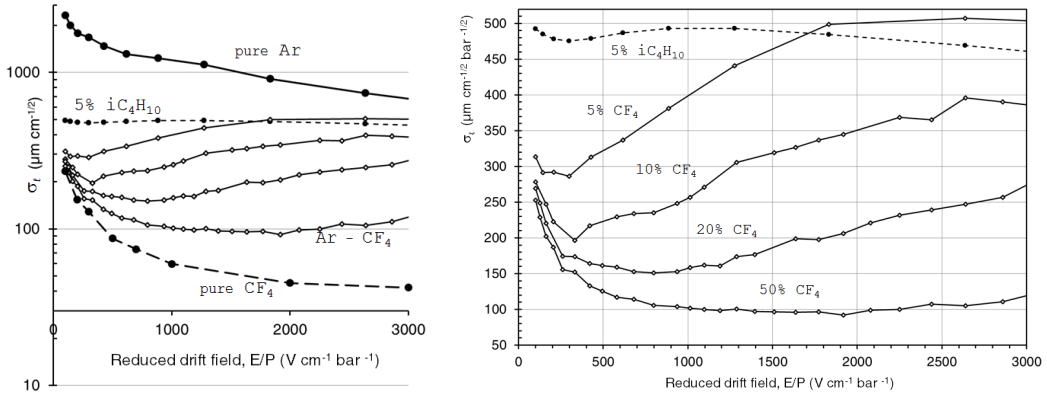

Figure 4.5: Longitudinal σ calculated with Magboltz. In the right a detail in linear scale for the mixtures. Notice the scaling factors E/P and $P^{1/2}$.

contributes to decrease the accumulated deviation. It seems a rule that increasing the quencher fraction and the electric field improves the diffusion. However a kind of optimum seems to be achieved for transversal diffusion around 20% of CF_4[8]. Besides the curve is more complicated in the case of the longitudinal diffusion, which is clearly correlated with the drift velocity's curve; it develops a minimum and so anomalous sections where increasing the drift field implies a diffusion worsening.

A scaling factor with N or P is assumed by the plots and it is exactly reproduced by the Magboltz program. It can be easily understood from the simple microscopic picture. Since $\tau \sim N^{-1}$, the number of collisions during the drift goes as $n \sim$

[8] A simple study for optimization of the Ar-CF_4 mixture for Dark Matter searches, taking into account also other considerations, is done in section 7.1.4, see figure 7.11.

$t/\tau \sim N$; on the other hand the mean displacement in a given direction $\lambda_x \sim N^{-1}$ and the mean accumulated displacements for a random walk is $\sqrt{n}\lambda$. Therefore $\sigma_x \sim \sqrt{n}\lambda_x \sim N^{-1/2}$.

4.2.2.1 Mechanisms to improve the diffusion.

One resource to minimize diffusion effects is the application of a magnetic field $\vec{B}$, the electron trajectories become helical instead of straight lines, what produces a net decrease of the diffusion constant transversal to $\vec{B}$ (see details in [116]):

$$\frac{D_T(\omega)}{D_T(B=0)} = \frac{1}{1+\omega^2\tau^2} \tag{4.12}$$

where $\omega = (e/m_e)B$ is the cyclotron frequency of the electron.

The drift of ions presents advantages from the diffusion point of view, since even the elastic collisions produce high energy losses and they are not isotropic (see [116]). However they have much slower drift velocities and the primary charges cannot be amplified as easy as with electrons; therefore only very high energy signals could be detected.

The concept of *the negative ion TPC (NITPC)*[152] tries to combine ions drift properties with usual electron amplification. The idea is to use an electronegative gas with the aim of attaching the primary electrons, what creates negative ions that drift, slow but with low diffusion. When they arrive to a region near the readout, they are dissociated again by means of a strong magnetic field; thus electrons can start the avalanche process (see section 4.4). The development of such a TPC means a technical challenge that is being faced by the DRIFT collaboration[47].

4.2.3 Attachment and recombination.

The *attachment* is the absorption of the electron by a molecule present in the gas during the drift. It produces an obvious impact on the detector signal strength and resolution. All the molecules have a certain attachment cross section (the lowest correspond to the noble gases), but attachment is generically caused by impurities with high electron affinity, specially air and water. A review about the different kinds of attachment mechanism is done in [18].

Another mechanism producing the same undesirable result is the *recombination* that happens when the electrons meet the positive ions that are drifting in the opposite sense (see an example in figure 4.13). Generically the probability of an electron surviving in the gas is accounted by any of the following formulations:

$$\frac{n}{n_0} = \mathrm{e}^{t/\tau_c} = \mathrm{e}^{r_a t} = \mathrm{e}^{z/\lambda_c} = \mathrm{e}^{az} \tag{4.13}$$

where the regarded parameter will be called electron's *mean lifetime* or *attachment rate* or electron's *capture mean free path* or *attachment constant*. They will be often

referred just as *attachment coefficient* and will be distinguished by the dimensions.

In order to avoid the attachment, for a gas with a given concentration of electronegative molecules, it is clear that increasing the drift velocity is an advantage, what usually requires higher drift voltages. This effect is not absorbed by the formulations of (4.13) in terms of length, since the attachment cross sections tend to decrease with ε, that is increased with E.

Although the micromegas' structure prevents the recombination, because the ion back-flow produced in the amplification is absorbed by the mesh and does not enter the drift region, the mesh itself introduces a fundamental limitation for the drift field intensity, which may be needed to avoid attachment and recombination. That will be the issue of the next section.

4.3 Mesh transparency.

Many of micromegas advantages are based on the practical division of the chamber into two volumes: the drift and the amplification regions. However a physical barrier, the micromegas mesh, is placed in between. The reason why this obstacle is not usually a problem in practice will be visually understood from figure 4.6.

Ideally the electrons will follow the lines of the electric drift field. Thus the *electronic transparency or transmission of the mesh*, i.e. the percentage of the electrons that reach the amplification region, would be computed from a given geometry as $\eta_e = \Phi_{13}/(\Phi_{13} + \Phi_{12})$, the Φ_{xy} are defined in the caption of figure 4.6.

The transparency relies on the increase of the density of the field lines produced in the amplification region with respect to the drift region; i.e. the field ratio FR $\equiv E_{\text{drift}}/E_{\text{amp}}$ works against the mesh transmission. The dependency of the signal amplitude on FR is often called the micromegas' *transparecy* or *transmission curve*. Experimentally it is explored by fixing E_{amp} and changing E_{drift}, i.e.

$$[\eta_e(E_{\text{drift}})]_{E_{\text{amp}}=E_0}$$

That should be named the chamber's *collection efficiency curve*, because other chamber features, like the drift field geometry, and effects due to processes associated with electrons transport, can be detected in the curve. In fact, taking a collection efficiency curve is one of the most useful diagnostic tests for a micromegas chamber.

Collection efficiency curves taken for several micromegas mesh's geometries (see figure 4.7 and table 4.1) are plotted in figure 4.8. The mesh transparency causes the fall of all the curves at high FR. A significant feature is that, for low enough FR, the signal saturates and become independent on FR, that is called *the plateau*. This fact suggests the mesh transmission to be near the 100% and so the signal strength is customarily normalized to the plateau value. The existence of a plateau is a crucial requirement for the proper performance of a micromegas detector.

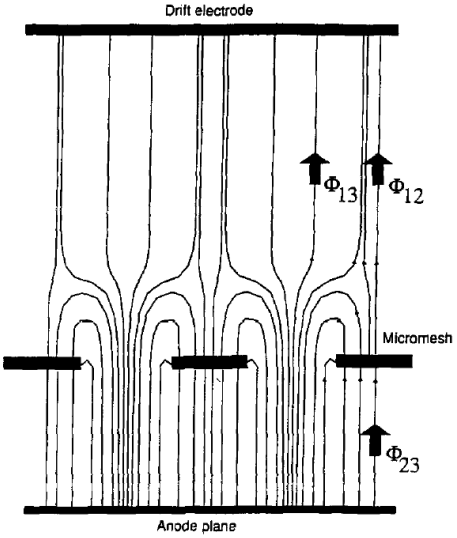

Figure 4.6: Electrostatic sketch of a micromegas chamber (extracted from [153]). Φ_{xy} means the flux to electrode x from electrode y, being 1: the drift cathode; 2: the micromegas mesh and 3: the anode.

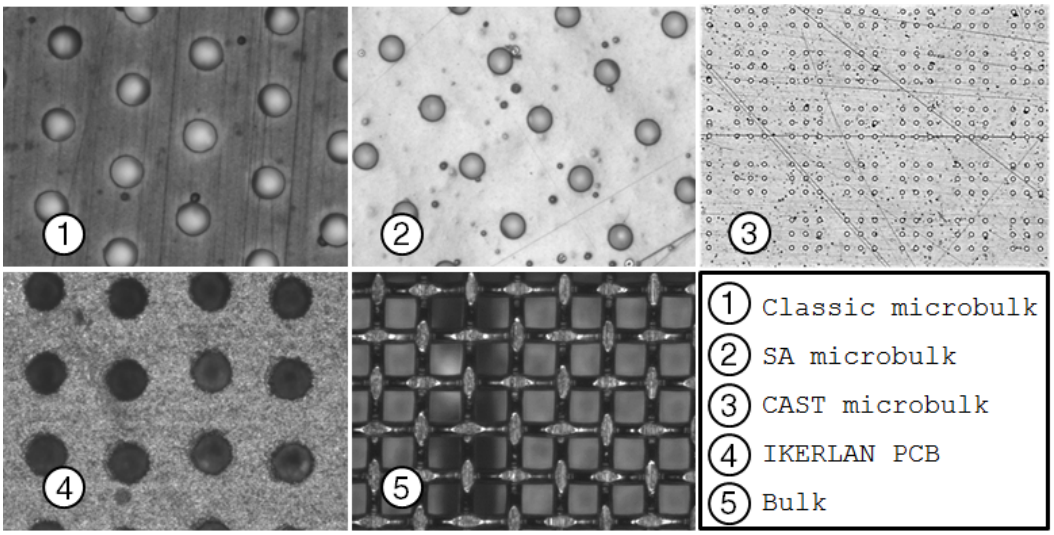

Figure 4.7: Mesh types whose transparency is compared in figure 4.8. The mesh design's parameters are collected in table 4.1.

#	name	pattern	pitch (μm)	$\varnothing$ (μm)	η_{opt}
1	classic	hexa	100	30	0.17
2	SA	sqrt	100	30	0.071
3	CAST	sqrt^2	100	30	0.038
4	IKERLAN PCB	sqrt	100	50	0.20
5	bulk	woven	80	50	0.44

Table 4.1: Mesh's parameters for the types photographed in 4.7. Types 1, 2 an 3 are microbulk. For the type 5, $\varnothing$ means the interior square's side.

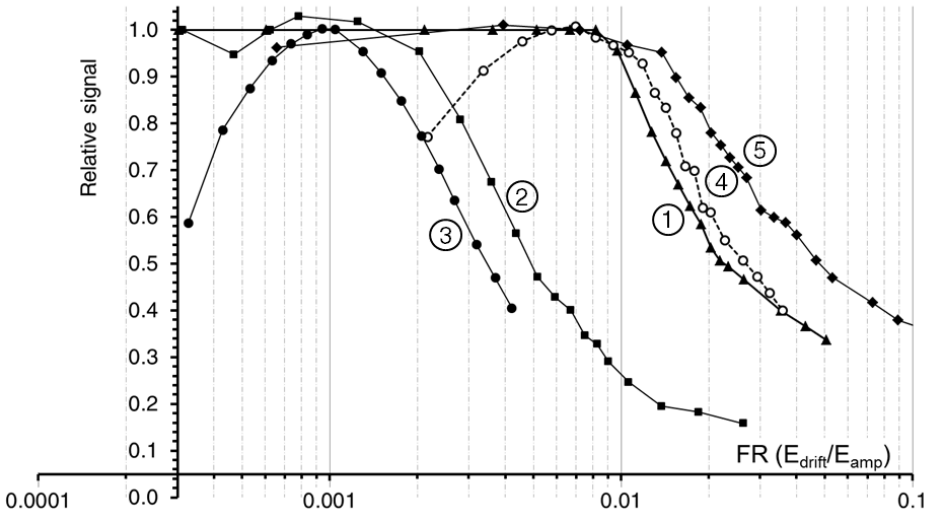

Figure 4.8: Collection efficiency curves taken for the different mesh types of figure 4.7 and table 4.1. The gas is Ar + 5% iC_4H_{10} at atmospheric pressure for all the curves, with exception of the number 3, taken at CAST operation conditions: Ar + 2% iC_4H_{10} at 1.4 bar.

If no plateau is observed, the identification of the maximum with $\eta_e = 1$ is not supported and the comparison with other curves may lead to error. That is often caused by electron drift problems, as attachment or recombination. The low FR part of the curve is useful for the diagnostic of the gas purity. An example can be found in the curve number 3, nevertheless it should be noted that it corresponds to a CAST detector's chamber, while the rest of them have been taken under tests conditions in specially dedicated set-ups, thus the CAST chamber is 3-6 times taller and the gas a bit slower. The case of curve number 4 has a different nature and its discussion will be postponed to section 4.3.2.

The correlation between the plateau extension and the optic transparency of the mesh, calculated as $\eta_{\text{opt}} \equiv$ (holes area)/(mesh area), is evident (see table 4.1). The hexagonal pattern of the first microbulks (called *classic*) produces a plateau up to $FR \simeq 10^{-2}$, which is dramatically reduced if the pattern is squared. Apart from the transparency, when operating in the plateau, the microbulk type 2 are as good as type 1. The type 3 is like 2, but the mesh holes are put into isolated groups (see section 8.2.2), the plateau ends at $FR \simeq 10^{-3}$, one order of magnitude worse than classic microculks.

The loss of transparency can be compensated by means of an enlargement of the holes size, up to recovering the optical transparency, as it is done with type 4. However this may entail secondary effects (see section 4.3.2). The bulk's woven mesh is the most transparent.

The consequences of the loss of electronic collection efficiency go beyond a soft degradation of the signal strength. A limited transparency, like attachment and recombination, entails a difficulty affecting the primary charges, what degrades seriously the energy resolution of the micromegas. In figure 4.9 left is shown a perfect inverse correlation between the transparency and the energy resolution and how the latter degenerates suddenly when the end of the plateau is reached. For a detector without a wide plateau, the transparency becomes a matter of tuning, limiting the operational range and stability (see figure 4.9 right).

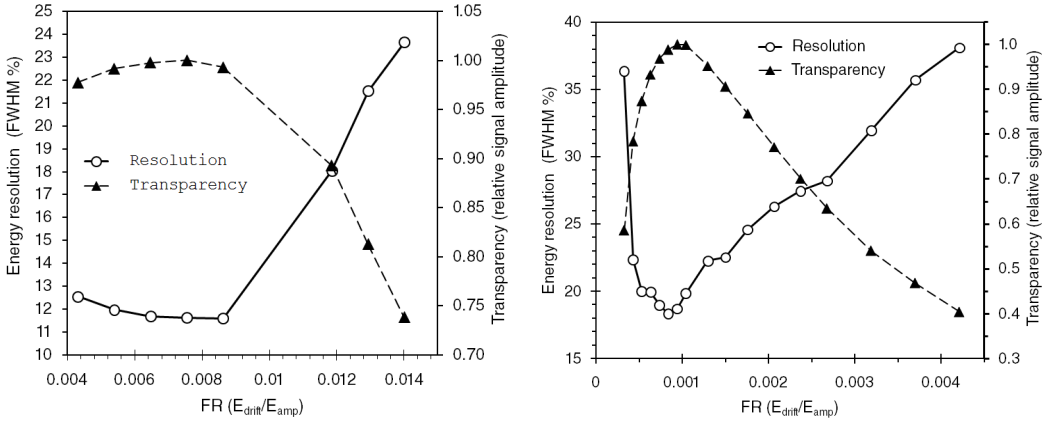

Figure 4.9: Correlation between transparency and energy resolution. Left: for a microbulk from the group CM, classic type 1. Right: for a CAST microbulk, detector M10.

4.3.1 Parametrization of the typical transparency fall.

The fall is well fitted to an exponential up to the transparency loss is around 50%, see for instance, figure 4.11. A simple fit for the first half of the fall is

$$\eta_e = \exp\left[-d(FR - FR_{end})\right] \tag{4.14}$$

where FR_{end} marks the end of the plateau due to the loss of transparency and d is the slope of the fall. The results from fitting the transparency curves of figure 4.8 are gathered in table 4.2 and plotted in figure 4.10.

micromegas #	1	2	3	4	5
FR_{end} ($\times 10^{-3}$)	8.704	1.523	1.176	10.04	11.33
d	56.35	185.3	298.5	49.26	25.56

Table 4.2: Fit results (fit 4.14) for the meshes described in table 4.1. The values are plotted versus the mesh's optical transparency in figure 4.10.

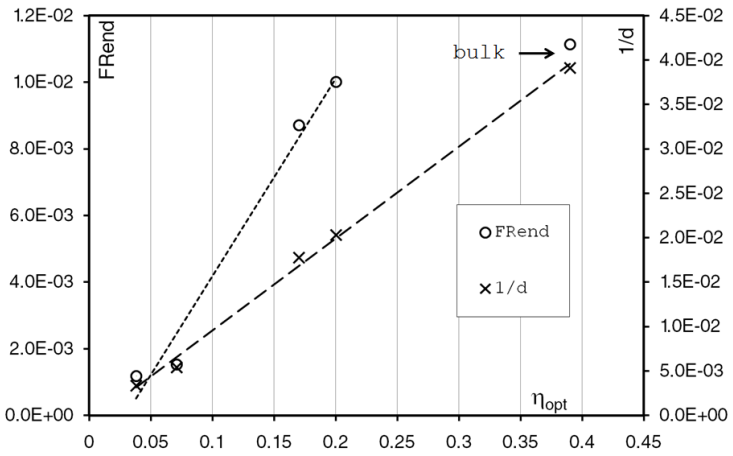

Figure 4.10: Results from table 4.2 plotted versus the optical transparency of the mesh. An approximate linear dependency can be found only with the exception of the plateau extension of the bulk.

The fall's slope becomes softer below 0.5. Since it is the most reproduced design for microbulks, the transparency fall of mesh type 1 is characterized in detail in figure 4.11. In order to describe the whole fall the following function can be used:

$$\eta_e = p_1 \cdot \exp\left[-p_2(FR - p_0)\right] + p_3(FR - p_4)^{-p_5} \tag{4.15}$$

taking the results for the parameters that are written in figure 4.11.

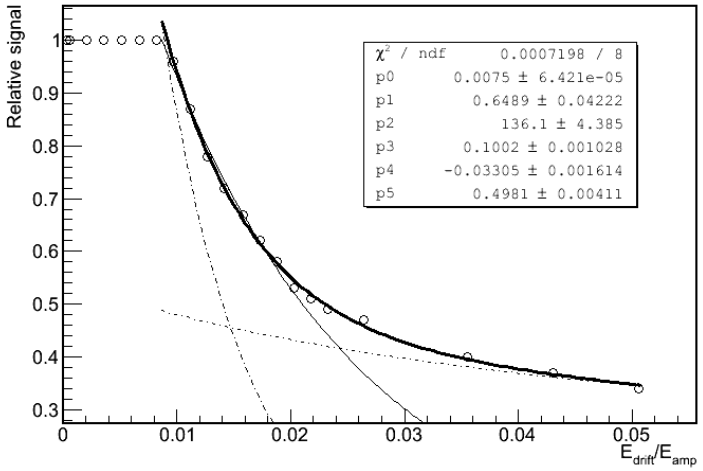

Figure 4.11: Reference for a micromegas transparency (from curve number 1 in figure 4.8). The simple exponential fit (4.14) is drawn with a thin line. The complete fit (4.15) is drawn with a gross line; the functions it consists on are also drawn with non continuous lines and the fit parameters are written in the legend.

4.3.2 Limits for the mesh design.

The degradation of the electronic collection efficiency for low FR observed for the curve number 4 in figure 4.8 is difficult to be attributed to attachment regarding the testing conditions (high gas flow and short drift gap of only 5 mm). The gas hypothesis is completely ruled out by the precise reproduction of the curve with a different specimen in a different laboratory (see figure 4.12).

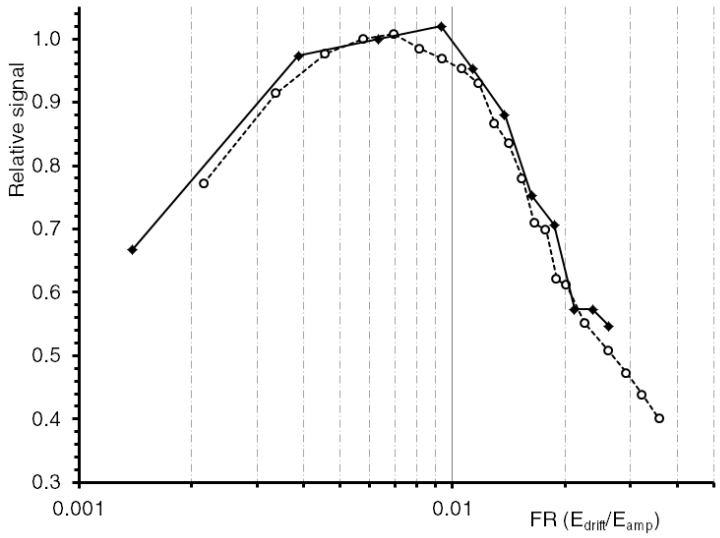

Figure 4.12: Transparency curves registered for IKERLAN PCB micromegas (mesh type number 4 in figure 4.7). Black diamonds and solid line: PCB2, Zaragoza's lab, Aug 2008. Empty circles and dashed line: PCB3, Saclay's lab, Oct 2008.

The absence of the plateau is a feature of the particular micromegas structure. Trying to explain the curve we come back to figure 4.6, in the sketch two zones with very well defined electric field are clearly distinguished above and below the mesh. These are E_{drift} and E_{amp}, and their sharp differentiation makes physics of micromegas be simple and effective. Nevertheless, it actually exists a transition zone originated by the deviation from the ideal parallel-plates geometry due to the required holes. Such a zone should be smaller as smaller are the holes with respect to the typical micromegas' lengths: the pitch and the amplification gap. If the transition is too slow, or the transition volume starts being comparable with the amplification volume, the fact that the micromegas gain is independent on E_{drift} can stop being true.

This should be the case for these IKERLAN PCB micromegas[9] with 50 μm diameter holes and 50 μm amplification gap. Therefore the left fall of the curves

[9]These micromegas were developed by the IKERLAN technology center (L. Fernández and D. Gassull) in collaboration with the LFNA, and are based on conventional lithography techniques.

cannot be due to electron transport problems neither to a transparency loss, but to a decrease of the gain through a dependence on E_{drift} (similar observations are made in [112] studying InGrid detectors). The peak must manifest a compromise between the gain and the transparency. These particular micromegas had a typical energy resolution of 16% FWHM at 6 keV which must be limited by the mesh pattern.

4.3.3 Transparency quench.

The concept of *quenching factor* as a dependence of the signal strength on the kind of particle is usually referred to the physical interaction (see section 3.1.5.1). However any other difference on the drift or the amplification processes would lead to the same result in practice. It can be imagined that the high density of charges generated by the α particles may disturb the electric field geometry in the transition region, between the drift and the amplification volumes, worsening the concentration of drift lines through the mesh's holes and causing a loss of electronic transmission. That space-charge effect could be named *transparency quench*.

It was already demonstrated in figure 4.1 that the effect is small when the micromegas is working inside the plateau. The measurements of figure 4.13 check whether the extension of the plateau itself is affected by the charge density. They show no distinction between the two kinds of events at high FR. On the contrary, for the dense electron clouds of α events the recombination reduces collection efficiency at low FR.

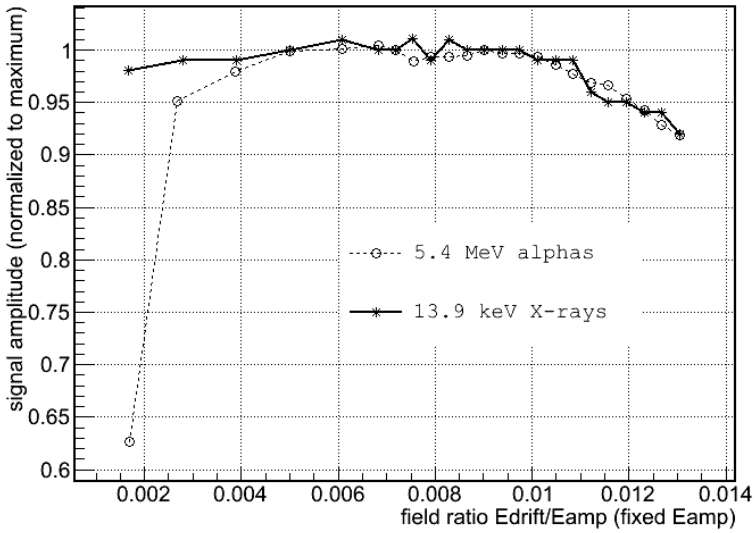

Figure 4.13: Electronic collection efficiency curves taken with a classic microbulk micromegas (type 1 in 4.1) in Ar with 5% iC_4H_{10} at 4 bar, using the set-up described in 4.4. Circles are calculated from ^{241}Am 5.4 α and asterisks from ^{241}Am 13.9 keV X-rays at the same time (during an only measurement run, using exactly the same gas and set-up conditions). E_{amp} is fixed to 88 kV/cm and E_{drift} varies from 0.15 to 1.15 kV/cm.

4.3.4 Transparency and diffusion.

Most of reasonings about the mesh transparency are made on the basis of electrostatic sketches as the one in figure 4.6. We must be aware of the implicit assumption that the drift electrons will follow the electric field lines is an idealization, the contrary may lead to think that the mesh transparency is a purely geometrical aspect. A rigorous study of the mesh transparency requires the Monte Carlo simulation of the electrons' trajectories, which are affected by collisions, and so it concerns the gas properties. Particularly the transversal diffusion can be seen as the degree of deviation from the ideal electrostatic model.

We think that figure 4.14 shows evidence that diffusion affects the transparency. Measurements are made for both bulk and microbulk (classic type, number 1 in table 4.1) sharing the same gas (see figure 4.15) for argon with 5% isobutane (iC_4H_{10}) and CF_4, whose diffusion properties have been studied in section 4.2.2.

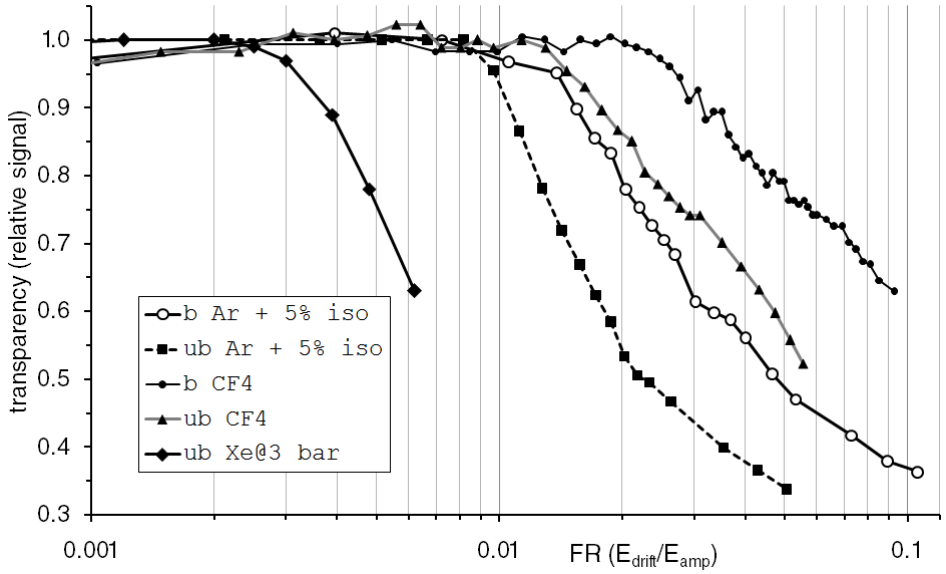

Figure 4.14: Transparency curves taken with a classic microbulk micromegas (ub), type 1 in 4.1, and a bulk micromegas (b), in Ar with 5% iC_4H_{10} and CF_{10} at atmospheric pressure, and pure Xe at 3 bar.

It seems that the improvement of diffusion by the CF_4 enlarges the end of the plateau and also softens the transparency's fall slope. It is remarkable the fact that the microbulk, when using CF_4, becomes more transparent than the bulk, if using iC_4H_{10}. A complete set of transparency curves for argon with several isobutane concentrations is reported in [154] and shows the same effect: the transparency plateau is extended as the isobutane concetration is increased. Similar observations with InGrids are made in [112].

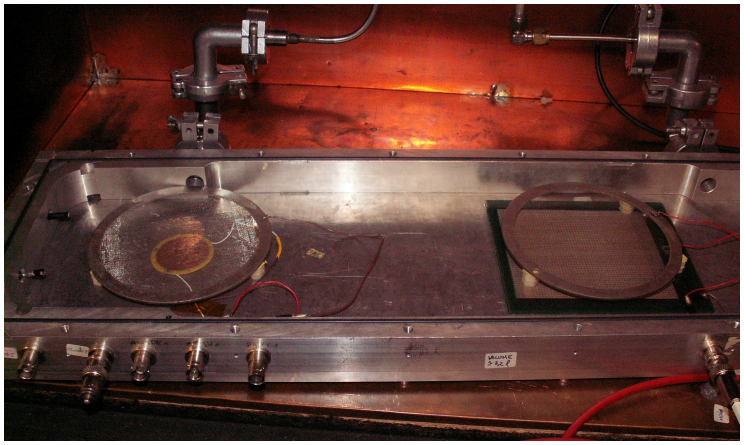

Figure 4.15: Saclay's micromegas lab tests chamber, where most of the gas and micromegas characterization measurements of present and next sections were carried out (courtesy of A. Giganon). Particularly the photo shows the set-up prepared for the measurements of figure 4.14, a microbulk (left) and a bulk (right) with individual drift grids inside the same chamber, Dec 2007.

A third transparency curve is added to figure 4.14 for a gas with much worse diffusion, pure xenon (only slightly better than argon in figure 4.4), using the same microbulk type, though in a different set-up (Zaragoza's HP-test chamber) and pressure. The complete set of measurements with pure xenon is plotted in figure 4.16; there how the plateau extends to higher FR as higher is the gas pressure can be appreciated.

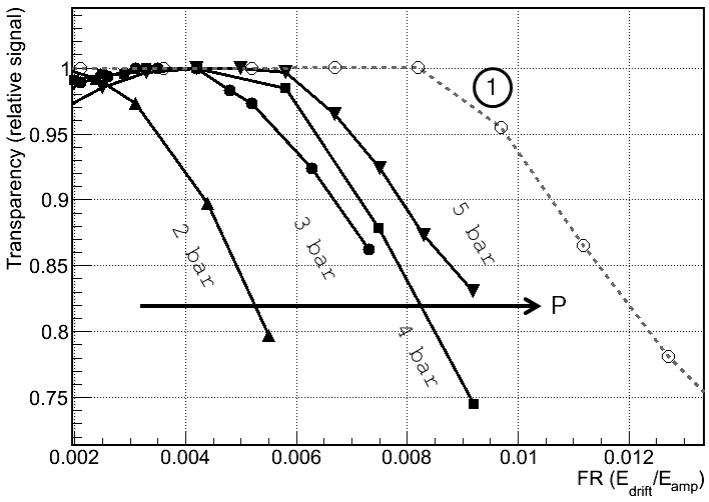

Figure 4.16: Transparency curves for pure xenon at different pressures, the reference curve number 1 from figure 4.8 is also plotted for comparison. Figure extracted from [155].

Such a behaviour could be connected with the $\sigma \sim P^{-1/2}$ general scaling rule expected from section 4.2.2. The effect of pressure in the plateau is much clearer in the set of measurements with xenon and 1.5% trimethylamine shown in [156]. The transparency curve at 1 bar is very similar to the one obtained in argon with 5% isobutane. Furthermore, as pressure is increased, the plateau's end moves to higher FR and the transparency's fall becomes softer.

4.4 Amplification: gain and energy resolution.

In this section the avalanche process that produces the amplification of the primary charges will be studied for the particular case of a micromegas, i.e. in an uniform electric field. Some representative experimental results will be reported.

4.4.1 The Townsend coefficient and the micromegas gain.

When an electron is accelerated by an electric field and becomes energetic enough, it can yield secondary ionization whose products will join the avalanche. The process of multiplication of the N electrons of the avalanche is described by the Townsend coefficient α, which is defined by the equation

$$\mathrm{d}N = N(s)\alpha\,\mathrm{d}s \tag{4.16}$$

where s parametrizes the development of the multiplication process as the length the avalanche progresses in the direction of the electric field. Basically $\alpha(\varepsilon) = \rho_e\sigma_i(\varepsilon)$ depending on the electron energy from the ionization cross section and proportional to the electronic density of the gas. However the useful definition of the coefficient incorporates the energy distribution of the electrons for the electric field E, $p_E(\varepsilon)$, and works as a mean (for high N)

$$\alpha(E) = \int_0^\infty p_E(\varepsilon)\alpha(\varepsilon)\,\mathrm{d}\varepsilon \tag{4.17}$$

therefore the Townsend coefficient is determined experimentally or computed with a Monte Carlo (see figure 4.17).

The discussion for a microscopic understanding of the avalanche development is made in similar terms of that of section 4.2, though the energies are higher and so the involved cross sections are different. The relevant processes are ionization, recombination, attachment by electronegative molecules, and excitation and desexcitation where photons in the UV range are implied. There are several popular semi-empirical expressions with parameters that depend on the gas, like the Rose-Korff's[157]

$$\alpha = P\,A\mathrm{e}^{-B\,P/E} \tag{4.18}$$

with P the gas pressure and where A and B are gas' parameters. Diethorn proposed a Townsend coefficient proportional to E[158]. According to figure 4.17, the linear approximation seems quite accurate for electric fields higher than few tens of kV/cm.

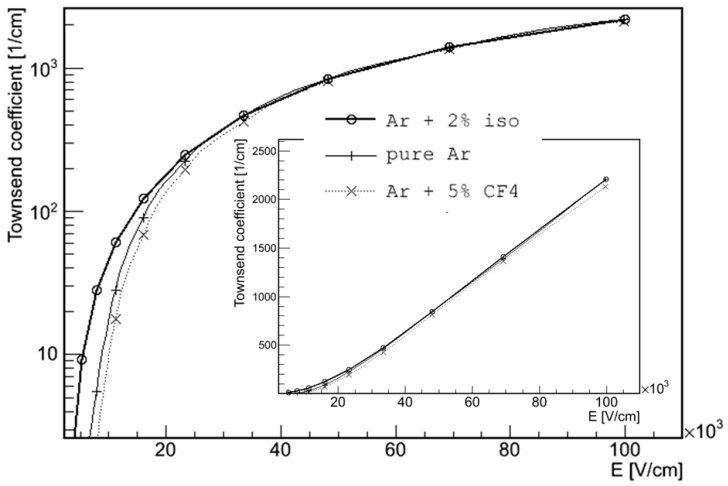

Figure 4.17: Townsend coefficient as function of the electric field according to Magboltz for pure argon and after the addition of two quencher gases. Detail in linear scale.

For a uniform electric field, the integration of (4.16) along the micromegas amplification gap d produces

$$G \equiv N/N_0 = \mathrm{e}^{\alpha d} \tag{4.19}$$

as the ideal expression for a micromegas gain.

4.4.1.1 The maximal condition of the micromgas gain.

One of the beneficial basis of micromegas can be deduced by combination of (4.18) and (4.19):

$$G = \exp\left(APd\,\mathrm{e}^{-\frac{BPd}{V}}\right), \tag{4.20}$$

with $V = Ed$ the voltage applied between the micromegas mesh and anode. It shows G as a function of the product Pd. The differentiation of (4.20) with respect to d,

$$\frac{\partial G}{\partial d} = G\alpha\left(1 - \frac{BPd}{V}\right), \tag{4.21}$$

finds that a maximum can be tuned for a micromegas depending on the gas and the operation conditions. It can be shown[159] that for argon based mixtures operating near atmospheric pressure, the operative values of the pair V and d (i.e. voltages

that produce a high gain inside stability) are close to the condition $BPd/V = 1$ for micro-gaps around 50 μm . Then, since working in the neighbourhood of a maximal point, the effect of the variations in the micromegas gap due to manufacturing imperfections are minimized, as well as the variations in the gas pressure. That brings benefits for the homogeneity of the micromegas response in space (energy resolution) and time (gain stability). The existence of the maximum is demonstrated in [159], not by testing micromegas with different gaps, but inducing equivalent variations of the pressure. In [160] three micromegas-like InGrid with gaps between 45 and 70 μm point to an optimum gap about 53 μm .

That condition will not be mistaken for a condition for achieving a maximum gain with a micromegas. The condition was interpreted as an optimum electric field for a given gas and conditions. Then the combination of E and d will result in a certain gain, in case E is applicable. Actually larger gaps usually achieve higher maximum gains despite working with lower fields. The limit on the gain of a micromegas has a different nature and is briefly commented in the following section.

4.4.1.2 Maximum achievable gain.

The real avalanche has a geometry where ions and electron charges are not uniformly distributed. The internal electric field induced by the charges can produce a spark breakdown if they are too numerous. A phenomenological limit known as the *Raether condition* predicts the breakdown when $G \sim 10^8$, i.e. $\alpha d \sim 20$.

In practice it is difficult to achieve $G > 10^5$ because other aspects can also trigger the spark. The most important is the induction of a second avalanche started by a secondary photon that induces a photo-electron in a gas molecule or the mesh material. Avoiding this is the main purpose of *the quencher* gas, which must have good absorption cross section for these photons and lead to the excitation of non radiative states (rotating, vibrating). In the absence of any quencher, pure argon or xenon break down before achieving $G > 10^3$ in typical microbulks[161]. The role of the quencher is then crucial in order to achieve high gain and stability; besides it can produce diverse effects that are left to section 4.4.3 for being illustrated in basis to some practical examples.

Both spark breakdown trigger mechanisms mentioned above are understandably reinforced for high stopping power particles and high trigger rate, i.e. by the time and space density of avalanches, since the photons generated by an avalanche can affect another one. The maximum stable gain obtained in figures 4.1 and 5.3 can be compared with typical gains, for example from figure 4.24; they are much lower in presence of α-particles, even though the trigger rate was decreased to few Hz by collimation of the source.

In this sense the microbulk geometry is thought to provide an advantage since the the amplification volume is divided in a kind of amplification cells isolated by $\sim$ 50–100 μm of kapton, which can absorb the photons acting as a *geometric quencher*.

Finally the design lengths and tolerance of materials can imply a limitation to the voltage applied to the micromegas. Specially particular imperfections in the softness of the mesh and anode surfaces and borders, the presence of a piece of dust or humidity, which tends to be persistent inside the micromegas structure, can limit the operation of a micromegas because of reasons that are not related with the avalanche process.

4.4.2 Avalanche fluctuations and energy resolution.

In order to characterize the avalanche fluctuations, an immersion in the microscopic picture associated to equation (4.16) is required (details are given in [116]). That means that $\alpha(\varepsilon)$ must be evaluated for the particular electron, what actually introduces a dependency $\alpha(s)$, even when E is constant, related with the particular electron history or the avalanche development.

A new electron, that is produced with nearly zero energy, needs to travel a distance longer than $s_0 = U_i/E$, with U_i the first energy of ionization of the gas, before being able to ionize as well. On the other hand, from (4.16) it can be defined an ionization mean free path for the electron $\lambda = 1/\alpha$. The comparison of both lengths is related with the relevance of the particular position the electron was released, and parametrizes the distributions of avalanches

$$\chi(E) \equiv \frac{s_0}{\lambda} = \frac{\alpha(E)U_i}{E} \tag{4.22}$$

χ is named the *relaxation parameter*. Note that from the definition of $\alpha(E)$ in (4.17), s_0 already influences $\alpha(E)$ because is related with the electrons' energy distribution and $\chi < 1$. Values of χ from Magboltz's description of $\alpha(E)$ (see figure 4.17) for an argon-based mixture are plotted in figure 4.18. Values of U_i: 15.8 eV (Ar) and 12.1 eV (Xe).

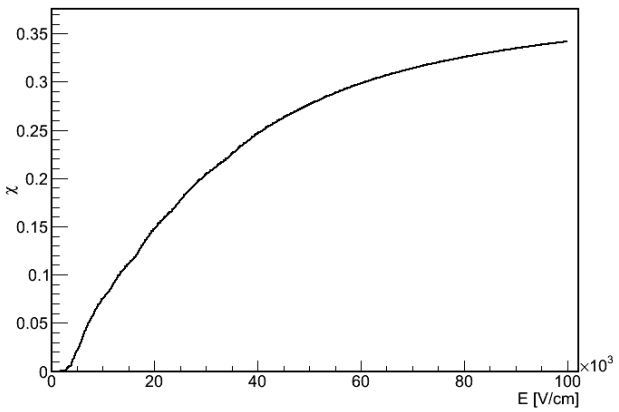

Figure 4.18: Relaxation parameter $\chi(E)$ plotted from expression 4.22 for argon based mixtures ($U_i = 15.8$ eV) and $\alpha(E)$ of Ar/iC_4H_{10} 98/2 taken from figure 4.17.

According to the typical dependency of $\alpha(E)$, $\chi(E)$ usually increases with E. Therefore the limit $\chi(E) \ll 1$ is called the *weak fields* approximation. In such a limit the electrons are energetic enough to practically ionize at every time, i.e. there is no history dependency since $s_0 \to 0$ and so the position the electron was released in is irrelevant. Thus the interpretation of (4.17) as a probability per path length is directly applicable. In agreement with this reasoning the electrons follow a purely stochastic cascade process which, after having advanced a distance s has produced a population N obeying the following probability distribution

$$P(N,s) = \frac{1}{\bar{N}(s)} \mathrm{e}^{-\frac{N}{\bar{N}(s)}}, \quad \bar{N}(s) = \mathrm{e}^{\alpha s} \tag{4.23}$$

The way the cascade is developed is actually independent on the particular scale given by α, i.e. $P(N,\bar{N})$, this means that for a given multiplication factor $G = \bar{N}$, the distribution is the same for any micromegas[10]. The lowest multiplication factors are always the most probable and there is no maximum. The distribution (4.23) has an associated variance

$$\sigma^2(s) = \bar{N}^2(s) \tag{4.24}$$

Note that (4.24) (*Yule-Ferry law*) does not introduce any relative advantage with the size of the avalanche, in contrast to what happens in the case of the primary charge generation with the energy of the interaction (see section 4.1.2).

If χ increases, *strong field limit*, s_0 entails a sterile path for the electron along which there is no charge yield. That introduces a kind of pattern with ionizations produced approximately every s_0, and so the the ionization process become more regular. Therefore the fluctuations are reduced and a most probable multiplication factor rises as a maximum in the $P(N)$ distribution.

The problem has been addressed by means of Monte Carlo models for the individual electron trajectories[162] or by introducing a dependency of the ionization probability with the current avalanche size[163]. Even tougth there are subtle differences between the different provided answers, the Polya distribution, also known as Negative Binomial Distribution, is found to reproduce quite accurately the distributions generated by single electron avalanches (for a comparison with the experiment using a micromegas see [164]):

$$P(m,N) = \frac{m^m}{\Gamma(m)} \frac{1}{\bar{N}} \left(\frac{N}{\bar{N}}^{m-1}\right) \exp\left(-m\frac{N}{\bar{N}}\right) \tag{4.25}$$

for $G = \bar{N}$ and m a parameter whose meaning will be shown just below[11]. The distribution (4.25) has a maximum at $\bar{N}(m-1)/m$ and a variance

[10] In fact that is also true for any dependency $\alpha(s)$, using in this case $\bar{N}(s) = \exp\left(\int_0^s \alpha(s')\,\mathrm{d}s'\right)$.
[11] Some authors use $\theta + 1 = m$.

$$\sigma^2 = \bar{N}^2 b \tag{4.26}$$

with $b = m^{-1}$ [12]. There is a connection between b and the relaxation parameter[165][13]

$$b(\chi) = \frac{(2e^{-\chi} - 1)^2}{4e^{-\chi} - 2e^{-2\chi} - 1} \tag{4.27}$$

Then b decreases with χ (see figure 4.19 left, the model has sense only for $\chi \leq \ln 2 \simeq 0.69$) and, since $\chi(E)$ is also monotonic in the usual range (see figure 4.18), b decreases with E (see figure 4.19 right). Therefore, as E is increased, the maximum of the distribution moves to higher values and the variance becomes narrower for the same gain (see figure 4.20). That is another advantage of the choice of micro-gaps that work at higher E. Note that the expressions (4.25) and (4.26) are reduced to the weak field results (4.23) and (4.24) for $m = 1$, i.e. $\chi \to 0$.

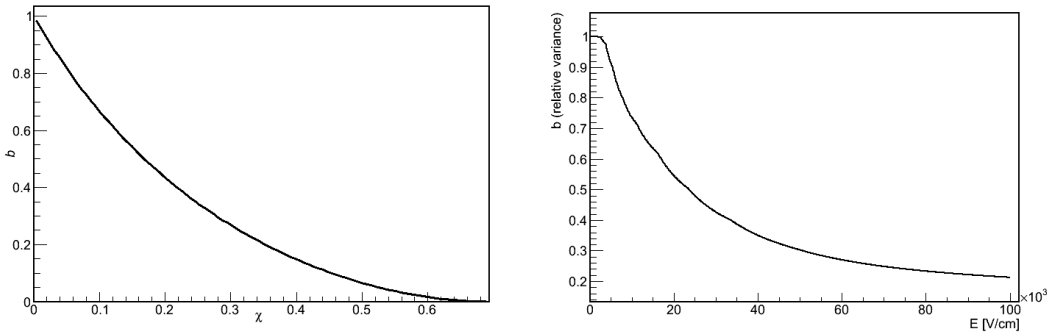

Figure 4.19: Left: single avalanche relative variance $b(\chi)$ as expression 4.27. Right: evaluated from $\chi(E)$ from figure 4.18 for Ar/iC$_4$H$_{10}$ 98/2.

4.4.2.1 Simulating avalanches.

The results compiled in the previous section provide an algorithm to simulate the micromegas signals' strength and fluctuations:

1. The multiplication factor $G = \bar{N}$ is evaluated using equation (4.19) with Magboltz's prediction for the Townsend coefficient $\alpha(E)$. See figure 6.13 left for reconstruction of the gain curve of a 50 μm micromegas working in Ar/iC$_4$H$_{10}$ 98/2 at 1 bar using the data plotted in figure 4.17. Alternatively an experimental measurement of the micromegas gain curve, $G(E)$, could be used.

[12] Some authors use $f_0 = 1/(\theta + 1) = b$.

[13] In fact expression (4.27) for the relative variance of the avalanche is more general an can be deduced analytically from Legler models' assumptions[162] without quoting the Polya distribution.

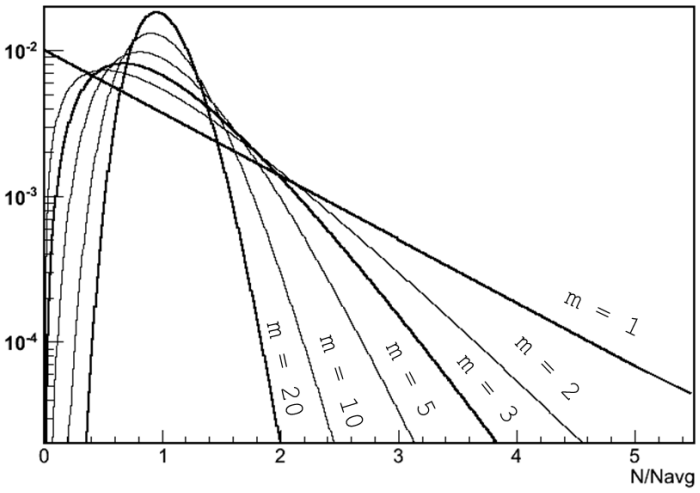

Figure 4.20: Polya distribution functions for single electron avalanches plotted from several values of m..

2. The relaxation parameter is evaluated using (4.22). That is done for the same example in Ar/iC_4H_{10} 98/2 in figure 4.18.

3. The parameter m of the Polya distributions is evaluated as $m = b^{-1}$ using (4.27) (see figure 4.19).

4. The Polya distribution $P(G, b^{-1})$ (4.25) is used, in a Monte Carlo loop, to generate the final number of electrons N resulting from each single electron avalanche.

5. n avalanches are simulated for the n primary electrons collected by the mesh, a particular pixel, etc. Thus the whole final charge relative σ scales with $1/\sqrt{n}$ because of the Central Limit Theorem (CLT). The relative variance b of individual avalanches for our particular example (see figure 4.19 right, relative FWHM $= 2.35\sqrt{b}$) is translated into a relative FWHM for ^{55}Fe X-rays ($n = 227$) as it is plotted in figure 6.13 right.

4.4.2.2 Final (but still ideal) energy resolution for a micromegas.

The process described in the previous section does not have into account the primary electrons number n already has fluctuations. The primary ionization process variance from section 4.1.2 is amplified by the multiplication process with gain g

$$\sigma_i^2 = nF \quad \xrightarrow{amp} \quad g^2 \cdot nF; \tag{4.28}$$

on the other hand the single avalanche variance from equation (4.26) is produced n times

$$\sigma_a^2 = g^2 b \quad \xrightarrow{CLT} \quad n \cdot g^2 b; \tag{4.29}$$

using $N/n = g$ and by convolution of both variances

$$\sigma_f^2 = \frac{N^2}{n}(F + b) \tag{4.30}$$

which can be arranged as the relative energy resolution as FWHM, and applying $n = E/W$ (section 4.1.1) it is written as:

$$FWHM = 2.35\sqrt{\frac{W}{E}(F + b)} \tag{4.31}$$

Therefore, because of the accumulation of n avalanches from n primary charges, the b enters in the expression at the same level as F and the final energy resolution scales with $\sim E^{-\frac{1}{2}}$.

According to the plots of our particular example, Ar/iC_4H_{10} 98/2 in a 50 μm gap micromegas (see previous sections), working with a typical field of $|\vec{E}| \simeq 6 \cdot 10^4$ V/cm corresponds to $b \simeq 0.3$ ($m \simeq 3.3$, $\chi \simeq 0.3$). Evaluating (4.31) also with $F = 0.2$ (see section 4.1.2) and $n = 227$ (6 keV) yields $FWHM \simeq 11\%$, what is certainly close to the experimental values obtained with small microbulk prototypes (see next section). Sometimes it is considered a more general parameter $G > b$ (it will not be mistaken for the micromegas gain) to include other causes of degradation of the energy resolution as noise, etc.

4.4.3 Experimental examples: gain curves and energy resolution.

A compilation of experimental measurements, taken during the R&D tasks which are part of this work, will follow with the aim of providing some references for very commonly used gas mixtures and illustrating the complex role of the quencher gas.

The measurements were carried out with the usual bulk and microbulk prototypes described in figures 4.21 and 4.22 in tests chamber like the one of figure 4.15 in Saclay or an equivalent one built in Zaragoza. The simple set-ups used, basically the mounting of a drift cathode, were always as photographed in the already mentioned figures, with maximum drift distance about 1 cm.

The electronic chain was a basic analogical line for spectroscopy measurements reading the mesh signal. In Saclay it was composed of an ORTEC 142 C charge preamplifier followed by an ORTEC 572 A amplifier. For measurements specified to be done in Zaragoza they were a CANBERRA 2004 preamplifier and a CANBERRA AFT 2025 amplifier. The signal strength was directly read from the Oscilloscope or using a Multi-channel analyser AMPTEK MCA-8000 A, also used for taking the spectra.

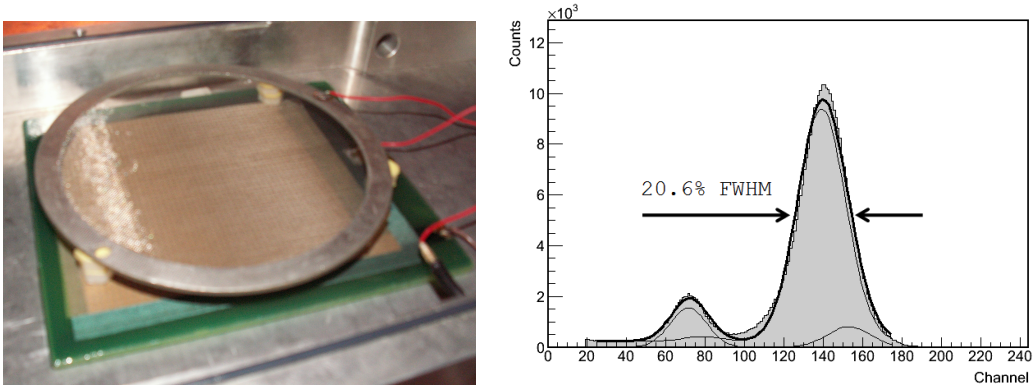

Figure 4.21: Bulk micromegas, 10×10 cm^2 active area and 128 μm amplification gap, manufactured in CEA/Saclay. In the photo (left), ready for being tested inside the tests chamber. Note how the pillars that support the cathode grid directly rest on the micromegas active area. Right: ^{55}Fe spectrum taken with this prototype in Ar/iC$_4$H$_{10}$ 95/5 at atmospheric pressure.

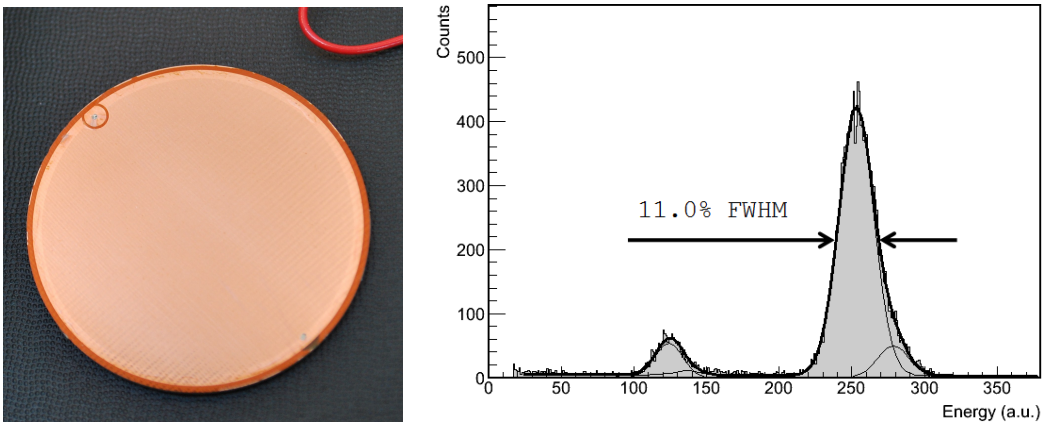

Figure 4.22: Left: 3.5 cm ∅ active area microbulk micromegas with 50 μm amplification gap. Right: ^{55}Fe spectrum taken with this prototype in Ar/iC$_4$H$_{10}$ 95/5 at atmospheric pressure.

All the measurements were done using a ^{55}Fe source which was not collimated and placed several cm over the micromegas. The energy resolution results refer to the 5.90 keV line (Mn K$_\alpha$), though the resolution is usually good enough to consider also the 6.49 keV line (Mn K$_\beta$); therefore a double peak fit is done fixing the relative areas of both peaks according to the charts. For bulks, however, it is often relevant to fit also the argon's escape peak, this time with a relatively free weight and position as it is only needed to approximate the main peak background. Finally an exponential decay is used to fit the residual noise base.

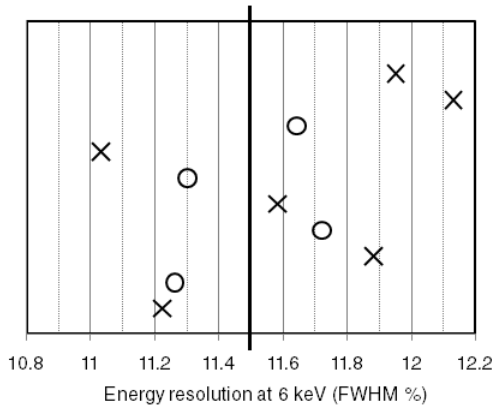

Figure 4.23: Resolution's dispersion for 3.5 cm ∅ microbulks (as the one in figure 4.22 left) from two series: GM, Feb 2009 (crosses); CM, May 2009 (circles).

The spectra of figures 4.21 and 4.22 are taken in Ar/iC_4H_{10} 95/5; that is the most common gas mixture used in our environment because of the relatively low cost of argon and the properties as quencher of isobutane (that will be shown just later), while the particular proportion is taken from considerations done in section 4.4.1.1. The resolution shown in figure 4.21 is certainly notable for a bulk. The bulk that was actually used for the rest of the measurements of this section performed 23.9% FWHM in the same conditions, this value must be kept as a reference for the rest of the bulk resolutions. Regarding the microbulk, the 11% FWHM value (so close to the theoretical limit according to the calculations done at the end of section 4.4.2.2) is nowadays routinely achieved by small prototypes. The figure 4.23 summarizes the result for two different series of microbulks characterized in Zaragoza.

The gain curves (see figure 4.24), $G(E)$, are suitable to be fitted to an exponential, as predicted by Diethorn and, at first order, by Rose and Korff (4.18). The operational electric field depends strongly on the gas. It can be checked how iC_4H_{10} and CF_4 produce opposite sense variations on the Townsend coefficient of argon from figure 4.17 and the corresponding shift in the gain curve; see also figure 4.25 for a direct comparison between Ar which has been added 10% iC_4H_{10} or CF_4.

That figure, 4.25, compares the reference mixture Ar/iC_4H_{10} 95/5 with the use of other typical quenchers and proportions. Some general rules can be extracted from it, however it actually shows a complex dependency on the exact mixture composition. The higher the quencher gas proportion, the higher the operational voltages; but the Townsend coeffcient α does not follow a direct composition rule; since very different cross sections are involved, small amounts of quencher produce deep changes and the shift in voltages saturates soon.

Other feature that is highly dependent on the gas composition is the maximum achievable gain. From figure 4.24 can be deduced that the sparks limit is not dependent on the strength of E but more on the size of the avalanche, since different gaps and gases needing very different operational electric fields finally achieve similar maximum gains. That fact agrees with the idea pointed out by the Raether limit, and with the density of photons having a fixed probability to generate a secondary

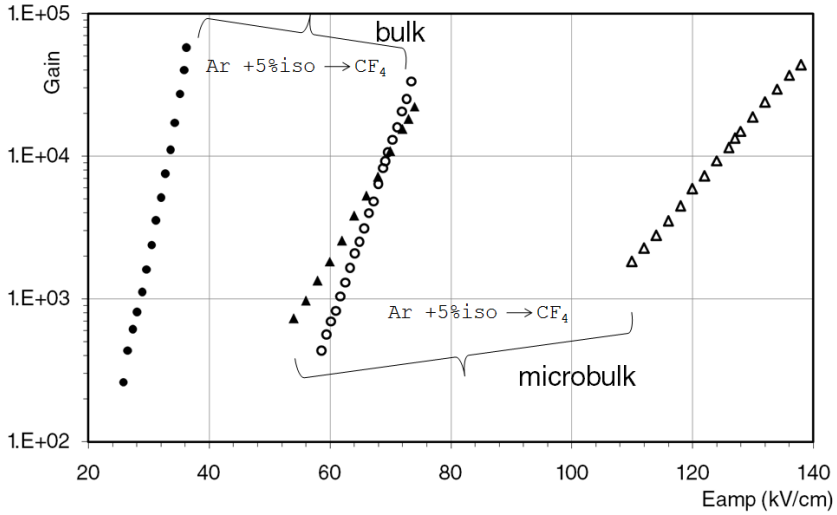

Figure 4.24: Comparison of gain curves for bulk (circles) and microbulk (triangles) micromegas in Ar/iC_4H_{10} 95/5 (filled markers) and CF_4 (empty markers). The maximum gain cannot be directly compared because different prototypes were used.

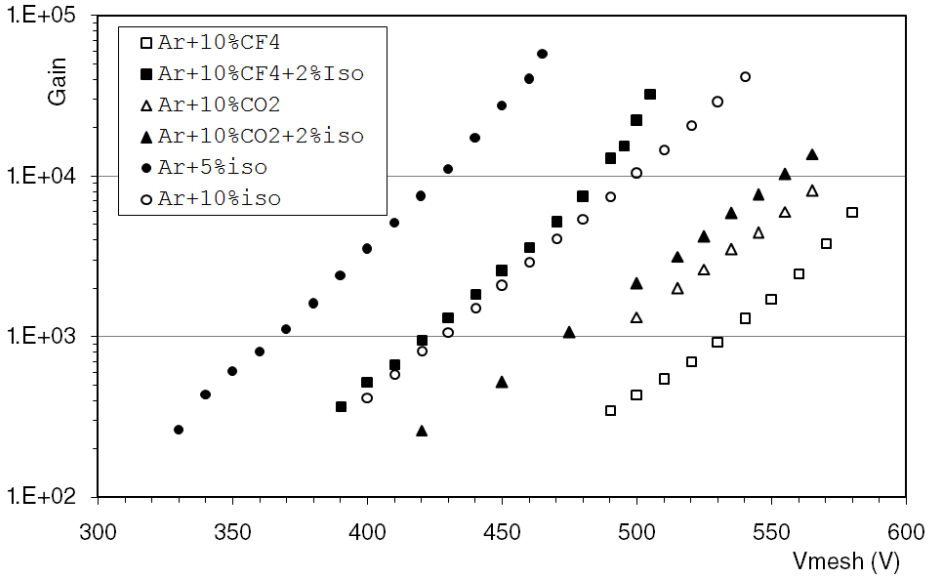

Figure 4.25: Gain curves for bulk micromegas using different gas mixtures. The last (highest) point of each series corresponds to the maximum stable gain.

avalanche (see section 4.4.1.2). However that fact is true for gas mixtures which actually have good quenching capabilities. Pure noble gases seems not to achieve gains higher than 10^3 (see section 5.2) and it is very notable the improvement of Ar/CF_4 90/10 with the addition of 2% iC_4H_{10} in 4.25.

The quencher gases affect the dynamic of the avalanche at different levels, changing the Townsend coefficient and the photons and electrons absorption cross sections. Therefore, the different quencher characteristics can be complementary. That seems to be the case of isobutane and CF_4. Isobutane has very good photon non radiative absorption, it allows very high gains at low electric fields and also good energy resolution. On the other hand CF_4 is more appreciated from the drift point of view (see section 4.2). Relatively high concentrations of CF_4 are needed to produce an efficient enough quenching effect to reach very high gains $> 10^4$, as a consequence very intense electric fields are required (see figure 4.24).

The ternary mixture $Ar/CF_4/iC_4H_{10}$ 88/10/2 (figure 4.25) balances both quenchers properties and seems to keep the isobutane and CF_4 mixtures individual advantages. $Ar/CF_4/iC_4H_{10}$ mixtures are studied with more detail in section 4.4.3.1. Isobutane can also relax the very high operational voltages needed for pure CF_4 operation, though the effect saturates soon with the iC_4H_{10} percentage (see figure 4.26). On the contrary, the effect of addition of isobutane to a CO_2 quenched gas is much more modest.

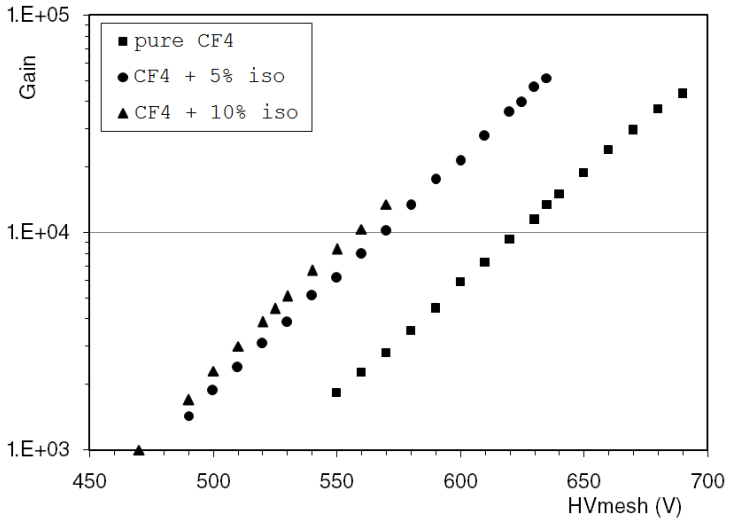

Figure 4.26: Gain curves for microbulk micromegas showing the effect of adding iC_4H_{10} to pure CF_4. The 10% isobutane mixture's curve is truncated because of microbulk's damage. The resolution was also slightly improved from 17.1% to 16.7% (with 5% iC_4H_{10}). These resolution values are equivalent to the result in Ar/iC_4H_{10} 95/5 for that particular microbulk.

Another interesting feature of the gain curve is the exactness of the exponential behaviour, i.e. the straightness of the series in the semi-logarithmic plots. It can be detected that the series show an over-exponential gain, which is more evident from some mixtures and becomes more clear at high gains. That behaviour could be due to the contribution of secondary avalanches triggered by photons (photon-feedback), and it is a prelude of the spark. This possibility implies new fluctuations that have

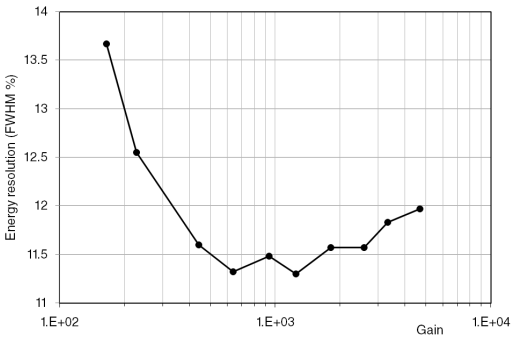

Figure 4.27: Resolution vs gain, taken with a CM microbulk in Zaragoza. No very high gains were tried during that test, so as not to risk the microbulk. Equivalent curves showing further resolution degradation at high gain can be found, for instance, in [100].

not been accounted in the single avalanche model, and the energy resolution degrades in the over-exponential behaviour piece of the gain curve. A typical energy resolution curve, figure 4.27, improves with gain since the signal-to-noise-ratio (SNR) increases, but there is an optimum after which the growing extra-fluctuations cause resolution degradation. Therefore a straight gain curve can be a sign of good, or at least stable, energy resolution.

Studying the measurements summarized in figure 4.25, one guesses that the prevention of the over-exponential behaviour and the tolerance of the secondary avalanches (not producing sparks) are different aspects of the gas mixture. The addition of quencher logically helps preventing the secondary avalanches, so the 10% isobutane curve is straighter than the 5%, thought the maximum achievable gain is similar. Comparing the energy resolution at high gain, $\sim 3 \times 10^4$, when the 5% gain curve is clearly over-exponential, the energy resolution is 25.9% (5% isobutane) while 21.8% (10% isobutane).

Isobutane seems to have a good tolerance that makes these mixtures develop a long stable over-exponential stage that allow them to reach gains $> 10^4$ with small quencher amount. Ar/CF_4 90/10 is also clearly over-exponential but, the bad photon quenching properties of CF_4, makes the secondary avalanche too probable still at low gains. Energy resolution is worse than 30% along all the curve. On the contrary, both Ar/CO_2 curves (with and without iC_4H_{10}) are completely straight up to the end and show no resolution degradation, 23.1% in the last point of Ar/CO_2 90/10 (it must be reminded Ar/iC_4H_{10} 95/5 performed 23.9% actually at a bit smaller gain); then, suddenly, the continuous sparking limit appears. Therefore CO_2 as quencher seems to prevent the secondary avalanches, but do not tolerate them. $Ar/CO_2/iC_4H_{10}$ mixtures are studied with more detail in section 4.4.3.2

4.4.3.1 $Ar/CF_4/iC_4H_{10}$ mixtures.

The effect of adding iC_4H_{10} to Ar/CF_4 90/10 is studied in figure 4.28 for several amounts of isobutane. The effect of lowering the operational voltage saturates soon, but higher maximum gains and more straight curves are obtained as higher the isobutane proportion is. The energy resolution is improved for a given gain, as it is shown in figure 4.29 for $G \approx 10^4$ with exception of the point with absence of iC_4H_{10}

($G \approx 2 \times 10^3$) and only 0.5% of iC_4H_{10} ($G \approx 4 \times 10^3$). A comparison of spectra at similar $G \approx 4 \times 10^3$ is down on the right[14].

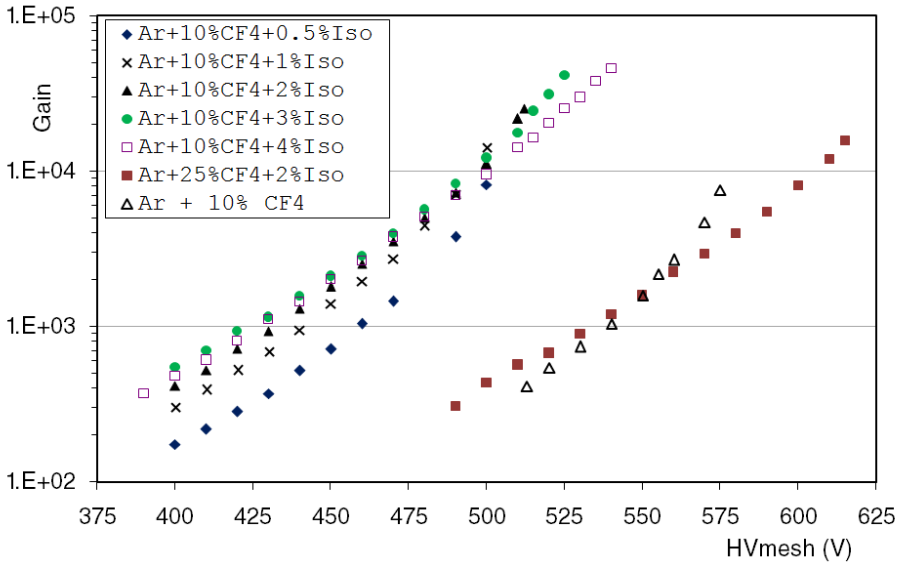

Figure 4.28: Gain curves for bulk micromegas in different Ar/CF_4/iC_4H_{10} mixtures. These are independent measures of those of figure 4.25, though taken with the same bulk.

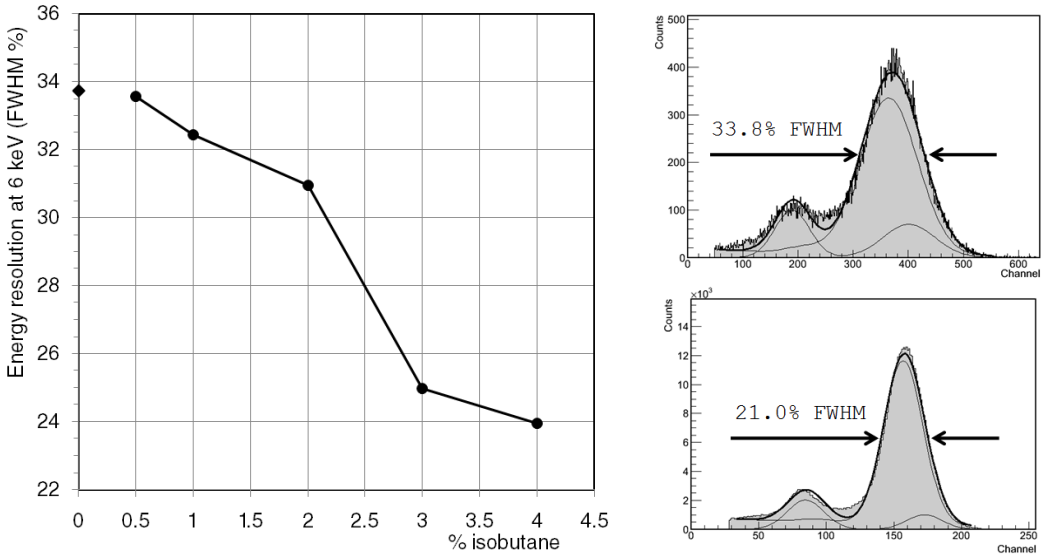

Figure 4.29: Left: energy resolution at $G \approx \times 10^4$ for Ar/CF_4/iC_4H_{10} $(90-x)/10/x$ mixtures. Right: spectra at $G \approx 4 \times 10^3$ for $x = 0.5$ (up) and $x = 4.0$ (down).

[14] Unfortunately a systematic characterization of the energy resolution was not carried out, since the main purpose of the work[166] was just to find a high stable gain and fast gas mixture.

To sum up, the addition of 4% iC_4H_{10} has led to obtain a gas mixture that should keep the Ar/CF_4 90/10 drift properties, but working at mesh-anode voltages which are 20% lower. Moreover it is able to achieve a maximum gain as high as Ar/iC_4H_{10} 95/5, but, due to the combination of both quenchers, with a softer over-exponential behaviour, what allows an improved energy resolution.

The same has been tried with a mixture with higher concentration of CF_4 for excellent drift properties. The particular mixture $Ar/CF_4/iC_4H_{10}$ 73/25/2 was checked to have a transparency curve as good as pure CF_4 (see figure 4.14) and the energy resolution that is demonstrated in figure 7.14.

4.4.3.2 $Ar/CO_2/iC_4H_{10}$ mixtures.

The CO_2 concentration was increased to 20% to test whether the maximum gain could be enhanced and the energy resolution as well (see figure 4.30). The obtained energy resolution value was notable (see figure 4.31) achieving 20.1% at 625 V, $G \simeq 7 \times 10^3$, the best energy resolution got during this study. The result is even more significant as it was taken only 20 V before the sparking limit, again in a completely straight gain curve. But the maximum gain was hardly increased and sparks appeared without any warning signal; it seems that CO_2 alone cannot tolerate the secondary avalanches, even in high concentrations.

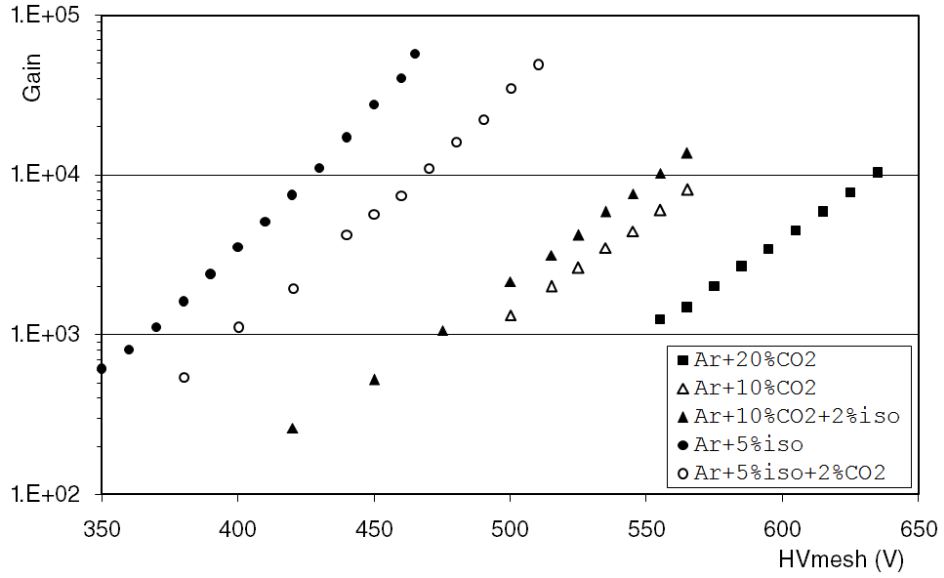

Figure 4.30: Gain curves for bulk micromegas in different $Ar/CO_2/iC_4H_{10}$ mixtures.

Since the addition of isobutane to the Ar/CO_2 90/10 mixture had modest results, the opposite approach was tried. Some CO_2 was added to the reference mixture Ar/iC_4H_{10} 95/5 in order to check if the straightness of the Ar/CO_2 gain curves, and so the good energy resolution, could be tranferred to it. The test was successful in producing a gas mixture with a maximum gain as high as Ar/iC_4H_{10} 95/5 at only

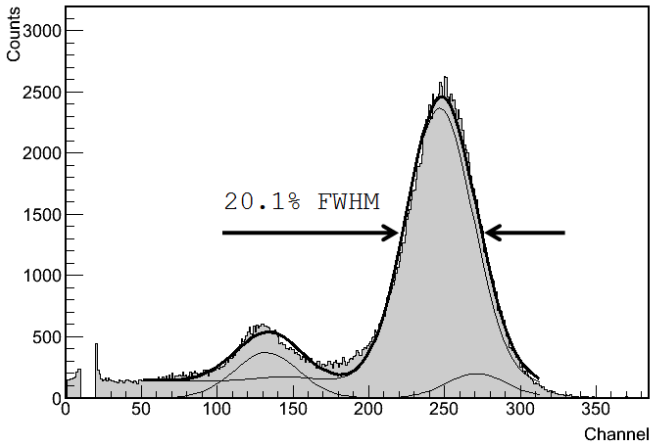

Figure 4.31: Spectrum taken with a bulk micromegas in Ar with 20% CO_2 at at 625 V, $G \simeq 7 \times 10^3$.

$\simeq$ 25 V higher voltages, but with notably more straight gain curve and enhanced energy resolution: 21.3% at 450 V, $G \simeq 6 \times 10^3$.

4.5 Signal induction. The Ramo's Theorem.

How the drifting charges induce electronic signals in the detector electrodes is described by the Ramo's Theorem[167], which stands for the charge induced in a particular electrode, numbered n, by a charge q to depend only on the electric field created by the n-electrode itself and the trajectory follow by q. If $\psi_n(\vec{r})$ is the *weighted potential*, what means the potential induced by the n-electrode with voltage V_n while the rest of the electrodes are grounded and the charge q is not present, the current induced in the n-electrode is

$$I_n^{ind}(t) = \frac{q}{V_n}\vec{\nabla}\psi_n\left(\vec{r}(t)\right) \cdot \frac{\mathrm{d}\vec{r}(t)}{\mathrm{d}t} = \frac{q}{V_n}\vec{E_n}\left(\vec{r}(t)\right)\left(\cdot\vec{v}(t)\right) \tag{4.32}$$

where $\vec{E_n}\left(\vec{r}(t)\right)$ is the *weighted field* associated to the n-electrode with voltage V_n[15] and $\vec{r}(t)$ is the trajectory followed by q. Pay attention to the fact that $\vec{r}(t)$ will be determined by the *real* electric field, instead of $\vec{E_n}$. Note also that the sign of the induced current depends on the sign of q but on the relative orientation of $\vec{v}$ and $\vec{E_n}$ as well.

In particular, for an infinitely long strip of width w and charges moving in the s direction of the avalanche's advance, perpendicular to the strip, it is obtained:

$$I_{strip}^{ind}(t) = \frac{4qw}{\pi[4s^2(t) + w^2]}\frac{\mathrm{d}s}{\mathrm{d}t}. \tag{4.33}$$

Equation (4.32) is the key in order to compute or simulate the electronic signals. However a corollary regarding the total induce charge is more often invoked in lab

[15]The weighted potential and fields are often defined specifying $V_n = 1$, thus V_n disappears from the equations.

reasonings. To compute the total induced charge we must integrate (4.32) along the q's trajectory. Since $\vec{E_n}(\vec{r}(t))$ is a conservative field

$$Q_n^{ind}(t) = \int_{t_i}^{t_f} I_n^{ind}(t)\,\mathrm{d}t = \frac{q}{V_n}\left[\psi_n(\vec{r}_f) - \psi_n(\vec{r}_i)\right] \tag{4.34}$$

the results depends only on the initial and final positions of q. If avalanche's charges are created in pairs q and $-q$ in the same initial point, that makes vanish the initial position dependence when both contributions are summed. Regarding the $\psi_n(\vec{r}_f)$, if the charges finally arrive to any electrode of the system, then by definition $\psi_n = 0$, if the electrode is different that our n-electrode (pixel or strip), and $\psi_n = V_n$ if the charge is caught by it. Therefore *the charge induced in a electrode is equal to the number of charges collected by it.* That justifies the simple picture one often has in mind, but stands for the total induced charge after an undefined transitory time. The only thing that can be actually said for electrodes which do not collect net charge (for instance, a mesh being crossed by primary electrons in absence of amplification) is that the induced current will be strictly bipolar, i.e. the negative an positive areas of the pulse will be equal.

Most of the electron-ion pairs are created in the last stages of the avalanche near the anode. That induces a fast rise in the signal due to the electrons, that is followed by a slower pulse produced by the drift of the ions along the amplification gap in the opposite sense (so inducing charge with the same polarity). Figure 4.32 contains a micromegas pulse taken with a fast current amplifier and shows the mentioned pulse structure for a single electron avalanche. The signal comes from the anode of a 100 μm gap micromegas working with He/iC_4H_{10} 90/10, a combination that allows a very high gain near 10^7[164]. The first fast rise, due to the electrons, had a distribution with mean around 3 ns and $\sigma = 770$ ps. The slower signal presents two peaks that are attributed to the presence of two kind of ions, from He and iC_4H_{10}, with different mobilities.

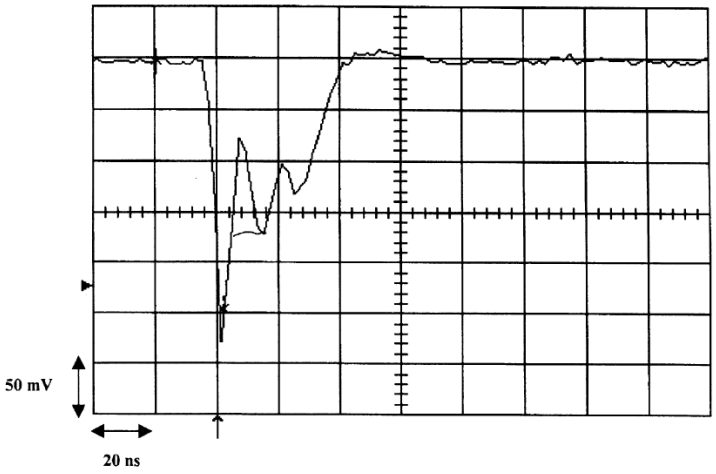

Figure 4.32: Single electron pulse caught with a fast current preamplifier. From [164].

Chapter 5

Micromegas' milestones for Rare Event Searches.

Contents

Many aspects of the performance that makes micromegas interesting for particle physics were shown in the previous chapter, and the principles that allow them as well. These operational principles can be put to the test because usually detector and target are the same entity: the experiment's sensitive volume. Therefore the gas choice and its conditions are often strongly constrained by the physics case. Besides new requirements and features can be demanded by rare event searches, depending on the experiment type. Thus rare event searches sometimes force TPCs and micromegas to the frontier of their conventional operation.

Some of the milestones demanded by rare event searches with TPCs are main aspects of the R&D program inside T-REX and are the subject of this chapter. The LFNA and close collaborators have already published several papers describing the status of these research lines and other Ph. D. works by LFNA researchers deeply study them, therefore here the challenges will be just addressed and we will only remark some general keys and cite the suitable references. As an exception, the last section 5.5 describes a work performed with the aim of adapting a last generation electronics, specifically designed for a rare event searches experiment with micromegas, for the T-REX researchers.

For rare event searches high trigger rate capabilities would probably be not relevant, however high efficiency is, for sure, essential. Moreover the detector has usually to fulfil the requirements of both a tracker and a calorimeter. Larger TPC's

are needed to increase the target mass and/or the detection efficiency, what entails difficulties for the readout construction, longer drift distances, etc. Increasing the gas pressure can be a smart alternative, however the feasibility of the drift and the amplification stages must be proven (section 5.1).

The definition of a TPC's fiducial volume, i.e. a virtual volume fully contained inside the TPC active volume without physical borders, can be essential to avoid radioactivity from the innermost TPC's surfaces. That includes the cathode and the readout plane, hence the reconstruction of the absolute drift coordinate, the t_0, is required. It will be explain (section 5.2) that this new feature may imply the operation with pure noble gases in absence of quencher.

Beyond the operation of the micromegas, higher pressure, longer drift distances and the lack of a quencher make the detector more susceptible to attachment due to gas impurities. The quality of gas becomes the first goal, an unavoidable requirement to explore the actual micromegas' possibilities. Moreover, the high cost of xenon requires gas recovering or recirculation. Before the detector, the supporting gas system requires our attention. The T-REX works started adapting the HELLAZ set-up at CEA/Saclay. Later a dedicated set-up was built in Zaragoza, implementing the learnt lessons. Both set-ups are described in the articles that will be cited, including consecutive upgrades of Zaragoza's lab. Here only their effects will be shown shortly in section 5.2 to illustrate also how to detect and deal with attachment when it is present in the data.

Specially for $\beta\beta0\nu$ decay searches, the energy resolution is capital. The Penning effect is a via to improve the essential limitations in energy resolution that were analysed in section 4.4.2.2, it is presented in section 5.3.

Finally, the TPC has to fulfil radiopurity requirements as all the low-background detectors. That entails restrictions in the detector materials that directly affect to very common materials, as stainless steel, and some common techniques, like soldering. We will focus in section 5.4 in the core of the TPC, the micromegas.

5.1 Behaviour at high pressure.

Microbulk micromegas do not seem to suffer from practical limitations when increasing the pressure, as it is shown by figure 5.1 up to 10 bar using Ar/iC_4H_{10} 99/1. The gain curves[169] were taken at Zaragoza's set-up using a microbulk micromegas prototype like the one described as *classic* type (number 1) in section 4.3 and photographed in figure 4.22. The same is true for the rest of the results showed in this chapter.

The gain series were taken with a low energy source, ^{57}Co 6.4 keV X-rays, and reaching the maximum achievable gain was not intended. The microbulk was not forced up to the breakdown limit. Nevertheless, a gain over 10^3 was demonstrated for all the pressures and considered enough for illustration purposes.

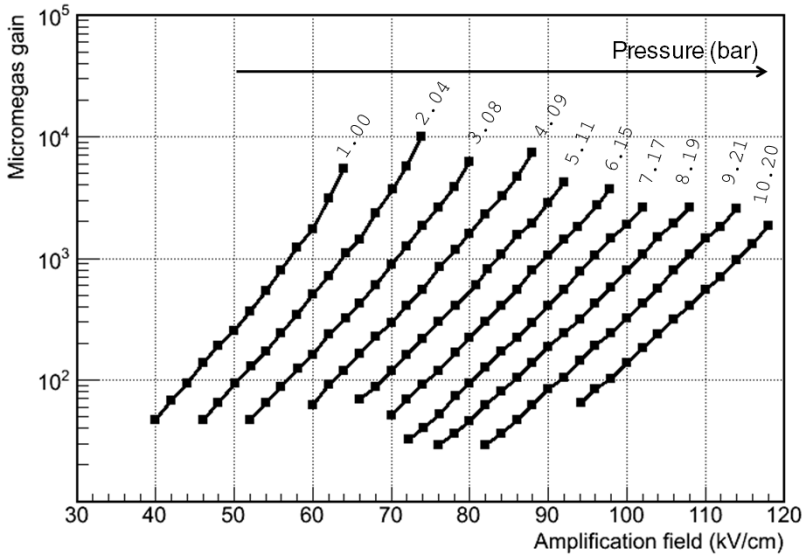

Figure 5.1: Gain curves as a function of pressure for Ar/iC$_4$H$_{10}$ 99/1[169].

The energy resolution degrades with pressure. At the same conditions for Ar/iC$_4$H$_{10}$ 95/5 from $(12.9 \pm 0.3)\%$ FWHM at 1.00 bar to $(17.1 \pm 0.4)\%$ at 4.09 bar[18]. However the effect saturates and $(17.2 \pm 0.4)\%$ is obtained at 10.20 bar.

The results at high energy, using 5.5 MeV ^{241}Am α[161] are even more encouraging. The kind of spectrum that is obtained (see figure 5.2 left) shows a tail that denotes small ionization losses on the cathode or source autoabsorption. These effects may be modelled by the convolution of a negative Landau function with the more fundamental gaussian distribution from which the energy resolution is estimated. A simple gaussian fit gives $\simeq 2\%$ FWHM while the *deconvoluted* gaussian yields a value under 1% FWHM (figure 5.2 left) for Ar/iC$_4$H$_{10}$ 98/2 at 4 bar.

Both limits, at high and low energy, are compatible using the square root rule for interpolating the resolution (expression (4.31)). The measurements have been reproduced for Xe-TMA (trimethylamine) mixtures at several intermediate energies of tens of keV in [170]. The interpolation suggests resolution $\sim 1\%$ around the ^{136}Xe[1] $Q_{\beta\beta}$ value $\simeq 2460$ keV.

The recombination of electron-ion pairs is an effect that increases with the density of the media. In order to assure the energy references taken for the interpolation to be correct, an immediate comparison (exactly at the same conditions during the same data-taking run, see details in [161]) of the gain deduced from the ^{241}Am X-rays (figure 5.2 right) and α-particles gain was carried out. For all the couple of points compared in figure 5.3 $Q = G_\alpha / G_{Xray} > 0.96$ was obtained.

[1] Xenon is, in principle, better for energy resolution than argon, because of its lower W-value. Values for xenon plus quencher are given in [170]. The case of pure xenon is the subject of the following section 5.2.

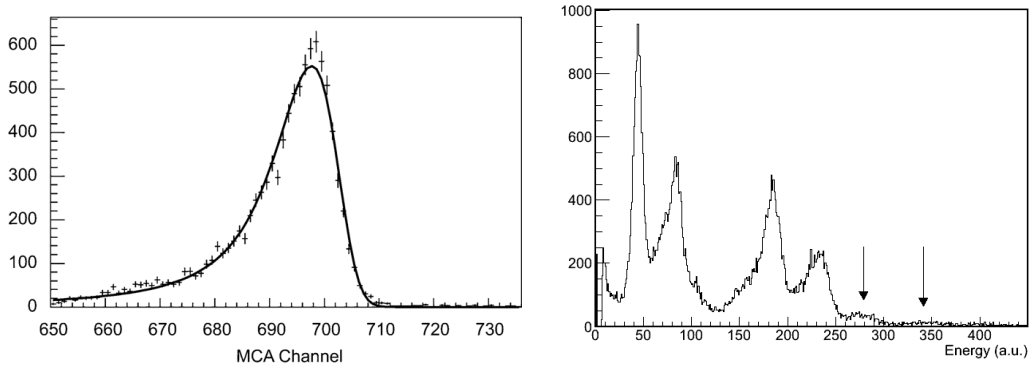

Figure 5.2: ^{241}Am spectra[161] in Ar/iC$_4$H$_{10}$ 98/2. Left: 5.5 MeV ^{241}Am α at 4 bar, a simple fit yields 1.8% FWMH and 0.7% FWHM is the *deconvoluted* value (see the text). Right: low energy 26.4 keV γ and 13.9, 17.7 and 21.0 keV X-rays; in addition 3.0 and 6.1 keV fluorescences from the chamber, taken at 2 bar.

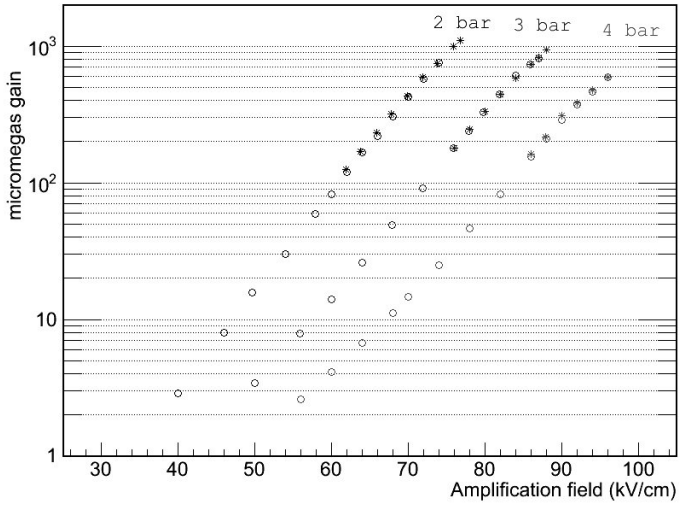

Figure 5.3: Gain curves for both α (circles, see figure 5.2 left) and γ (crosses, 17.7 keV peak in figure 5.2 rigth), for Ar/iC$_4$H$_{10}$ 95/5 at 2-4 bar[161].

An interesting fact is that when the isobutane concentration is increased from 2% to 5%, the energy resolution for α becomes slightly worse 0.9% (2.0%) FWHM from the convoluted (simple) fit. It could be understood from the discussion of section 4.4.1.1 that the optimum gas mixture and amplification gap should be varied with pressure and lower isobutane concentrations are more suitable for higher pressures. That points to a new research line and enables expectations for further improvements.

5.2 Use of pure noble gases.

There are several mechanisms proposed to reconstruct the absolute position of the event in the drift direction. A cathode that were sensitive to the ions arrival would work by time difference with the electrons arrival to the anode. However that solution has to deal with the challenge of ion drift and positive ion detection, probably in a big and pressurized chamber. A granulated readout can recognize the diffusion effects and make a rough estimation of the drifted distance, nevertheless this solution could be conflicting with excellent topological capabilities for the detector. If both t_0 and topology are required the detection of the primary scintillation light seems the most feasible strategy. That solution implies not only the installation of photo-sensors in the chamber[2], but also the necessity of the gas to be transparent to UV light, which entails the use of pure noble gases, otherwise the quencher would *quench* the primary photons.

The series of measurements[161] plotted in figure 5.4 show that micromegas are able to work reliably at modest but practical gain in pure xenon. Using ^{241}Am α the maximum achievable gain was always higher than 180 and almost independent on pressure, at least up to 4 bar.

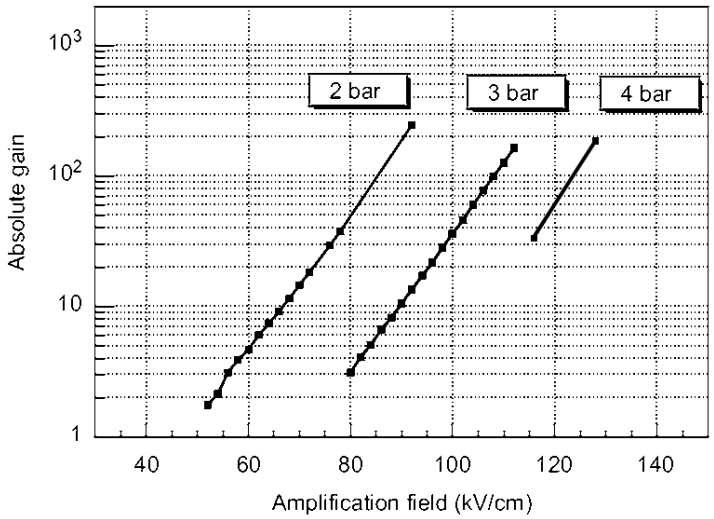

Figure 5.4: Gain curves for pure xenon at pressures 2–4 bar[161]. The maxima correspond to the last point after which instabilities begun.

If events with lower charge density are used higher gains are possible, in the work [171] gains of 4×10^2 up to 5 bar for 22.1 ^{109}Cd X-rays are shown. At higher pressures the maximum achievable gain starts decreasing exponentially with pressure, however 2×10^2 is still reached at 10 bar. In [171] a microbulk prototype very

[2]The micromegas itself can act as photosensor if any inner surface of the chamber is photosensitive (like the micromegas' mesh). Depositions of CsI, for example, generate photoelectrons that can be drifted to the micromegas[164, 18, 19].

similar to ours was used, nevertheless with smaller mesh holes, only 25 μm . The dimensions of the micromegas *avalanche cell* could be relevant here, since the division of the amplification process in isolate regions may prevent the photon-feedback (the *geometric quench*, see section 4.4.1.2). It could be the key to explain the fact that micromegas (only microbulk has been tried as far as we know) seems to be the only MPGD able to reasonably maintain the gain in pure xenon when pressure is increased, yielding the highest gain for pressure higher than 5 bar[171].

The energy resolution is worse than with quencher. Nevertheless the values are still affected by attachment (see figure 5.5). The very slow drift velocity of electrons in xenon makes attachment the main handicap. It was found that, for the α-particles measurements, recording the preamplifier pulses was a useful practice for detecting the attachment effects and performing some estimations.

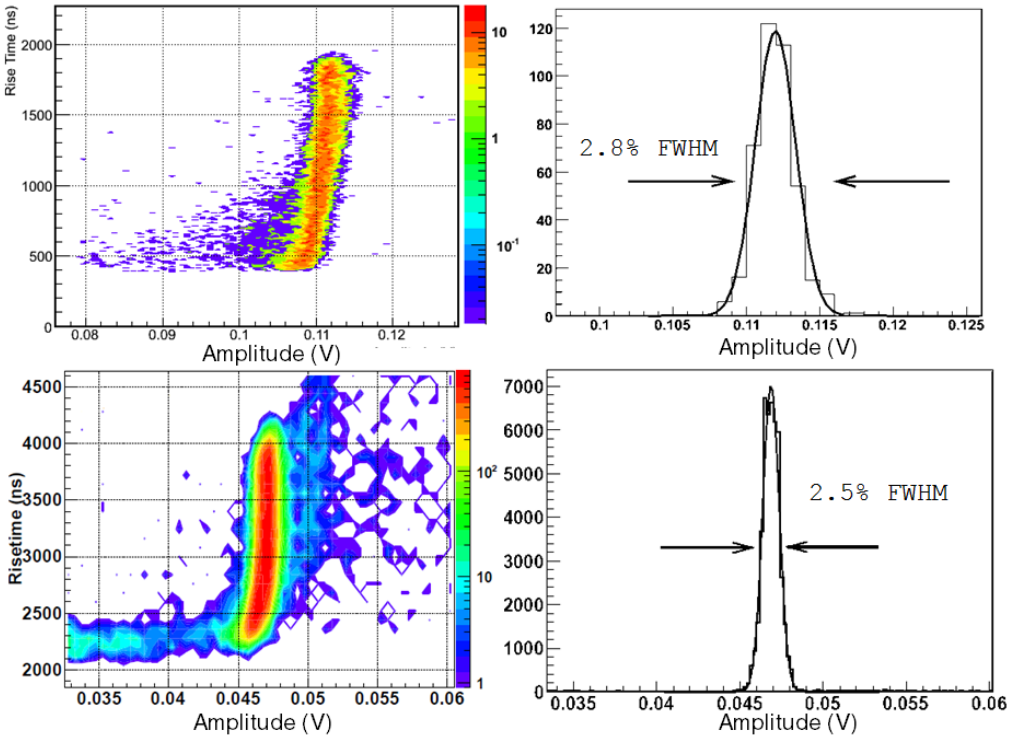

Figure 5.5: Risetime vs amplitude plots and energy spectra of ^{241}Am α for pure xenon in *up:* Saclay's set-up at 2 bar with E_{drift} = 480 V/cm[161] and *down:* Zaragoza's set-up at 4 bar with E_{drift} = 300 V/cm[155]. Note the drift field is lower in the second case (specially the reduced field E/P) while the maximum drift distance has been doubled from 3 to 6 cm. However, the upper spectrum has been obtained applying the constraint 1800 < risetime < 2000 ns and in the downer the whole pulses distribution is fitted.

The key is the risetime and amplitude correlation observed for the pulses, specially when the gas conditions were not the best[161]. The explanation is that the α tracks are very straight, with lengths of $\sim$ 2 cm/bar in xenon, and a big part

of the ionization is concentrated at the end (an experimental track reconstructed from a micromegas measurement can be seen in figure 5.12 of sect 5.5). Thus the mean drifted distance is strongly dependent on $\cos(\phi)$, the angle between the α-particles' track and the drift field. The same applies for the risetime, related with the projection of the track on the axis. If the drift distance represents a disadvantage for the electron, because of a relevant probability of being attached, then the shorter pulses (more horizontal tracks) will show smaller amplitudes. A comparison between figure 5.5 left, up and down, shows the improvement in energy resolution achieved in the Zaragoza's set-up[155] and explains it from the point of view of the risetime-amplification plot. The most recent description of the set-up and operational procedure is done in [170].

Off-line analysis of the preamplifier pulses acquired with an oscilloscope brings the possibility to estimate the energy resolution[3] by selecting a slice in the risetime-amplitude plot (see figure 5.5 up and right). However the estimation is still rough and pessimistic, since the Zaragoza's set-up improved the estimation from Saclay data even without risetime selection. However, the 2.5% FWHM obtained at 4 bar still decreases to 1.8% FWHM if a risetime selection is applied, therefore attachment still affects these results.

5.3 Penning mixtures.

In *Peening mixtures* the quencher gas, B, has an ionization potential lower than the main gas, A, excitation potential. That enables the *Penning transfer*:

$$A^*B \rightarrow AB + e^- \tag{5.1}$$

where the metastable state A^* finally contributes to one electron release. That process increases the ionization yield and, moreover, reduces the sterile pathways what produces the decrease of the Fano factor. Therefore both F and W are smaller for the reduction of the gain fluctuations in

$$FWHM = 2.35\sqrt{\frac{W}{E}(F+G)} \tag{5.2}$$

The process also affects G, the avalanche fluctuations, as the transfer also works during the multiplication process[172]; however one of the most remarkable merits

[3] The ^{241}Am source became a very useful tool for some quantitative analysis. Simulations are used characterize the α'-particles' track length. They show that straggling is really small and length is practically inversely proportional with pressure. Then, under the assumption of straight tracks characterized by ϕ, the drift velocity can be deduced from the maximum risetime and the electron's meanlife from a linear fit of the risetime-amplitude distribution. See details and examples in [18]. The coincidence of independent detection of the α-particles and the X-rays allows to know the absolute position of the X-ray interaction in the chamber (see [19]).

is that the Penning effect improves the primary statistics of the ionization process, hence it is useful for all the gaseous proportional counters[4].

It seems that the Penning effect is highly dependent on the gas pressure and the mixture composition (not only on the gases ionization and excitation potentials but also on the molecular structure) and the quencher proportion. The optimum proportion is usually of few % of quencher. Inside T-REX the Xe-TMA mixtures were studied finding the optimum TMA proportion to be around 2%[170]. Besides the benefit on the gain and energy resolution (see figure 5.6) is very notable compared with pure xenon.

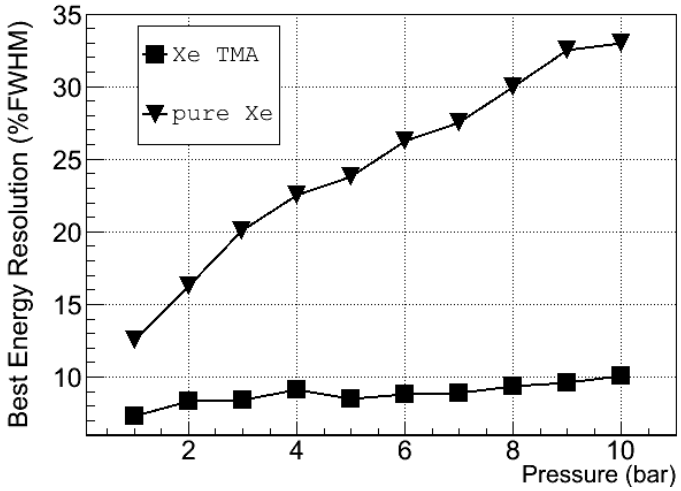

Figure 5.6: Energy resolution vs pressure for 22.1 keV X-rays, data for pure Xe from [171] and Xe-TMA[170].

The addition of any quencher is, in principle, conflicting with the measurement of t_0 since the primary scintillation light would be extinguished. However it may be expected that the quencher molecules could be excited too, thus a wavelength shift will happen, but light could be still detected[174].

5.4 Radiopurity.

Besides their advantage in geometrical accuracy and operation stability, the great potential of microbulk micromegas for rare event searches relies in the fact that the

[4]There is another trendy technique to surpass the limitations of expression (5.2), this time improving the fluctuations during the amplification process. The *electroluminescence (EL)*[173] relies in the acceleration of the primary electrons, but by electric fields weaker than with MPGD, so as the electron is able to excite the gas molecules but do not ionizes the media, the secondary light is register by a photosensor. Therefore EL is a simple multiplication process instead of a geometric progression, what means that the avanlanche fluctuations, b, in equation (4.31) is not included in the G of (5.2). The EL stage of a TPC can be complemented with a micromegas, that would receive the primary electrons after EL, for tracking purposes.

raw materials used for their manufacturing are included in the group of the most radiopure: copper and kapton (double copper clad polyamide laminate Sheldahl G2300). However the intrinsic radiopurity of the final micromegas is not, in principle, guaranteed since several chemical baths are used for the kapton etching and adhesive (epoxy, Isola DE156) is needed to glue the micromegas foil to a mechanical support. It must be noticed that the manufacturing process has not been thought with the goal of minimizing the radioactive impurities. Moreover, if a readout layout is needed, additional Kapton-Cu layers can be glued to avoid conventional PCB technology, that is known to be too radioactive, what requires further epoxy and new processes to print the circuit. Therefore the LFNA, in collaboration with R. de Oliveira from the CERN MPGD's Workshop, undertook a series of measurements with the aim of confirming the final intrinsic radiopurity of microbulks using a p-type germanium detector in the Canfranc Underground Laboratory (LSC)[175].

The measured samples included the microbulk raw materials (Cu-Kapton-Cu and Cu-Kapton structures), and two elaborated (up to different level) structures coming from CAST microbulk detectors (see section 8.2). The first one (figure 5.7 left) is a complete microbulk with a 2D readout, which requires two additional epoxy-Kapton-Cu layers. The second sample (figure 5.7 rigth) consists of the 2D readout layout of a classical CAST micromegas whose mesh-pillars structure has been removed. That readout was built from the same basic Cu-Kapton-Cu structure of posterior microbulks. The measurement of the microbulk raw foils checks whether these structures mantain the radiopurity of the isolated kapton and copper; the old 2D-readout should reflect the contribution from the basic processes for circuit printing of strips, vias, etc; the complete microbulk adds epoxy (though the old 2D-readout can obtain residual epoxy) and the results of a more aggressive kapton etching process. The measurements are summarized in table 5.1.

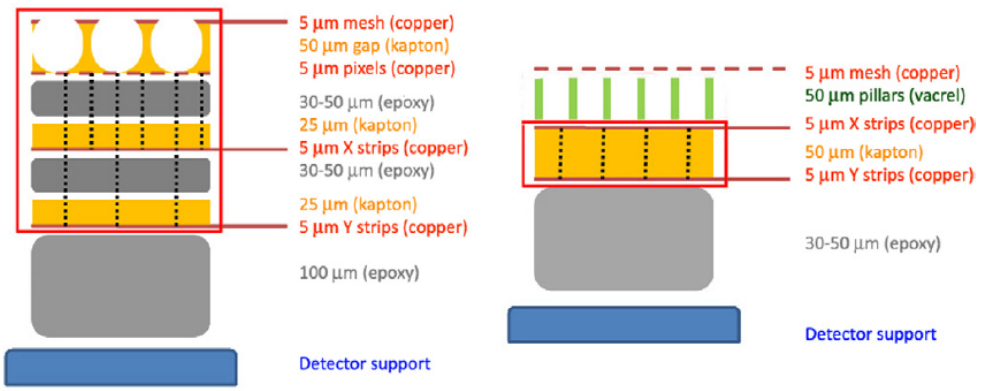

Figure 5.7: Sketch of the two CAST micromegas from which the samples (squared) were taken. Left: CAST microbulk with 2D-readout. Right: CAST classic with 2D-Readout.

The potential of microbulk micromegas is better appreciated if compared with the values of a light readout used by the XENON 100 experiment that is composed

sample	^{232}Th	^{235}U	^{238}U	^{40}K	^{60}Co
Kapton-Cu foil	<4.6*	<3.1*	<10.8	<7.7	<1.6*
Cu-Kapton-Cu foil	<4.6*	<3.1*	<10.8	<7.7	<1.6*
Old 2D-readout	4.6 ± 1.6	<6.2	<40.3	<46.5	< 3.1*
CAST microbulk	<9.3	<13.9	26 ± 14	57 ± 25	<3.1*
Hamamatsu R8520-06[176]	28 ± 10	-	<37.2	1700 ± 310	93 ± 16

Table 5.1: Radioactivity levels in μBq/cm^2.*Level obtained from the minimum detectable activity of the detector.

by an array of PMTs[176]. XENON100 is currently the most sensitive Dark Matter experiment, apart from other merits, because of a carefully selection of materials that includes the development of these particular low-background PMTs. The micromegas' activity is specially lower for ^{40}K and ^{60}Co.

Regarding our series of measurements, the only relevant increase of activity (despite being compatible with zero at 2σ) is registered for the complete microbulk, specially in the ^{40}K. This facts points to the epoxy and/or the chemical baths (KOH is used during the etching process) as the origin of its radioactivity and, therefore, a potential improvement by optimization of the manufacturing process. A direct exploration of the practical limit of the micromegas background due to its intrinsic radiopurity has been carried out for an equivalent CAST microbulk by means of underground data taking with special shielding configurations and is summarized in section 10.3.

5.5 Electronics. T2Kelectronics library.

The last strategy for decreasing the background is the development of discrimination criteria based on the detector's topological capabilities, the main argument for a gaseous TPC. The readout potential must be enhanced by the use of state of the art electronics. One goal of this work has been the acquisition of experience with last generation electronics for TPCs and the development of tools that make them available for the test-bench activities of T-REX.

5.5.1 T2K electronics set-up.

We focused on the electronics developed by the CEA/Saclay for a rare event search experiment using micromegas: T2K[177]. The electronics core is the AFTER ASIC[178], which is continuously recording every channel in a buffer with capacity for 512 samples with 12 bit precision at 100 MHz maximum sampling rate. Each channel has been pre-amplified and shaped, being the faster peaking time 100 ns, and with an also tunable gain. The basic T2K electronics unity is able to read 1728 channels which are delivered via optical link.

The basic unity of the electronics set-up is a light set of at least 2 cards (244 channels) and up to 7 cards (1728 channels), quite compact and robust (see figure 5.8), which needs a low voltage DC power supply. An intermediate commercial Data Concentrator Card is required to finally send the data to the PC via Ethernet.

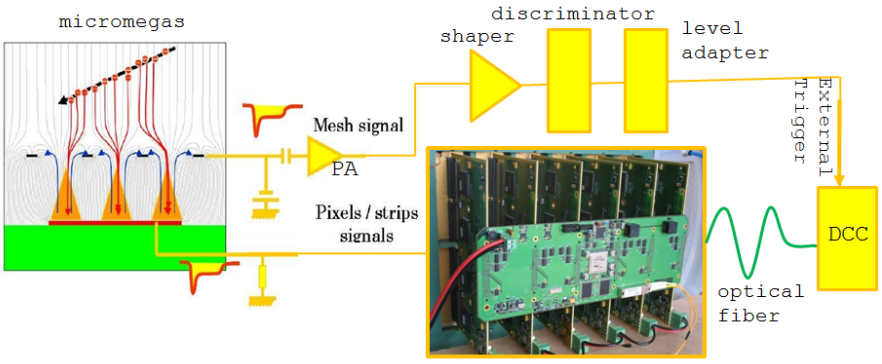

Figure 5.8: T2K electronics set-up sketch for reading a micromegas: the electronics unit is composed by a mother board (FEM) plus from 1 to 6 front-end cards (FECs). The trigger is produced by pre-amplification and shaping of the mesh signal, which must exceed the discriminator threshold. The logic signal may need of a level adaptation stage before be given to the Data Concentration Card (DCC) which triggers the DAQ pause and data transfer.

The electronics must be provided with a logic TTL signal as external trigger. One advantage of micromegas is that the mesh signal is a suitable trigger signal because, since it is induced by the whole event charge, it is relatively intense and common to every event. Essentially the typical analogic electronic chain plus a discriminator will be needed (see figure 5.8 sketch).

5.5.2 T2K electronics library.

T2Kelectronics library is the software tool developed to handle the data acquired with the T2K DAQ. It is written in C++ and makes use of ROOT classes (as customary in the LFNA, see RESTSoft chapter 6). It has four essential components: a low level class, *T2Kreader* (based on a program by David Attie from CEA/Saclay), which directly deals with the binary output files of the T2K DAQ, absorbs the T2K data format and can load in memory the recorded pulses and provide fast visualization; a general holder class, *T2KrawEvent*, to handle and store the data already as a ROOT *TObject*; the method to write *T2KrawEvent*s ROOT trees from T2K binary files and a practical description of the set-up.

The set-up description distinguishes between the electronics' configuration and the detector's architecture. *T2Kreader* requires the electronics structure which is read, number of cards, channels, etc. The auxiliary class *T2Kconfig* is able to deduce it from a simple configuration text file, together with other parameters which can be

useful for other methods. An associated class, ReadoutDecoding, provides a model to implement the relationship between the electronic channels and their physical meaning for a particular detector and cabling (the decoding task). Several readout-decodings, corresponding to real set-ups, have been written and can be taken as templates.

T2KrawEvent is thought to be versatile and powerful, therefore simple in structure but relying on advanced objects; it is basically a collection of a variable number of ROOT histograms that hold the recorded pulses plus the event time. Every histogram is assigned a channel number, to address its origin, and two more optional numbers to describe the physical position of the signal, generally called *row* and *column*. *T2KrawEvent* can absorb the decoding result, but there is the alternative to use its pointer to a *ReadoutDecoding* object too. Therefore *T2KrawEvent*, when used by other methods, can provide the physical position of every signal either because a previous decoding process result was already recorded on it or directly by making it on-line. The variable size of *T2KrawEvent*, which is independent on the electronics configuration, allows off-line data selection methods.

The main method that produces the *T2KrawEvent* can optionally perform a selection by threshold and the decoding during the format data transformation process. It also reads the DAQ *time stamp* and reconstructs the relative time. It is an especial case in the *T2Ktools* class, which is not conceived as a C++ class, but more exactly as a set of functions to handle *T2KrawEvent*s using, if necessary, *ReadoutDecoding* and *T2Kconfig*. It includes very basic functions together with elaborate analysis and drawing methods; they are the basis for the programs which are written for practical use. Figure 5.9 contains representations of events recorded with a CAST micromegas detector using T2K electronics. They (and the rest of figures in this section) has been generated with *T2Ktools* methods and have the purpose to demonstrate the detector, the electronics and the software possibilities.

5.5.3 TPC event reconstruction.

A full event reconstruction[5] method can only work with a pixelized readout. The microbulk micromegas in figure 5.10 left was specially designed for this purpose to fit Zaragoza's lab high pressure chamber (see section 6.2.7.2 and [169]). It has got an active area with 12×12 pixels in 10×10 cm^2, what was a world record at its time (Summer 2009) doubling CAST microbulks size.

Its performance is remarkable because it supposed a milestone in scaling-up potential of microbulks. The resolution obtained using a non collimated ^{55}Fe source was 12.6% FWHM, only slightly worse than the usual microbulk prototypes of almost 15 times smaller size (see section 4.4.3, in particular figures 4.22 and 4.23). Spectra like the one in figure 5.10 right, which has been taken from the mesh pulses,

[5]Here, for *event reconstruction* it is understood just the deduction of its three-dimensional structure, no physical interpretation is done.

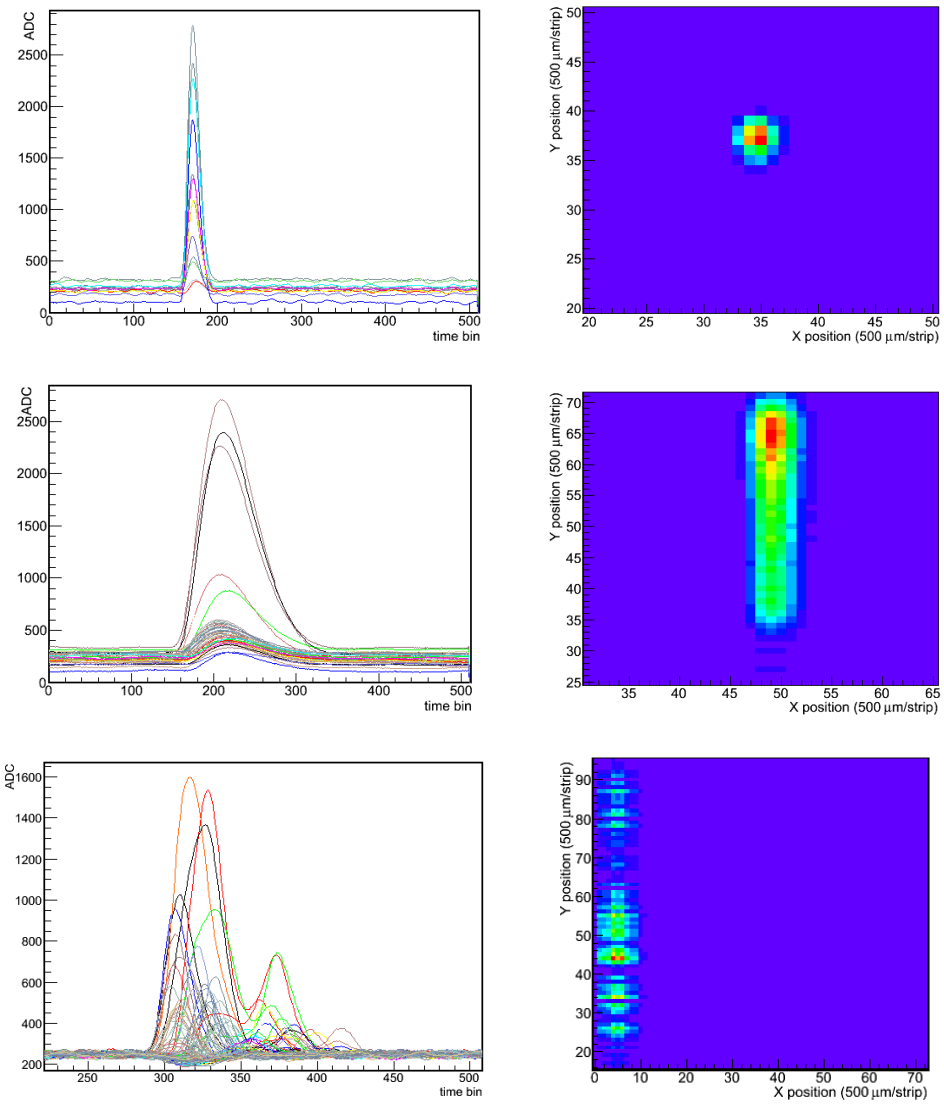

Figure 5.9: Events as registered with CAST bulk micromegas B5 (strips readout): recorded pulses and readout projection (each bin amplitude is the product of the amplitudes of the corresponding strips). Top: a ^{109}Cd 22 keV γ. Center: ^{241}Am 5.5 MeV α. Bottom: cosmic muon.

show that the increase of the electrodes capacity was not limiting the detector threshold and resolution.

It is also noticeable the way other auxiliary detector aspects were developed at the same time. For these measurements a new feedthrough design by J. P. Mols from CEA/Saclay (figure 5.11), based in a SAMTEC high density connector[179], it was used to extract the signals from the high pressure vessel. The signals are driven by plane and flexible cables called *limandes*.

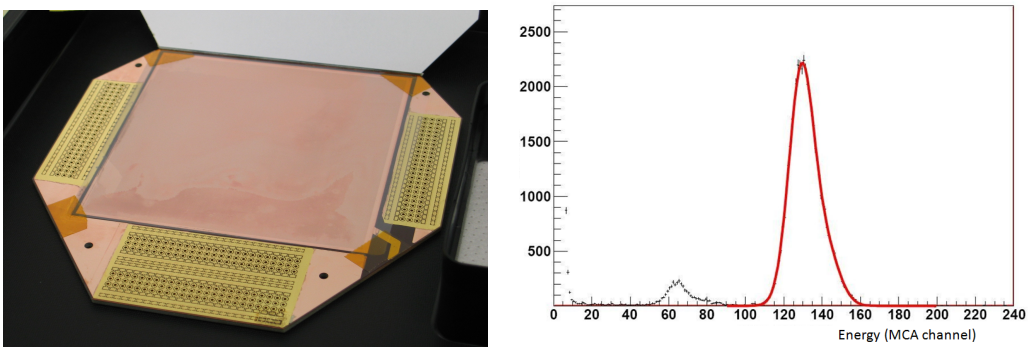

Figure 5.10: Left: Microbulk micromegas with pixels readout. Right: ^{55}Fe spectrum taken with this micromegas, collimating the source at its center. Energy resolution is 11.9% FWHM and the energy threshold is below 0.5 keV.

The feedthrough leak tightness was tested at vacuum and high pressure obtaining no deviations from previous tests with the same vessel. Anyway the chamber with the feedthrough could operate perfectly with a 6 cm drift distance using pure argon at drift fields lower than 50 V/cm, as the following event reconstructions will show. Later versions of these feedthrough are currently extensively used in the NEXT-1-MM prototype.

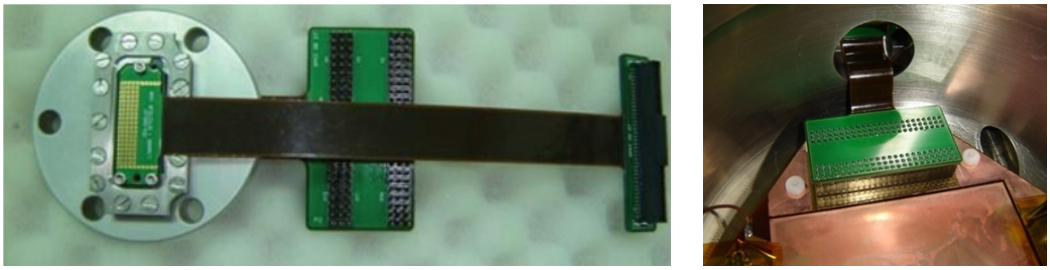

Figure 5.11: Left: the feedthrough, a SAMTEC connector[179] integrated in a CF60 outlet, with limandes. Right: the feedthrough installed in the high pressure chamber and connection to the pixelized microbulk.

The reconstruction algorithm written for the third dimension is very simple. The pulse is sampled around its maximum position with a period which should be related with the electronics peaking time; then, when a significant time extension of the signal is found (i.e., basically when the pulse's width is longer than the shaping time) a secondary charge core, or 3D-pixel, is added to the event representation (see figures 5.12 and 5.13). A more advanced idea for the reconstruction could rely in a deconvolution of the signal using the electronics shaper typical response, following the inverse operation of that explained in section 6.4.

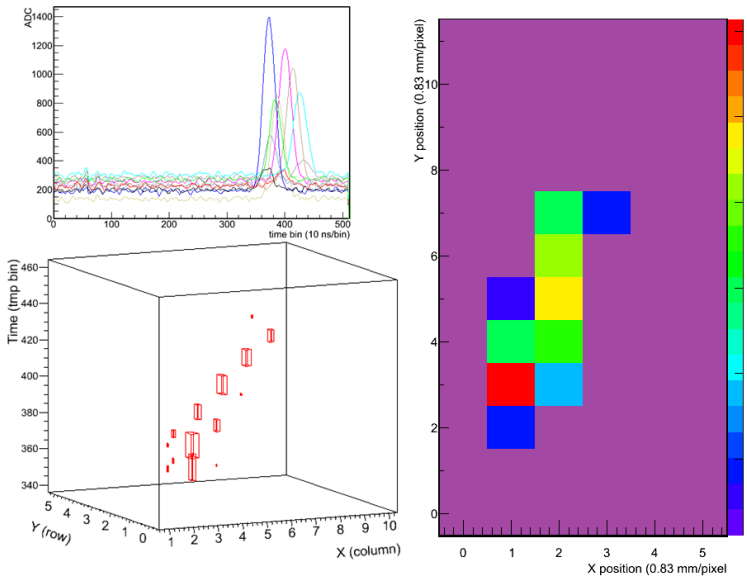

Figure 5.12: ^{241}Am 5.5 MeV α event in Ar with 2% iC$_4$H$_{10}$ at 1 bar and $E_{drift} = 30$ V/cm. The mean length of the α tracks is 5.3 cm. T2K electronics working at fastest mode: 100 MHz sampling rate and 100 ns shaping time. Right: individual pixels maximum amplitude. Top left: recorded pulses. Bottom left: event reconstruction.

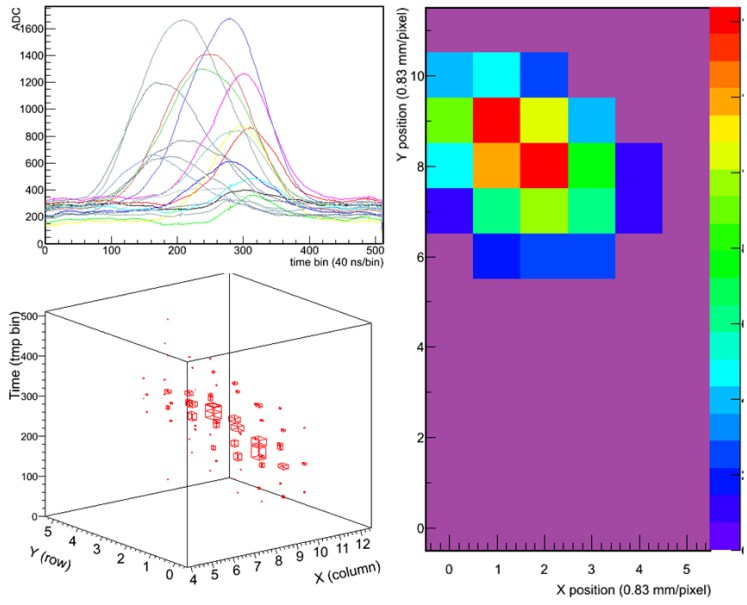

Figure 5.13: ^{241}Am 5.5 MeV α event in pure Ar at 1.23 bar and $E_{drift} = 20$ V/cm. The mean length of α tracks is 4.3 cm and longitudinal σ for 6 cm drift is 8.6 mm. T2K electronics configuration: 25 MHz sampling rate and 1 μs shaping time.

5.5.4 Outlook.

Today T2K electronics are used in Zaragoza labs to read CAST detectors, the NEXT-1-MM prototype (see figure 5.15) and a prototype for high sensitivity radon detection and soon new T-REX prototypes for Dark Matter. Besides the CAST acquisition upgrade expected for 2013 is based on T2K electronics.

The T2Kelectronics library was conceived as a BETA version (see figure 5.14), with absolutely general assumptions and only a basic functionality, however it produced a set of simple demonstration programs which are still intensively used by the former set-ups operators. It was thought as an outline for future more formal and specialized versions.

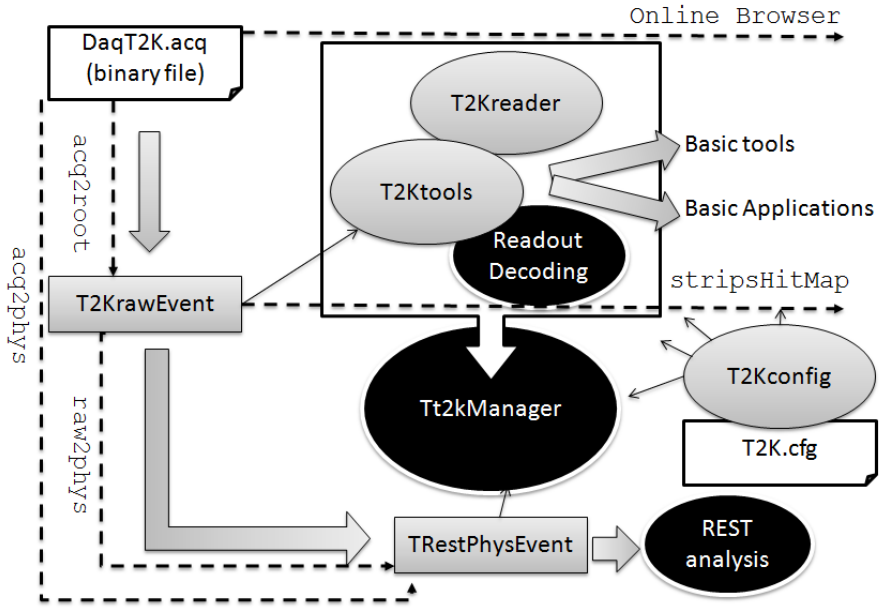

Figure 5.14: Sketch of the classes involved in the T2Kelectronics library. There are at least three levels of data evolution, from the binary output to the reconstructed event (*TRestPhysEvent* class, see section 7.3) through the raw event. See section 7.3 to relate T2Kelectronics librare with RESTSoft package via the *Tt2kManager* class. Dashed lines represent the information flow via some practical programs based in T2Kelectronics library.

That process has started thanks to the work by younger researchers with the establishment of stable particular versions for data management of CAST detectors, the possibility to emulate CAST classic DAQ (see section 10.4) and the development of new analysis based in *T2KrawEvent* for CAST and NEXT-MM. Furthermore see section 7.3 for a connection with RESTSoft libraries.

A specially useful achieved goal has been setting up a combined DAQ which uses T2Kelectronics for reading the detector segmented anode and an oscilloscope[180][6]

[6] Oscilloscope libraries by J. Galán and J. A. García, who also provide a on-line DAQ GUI.

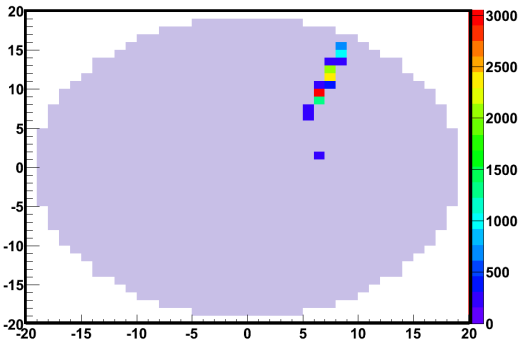

Figure 5.15: Cosmic muon as registered with T2Kelectronics and drawn with T2Kelectronics library in the NEXT-1-MM chamber[107]. The readout was a 30 cm diameter bulk micromegas with 1252 pixels, though a microbulk version is currently in operation[19].

for the acquisition of the mesh pulse and the configuration of the common trigger. This relatively portable set-up is quite versatile thanks to the adaptability of the oscilloscope for any kind of signal and because the DAQ inherits from the oscilloscope the capability of naturally configuring complex trigger criteria, including coincidences between different signals.

Chapter 6

Simulations for Rare Event Searches with TPCs

Contents

Monte Carlo-based simulations are powerful tools on the hands of the experimentalist. Two are the typical situations where a simulation is required: the planning of a new experiment or the analysis of an existing result. In the first case, a virtual realization of the experiment can be done, what allows to evaluate the probable quality of the result, perhaps to modify the set-up design and, finally, to decide if it is worth to be materialized. In other cases, when a real result needs to be confirmed or requires better understanding, the simulation provides the perfectly controlled environment where the cause-effect chain is registered.

6.1 RESTSoft.

The TREX activities need an associated software framework which must include both simulations and the management of data for later analysis. It works sometimes as a support for ongoing R&D experimental lines; but other research lines are started, and largely continued, purely as simulations, and so completely developed inside this framework.

The RESTSoft (Software for Rare Event Searches with TPCs) architecture and philosophy was firstly drawn by Igor G. Irastorza and the ulterior developments, mainly by Francisco J. Iguaz and A.T., have tried to keep its affinity with the original plan. RESTSoft is written in C++, therefore it is conceived by means of objects (C++ classes), and uses ROOT[181] classes as immediate analysis tool (maths functions, arrays, graphs, fitting, etc) and for serialization (objects storage and management).

It is not thought to be a very big and complete program but a collection of classes as tools for the users to write their own programs. This conception sets requirements for the RESTSoft classes: they must have a very concrete purpose and they must be prepared to work in a modular way. This means that a program based on RESTSoft should be written as a sequence of classes which acts one after the other, each one performing some transformation in the data or producing a result at certain level. In order to become a really useful packet, the classes need to interchange information efficiently and must be as versatile as possible.

Therefore the RESTSoft users are expected to have basic skills in C++ programming, however their task should be made easier. The RESTSoft classes functionality must be clearly exposed, i.e. they should contain methods with a very descriptive and unambiguous purpose as "add diffusion effects to this event" or "the resolution of the micromegas will be 14% FWHM at 5.9 keV". Even if the class contains some complex algorithm, the code must be readable thanks to interface functions for input, output or configuration (*Setter* and *Getter* methods). In addition, it should provide different ways to be used, trying to anticipate likely situations or future development needs. This can increase notably the work and is one of the main differences between writing a single program and preparing a library, but it will allow the RESTSoft users to do only high level programming.

We could need different codes to work together with RESTSoft libraries: an external program, other libraries out of RESTSoft or simply to import or export data in a different formats. This is actually what happens in most cases: we use a common simulation application, a database, a previously developed method or we could need to communicate with a real acquisition. The relationship between RESTSoft and some codes is, in fact, so repeated that suggests to develop stable piece of code. Pure RESTSoft code must be well distinguished from external codes, which do not have to follow the RESTSoft scheme; so specially devoted classes must act as *bridges* between RESTSoft and external codes. They must contain the keys

to deal with the external code (format, configuration, etc) but also methods for the RESTSoft user not to have to go down from the high level programming. All the pure RESTSoft classes are named as *TRestX*, while for bridge classes the convention is just *TX*.

In the last years RESTSoft libraries have been evolving in parallel with the proliferation of programs which answered to particular research necessities. The paradigmatic case is a simulation chain plus following analysis, which starts with a Monte Carlo simulation that is carried out using an external application. Some of these programs have been equipped with user interface methods (as configuration files) that have allowed external users (who do not need to now how RESTSoft classes work) to deal with them. This way RESTSoft has been intensely used. The best way to describe these simulation chains, and RESTSoft itself, may be to show some examples in which simulations were used up to different levels of the chain, so they will be inserted in the description along the next sections.

6.2 The RESTSoft GEANT4 application.

There are very tested programs for Monte Carlo simulation of interactions of particles with matter. RESTSoft does not intend to substitute them but to use them and complete them for our particular needs. *GEANT4* [182, 183] is a general purpose simulation tool-kit for particles and radiation widely used in High Energy Physics, for instance for the simulation of LHC detectors. However it has the aim of extending its application to other fields, specially towards the low energy (below 10 MeV) Physics. In fact, it has absorbed other tested codes which were previously well appreciated for specialized simulations. GEANT4 itself shares the same philosophy as RESTSoft, it is a collection of classes one have to assemble to build an application that will perform some concrete simulation. Most of the classes we will describe in the following sections inherit from GEANT4 prototypes.

For RESTSoft, a GEANT4 application for the simulation of gaseous TPCs was built in closed collaboration with F.J. Iguaz. There was much previous experience in the LFNA with GEANT4 simulations for Rare Event Searches, directly the work by Susana Cebrián[143], María Martínez[144] and others, which was a starting point. The main difference with previous simulations, mainly about solid state detectors, was the amount and nature of the information to extract, as the new goal was a simulation of a detector with topological capabilities.

6.2.1 Basic description of a simulated event in a TPC.

The information we are concerned about in a simulated event which is held in a TPC is a basic description of the energy deposition path by ionizing particles. This path is built step by step, each one generated from the previous one. For each step we are given a new position and state (energy, momentum, etc) of the particle and, perhaps, an energy loss during its travel. We assimilate these *steps* into *hits*, each

one defined by a position and an amount of energy deposited in the gas; though there is a subtle difference between both concepts. When energy is lost by the particle, the GEANT4 step provides also the physical process which caused it. In the case of energy deposited in ionization by a charged particle, we cannot assume that all the energy was deposited exactly in that place we are going to allocate for our hit; the GEANT4 program considers the material the simulated particle is passing by as a continuous, and it calculates the likely energy loss due to that process according to its cross section tables or formulas.

This is the reason why simulating in detail gaseous detectors was more difficult, since very thin absorbers are worse described and much more unpredictable (see section 3.1.3); but GEANT4 has improved a lot in this sense in its last releases (always newer than 9.2 patch 01 version). Of course, the amount of energy loss is not always the same for the same step length and it can be even zero if the step is short enough. Therefore the choice of the step length is important, it should be long enough for having a realistic (and not too slow) simulation and, on the other hand, it is directly related with the simulation quality.

It may be a convenient cross-check to have a look to the passing of MIPs through the simulated TPC at this point. 1 MeV electrons ($\gamma \simeq 3$) are launched so as to cross chambers (like those of figure 6.1 left in a 3 cm height chamber) of several heights filled with argon with 2.3% isobutane at 1.4 bar. The resulting energy spectra are plotted in figure 6.2, scaled to the 3 cm height chamber ($\mathrm{d}E/\mathrm{d}x \times 3\mathrm{cm}$) for better comparison. Only the 6 cm chamber spectrum fits well to a Landau distribution; for the 3 cm an irregular structure is already evident (compare with plots in [116] page 19) and for 0.5 cm thickness we have something near a discrete distribution reflecting the possibility of 1, 2, 3 or n clusters along the path. For 6 and 3 cm the most probable value is proportional to the chamber height (≈ 6.5 keV/cm) but the same is not true for the mean value which is 19.83 keV (6 cm), 10.74 keV (3 cm) and 3.25 keV (0.5 cm).

In GEANT4 the step length is naturally related with an energy cut-off[184]. Every particle has a mean free path for each physical process and material, particles with shorter mean free path than the maximum step length have few possibilities to produce any visible effect at the desired degree of detail of the simulation; therefore it is not worth to devote computation time to simulate them and the simulation just assumes all their energy was deposited right there. That cut plays the role for a hit as the cut-off in the restricted energy loss stopping power (see section 3.1.4) for the chamber dimensions or readout pitch. The same stands for secondary particles, so it is important to be sure that the energy cut in a material is below the threshold of a physical process which is relevant for our simulation purposes, otherwise it would be inhibited. For example, we must be sure the step length is related with an energy lower than 3.2 keV in argon if we want to have argon K-fluorescence in order to reproduce escape peaks in our simulated spectra (see section 3.2.1.1).

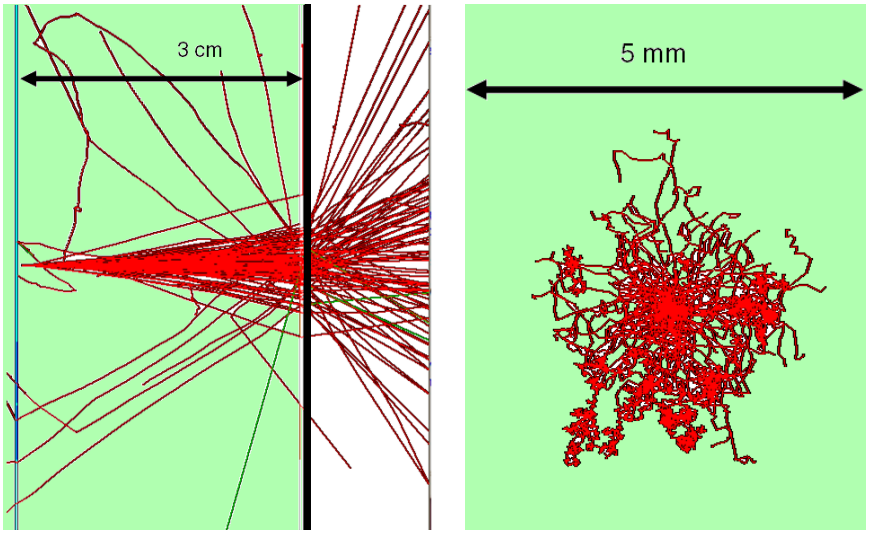

Figure 6.1: Left: Simulated tracks for 1 MeV electrons. Right: 6 keV electrons.

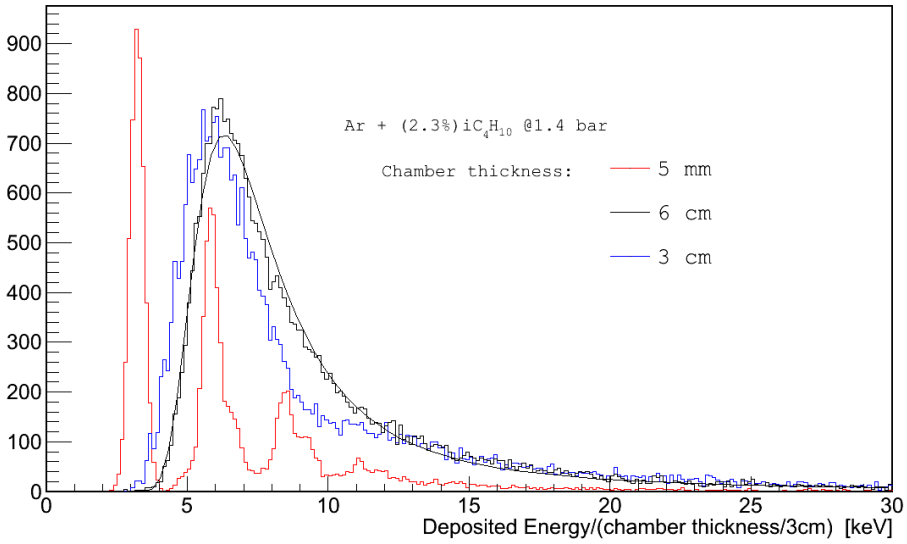

Figure 6.2: Simulated energy spectra produced by 1 MeV electrons. The Spectra are normalized ($\mathrm{d}E/\mathrm{d}x \times 3\mathrm{cm}$). The 6 cm histogram is fitted to a Landau.

In the geometry defined for the detector simulation a volume called *target* is defined, it is part of the conversion volume of the TPC and works as the *sensitive volume* of the simulation, i.e. the interactions which are produced inside it are registered as a collection of hits: *the track*. The step length inside the target is limited to a maximum that is independent on the general one, which can be regulated via the application configuration file. It has been found that for a TPC with gas at pressure less than 10 atm, a step limitation around tens of microns, which is appropriate for

current micromegas granularity, gives sometimes steps with no energy loss and also steps that were interrupted by a relatively high deposition of energy (in this case the GEANT4 algorithm forces the pause of the simulation and the generation of an early step).

The mechanism is illustrated in the following plots which have been obtained from a simulation of $3 \cdot 10^4$ 6 keV photons (like those of figure 6.1, right) in argon at 1 bar with the step delimiter set to 50 μm , where we focus in the first step recorded by the GEANT4 application. In figure 6.3 the first step's length (more exactly the distance to the starting point of the electrons from the first hit position) is plotted. It can be seen that many of the steps, $\sim 1/3$, have exactly the maximum length set. That happens when the *StepLimiter* process pauses the simulation and refresh the particle status. After taking into account multiple soft scattering processes, it delivers a variable amount of energy deposited into the gas, which is usable for primary charge generation (a process which is out of the scope of the GEANT4 simulation).

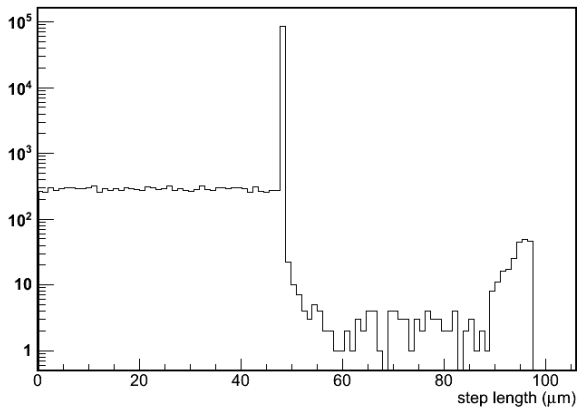

Figure 6.3: Step lengths distribution for the first step of 6 keV electrons.

Other times the step is prematurely finished by a physical process, which can be just the same *MSC (multiple scattering)* when the accumulated energy deposition rises the energy cut or, in $\sim 10\%$ of cases, *LowEnergyIonization* if a deep electron (with binding energy higher than the energy cut) has been released or a knock-on collision occurred with production of a δ-ray with energy higher than the energy cut-off. Thus a distribution of lengths appears below the step limitation peak, which is flat as corresponds for processes that have a mean free path long compared with the maximum step length. A kind of duplication of the distribution can also be detected on the right, like a pile-up spectrum, and this is basically what it is. Since the electron is allowed to experiment no interaction after one maximum step length and, in that case, no hit is registered by the program, what is actually plotted is the distance from the second hit.

In figure 6.4 the energy loss along the first step is plotted. The histograms with non filled area correspond to the energy deposited in the gas, that is to say, the energy that is assigned to the hit. We distinguish between normal steps and steps whose end was suddenly caused by the ionization process. The former cannot exceed the energy cut, which for our conditions is slightly higher than 200 eV, and the energy loss is equal to the energy deposition. For the second, the absorbed energy can be higher than the energy cut and lower than the energy loss if secondary particles (with initial energies higher than the energy cut-off) are generated. The L-edges of argon at 250 and 310 eV (above the energy cut-off) are clearly visible in that distribution (another peak at 3.2 keV, K-edge, is out of range). The second part of the distribution, caused by the presence of the L-edges, ends necessary at 510 eV since that is the sum of the energy cut-off and the most energetic absorption line. Both distributions are described (with exception of the atomic edges) by Gaussian statistics, as the sum of many independent energy depositions.

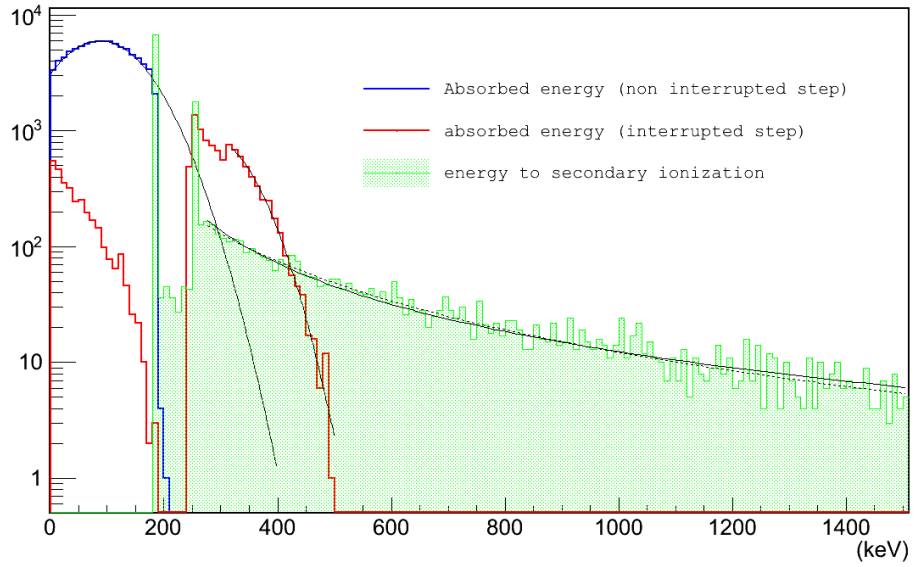

Figure 6.4: Energy loss along the first step of 6 keV electron tracks.

The difference between the energy loss and the deposited energy is the energy invested to secondary particles, which is represented by the solid area histogram. It can be fluorescence photons and Auger electrons (see section 3.2.1.1) related with the atomic bound or δ-electrons (see section 3.1.4). If we had chosen the energy cut-off higher than the binding energies, the related secondary particles would not have been simulated with consequent acceleration of the simulation. These are accumulated in peaks while the δ-electrons should draw a continuous distribution, however the distribution we see is not directly the δ-rays energy production distribution, that can be the sum of several secondary particles. Ignoring this last detail, a completely different distribution is expected here, according to section 3.1, the

Coulomb scattering one (see equation 3.1), however ΔE is still not much higher than the binding energies. The solid line, which is a fit with shape $\sim 1/E^x$, is not able to reproduce such a long tail for a wider range than plotted in figure 6.4 and gives $x = 1.59$ instead of the expected 2. The distribution fits much better to a Landau tail (dotted curve).

To sum up: the way the track is developed in the simulation is similar to the real case, in which discrete clusters are generated; however we should keep in mind the subtle difference existing between actual clusters and the hits of the simulated ionization track, due to the fact that ionization is a treated (most of times) as a continuous process. In contrast, when a photon is simulated there is no ambiguity to decide where a conversion into an electron by photoelectric effect or where it was supposed to suffer a Compton scattering.

The basic description of the track inside the target, as a collection of hits with positions and energy depositions, is completed with the physical process that defined the new step (recorded following a numerical code) and the trackID, which numerates the concrete particle which caused the hit. The trackID can be useful, e.g. to distinguish between the primary ionizing particle track and secondary ones.

6.2.2 Physical processes.

The Physical processes which can happen during a GEANT4 simulation are defined in its *PhysicsList* class for each particle. The RESTSoft GEANT4 application's *PhysicsList* started from previous lists developed for simulations of the Dark Matter experiment ANAIS[43], which are described in [143, 144], themselves based on the Underground Physics advanced example of GEANT4.

Only relevant processes for low energy Physics are included (using the low energy versions of GEANT4 process and models). For electrons, in particular, the ionization and multiple scattering presented in the previous section plus Bremsstrahlung and annihilation for positrons. For X-rays and γ's, all those presented in section 3.2.1; but optical photons are not considered since it is (still) not intended to simulate an optical readout. A special case is the *Radioactive Decay process* that can generate the natural decay of isotopes.

In summary, the simulation is simple from the point of view of the amount of relevant particles and processes involved, but it must be detailed, therefore secondary processes as fluorescence, PIXE and δ-rays are activated with energy threshold related with the step length as was already discussed in the previous section.

6.2.3 Geometry.

For a simulation of a particular detector its geometry has to be implemented. Nevertheless all the simulations have some common features and many times only some dimensions and materials arrangements are enough in order to essentially reproduce

the situation. A configuration file is available and the application is able to interpret it and build automatically a simple but versatile geometry.

Basically the general geometry can be described as a set of cylindrical layers, in *onion-like* scheme, plus two levels to define the electrodes (see figure 6.5). The target is, of course, contained in a gas volume which corresponds to the conversion volume of the TPC. The target is defined as the volume that is projected onto the micromegas' surface (which is supposed to be at the bottom of the chamber) up to a certain level, usually that of the cathode position. The fact of distinguishing the target from the gas and conversion volume (volume between the electrodes, mesh and cathode) allow to consider realistic dead zones in our chamber. The simplest geometry is defined just by three parameters: the chamber's height and radius, and the micromegas mesh radius.

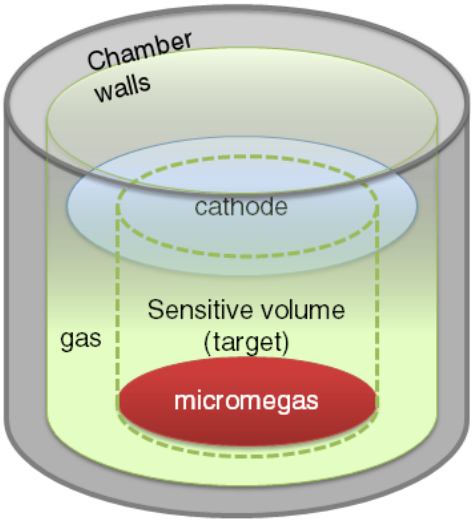

Figure 6.5: Sketch of the *onion-like* geometry of the general RESTSoft GEANT4 application. The optional shielding layers are not drawn for clarity.

The following layers are defined by their thickness and are build so as to perfectly adjust to the immediate inner layer. The first one may represent the chamber structure and could be important in case the chamber would contribute with fluorescences. For the same reason, the micromegas mesh itself is represented as a thin layer of copper (in case of a microbulk) or stainless steel (if a bulk) and the readout behind with copper-kapton layers. The outer layer can be used to add a basic shielding in case we would like to study the effect of an external source.

The gas inside the chamber is, by default, pure xenon or a mixture of argon and isobutane. The mixture proportion and the gas pressure can be set through the configuration file too. In the geometry class of the program, *mMDetectorConstruction*, there is a simple method to properly define the mixture of gases (whose proportions are given in volume), which can be generalized easily to other kind of gases.

6.2.4 Event generation.

The *eventGenerator* class determines the initial conditions of the event to simulate: the number, nature, position and state (the initial vertex) of the particles that will originate an event that may be registered in the TPC. This class contains a collection of functions, some of them to set the position of the vertex and others to take care of the particles' initial states, which are combined. These functions can make reference to geometrical parameters, therefore the generator class has access to the geometry builder, *mMDetectorConstruction* class, and the user-developer must be aware that a contradiction could be produced when the geometry is modified. The *evenGenerator* uses an auxiliary class, *ProbGen*, which generates some useful distributions, as isotropic directions, or homogeneous positions in simple geometrical volumes.

This way methods to simulate some radioactive source commonly used in the lab, or some kinds of radiation fluxes or the result of key decays have been written (^{55}Fe, ^{109}Cd, general β-decays electron spectra, cosmic muons, etc.). The class is also able to interpret a Decay0[185] generated file for double beta simulations. The most typical uses can be chosen and configured through the configuration file.

As usual, the time is used as a *seed* for the Random Numbers Generator (GEANT4 make use of CLHEP libraries[186]). However simulations are often performed as parallel processes which are sent to a cluster queue, and it is not rare that some of the programs are accepted, and start running, at the same time. To assure independent simulations an index can be given as argument to the RESTSoft GEANT4 application to be combined with the time in order to produce the seed. Thus a script can send simulation tasks with different arguments to the cluster's queue in order to produce independent events.

6.2.5 Simulation control.

Our main goals are to save events which deposited energy in the sensitive volume inside a predefined energy range of interest (RoI), but also to evaluate the probability of such an event happenning. Apart from that, we could also need to reconstruct the trigger rate (probability of events which deposit energy in the sensitive volume above a threshold). In principle, at the time we are going to launch the simulation, these probabilities are completely unknown.

There are basically two types of conditions in order to decide if a simulation has been completed. The limitation of the number of stories to simulate is the usual one when there is a high probability to have a count (an event registered inside the RoI) per simulated story, what we call *TIME* end condition. This is usually the case when we are directly simulating the signal, for example, if we are simulating a calibration. In contrast, if there is no previous indication about the ratio of stories needed to have a count, as it happens typically when investigating the influence of any factor on a background, one would ask for a minimum acceptable amount of

counts before finishing the simulation. That is called *STATISTICS* end condition. By means of its configuration file both end conditions can be established and the application is able to execute the most restrictive one. The *DataOut* class is in charge to apply this criteria and reports the general progress of the simulation.

However, many times the simulation is not finished by none of the previous conditions. During very long simulations it happens frequently that any external cause stops the program: a surprising shut down, an unexpected error or simply that our time is finished in a cluster queue. In consequence, *DataOut* must save in disk the selected events as they are produced, with all the information necessary for the partial simulation to be absolutely operational. The point is basically to save every time the simulated number of stories. The most robust manner to do it is to save together with each event the number of stories that were simulated between it and the previously saved event. This way the total amount of stories can be recovered at any time with absolute precision, even it the final number is very large.

During the course of long simulations checking their correct development is also necessary. The application has an adjustable verbosity level and can print partial information every time a story is simulated, an event is saved or just periodically (or it can be even more detailed for debugging purposes). Every (also adjustable) stories period, a picture of the simulation partial result is saved in the form of a spectrum with the energies deposited by the events in the sensitive volume. The last bin accumulates the events which deposited energy over the maximum defined for the spectrum, which allows to reconstruct the trigger rate.

When very few events are saved in the course of a simulation, our strategy of saving the number of simulated stories together with the saved event can fail. Even a simulation with no saved event is giving relevant information about the rareness of such an event. Because of that reason, every stories period the number of these periods which have been completed is saved in the same text file and, if necessary, it would allow to recover the statistics with the precision of the stories period. In contrast to the individual event data recording, the spectrum routine is not implemented in *DataOut* but in the *main*, since it does not need to follow the simulation evolution and just works periodically and at the end of the simulation.

The range of interest (RoI) is defined in the configuration file by a lower and an upper limit. The simulation can be interrupted if there is no possibility to produce an event in the RoI, i.e. if the energy already deposited in the sensitive volume is over the upper limit or the remained available energy is not enough to reach the lower limit. This way the simulation is accelerated. That is specially siutable for the simulation of double beta decay, where there is a narrow RoI in a relatively high energy region. The same example is good to illustrate the following possibility: counts out of RoI can still be interesting in order to reconstruct the context. However the space needed in disk would be used for uninteresting events (which usually are many more than the interesting ones). In the configuration file a proportion of these events can be defined to be saved by chance, that is called the *Russian roulette*.

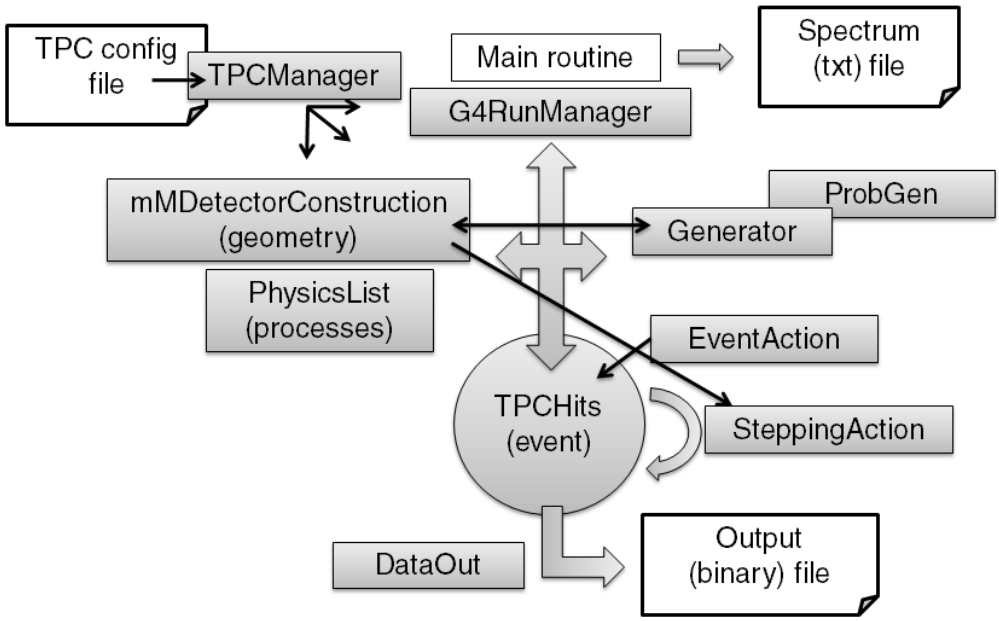

Figure 6.6: Elemental sketch of the RESTSoft GEANT4 application. *G4RunManager* is the GEANT4 class that coordinates the rest of them. The configuration options loaded by the *TPCManager* are available at any point of the program. Together with *TPCManager, ProbGen, TPCHits* and *DataOut* are the only classes that do not inherit from a GEANT4 prototype.

6.2.6 Information management. Study of cases.

The GEANT4 *SteppingAction* class gives the opportunity to write code that will be executed every time a new step of the Monte Carlo has been produced. It is at this level where most of the decisions about information management are taken. *SteppingAction* works in close collaboration with the *TPCHits* class, which holds the event information. It does not only contain the event description information, as it was explained in the section 6.2.1, but auxiliary information about the course of the event simulation. For instance, the total amount of energy deposited in and out of the target, relevant information about previous steps (as the initial vertex), and some number of flags that the user-developer can define. Combining this information and configuration settings, the program decides, for example, if to abort the event. Step by step, hit by hit, *SteppingAction* is gathering the event description and *TPCHits* holds it.

Once the event simulation finishes, *DataOut* (see previous section) examines the *TPCHits* content and decides if it will be saved in disk, before resetting the class. In the case of an event generated by radioactive decay (or natural radioactivity simulation of detector materials) the game between the triangle *SteppingAction*, *TPCHits* and *DataOut* is more complicated because, in GEANT4, all the radioactive chain is simulated as a single event. The consecutive decays can be separated by

seconds or years and then (if producing a count in the target) they must be recorded as separate events. At the same time, it must be registered that they have been originated by the same primary decay and save at which level of the chain (the name of the father) this happened.

Beyond the basic description as a hits collection (explained in section 6.2.1) and the vertex that originated the event (number, state and nature of initial particles), less obvious information can be relevant for a deeper understanding of the cause-effect relationships which drove to the result of the simulation. This information is usually related with what happens out of the target volume, however all the hits produced in the whole geometry cannot be systematically saved. The interesting cases must be classified in advance and recognized on-line by *SteppingAction* with the help of the information recorded in *TPCHits*. The idea is to put a label in the event that would mean something so complex as: "this event happened in the TPC because an incoming photon suffered a photoelectric in that part of the shielding and the resultant electron produced intense bremsstrahlung". These labels, together with a brief description, allow to try a *study of cases*, which many times eloquently resumes our understanding of the Physics that dominates in the detector.

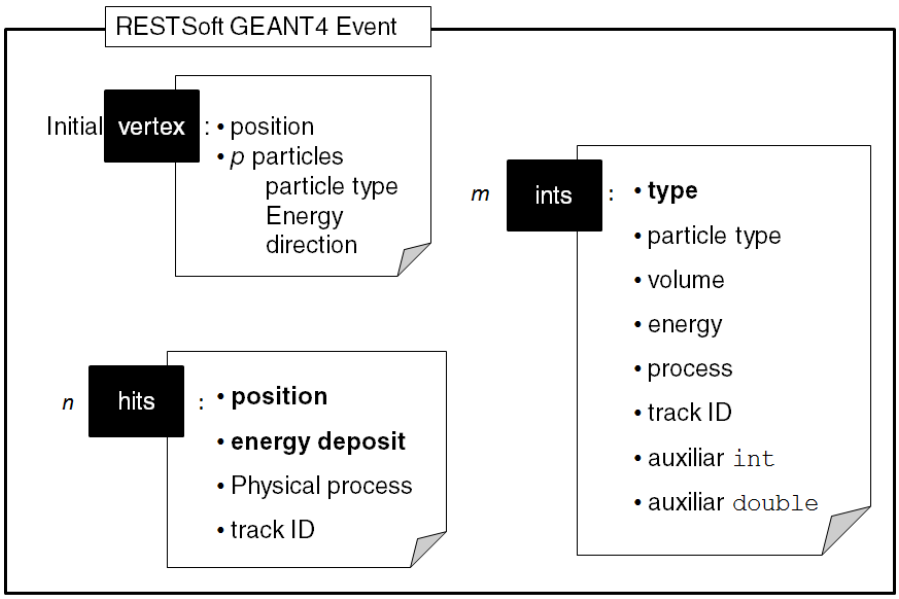

Figure 6.7: RESTSoft GEANT4 event model.

In analogy with the *hit*, that is used to describe the point-like energy depositions inside the sensitive volume which draw the track in the TPC; the *interaction* is defined to describe the highlights that happened in, or around, the sensitive volume, before or after the energy deposition on it, and *draw* the cause-effect chain which may explain the presence of the count in the spectrum. An interaction is described by the following fields: number codes for the particle, the place (a defined volume in the simulation) and the physical process of the step more closely related with the

interaction and the kinetic energy of the particle. The circumstances which define an interaction can be more complex than simply a special step; an interaction *type label* will simplify notably the off-line analysis. Two more auxiliary fields are still available, and their meaning can be differently defined for each interaction type.

Enabling this tool needs a considerable effort and skill by the user-developer. It has been far developed for the NEXT and CAST simulations and the current appearance of the general *SteppingAction* class is that of a template for building a new study of cases or *labelling rule*. Many of the types are quite general, in particular the ones which define the three common ways an event is produced inside a TPC in low energy physics: a photon produces a photoelectric in the gas (type 5), a photon suffers Compton scattering in the gas (type 6) and an electron directly bursts in the gas (type 1).

6.2.7 Direct applications of the RESTSoft GEANT4 application. CAST micromegas quantum efficiency and HPXeTPC spectrum.

The RESTSoft GEANT4 application is the perfect example of an external program related with RESTSoft. In order to extract all the information the simulation gathered an interface (what we called *bridge class*) between its output and the RESTSoft classes has to be used. The GEANT4 application has been the origin of most of the simulation works done inside TREX; besides, it has shown enough versatility and the capacity to produce results independently. In many cases dealing just with the information we described in the former subsection, spectra and probabilities, can be enough. Researchers that may be not interested in complex simulations can take advantage of the GEANT4 application alone and deal just with simple objects like spectra saved as texts files. In this subsection two examples of use of the RESTSoft GEANT4 application, which have physical meaning by themselves, are showed.

6.2.7.1 CAST micromegas quantum efficiency.

The efficiency of the detector is the probability of an event, in the case of CAST (see section 8), an X-ray coming from the magnet's bore, being registered and positively identified. The most fundamental aspect of the efficiency is the probability of an X-ray interacting in the detector, it is called *quantum efficiency* because involves the cross section of the X-ray with the gas atoms.

Moreover, the probability of the photon surviving from the cold-bore to the detector gas must be evaluated. In the case of the CAST sunrise micromegas docking place there is a trip longer than one meter and a half which is irrelevant, because the pipe is under vacuum. However the photon has to cross three windows that separate different volumes, and they compromise the quantum efficiency. Two of these windows are reinforced with metal grids, called *strong-back*, because they separate regions with different pressures: the cold window between the cold-bore (which in CAST phases II and III contained ^{4}He and ^{3}He) and the vacuum pipe,

and the drift window between the vacuum pipe and the detector gas, which is in overpressure (just for increasing the quantum efficiency). X-ray are blocked by the strong-back bars, so that introduces a geometrical loss for the efficiency. In addition there is the probability of the photon being absorbed or dispersed in the window material. The drift window is an aluminized mylar foil of 5 μm thickness (plus negligible aluminium thickness), the cold-bore window is 14 μm polypropylene thickness and the differential window, which is placed in the middle and has no strong-back, adds 4 μm extra of polypropylene.

Finally the detector geometry and the gas conditions, basically the gas mixture (Ar with 2.3% iC_4H_{10}) and pressure (1350 mbar) are essential; but it regards also the definition of the sensitive volume. The latter concerns to border effects and the probability of secondary photons escaping the detector. They are important because events that deposited less than the photon initial energy will not be accounted for positive detections.

Using the GEANT4 geometry model for the CAST micromegas detector exposed in section 9.1.1 with addition of the two windows of the vacuum system with the help of the RESTSoft GEANT4 application we can calculate the CAST micromegas' quantum efficiency. A general method from application's *Event Generator* class is used to launch the photons in perpendicular direction to the micromegas plane (as they would come if originated by solar axions) homogeneously scanning the cold-bore area with random energies between 0.5 and 10 keV. Imposing that the event deposited energy in the gas is the same as the photon initial energy, a graph proportional to the quantum efficiency is obtained directly from the spectrum output of the simulation.

In figure 6.8 right several curves show the simulation step by step. First, a calculation of the chamber's conversion volume efficiency. This curve is almost coincident with the one we can just calculate from NIST cross sections database[138] for the argon using the gap length and gas pressure (see the introduction of section 3.2.1). The only notable difference can be detected above 3.2 keV, where the K-layer of argon is placed. The difference is reflecting the probability of a secondary 3.2 keV photon from argon fluorescence escaping the chamber (see section 3.2.1.1).

It can be observed how Quantum Physics limits the efficiency at high energies. Only replacing the gas, increasing its pressure or upgrading the chamber size could improve it. The rest of the curves are obtained by consecutive addition of the drift window and the other two. In the figure 6.8 left we have the contour map obtained for the complete simulation, showing the shadows of both superposed strong-backs. However, similarity between curves at high energies is telling us that the strong-backs do not represent a big disadvantage. We see now how the windows accumulated thickness is the factor which limits the efficiency at low energies.

This way the GEANT4 application alone, just by drawing the output spectrum, has been able to produce one estimation that is capital for the CAST experiment.

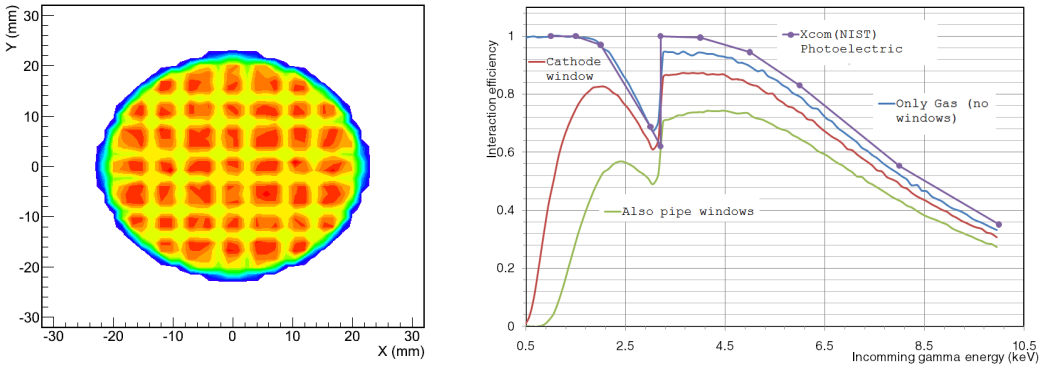

Figure 6.8: Left: readout projection of the interaction position where the shadows of the two consecutive windows grids (strong-back) are superposed. Right: "step by step" simulated quantum efficiency and comparison with NIST XCOM database[138].

6.2.7.2 Reproduction of one spectrum in the HPXeTPC.

Another example is the planning of a test in the Zaragoza's high pressure test chamber. This vessel is designed for high pressure, leak-tight and low out-gassing, since it was thought to test pure noble gases[107] (HPXeTPC, high pressure xenon TPC). The idea is to measure energy resolution for medium energy gammas (higher than the usual 6 keV from ^{55}Fe or 22 keV from ^{109}Cd) in pure xenon at high pressure in order to do a more feasible extrapolation to the double beta decay Q value at 2448 keV. A limitation for that is the efficiency of the chamber whose conversion volume of 6 cm maximum drift distance is defined by rings of 8 cm inner diameter, while the size of the micromegas prototypes installed there is usually only 3 cm diameter. These dimensions can be used in the REST GEANT4 application to simulate such a chamber filled with pure xenon at 4 bar (see figure 6.9).

To obtain the graphic in figure 6.10 a mono-energetic isotropic point-like source placed on the top of the conversion volume (see figure 6.9) has been simulated for γ energies between 10 and 100 keV. Like in the former example, the output spectrum is enough to define the efficiency. The green solid line in the plot corresponds to the calculation one easily would do (see section 3.2.1) from NIST cross sections database[138] considering the photoelectric probability, γ trajectories orthogonal to the read-out/cathode planes and the maximum drift distance. The simulation will also take into account the solid angle and the electrons finite path range .

In addition, from the simulation we distinguish the *detection efficiency* (possibility of interacting in the sensible volume limited by the micromegas surface) and the *photo-peak efficiency* (possibility of deposition of the whole energy in the sensitive volume, so contributing to the photo-peak and having a really useful event). At low energies both efficiencies are almost coincident since the photoelectric cross section is by far dominant compared with Compton (see figure 3.14 right). On the contrary,

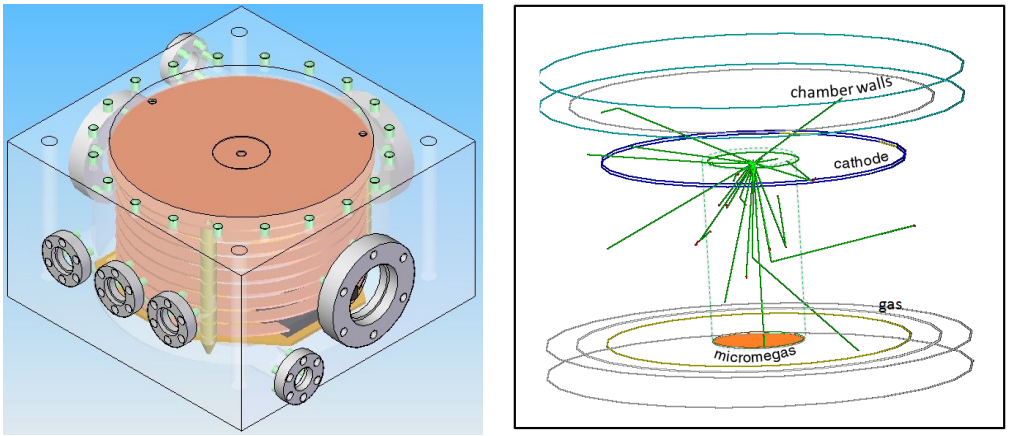

Figure 6.9: Sketch of the HPXeTPC (left) and its model in the RESTSoft GEANT4 application (right). Few γ's trajectories are drawn in green and some photo-electric and Compton effects can be recognized, with induced electrons paths drawn in red. The sensitive volume for efficiency calculation is the one between the mesh and the cathode and delimited with the dashed line.

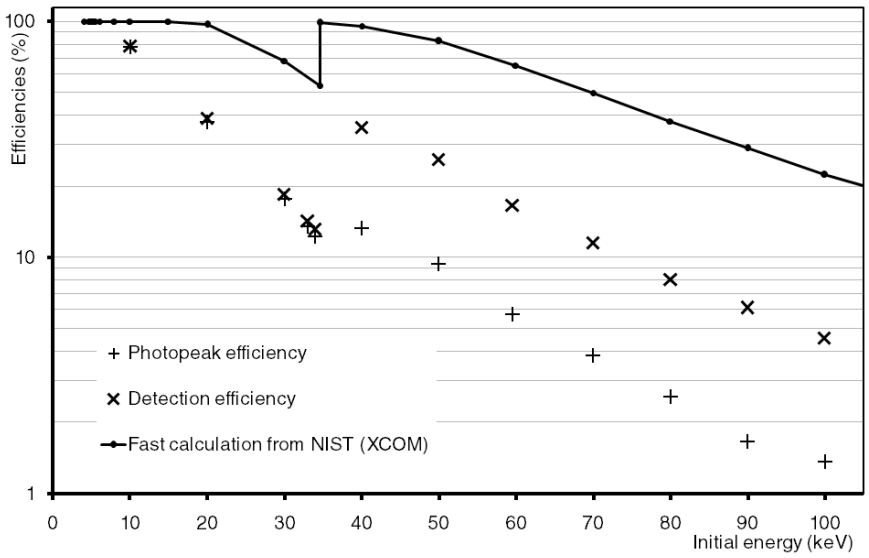

Figure 6.10: Detection efficiency for γ-rays in the particular set-up drawn in figure 6.9.

a big difference appears when energies reach the K-edge of Xe and we start having the possibility of a secondary photon carrying a part of the global energy. The difference between the detection and the photo-peak efficiencies can be interpreted, almost directly, as the probability of having a count in a scape peak; because the electrons path projected range $\approx$ 1mm (see figure 3.4, keeping in mind that $P = 4$ bar and ranges in xenon $\approx 1/2$ of ranges in argon), still small compared with the micromegas radius.

Once the experiment is finally carried out (measurements by Diana C. Herrera[107]) using the 60 kev (59.54 keV) γ-rays from an ^{241}Am source, the simulation is required again to properly interpret the experimental spectrum (black line in figure 6.11). That is necessary to choose the most suitable fit function that will be used to extract the energy resolution. The situation in the chamber is rather complex as, apart from the 60 keV γ's, we could find: escape peaks shifted at ∼30 keV (Xe Ka), ∼33 keV (Xe Kb) and ∼3.5 keV (Xe L); their corresponding fluorescence peaks and the 26.3 keV line from the ^{241}Am source.

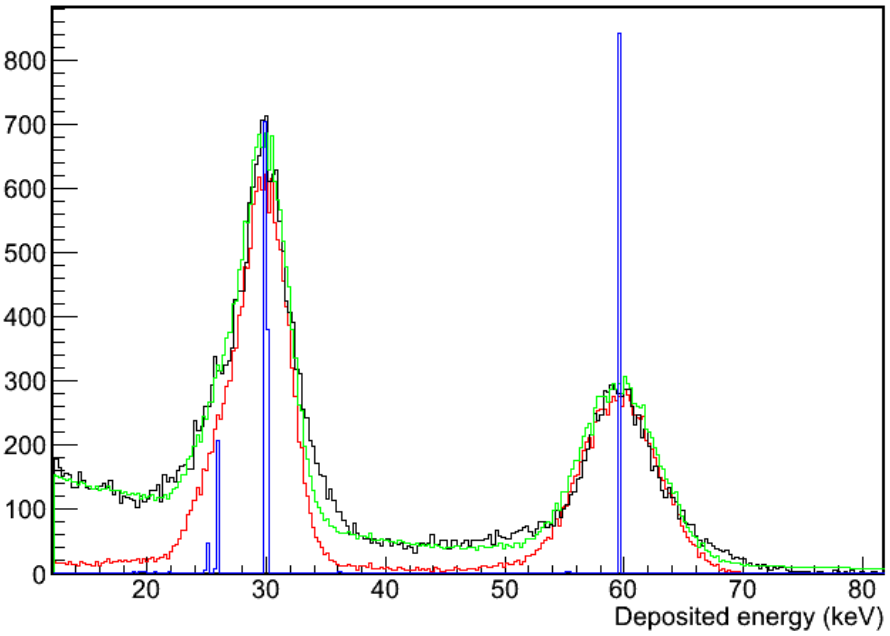

Figure 6.11: Experimental versus simulated ^{241}Am γ-rays spectrum in Xe at 4 bar.

Looking again at figure 6.10, the efficiency at ∼25 keV is still comparable with the efficiencies at 60 keV, while the intensity of the 26 keV line of the ^{241}Am source is 15 times lower. Therefore, in first approximation, its contribution to the total spectrum is negligible. From the simulated spectrum (blue line in figure 6.11), where only 59.54 keV gammas were launched, the relative weights of each contribution are easily identified since the energy resolution is ideal.

The mean free path for all the involved photons is large compared with the sensitive volume, with the exception of the 3 keV one. Thus all the escape peaks are relevant, with the exception of the $60 - 3$ keV peak and the 60 keV peak can be considered as a single peak for the fit. The same is not true for the fluorescence peaks which, to appear in the spectrum, need a primary interaction to happen out of the sensitive volume and the fluorescence photon to be captured by the narrow gas column over the micromegas. That is very unlikely in practice. So, to fit the large escape peak, two contributions are needed in 30 $(60 - 30)$ and 27 $(60 - 33)$ keV (escape peaks), but not in 33 keV (fluorescence peak).

The ideal spectrum directly obtained from the Monte Carlo can be convoluted to emulate the detector energy resolution and check if simulation certainly gives the relative weights for all these pieces of the fit. This is done to build the red line in figure 6.11, using a energy resolution depending on the energy as usual with the inverse of the square root. For a direct comparison the noise can be modelled with the addition of an exponential decay (green line). The energy resolutions used to convolute the peaks are 12% at 27 keV and 9% at 60 keV, which extrapolates to 1.4% at the $Q_{\beta\beta}$ value, a result surely limited by the noise.

6.3 The RESTSoft TPC simulation chain and Event Model.

The simulation of the physical processes that affect the ionization path in a gaseous chamber was the first motivation for RESTSolft, since they are not considered in general purpose codes. It includes the generation of primary charges, the diffusion and, eventually, the attachment along their drift to the mesh. It can be useful, in addition, some transformation to reproduce some limitations in time and spatial resolution simulating realistic readouts, as a kind of ideal pixelization. These transformations can be operated one after the other in clearly separated steps and by specialized classes which make up the RESTSoft TPC Simulation Chain. This is the modular philosophy that was advanced in the introduction to RESTSoft (section 6.1).

A transformations chain works better if is complemented with a versatile *Event Model*. The event model is the definition of the information which describes the event and is susceptible to be saved in disk for later manipulation or analysis. But furthermore, the event model is the way this selected information can change from one stage of the simulation to the other, the way we manage it and the relation between the different classes that hold it.

It was thought that the simplest, and so the most powerful, way to implement this would be to define a very basic class to be the object of all the methods involved in the TPC simulation chain, i.e. being input and output at the same time. This idea entails that such a class must be the most general and simplest possible description of a TPC event: a 3D charge distribution as a collection of hits. It will be shown how this description is suitable at the different stages of the TPC simulation chain. It is implemented in the class named *TRestPhysEvent* that contains *fNHits* hits, which are described in three *TArrayD* (double precision ROOT array class), for the hits position and one *TArrayI* (integer ROOT array) for the hits charge as multiplicity of the elementary charge; the total charge of the events is saved as well. The four arrays are easily and efficiently re-dimensioned if *fNHits* is changed thanks to the usage of the ROOT classes. The *TRestPhysEvent* class itself inherits from the *TObject* ROOT class, what means that it can be automatically serialized in ROOT trees and then saved as ROOT files.

6.3.1 Primary charge generation and *bridge* classes

Monte Carlo simulations usually give results in terms of energy depositions, however the transportation processes in the gas involve the electrons released by this energy which finally start the amplification in the micromegas. The generation of the primary charge requires an interpretation of the information obtained from the Monte Carlo program *X*, therefore the process is dependent on the origin of the data. A *bridge class*, *TX*, should be on charge of dealing with the Monte Carlo simulation output. Whatever the format it uses, it must be translated into data which follows RESTSoft conventions. That means that it should be rewritten as *TRestPhysEvents* or as another event class which must inherit from *TRestPhysEvent* (i.e. which at least contains a *TRestPhysEvent*). Finally *TX* has to generate the primary charges from the Monte Carlo available information so as to fill the charge array of the *TRestPhysEvent*.

The process by which the energy is translated into charge is, on the contrary, common. The translation into charge of an energy deposition is implemented in the *TRestCharge* class, the first stage of the TPC simulation chain. A database on W-values (the mean energy to free an ion electron pair, see section 4.1.1) is needed; *TRestCharge* creates a table whose values are taken from [115] and is able to calculate W for mixtures using a weighted sum rule (4.2). Since the primary generation charge process is not Poissonian (see section 4.1.2), in order to give a charge to the hit with energy deposition E, a Gaussian distribution with mean E/W and width

$$\sigma = (E/W) \cdot F \tag{6.1}$$

being F the Fano factor, is used to generate the amount of elementary charges of the hit (which can be zero).

6.3.2 Importation of a GEANT4 simulation.

The information per event described in sections 6.2.1 and 6.2.6 (see figure 6.7) is encrypted in binary files. When this event description is compared with the *TRestPhysEvent* definition a natural affinity is discovered because both make use of a collection of hits. But there are also differences since the GEANT4 description of the hit is more complex (energy process, track ID) and there is also an event's global description (the predefined interactions and types), information about the event origin and control parameters to recover statistics. A new event class is defined, *TRestG4Event*, which contains a *TRestPhysEvent* that will be used to hold the charge distribution, and the rest of information extracted from the Monte Carlo.

The main method of the *TGeant4* bridge-class is able to load from the binary outputs the information concerning one event and generate the associated *TRestG4event*. The positions of the GEANT4 hits are directly converted into those of the *TRestPhysEvents* hits. The energy deposition is used to generate primary

charges only if the responsible physical process is ionization or multiple scattering. Equally, the track ID can be used if only the main particle track is considered (or to apply another similar criteria). The total amount of primary charge is summed during the process and recorded. Case study's labelling and the initial vertex information are just pasted as new fields that make the elementary *TRestPhysEvent* evolve to a *TRestG4Event*. This way, apart from the size *fNHits*, the *TRestG4Event* has *fNInts* and a set of associated arrays of the same size to hold the *interactions' description* that was explained in section 6.2.6. The *TRestG4Event* is ready to be saved in a ROOT tree, for analysis that needs the whole GEANT4 information, or to continue to the following stage of the TPC simulation, since it contains a complete *TRestPhysEvent*.

TGeant4 can translate a binary output file in a ROOT file containing a tree of *TRestG4Events* and write reports concerning statistics during the process. Different output files can be combined if they correspond to parallel simulations. Once the information is written in this way, ROOT becomes a powerful tool to explore it and immediately produce plots. In addition, there exists a little version of *TGeant4* which is written as a ROOT macro, called *Out2REST.C*, that has almost all the functionality of *TGeant4* and is thought to be used even where the RESTSoft libraries have not been compiled (it needs only the *TRestG4Event* and *TRestPhysEvent* classes). It is useful when no more simulations stages are needed (as in the previous section examples), but more often it is used just for data format transformation before moving the data (together with statistics reports) from a cluster. That is convenient because, thanks to ROOT compression, even thought the ROOT files contains more information, they weight approximately one half than the binary ones. This macro also contains tools for typical fast analysis, as output spectra drawings, compilation and basic treatment (convolution for realistic energy resolution and energy calibration). Another set of macros, which work on the *TRestG4Event* tree, has been developed for fast analysis and are frequently used.

6.3.3 Simulation of drift effects and attachment.

If an event is written as a *TRestPhysEvent* (or any upgrade of this class) it is ready to be drifted by the *TRestDrift* class. This class treats electrons individually to emulate the plausible effects of the drift from the z position of the hit to the mesh level. Individual electron's paths are not simulated step by step, what would slow dramatically the data transformation. In fact, we are not interested in the path itself, but only in the final accumulated effect and, since the number of primary electrons is relatively hight (227 electrons in average for a typical ^{55}Fe X-ray in argon), the end of each electron independent story is just derived from the statistical description of the phenomenology, based in mean values and deviations.

The electric drift field is assumed by the drift algorithm to go in direction z, orthogonal to the micromegas mesh plane, which is expected to be at $z = 0$, and so the drifted distance is equal to the initial z of the electron, $d = z_0$. *TRestPhysEvent*

has its own methods to perform a translation or a rotation of the event that can be used in order to adapt it to the *TRestDrift* assumptions. The final z, z_f, for all the electrons will, of course, be the mesh level and, after the drift, this coordinate should be expressed as a time. However *TRestDrift* just adds the diffusion deviation Δ_z because of practical reasons (see section 6.3.5):

$$z_f = z_0 + \texttt{Gauss}\left(\sigma_l\sqrt{d}\right) \tag{6.2}$$

where $\texttt{Gauss}(x)$ is a value obtained from a Gaussian distribution centered in zero with $\sigma = x$ and σ_l is the longitudinal diffusion coefficient (see section 4.2.2). For the transversal deviation:

$$\Delta r = \texttt{Gauss}\left(\sigma_t\sqrt{d}\right); \tag{6.3}$$

$$x_f = x_0 + \Delta r\cos\phi, \qquad y_f = y_0 + \Delta r\sin\phi \tag{6.4}$$

where σ_t is the transversal diffusion coefficient and ϕ is randomly generated between $[0, 2\pi]$.

Similarly, if the attachment is considered, the definition of the electron mean free path in the gas (4.13), λ_{attach}, is directly applied to compute:

$$P_{\text{attach}} = 1 - \mathrm{e}^{-A\cdot d} \tag{6.5}$$

being $A = 1/\lambda_{\text{attach}}$ the attachment coefficient and P_{attach} the probability of the electron being attached along its drift path.

The coefficients used in these formulas can be loaded from the RESTSoft *Gas Data Base*, a collection of files with tables describing drift properties for customary or interesting gases. These files are product of MAGBOLTZ[150] calculations. Values for the drift velocity, the longitudinal and transversal diffusion coefficient, the Townsend coefficient and attachment coefficient are available for a range of electric drift field between 10^2 and 10^5 V/cm (the magnetic field is not considered). There is the *TMagbolzGas* bridge class designed to manage these data. It reads the data tables from a MAGBOLTZ ouput text file and load them as ROOT graphs (gas feature vs electric drift field). Using *TMagboltzGas* constructors together with the RESTSoft *Gas Data Base* users can load drift properties of pure gases, binary or ternary mixtures at different pressures as an interactive object. The *TRestDrift* class can adopt a *TMagboltzGas* as the drift gas definition (only an electric field is needed to choose all the gas drift properties). The parameters to be used by TRestDrift can be later modified or completely put by hand by means of *setter* methods.

The *TRestDrift* main method takes the *TRestPhysEvent* part of the event (for instance the *TRestPhysEvent* object inside a *TRestG4Event*) and only transforms it (see figure 6.12). The new *TRestPhysEvent* has as many hits as the total elementary charges, because every electron acquires a new final position, and all the new hits have charge one unit.

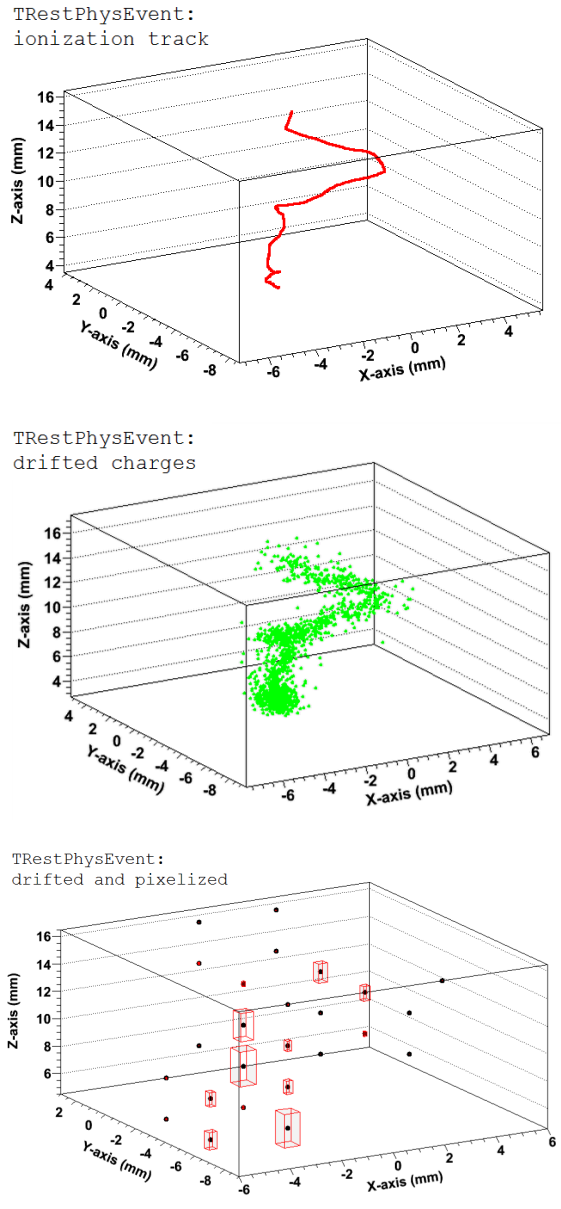

Figure 6.12: Evolution of a 60 keV electron event along the steps of the RESTSoft TPC simulation chain. Up: the electron path as registered by the GEANT4 application. All the hits that compose the track do not have to give rise to clusters, many of them are just marks to help to visualize the electron trajectory. The primary charge distribution is more evident after the addition of diffusion displacements (figure in the center). For instance, the charge accumulation at the track end, many times called *blob*, is clearly identified. Even an ideal read-out (1 mm pitch identically for the three dimensions), could not aspire to compose an event picture better than the representation of the figure at the bottom. The dots are *3D pixels* (see section 6.3.5) that were activated and the boxes have a size proportional to the pixel signal. All the drawings were produced from a *TRestPhysEvent*.

6.3.4 Mesh transparency and micromegas amplification.

Although the hits' final position z after the drift simulation was not explicitly *drifted* to the mesh, the electrons are supposed to pass through the micromegas mesh and, if they survived to the entrance, been amplified, one by one, in an avalanche process: that is the work done by the *TRestMM* (MicroMegas) class.

The way that avalanche products are gathered inducing signals in the readout depends on the micromegas specific design, X, and should be implemented in a specific method for a new event container class, *TRestDaqX*, which can differ fundamentally from *TRestPhysEvent*. However, the main methods for amplification and mesh transparency are common and therefore *TRestMM* is a general auxiliary class. In fact *TRestMM* can transform a *TRestPhysEvent* into a second one which reflects the effects of the micromegas transparency and/or amplification.

The mesh transparency is simulated by direct interpretation of the mesh transparency curve (see section 4.3) as the electron probability passing through the mesh into the amplification gap. This curve can be defined by the parameters of the associated fit formula (4.15); the values from figure 4.11 are loaded as default; or through file, by introducing experimental series that will be fitted. Once the fields ratio $FR = E_{drift}/E_{amplification}$ is given, the probability would be equal to the unity if $FR < FR_{end}$, being FR_{end} the FR at which the transparency plateau ends (defined as the point for which the fit equals to the unity); while if $FR > FR_{end}$ it is evaluated from the fit.

For simulations of the individual avalanches the Polya functions (see section 4.4.2) are implemented. The parameters they need, concerning the average gain and the relative variance for the individual avalanche, can be given directly or alternatively *TRestMM* can estimate them from a macroscopic reference, like the FWHM measured for a peak or a gain curve exponential fit. Another possibility is calculating them from the Townsend coefficient making use of the Legler-Alkhazov model (see section 4.4.2); *TRestMM* can reconstruct the electric field dependence of these parameters relying on a *TMagtbolzGas* and produce theoretical gain and resolution curves as those plotted in figure 6.13 (see section 4.4.2.1).

Alternatively, the avalanche can be simulated with a Gauss distribution for which some primary electrons can even been collected in groups. This practice would dramatically reduce the simulation time consumption. The avalanche must be modelled with the Polya functions, but the question is when do they produce results that are essentially different from those obtained with the much "cheaper" Gaussian model. We tried to illustrate that in figure 6.14 which shows distributions of avalanche yields summed for several values of N, the number of initial electrons.

The avalanches are obtained from Polya functions using $m = 2$, relative variance $b = 1/m$, which, we can see from figure 6.13 right, is actually an unfavourable case, i.e. with single avalanche distribution very different from a Gaussian, because typical values from argon with 2% isobutane lie in the range $2 < m < 3.5$. It can

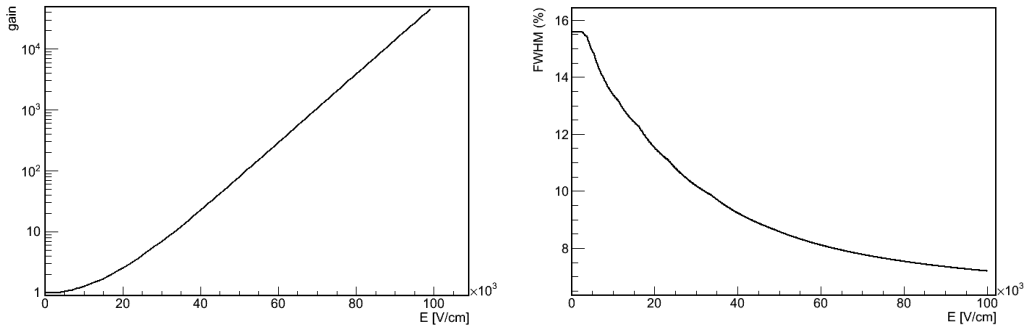

Figure 6.13: Gain (left) and resolution (rigth) curves obtained by the TRestMM class using MAGBOLTZ resuls for Ar with 2% isobutano at 1 bar.

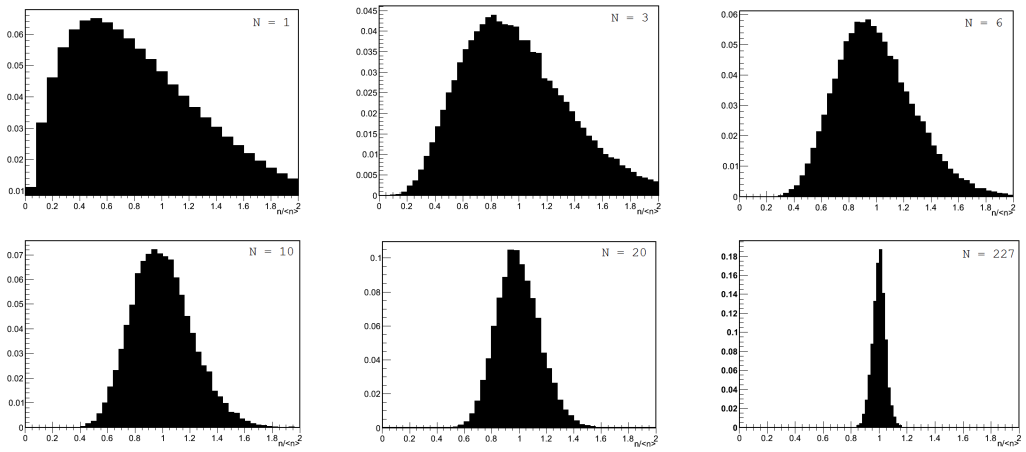

Figure 6.14: Distributions of the sum of N avalanches yield with single avalanche simulated with a Polya($m = 2, \bar{N} = 100$).

be clearly appreciate how the Central Limit Theorem of Statistics works and the accumulated avalanches yield distribution approaches to a Gaussian as N grows up. It could be said that, if the number of primary electrons collected by a pixel (or any kind or readout segmentation unity) is higher than 20, the expected signal strength distribution has a Gaussian behavior. The only case it can be worth simulating the proper Polya distribution is that of a low energy signal which triggers a high multiplicity event, as can be the passing of MIPs or a directional Dark Matter TPC.

6.3.5 Pixelization.

The last goal of the simulation is often to produce the information that would really be available, even though in an ideal TPC, in order to make a meaningful analysis. That would require a full description of the read-out working and electronics (see

section 6.4 and chapter 9 for an example of such kind of approach) which may have not being defined at all, or simply be beyond our interest. However, at least restrictions in 3D spacial resolution are usually imposed. This position assumes that the TPC read-out has ideally reacted to the stimulation (the drifted *TRestPhysEvent*) and, in addition, the off-line analysis has properly reconstructed the event as a 3D charge distribution, but with a limited resolution.

The *TRestPixel* class is often the last link in the RESTSoft TPC simulation chain and, again, works performing a transformation in the necessary *TRestPhysEvent*. A 3D net is built from the definition of a *3D pixel* which is delimited by the three independent dimension resolutions $\mathrm{d}x$, $\mathrm{d}y$ and $\mathrm{d}z$. The new hits have the position of the 3D pixel center and the charge contained inside them.

Because small pixel sizes are frequently used, directly building such a 3D net would cause memory troubles, the algorithm works with a different philosophy that is slower but optimizes memory consumption. It starts with the first hit of the input *TRestPhysEvent*, it identifies the associated 3D pixel and creates the first hit of the output *TRestPhysEvent*. It goes on, hit by hit, gathering the charge for this pixel until it recognizes a new 3D pixel has been invaded, and then adds a new hit to the output event. Every time this happens, the algorithm has to check that the new 3D pixel had not already been activated and, in that case, just adds new charges to it. This method has also the advantage that the chronological order of the pixels is conserved, what certainly is not the kind of information available in a common TPC, but can be of interest for some kind of investigations.

The resulting event is once again a *TRestPhysEvent*, a collection of hits containing elementary charges, but with regularly restricted 3D positions (see figure 6.12). The amount of hits has been dramatically reduced, and so the disk space and also the computing time in later analysis; but the effects of diffusion simulated by each independent electron are fully reflected.

At this point it must be clear why working with *TRestPhysEvent*, or other classes which inherit from it, is desirable: this way the TPC simulation chain classes can directly deal with it. Finally, there must be a program where these methods sequentially act on the data; following the RESTSoft event model philosophy data from different origins can naturally be mixed and compared. The program can load data from some simulation and complete the data whole transformation directly for its analysis (see sketch in figure 6.15).

Besides the chain can be implemented so as to generate data tree-like structures, for instance, from one simulated event a set of drifted events can be produced in different drift conditions or gases; and each subsequent one, can give rise as well to a new set where different read-out capabilities are tried (see figure 6.16). In each step all the original information can be transferred to the later one by using a big class (always containing a *TRestPhysEvent*) or, on the contrary, a different class can be used for description of each step event with only the relevant information at this point (perhaps only the *TRestPhysEvent*), and one can always browse between

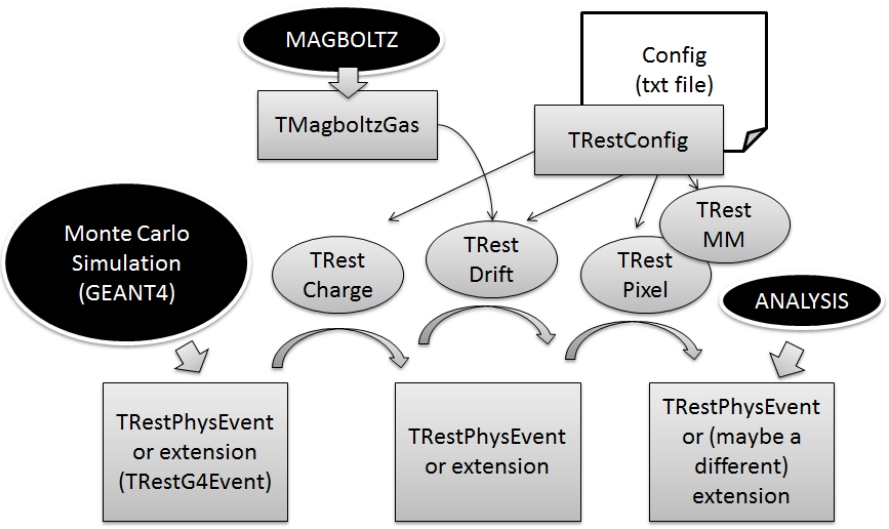

Figure 6.15: Sketch of a program implementing a serial TPC simulation chain.

the associated events. In the next chapter some examples of these kind of uses are described.

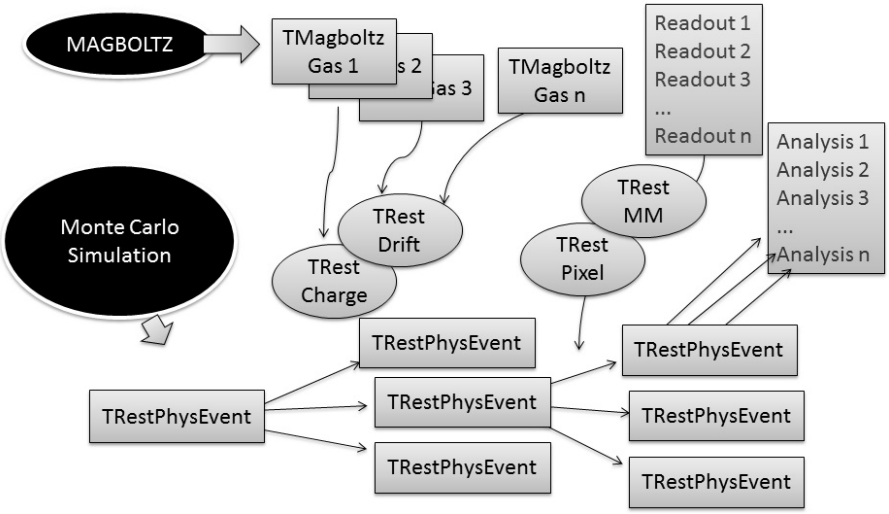

Figure 6.16: Sketch of a program implementing a tree-like TPC simulation chain.

6.4 Simulation of electronic signals.

Sometimes the experiment analysis works at lower level than that of reconstructed events, for instance to apply *pulse shape analysis*. That forces the simulation to perform a new step in order to generate the electronic signals induced in the read-out electrodes. This way a new reconstruction algorithm can be trained with simulated

low level data, or an already existing analysis can be indistinctly used with both experimental or simulated data for a direct comparison (see chapter 9).

The number and features of the induced signals will depend on the specific read-out design and electronic set-up, *X*. That is the end of the *TRestPhysEvent* class domain, which must give place to a specific holder class *TRestDaqXevent*. However, the basic process is again common: a certain time distribution, which describes the arrival of the charges to or near the electrode, should generate an electronic signal, which could be integrated (giving a number) or recorded (producing a pulse).

TPulseShaping is the class which is able to generate an electronic pulse from a given input intensity time signal, therefore it simulates the work done by a preamplifier followed by a time-amplifier, or shaper; i.e. the typical read-out electronic chain. The class was adapted to RESTSoft from an original program by Javier Galán. It has two alternative signal generation algorithms: pulse generation by solving the associated virtual RLC circuit or pulse construction by convolution with the typical amplifier response function. The former is faster and has the advantage that all their parameters are real numbers which can be continuously adjusted for fitting, while the latter is more intuitive and easily predictable and can be assigned to a generic type of shaper.

6.4.1 Generation of electronic pulses by RLC circuit solving.

This method was already written in the original routine by J. Galán and is deeper explained in [187]. *TPulseShaping* deduces the output pulse $v(t)$ by solving the second order differential equation that describes a virtual RLC circuit:

$$\frac{1}{\omega_C}\frac{\mathrm{d}^2 v(t)}{\mathrm{d}t^2} + \frac{\mathrm{d}v(t)}{\mathrm{d}t} + \omega_L v(t) = R\frac{\mathrm{d}i(t)}{\mathrm{d}t} \tag{6.6}$$

where $i(t)$ is the incoming intensity pulse, closely related with the distribution of the time arrivals of charges to the electrode, which is the input to *TPulseShaping*. The algorithm parameter R can be absorbed by the electronics gain, which is a configuration parameter of TPulseShaping. The other ω_C and ω_L come from the characteristic times of the circuit and determine the pulse shape; the former has a direct effect on the rise of the pulse, while the second in its fall.

J. Galán composed tables with the values of both frequencies which fit the pulses produced by ^{55}Fe X-rays (in principle, point-like events with ideal $i(t)$) in a CAST micromegas detector for the different settings of an ORTEC 474 Timing Amplifier. These tables are included in TPulseShaping, but they are only valid for the same electronic chain used during the test: an ORTEC 142B Preamplifier followed by the previously cited amplifier.

6.4.2 Generation of electronic pulses by convolution with the response function.

The output signal $v(t)$ can be produced from the stimulation signal $i(t)$, induced in the electrodes, from the characteristic response of a generic time amplifier, or *shaper*. In this section we follow chapter 6 of [116]. For a linear and causal system:

$$v(t) = \int_0^t w(t-t')i(t')\,\mathrm{d}t' \tag{6.7}$$

where $w(t)$ is the *delta response* of the system, i.e. $v(t) = w(t)$ if $i(t) = \delta(t)$ the Dirac function; in other words, it is the response of the shaper to an standard fast pulse. The delta response is customarily factorized as $w(t) = gh(t)$ with $h(t)$ the delta response normalized to have height the unity. Thus g is called the *sensitivity* of the *charge amplifier* because, if $i(t)$ is narrow compared with $h(t)$, then

$$v(t) = g\int_0^t h(t-t')i(t')\,\mathrm{d}t' \approx gh(t)\int_0^t i(t')\,\mathrm{d}t' = gh(t)\cdot Q \tag{6.8}$$

and the peak value of the shaped signal is proportional to the total charge induced in the electrode.

TPulseShaper allows to define the delta response functions of ideal n-degree *unipolar* and *bipolar* shapers (which are plotted inf figure 6.17):

$$h_{uni}(t) = \mathrm{e}^n\left(\frac{t}{n\tau}\right)^n \mathrm{e}^{-\frac{t}{\tau}}\Theta(t) \tag{6.9}$$

$$h_{bi}(t) = \frac{\mathrm{e}^r}{\sqrt{n}}\left(n-\frac{t}{\tau}\right)\left(\frac{t}{r\tau}\right)^{n-1} \mathrm{e}^{-\frac{t}{\tau}}\Theta(t) \tag{6.10}$$

where τ is the *shaping time* constant, $r = n - \sqrt{n}$ and $\Theta(t)$ is the step function so as to assure the causality of the system. These functions peak at $t_p = n\tau$ (unipolar) and $t_p = r\tau$ (bipolar, with $n > 1$). It can be more convenient to parametrize them as a function of their *peaking time* constant (an alternative definition also considered in TPulseShaper):

$$h_{uni}(t) = \left(\frac{t}{t_p}\right)^n \mathrm{e}^{n(1-t/t_p)}\Theta(t) \tag{6.11}$$

$$h_{bi}(t) = \frac{1}{\sqrt{n}}\left(n-\frac{rt}{t_p}\right)\left(\frac{t}{t_p}\right)^{n-1} \mathrm{e}^{r(1-t/t_p)}\Theta(t) \tag{6.12}$$

The sensitivity, g, coming for the ideal circuits is not presented as it is, in practice, absorbed by the gain of our virtual shaper.

Regarding the parameters' settings, t_p is obviously related with the *rise time* of the pulse and is the shorter semi-width of the response function; therefore it is

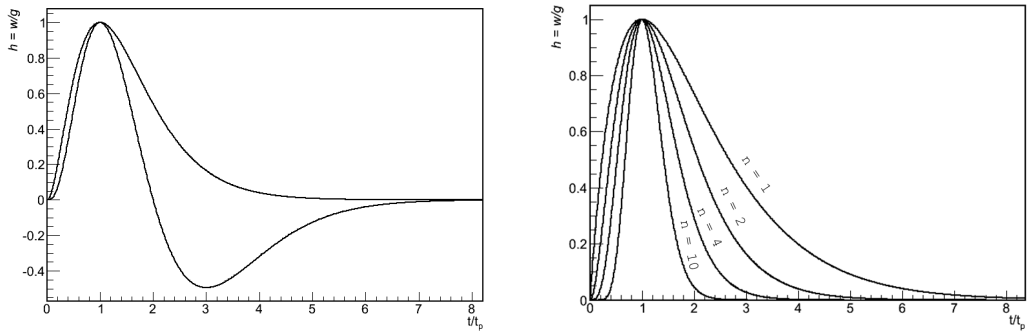

Figure 6.17: Left: unipolar (n = 2) and bipolar (n = 4) delta responses. Rigth: unipolar delta responses for several values of n.

the time reference to compare with the duration of the stimulation signal which, if comparable to t_p, can make the approximation 6.8 not valid and the condition of charge amplification would be lost, what is called *ballistic deficit* (see figure 6.18 left). The asymmetry of the pulse is related with n, more Gaussian the peak as higher the n (see figure 6.17 right).

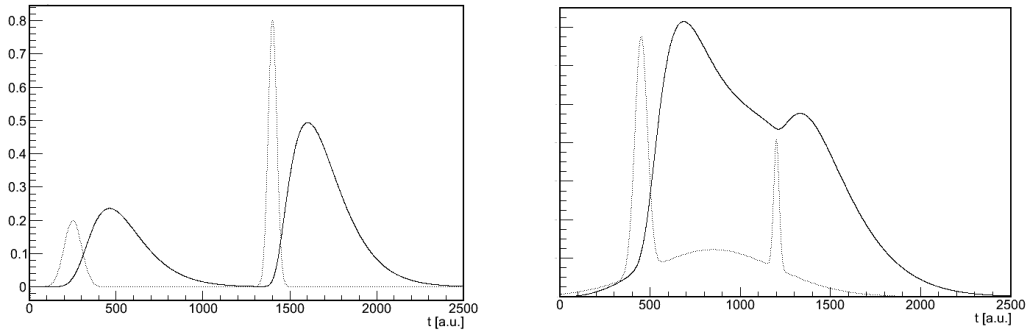

Figure 6.18: Examples of $i(t)$ and $v(t)$ drawn together after simulating an unipolar shaper with n = 2 (see figure 6.17) with $t_p = 200$ a.u. Gaussian distributions are used as the typical shape of signals induced by point-like clusters after drift diffusion. Left: shaper response to two gaussian clusters with the same area (charge) equal to 0.5 a.u., but different widths ($\sigma = 50$ and $\sigma = 25$). The second stimulation pulse is fast enough and the shaper pulse has the proper height value, while the first one is much shorter due to the ballistic deficit. Rigth: the same simulated shaper dealing with a more complex event.

6.4.3 TRestShaper.

TPulseShaping is a relatively low level class, derived from a simple program, with just the pulses as input and output. It is desirable that it keeps being so simple, however it is convenient to have a more powerful interface to join the simulation chain. *TRestShaper* can control *TPulseShaping* incorporating more advanced options (virtual shaper description, noise addition, trigger position, pulse array preparation, etc.), using *TRestConfig* for shaping configuration by file, dealing with holder classes like *TRestPhysEvent* or *TRestDaqXevent*, instead of only pulses in arrays, or with an intermediate preamplifier pulse.

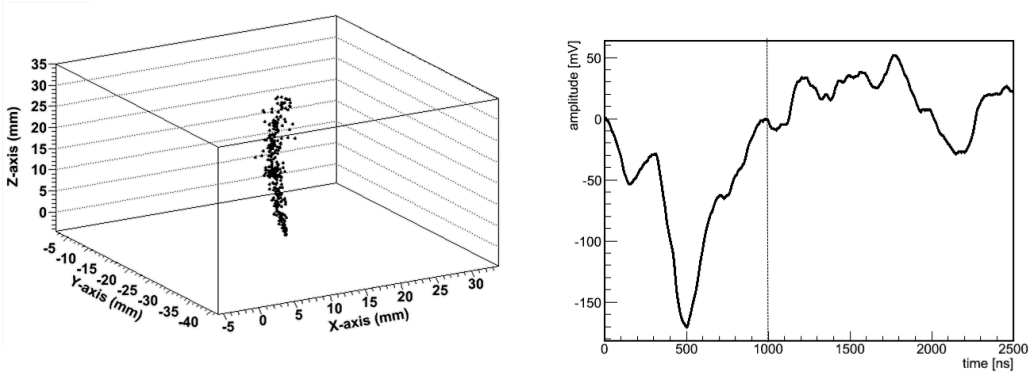

Figure 6.19: Left: an initial 3D charge distribution (from a drifted *TRestPhysEvent*), with a long time structure and the resulting pulse (rigth) using *TRestShaper*. The drift time distribution of the primary charges takes only the first 1 μs long; *TRestShaper* configuration is producing a quite bad signal to noise ratio. With a short shaping time of 50 ns (optimized for X-rays), the simulated shaper suffers of severe ballistic deficit before that MIP signal, and only a casual charge accumulation in the center of the event 3D structure (likely a δ-ray) was able to generate a peak.

Chapter 7

Applications of RESTSoft on High Level Analysis Challenges.

Contents

7.1 Electron/recoil discrimination with a Dark Matter TPC (TREX-DM).

Even though the ultimate motivation of a TPC for DM search is the recognition of the directional signature (see section 1.2.2.2), a chamber operating at no too low pressure and working as a proportional counter could be a milestone towards the demonstration of the technique, if it would be able to prove higher discrimination capabilities with a low energy threshold. That was the first scenario where RESTSoft was applied, and it can be a representative example of a project based on RESTSoft libreries. The work is situated inside the Dark Matter section of TREX (TPC's for Rare Events Experiments) R&D project([1]).

7.1.1 Project architecture.

The programs used for the primordial Monte Carlo simulation of the two kind of events that would be faced are different: SRIM (see section 3.1.5) for nuclear recoils (the signal) and the GEANT4 application (see section 6.2) for the electrons, which would had been produced by γ, (background). The introduction of SRIM requires a

RESTSoft *bridge*-class, TSrim (in analogy with *TGeant4*, presented in section 6.3.2) due to F.J. Iguaz, which can configure and launch SRIM and interpret its output. It contains the already mentioned (see section 3.1.5.1) algorithm for the complex simulation to construct the complete recoil with their secondary branches (see figure 7.1 left) and finally produces events which are saved as *TRestRecoil*, an extension of *TRestPhysEvent* (as *TRestG4Event* in section 6.3.2).

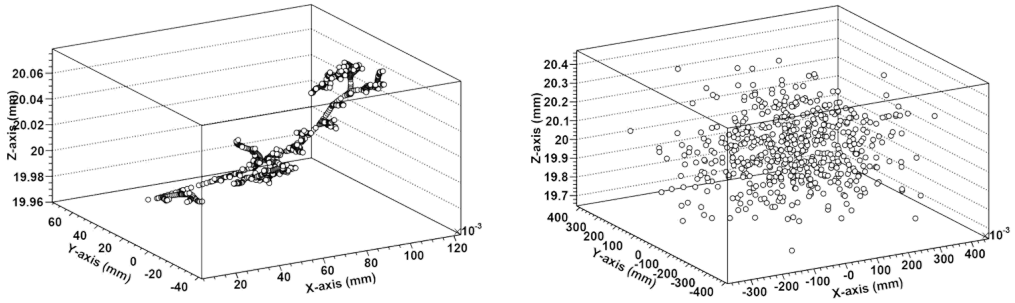

Figure 7.1: A 40 keV nuclear recoil in Ar at 1 atm before (left) and after (right) the diffusion process along 2 cm drift using $\sigma = 100\,\mu$m cm$^{1/2}$ as transversal and longitudinal diffusion coefficients.

Since then, the RESTSoft simulation chain (section 7.3) is common up to both kind of events are ready for analysis (see figure 7.2). The program is not typically launched in such a linear way, but in a tree-like structure to compare different drift properties, pixel sizes and chamber heights, as in figure 6.16. The analysis object (in this preliminary study) is a TResPhysEvent which has been pixelized.

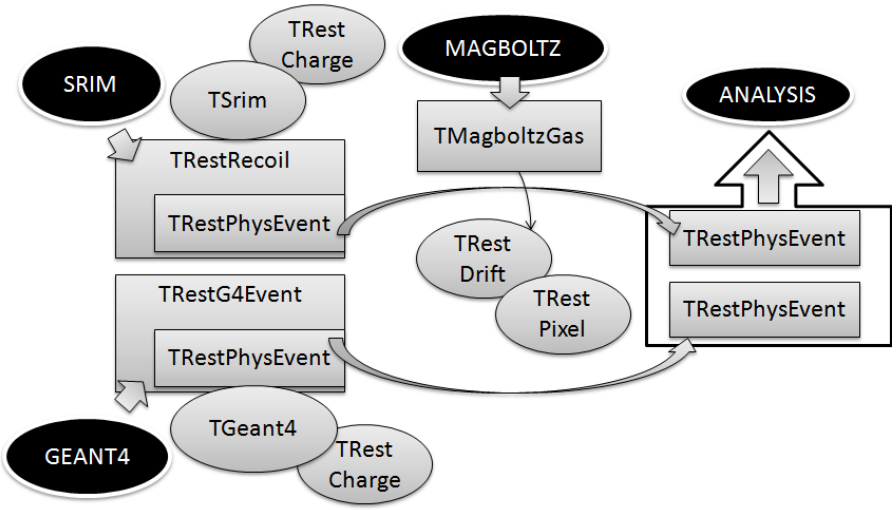

Figure 7.2: Sketch of the program. Note how TSrim and *TGeant4* make different use of TRestCharge to produce the *TRestPhysEvent* needed to start the chamber simulation chain.

7.1.2 Preliminary discussion of the scenario.

We will study a chamber at atmospheric pressure and a 3-d pixel size of 300 μm (ideally equal in the three dimensions), that was the pitch in the first CAST micromegas. In such a chamber the nuclear recoil's topology information has been sacrificed (see figures 7.1 right and 7.3), indeed, the absence of any topology can be considered as the recoil signature. A three dimension gaussian density distribution, product of the diffusion along the drift, must be the expected signal, like if originated by a point-like event. In contrast, for a γ/electron event we expect any topology mark or, in the case diffusion and pixelization, or just bad luck, has washed out, perhaps a deviation in the event size can be detected (see figure 7.4).

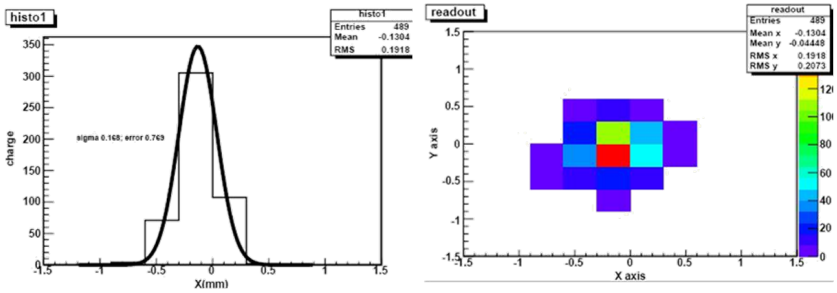

Figure 7.3: The nuclear recoil of figure 7.1 as it would be seen by our ideal read-out. There would be three axis views, but them all are practically like the one on the left.

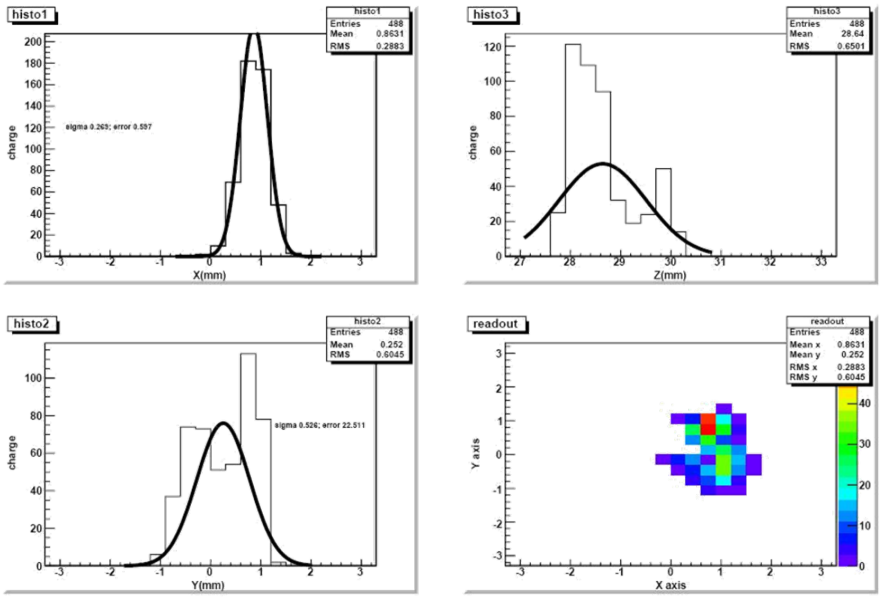

Figure 7.4: Ideal read-out views for a 12 keV electron event, that is the electron equivalent energy for a 40 keV recoil.

The size-energy correlation is an obvious possibility to distinguish recoils from electrons, though the quenching of the primary charge generation of recoils[1] makes the recoils face less energetic (and so shorter) electron tracks. Because of the chaotic path of the low energy electrons (see figure 6.1 right), the definition of the size can strongly influence its performance as discriminators. For instance, the ranges of 3.4 have a wide distribution, in addition skewed to lower values. A closely related observable implemented for a pixelized event, the longest distance between pixels, R_{max}, is studied in the figure 7.5 left. It looks like 1-dimension observables are giving an incomplete description of the size; the 3-d multiplicity (the number or active 3-d pixels) has a narrower distribution well separated from zero (figure 7.5 right) and a lineal dependency with energy for both kind of events (figure 7.6).

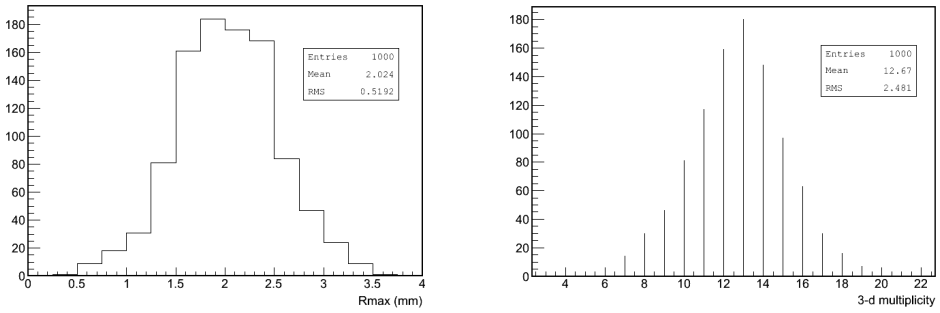

Figure 7.5: Distributions of the longest segment, R_{max}, and the event volume, 3-d multiplicity, computed for 12 keV electrons without simulation of diffusion.

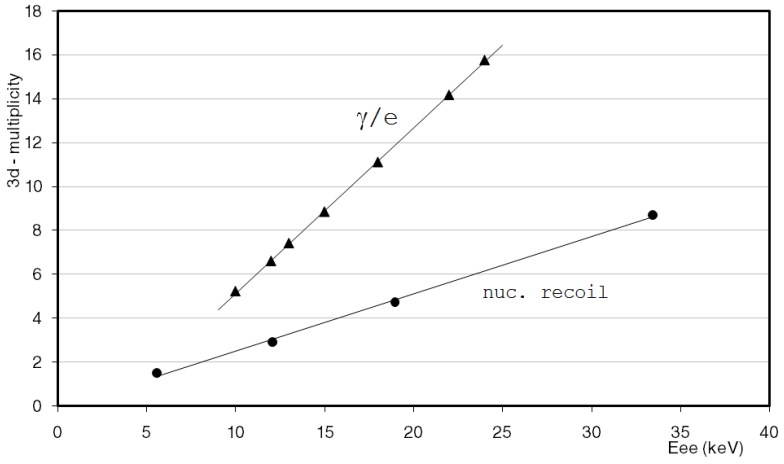

Figure 7.6: Linear behavior of the event volume calculated as the 3-d multiplicity. To show it clearer the pixel used for the recoils has been reduced from 300 to 50 μm side.

[1] The issue has already been studied inside RESTSoft in section 3.1.5.1.

The σ_x obtained from a fit of the partial charge distribution is a natural measurement of the size for a small diffused event; moreover the quality of the fit is significant as the similarity degree with a gaussian shape, and then a measurement of the topology residue. Figure 7.7 shows the mean values of σ_x as a function of the drifted distance root squared for a pair of series of recoils and electrons with equivalent energies. The series follows a a linear dependency with slope similar to σ (the used diffusion coefficient), that is the minimum size allowed by diffusion, except when the finite size of the event path becomes no negligible.

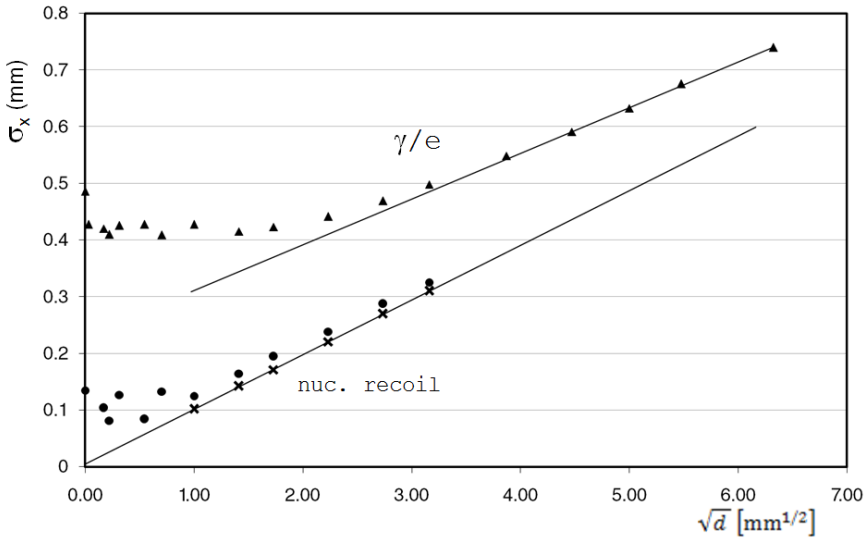

Figure 7.7: Event size, as σ_x, as function of the drifted distance for 12 keV electrons (triangles) and 40 keV recoils (circles). The recoils tendency line has been obtained by fitting the recoils mean values for distributions before pixelization (crosses). From the fit $\sigma = 96.5\,\mu$m cm$^{1/2}$ results as slope ($\sigma = 100\,\mu$m cm$^{1/2}$ was used).

We found that, for a given diffusion coefficient and an electron typical size (that is to say, for an energy), there is a limit for the chamber height since recoils charge distributions, after drifting that distance, get a size that is not smaller than electrons R_{max}. We surely could still distinguish attending to the fit quality; however if one tries to define the condition for the topology to be washed out as the drift distance that produces a mean diffusion comparable to the event size:

$$\sigma\sqrt{d_{max}} \approx R_{max} \tag{7.1}$$

what we found to be essentially the same condition above.

Looking how both tendency lines still keep rather separated during a long way, one immediately would think in the possibility of an absolute z measurement so as to apply a size discrimination criterion dependent on the drift distance. Unfortunately it seems there is a fundamental conflict between such a measurement and

the extremely good diffusion properties needed, because absolute z measurement approaches use to be related with primary light detection, what usually rejects the use of quenching additives; besides high gain is needed for DM searches low energy threshold, while high intensity signal is required for primary light detection.

The points in the plot of figure 7.7 are just the mean values; the electrons distributions extend deep down to the recoils line. The situation is more clearly showed in figure 7.8, where the event drift distance has been selected randomly inside a 10 cm height chamber. The recoils signal zone is well defined as the limitation for the chamber height, almost independent of the energy once the mean diffusion distance associated with it is higher than the electron path length.

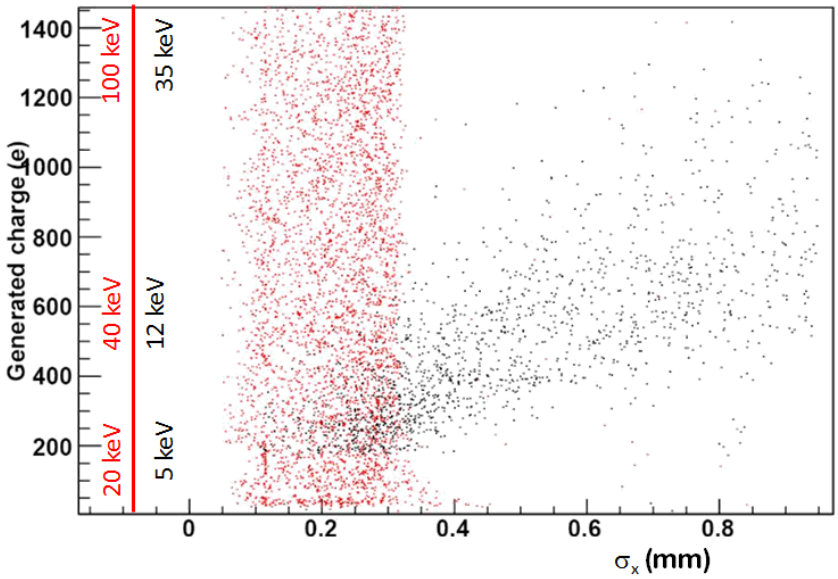

Figure 7.8: Discrimination plot for the observable σ_x for a 10 cm height chamber using $\sigma = 100\,\mu$m cm$^{1/2}$. Recoils are presented in red and electrons in black. The Y axis is the energy measurement as the number of primary charges, auxiliary energy equivalent axis are drawn for both kind of events.

7.1.3 Preliminary results.

From simulations like the one in figure 7.8, the discrimination capabilities of the chamber as a function of the event energy is calculated by applying a size cut with the size defined as the smallest σ obtained from the three dimensions fits. The *discrimination power* is expressed as $1 - rejection$ being *rejection* the ratio of γ/electron events rejected by the size-cut. Therefore the discrimination power is the probability of a γ/electron event invading the zone defined for the nuclear recoils. The simulations were carried out for two different chambers:

- A CAST-like chamber (see section 8.2), with 300 μm pixel side and 3 cm height, working at atmospheric pressure with the CAST gas slightly modified to improve diffusion properties: Ar/iC$_4$H$_{10}$/CF$_4$ 90/5/5%, which, according to MAGBOLTZ, gives 268.8 and 136.2 μm cm$^{1/2}$ as transversal and longitudinal diffusion σ's for drift fields at 700 V/cm. The goal of this simulation is to check the possibilities of a chamber of straight forward construction.

- The previous scenario is modified for a bit more ambitious DM experiment: the chamber height is enhanced to 10 cm, but we use a really good gas with $\sigma = 100\,\mu$m cm$^{1/2}$ for both directions. This value is not completely unrealistic (see figure 7.11).

The resulting plot (figure 7.9) shows how the good diffusion is capital, allowing to improve the background rejection even with a more than 3 times taller chamber for the second mixture.

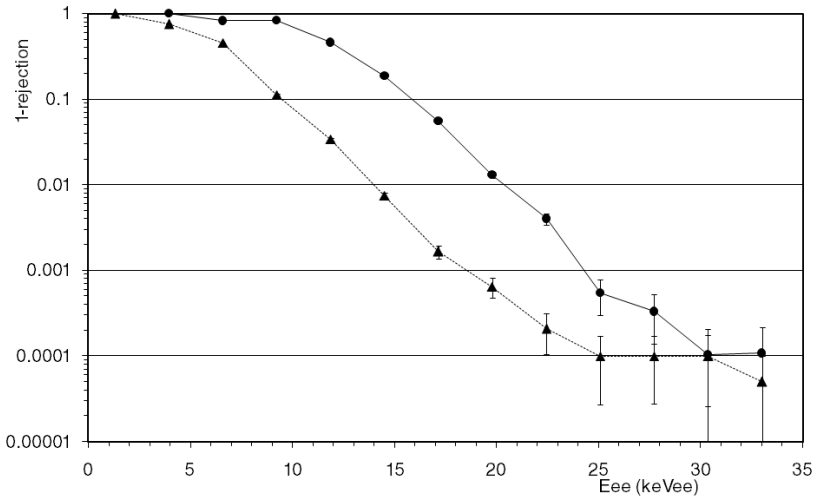

Figure 7.9: γ/electron events rejection via size cut with the cambers explained in the text: circles for a 3 cm height chamber filled with Ar/iC$_4$H$_{10}$/CF$_4$ 90/5/5% and triangles for another with 10 cm an and ideal $\sigma = 100\,\mu$m cm$^{1/2}$. 10^{-4} is the statistics limit for each group of electron events simulated.

7.1.4 A second discussion and optimization.

The previous result motivates a search of a real optimized mixture, the obvious election is Ar with addition of CF$_4$. We try to maximize the Ar mass which can contribute with acceptable background rejection with independently on the detector area. The consideration due in 7.1 can be useful here to define the *chamber discrimination height*, h_{disc}, as

$$h_{disc}(E_{ee}) \equiv \left(\frac{R_{max}}{\sigma}\right)^2 \tag{7.2}$$

which is explicitly defined for every pair of energy equivalent recoils and γ/electrons. Its meaning sounds quite ambiguous as *the height behind which most of the background events are positively rejected*. Looking at figures 7.7 and 7.10 looks like using the minimum σ is too restrictive and $R_{max} \approx 5 \times \sigma_{mininum}$ surely too permissive. However the use of a factor in the event topology typical size (there is a factor 25 between the two mentioned possible definitions of h_{disc}!) does not have influence for optimization purposes. We will focus in the 40 keV recoils, $E_{ee} = 12$ keV, to study h_{disc} being the amount of CF_4 our free parameter.

First, the RESTSoft program 7.2 is used again to characterize R_{max} as a function of the mixture. Remembering the Bethe-Bloch equation 3.5, the range is expected to inversely depend on Z:

$$R_{max} \approx \int_{\text{path}} \mathrm{d}x = \int_{E_0}^{0} \left(\frac{\mathrm{d}E}{\mathrm{d}x}\right)^{-1} \mathrm{d}E \propto \frac{1}{Z} \tag{7.3}$$

what is confirmed by the simulation after analysis (see figure 7.10) using $Z_{eff} \equiv 18x + 42(1-x)$ being x the Ar fraction in the mixture. The fit is:

$$R_{max} \simeq 42.069 \frac{1}{Z_{eff}} - 0.3256 \tag{7.4}$$

Then the addition of CF_4 has a negative effect since higher its concentration, shorter the electron track.

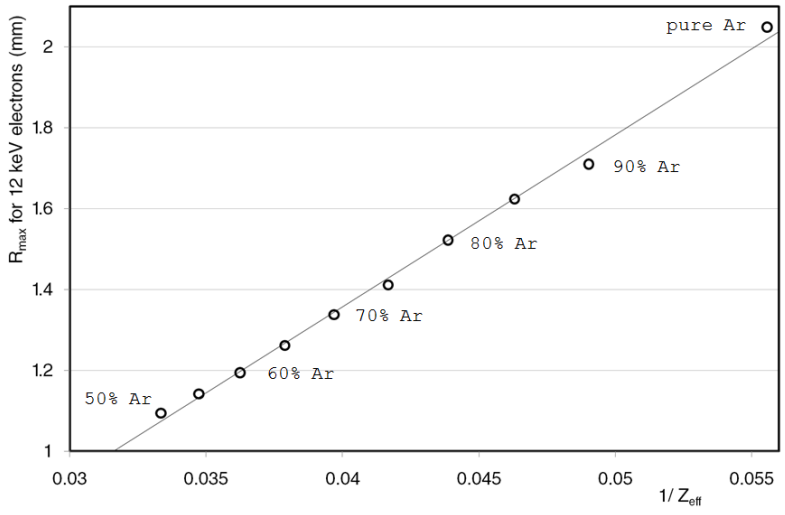

Figure 7.10: R_{max} for 12 keV electrons in Ar-CF_4 mixtures as function of the effective Z.

The RESTSoft gas database can be explored (with the help of *TMagboltzGas* class) to produce the figure 7.11. Because σ_T is always higher than σ_L, it is tried to be minimized as the main limitation due to diffusion. Then the σ_{min} series in the plot is the minimum σ_T achievable by tunning the electric drift field E_d, which is always a reasonable value, between 300 and 430 V/cm for low CF_4 concentrations (with exception of pure Ar), 620 V/cm for 20% of CF_4, around 900 V/cm near 30% and 1275 V/cm are needed to achieve these values between 40% and 50%. The $\sigma_m in$ serie can be fitted with a parabola in the range 50-90 % of Ar:

$$\sigma_{min}[\mu\text{m}] \simeq 866x^2 - 9.71x + 381.7 \tag{7.5}$$

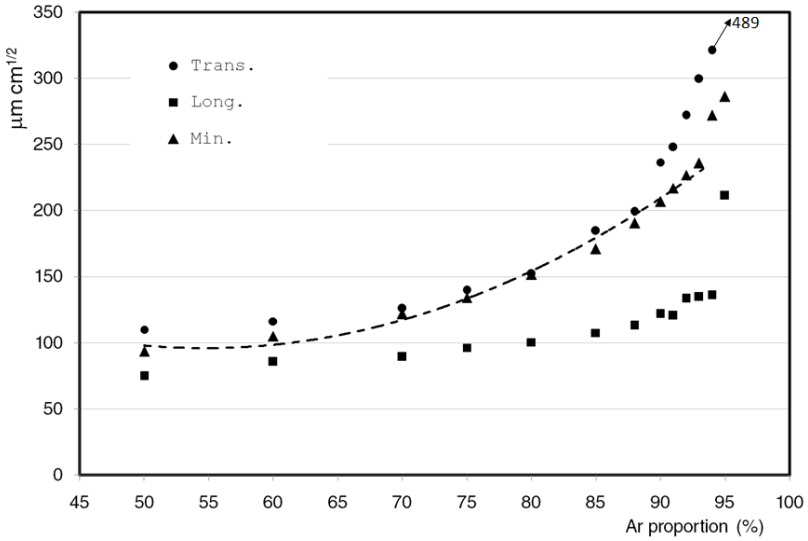

Figure 7.11: Diffusion σ's for Ar-CF_4 mixtures with electric field 700 V/cm. The minimum σ_{min} is the minimum achievable σ_T with a tunable electric field and it is fitted to (7.5).

Now we can draw h_{disc}(12 keV) as a function of x, the CF_4 ratio (figure 7.12 left) which basically maximizes the R_{max} $\sigma_m in$ ratio. In order to choose the better gas we must look for a maximum in the expression:

$$M_{act} \equiv x \cdot h_{disc} \tag{7.6}$$

that is proportional to the Ar mass achievable under our condition for good background rejection. Figure 7.12 right shows that it maximizes around Ar/CF_4 70/30.

A gas mixture very close to the optimum, Ar/CF_4 75/25, was used for a new simulated discrimination run in a chamber of 10 cm height for a direct comparison with the results of figure 7.9. As expected, the circles serie in figure 7.13 lies between both former results, not as good as the ideal mixture but notably better than the CAST-like chamber. The result is tried to be improved by applying event shape

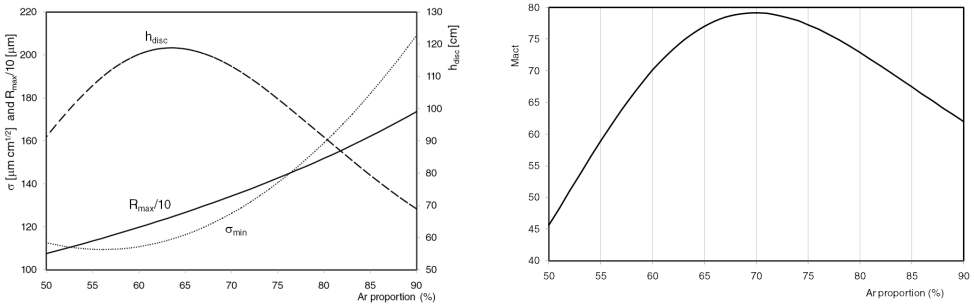

Figure 7.12: Left: chamber discrimination height build from R_{max} and $\sigma_m in$ ratio. Right: The active mass figure of merit.

based cuts and not only size based (the chamber is still far from our h_{disc}. The additional cuts are limits for the goodness of the three gaussian fits and the dispersion in the three sigma values. The effect of its application, after the size cuts, is plotted in figure 7.13 as the triangles serie. The conditions for shape allow sensible discrimination power at very low energies, when the electron track is still too short to be rejected by size; besides the shape discrimination power increases with energy.

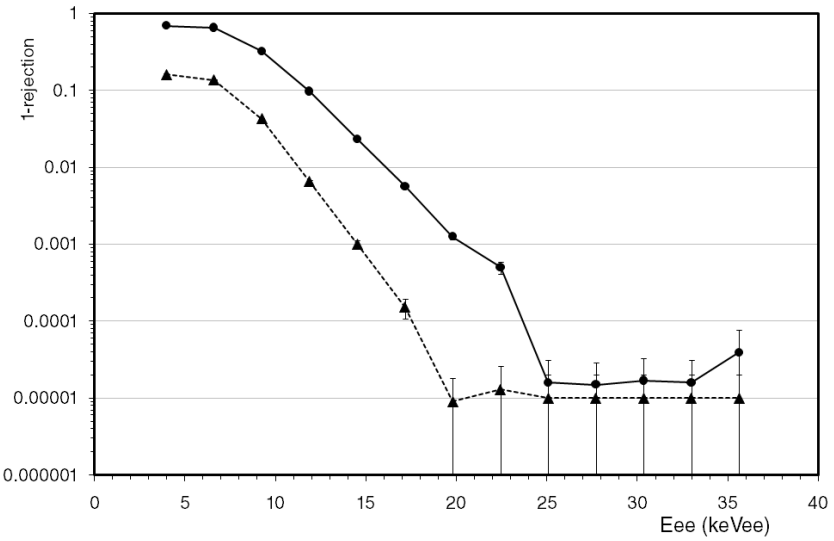

Figure 7.13: γ/electron events rejection for a 10 cm height chamber filled with Ar/CF_4 75/25 at atmospheric pressure using an electric drift field that minimizesσ_T. Circles: discrimination power only by size cut (biggest gauss from the fits); triangles: additional event shape cuts. 10^{-5} is the statistics limit for each group of electron events simulated.

The feasibility of such a mixture was checked experimentally, a little addition of a 2% of iC_4H_{10} improves the energy resolution and allows more lower values of HV_{mesh} (see section 4.4). The gain and energy resolution, even tough a bulk micromegas

was used, were found to be almost equivalent of those of usual Ar-iC_4H_{10} mixtures (see figure 7.14 and compare with plots in section 4.4).

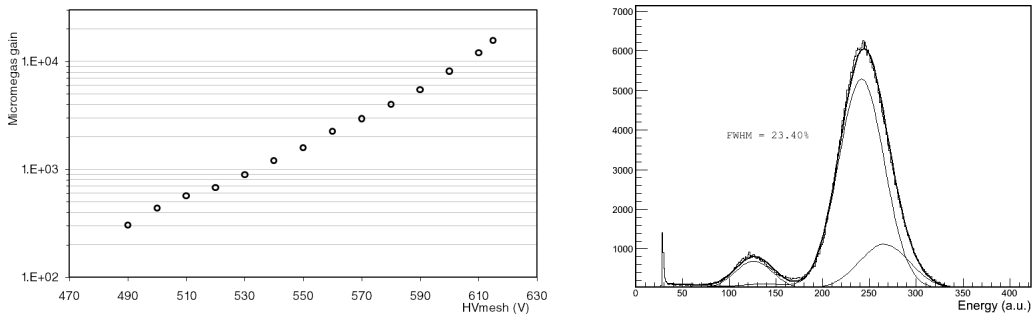

Figure 7.14: Performance of Ar/CF_4/iC_4H_{10} 73/25/2 in a bulk micromegas. Left: gain curve, with $E_{\text{drift}} = 800$ V/cm. The highest voltage point corresponds to the highest achievable stable gain. Right: resolution at optimum operational point: $E_{\text{drift}} = 600$ V/cm and $\text{HV}_{\text{mesh}} = 580$ V (Amplification gap is 128 μm).

7.1.5 Outlook.

The work summarized in this section represents just an starting point that shows optimistic prospects of electron/nueclear recoil discrimination at atmospheric pressure. The analysis is just outlined, and shows many common view points with the, much further developed, CAST analysis (see section 8.3) since essentially both select point-like events. The current goal of TREX-DM (motivated by the results summarized in chapter 10) is the commissioning of an enlarged CAST-like chamber (with a strips read-out very similar to CAST's, described in section 8.2) using T2K electronics (see section 5.5) for a real TPC performance in order to try some upgraded version of CAST analysis. The associated simulations (a mixture between CAST RESTSoft program and the version described in this section) are ongoing[2]. However, there is a fundamental difference between both analysis because for CAST X-rays are, by definition, not rejected. CAST analysis must be somehow (experimentally or with simulations) proved to be efficient for nuclear recoil events. The fully three dimensional observables, as the mentioned event volume, has not been systematically studied yet, and such study could conclude if a truly pixel read-out is required. An study following the same approach as this section has been recently published[188].

[2] J.G. Garza and F.J. Iguaz.

7.2 Background of a $\beta\beta0\nu$ HPGXe TPC (NEXT).

According to the HPGXe TPC Physic case discussed in section 1.2.1, only three processes are relevant for the background: the 2614.5 keV γ from the ^{208}Tl decay, the 2447.9 keV γ from the ^{214}Bi and the two simultaneous γ (1173 and 1332 keV) emitted in the ^{60}Co β-decay. RESTSoft has been used by the LFNA to develop and train topological algorithms for the discrimination of these events from the true $\beta\beta0\nu$ signal for the NEXT experiment. Once any version of the algorithms is operative it can be applied to simulations to study the nature and weight of the contributions of the background sources for different experiment set-up possibilities. The study is done over events simulated with the RESTSoft GEANT4 application in Xe at 10 bar using Decay0 for event generation (see section 6.2) as pixelized events, after the transformation by the RESTSoft TPC simulation chain (see section 7.3), assuming absolute z recognition capabilities. Here only a draft will be presented to show of the use of RESTSoft for high level analysis on events with topology[3].

7.2.1 Topological discrimination algorithm.

The topological signature of the $\beta\beta0\nu$ signal that of one event with one unique track presenting two denser ionization clouds, called *blobs*, in both track ends. Every algorithm must start with the event reconstruction and the recognition of these three aspects, which can be evaluated. The algorithm draws the event track (which should be the addition of two electron paths with a common vertex) following the denser ionization trajectory, as a set of segments and points that join the activated pixels. It finally finds the track ends, which should be associated with a charge accumulation point. Then, the track line, its length and the blobs coordinates are extracted (see figure 7.15).

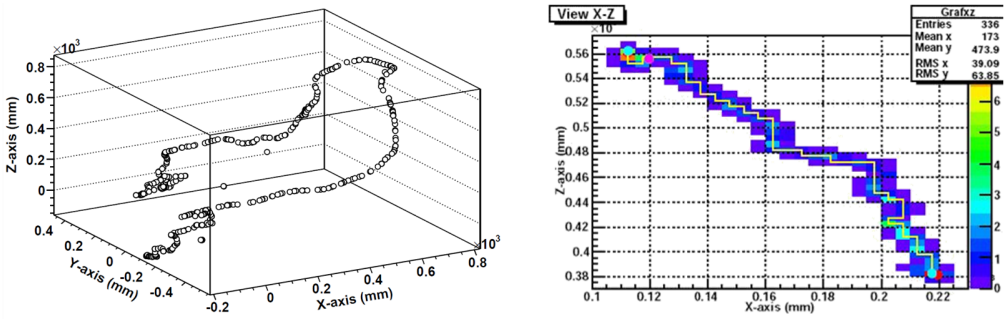

Figure 7.15: Left: A $\beta\beta0\nu$ event as is simulated by GEANT4, drawn as a set of energy deposition hits. Right: a $\beta\beta0\nu$ event reconstructed by the algorithm (only one of the three projection is showed).

[3] An extensive exposition of the pioneering work by F.J Iguaz can be found in [18], which has been continued by L. Seguí and G. Luzón in [19].

The event description delivered by the algorithm can be inexact even for true $\beta\beta0\nu$ events, because of *physical accidents* (bremsstrahlung secondary clusters, δ-rays and irregular electron paths producing fake blobs). Evaluating the quality of the reconstruction is an essential first step, which means a discrimination criteria by itself and, moreover, it is favour of a proper definition of the rest of discrimination criteria. The performance of any applicable cut is evaluated by the figure of merit $f \equiv \varepsilon\sqrt{F}$, where ε is the cut efficiency (when applied to signal events) and F is the achieved background reduction factor. The cuts often have several parameters whose values have strong influence in ε. Many times they depend also on the read-out and gas diffusion features and must be adjusted by patient trial and error process. The F depends also of the kind and source of background. The basic cuts defined are:

- **Goodness of track**: as explained above, this cut looks for a compromise between efficiency and becoming more selective with the shape of the event in order avoid the kind of accidents that permits the background events to fake the $\beta\beta0\nu$ signature. When that happens, background events tend to be more complex and worse described by the reconstruction algorithm. The evaluation of the goodness relies in the *covering* figure, that is the ratio of the total charge of the event respect the charge contained in the track (the charge accumulated by the pixels directly joined by the reconstructed trajectory and those pixels whose centers are closer than a given distance).

- **Fiducial cut**: The definition of a fiducial volume prevents background from inner surfaces contaminations. It needs the sacrifice of an active volume near the TPC cavity limits. The events with any deposit of charge closer than a given distance to the walls are cut.

- **Mono-track cut**: A segment, longer than a given value, between active pixels which does not pass through an active pixels make consider the event as containing more than one cluster. Ideally only mono-cluster events are expected. However simulations show that only 59% $\beta\beta0\nu$ are real mono-cluster events due to bremsstrahlung losses. Secondary clusters can be tolerated depending on its relative weight and proximity to the main track in order to optimize f.

- **Blobs cut**: The reconstruction algorithm delivers always two blob candidates. For background events at least one candidate is expected not to be a true blob. Alternative definitions of the goodness of the blob (mostly based in the density of the charge around their coordinates and their geometrical shape) can be used and combined to reject the event (see figure7.16).

7.2.2 Examples of background simulations.

The figure 7.16 right shows the background induced by a combination of 2614.5 keV ^{208}Tl and 2447.9 keV ^{214}Bi γ simulated as external environmental radiation over the TPC. The ^{214}Bi photo-peak is reduced mainly thanks to the blobs cut while

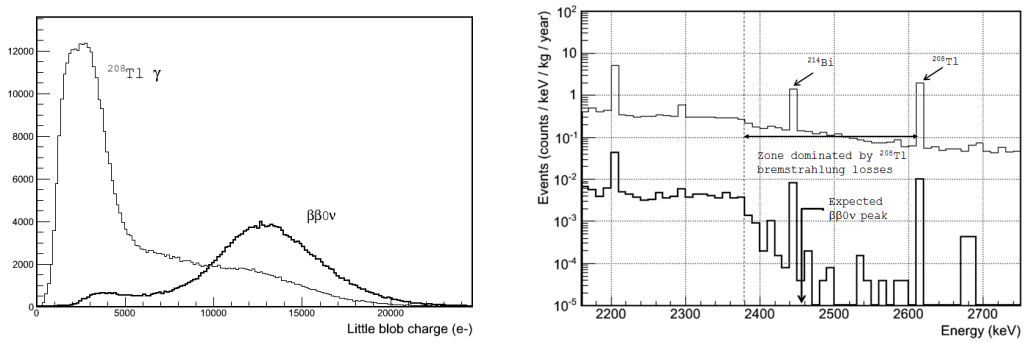

Figure 7.16: Left: charge evaluated for the smaller of the two blobs found by the algorithm for $\beta\beta0\nu$ events and ^{208}Tl events. Right: Effect of application of the cuts on a simulated background generated by a composition of ^{208}Tl and ^{214}Bi decays near the TPC (simulation and analysis performed by L. Seguí).

for ^{208}Tl the reduction is stronger because the range of interest (RoI) is situated between the ^{208}Tl photo-peak and Compton edge (see figure 7.16 right), what make a complex event needed to produce a count inside, therefore all the cuts are more active, somehow revealing these cases. These source of background can be simulated as a function of the shielding thickness covering the TPC, but then the impurities of ^{208}Tl, ^{214}Bi and ^{60}Co in the shielding material themselves must be simulated as well. The figure 7.17 show the simulation of superficial impurities in the interior of the TPC. These kind of simulation allow to define the experiment tolerance for the radioactivity of the materials.

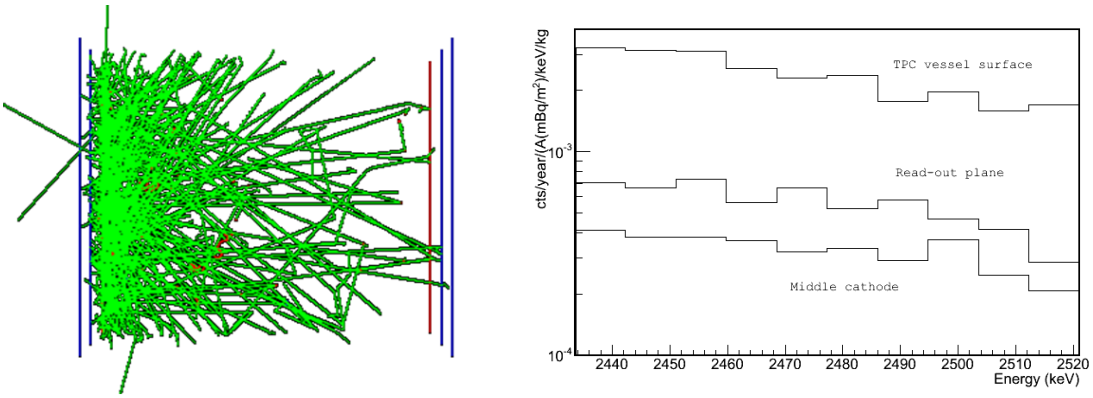

Figure 7.17: Left: GEANT4 view of a simulation of ^{208}Tl decays on the read-out plane of the TPC. Right: Final background levels from these kind of simulation for ^{208}Tl contamination on several inner surfaces of the detector as the function of the activity.

Another kind of analysis one can do with RESTSoft if the Casuistics of the background events (see section 6.2.6, trying to elaborate a portrait of the background nature for every case. A case recognition pattern has been implemented in the $\beta\beta$ version of the RESTSoft GEANT4 application to mark the these interesting cases: 1) Compton + photo-electric, no escape γ; 2) double Compton, one escape γ; 3) previously to interaction in the sensitive volume, there was a Compton in the TPC vessel (these event might be vetoed with an active veto); 4) single photo-electric event in the sensitive volume + energy radiated by bremsstrahlung to the vessel (these event might be vetoed with an active veto). The tab 7.1 contains the story description of the background induced by external ^{208}Tl γ flux for two different set-ups.

Physic case	only 3 cm vessel	5 cm vessel + 5 cm shielding
1	68%	67%
2	12%	9%
3	14%	18%
4	5%	3%

Table 7.1: Casuistic analysis for an external ^{208}Tl γ flux induced background in the HPGXe TPC with two different configurations of stainless steel vessel and lead shielding. The flags are explained in the test.

Note how the case 1, in principle a double cluster event, is dominating the background: that suggests that mono-cluster cut should increase its rejection power; however that can be not so easy as events so intriguing as the one of figure 7.18 occur.

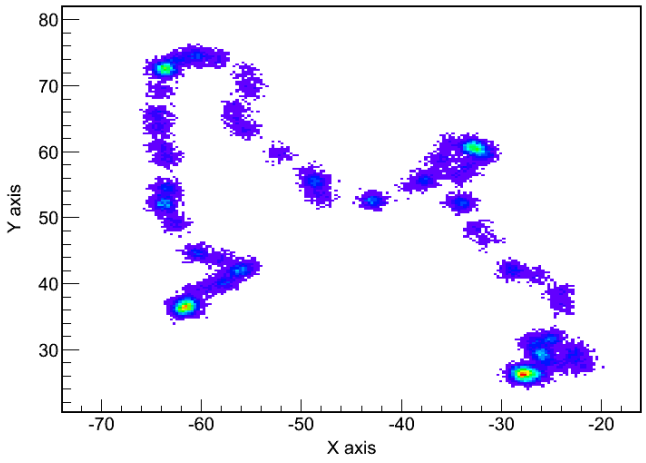

Figure 7.18: A ^{208}Tl γ producing a Compton cluster followed by a photo-electric interaction with radiation of energy by bremsstrahlung in that manner the whole deposition is situated in the $\beta\beta0\nu$ ROI.

Even when the secondary events (flag 3) are slightly increased with the shielding, most of the events surviving the cuts are still due to γ which are able to reach intact the TPC gas, therefore (unless a serious material contamination) increasing the shielding thickness is still favorable. The performance of an hypothetical active vessel is still low (according to the small percentage of event with flags 3 and 4.

7.3 Importation of real events into the RESTSoft framework.

A continuation of the method described in section 5.5.3 naturally leads to an event described as a *TRestPhysEvent* (see section). We just need to interpret the temporal axis in length units on basis of the gas drift speed. If expressing the amplitude in terms of energy or primary charge is wanted too, using the electronics amplifier and micromegas gains will be also needed. In the previous chapter we made an effort to show that means to join the RESTSoft core, therefore the new experimental data will be ready for the analysis routines written for abstract TPC events and surely trained with simulated data. This is a last advantage from using a general and abstract event holder class.

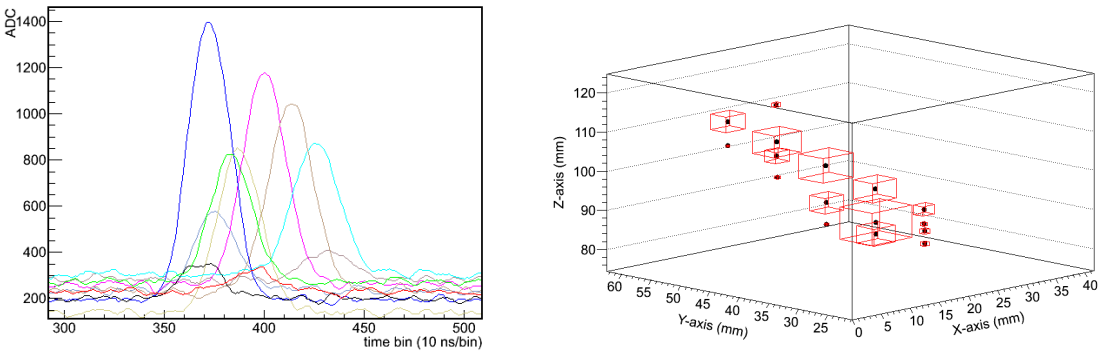

Figure 7.19: Signals on the left, induced by an ^{241}Am 5.5 MeV α are interpreted as a *TRestPhysEvent* which is drawn in the plot on the right. Back solid dots represent the pixel position and the red boxes are proportinonal to the hit energy.

For a better connection with RESTSoft it has been written the bridge-class *Tt2kManager*. In contrast to T2Ktools (section 5.5.2 this is a proper C++ class that is thought for the advanced RESTSoft user to access comfortably the T2Klibrary main functionality. In principle a RESTSoft user should be able to compose a program that imports data from acquisition original format and reconstructs it as *TRestPhysEvent*s without worrying about how the data was taken or T2Klibrary works, as it has been done to produce figure 7.19.

Chapter 8

The CAST experiment and its detectors.

Contents

8.1 The CAST experiment.

The CAST experiment (CERN Axion Solar Telescope) is the most sensitive axion *helioscope* (see section 1.2.3.2) up to now. CAST takes advantage of an LHC decommissioned prototype dipole magnet to implement the helioscope axion-into-photon conversion volume (see figure 8.1). The magnet is able to maintain a 8.80 T transverse magnetic field along its 9.26 m length inside its two bores, 14.52 cm^2 each one. The helioscope points the Sun twice per day, about 1.5 hours during the sunrise and the sunset. Therefore, each one of the four X-ray detectors placed at the magnet ends can look for axions during 1.5 hours per day, while taking *tracking* data. The rest of the time is devoted to define their background, stopping only for calibrations.

8.1.1 The CAST axion search program and the need for low background detectors.

During its first data-taking campaigns, 2002–2004, CAST operated with empty magnet bores (*CAST Phase I*). The limit for the axion-to-photon coupling constant was improved more than one order of magnitude respect to the previous searches with crystals and about a factor 6 with respect to Tokyo Helioscope[189] (see figure 8.2).

Figure 8.1: Picture of the CAST helioscope, a materialization of the principle represented in figure 1.9. Detectors are installed at both magnet ends, two face the sun during sunrise (in the photo on the right) and the other two at sunset (on the left).

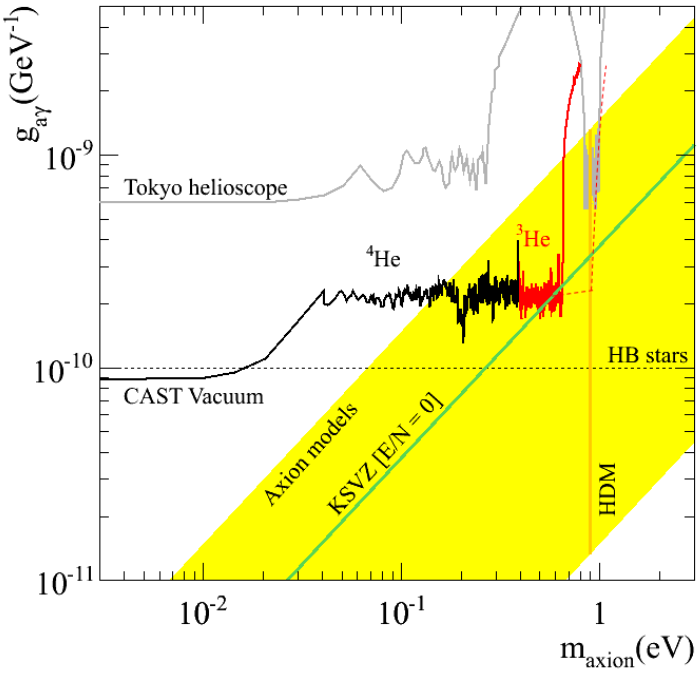

Figure 8.2: CAST exclusion plot for axions. The *Vacuum phase* or *Phase I* (2003–2004), yields a more restrictive limit for the coupling constant at lower axion masses). The ^{4}*He Phase II* (2005-2006), also in black, presents some spikes due to the discrete changes of cold-bore pressure. A partial result of the ^{3}*He Phase II* (2007–2011) obtained mainly from the 2008 data is plotted too. The red dashed line represents final ^{3}He results expectation; the measurements were finished in 2011 reaching a pressure which made CAST sensitive to 1.18 eV axions (still pending on final analysis).

In order to extend the exclusion line to higher masses, up to the limit of hot dark matter (HDM) abundance in the universe around 1 eV, the magnet had to be filled with gas (see section 1.2.3.2), that mass coverage period was named *CAST Phase II*. ^{4}He was first used up to 2006[190], when the magnet pressure reached the condensation point of ^{4}He at the magnet operation temperature of 1.8 K. The use of the expensive ^{3}He entailed am upgrade of the experiment which is described in [187]. The goal was finally achieved in the fall of the 2011 data-taking campaign[192]; the 2008 campaign published results had already yielded the most restrictive experimental limit to the axion-to-photon coupling constant in the sub-eV axion mass scale, crossing for the first time the KSVZ axion model line[191] (see figure 8.2).

The limit which can be obtained for the coupling constant g (so the discovery potential of the experiment) depends on the helioscope parameters (see section 1.2.3.2), the magnetic field intensity B, the coherence length L, the magnet bore area A, the exposition time t, the detectors efficiency ε and background level b:

$$g^{-1} \propto B^{1/2} L^{1/2} A^{1/4} \quad t^{1/8} \quad \frac{\varepsilon^{1/4}}{b^{1/8}} \tag{8.1}$$

The first group of terms, related with the magnet properties, has the greatest weight in the discovery potential. However, since CAST relies on the LHC magnet, they are fixed in practice (until a new experiment is proposed[193]). Increasing the exposure time is expensive and affects only with the 1/8 power. Even though the last group, regarding the detectors performance, has a soft influence, it represents the easiest way to enhance the helioscope results.

Only the CCD detector [194] has remained in one sunrise bore during all this time; the rest of detectors, all them gaseous chambers, have been replaced and upgraded. At the end of the ^{4}He phase, the general shutdown of the experiment was used to perform an important upgrade of the detectors[198] (see also section 8.2.1.2). The impact of those and posterior upgrades (see figure 8.3) on CAST results has motivated that the ^{4}He covered region has been revisited five years later with 2012 micromegas detectors (section 8.2.1.3) and the same is planed for the CAST Phase I (see figure 8.4).

8.2 The CAST micromegas detectors.

The evolution of the CAST micromegas detectors run parallel to micromegas developments. CAST has likely been the most exigent test-bench for new micromegas techniques and, at the same time, the experiment which more, and more immediately, has benefited from micromegas achievements. The continuous advancement on detectors performance due to detector design, readout patterns and new manufacturing techniques often had as a consequence the background decrease as they enhance the discrimination capabilities. The improvement of the background has also been accelerated by means of set-up upgrades (replacements of radioactive

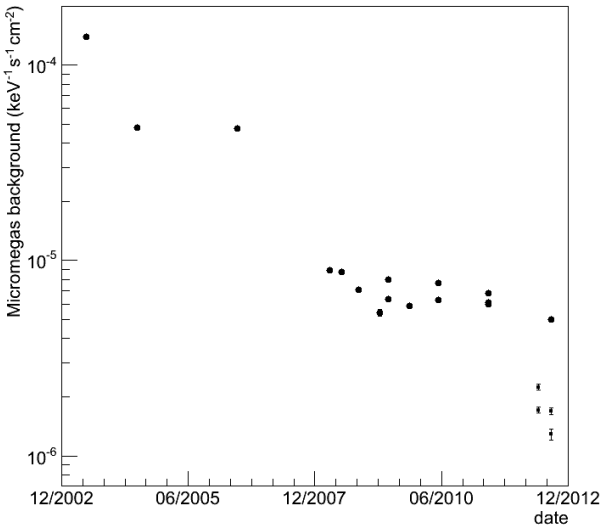

Figure 8.3: CAST micromegas background levels along time. The points correspond to detectors mounted in CAST and taking data. There can be detected three main milestones: the improvement of the strips signals in 2004, the installation of the first light shielding and the introduction of bulk and microbulk technologies in 2007 (then a continuous decrease) and the sunset upgrade to a heavy shielding in 2012 (sunset values with square markers and error bars). The last five points correspond to average values for Summer 2012. The difference between the two pairs of sunset values are due to the installation of a preliminary cosmic veto, and they point to a potential new sharp decrease.

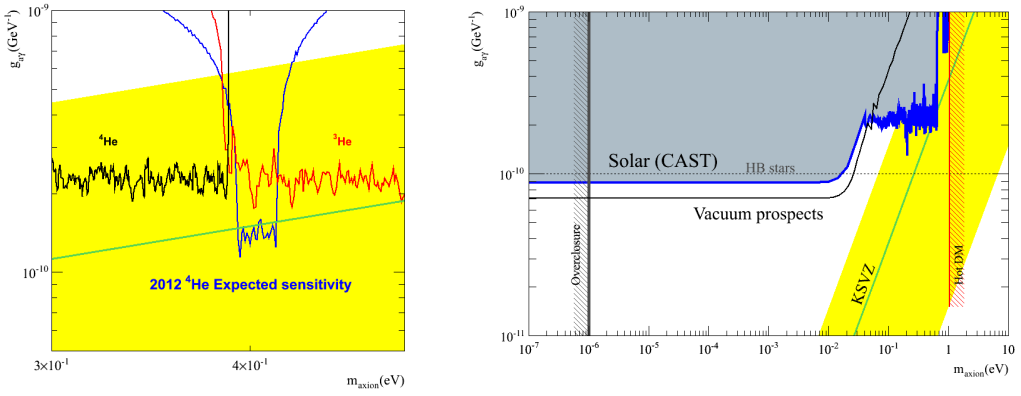

Figure 8.4: Left: Expectation for the 2012 exclusion plot from simulated runs assuming present detectors background levels, the KSVZ axion model line should be excluded at the revisited mass range thanks to the detectors improvement. Right: Expectations for a new 9 month data-taking campaign in vacuum using 2012 detectors background levels. Monte Carlo calculations and plots produced by J. A. García.

materials, shielding, etc.), acquisition upgrades and new analysis developments. Besides, CAST requires high efficiency during long periods of data-taking; stability and reliability are indispensable characteristics as well.

Perhaps the most eloquent sign of the performance and reliability of the early CAST micromegas is the replacement of the original TPC detector[195] with two micromegas at the sunset side[1] in the 2007 general upgrade. The TPC was a multiwire chamber intended to provide a reference based on a robust and conventional technology in front of the novelty of the sunrise detectors. By 2007 it can be said that micromegas technology had became mature enough so as to replace the conventional TPC. Since it was responsibility of the Zaragoza group, the TPC detector pioneered the introduction of low background techniques as the installation of a shielding and the realization of background studies based on Monte Carlo simulations[196], which were lately extended to the other detectors[197][2].

In this section the evolution of CAST micromegas detectors will be briefly reviewed, which will be useful to finally describe present CAST micromegas. The more recent results will advance some of the conclusions obtained from the studies reported in the following chapters

8.2.1 The CAST micromegas detectors evolution.

The CAST micromegas (see figure 8.5) have an active area of 36 cm^2 for the last designs, that was 45 cm^2 for the early ones, which comfortably covers the magnet cold-bore area of 14.55 cm^2. Thus it allows to avoid border effects. The readout is two dimensional with X and Y strips ($\lesssim$ 0.5 mm pitch) printed in copper on a Kapton foil which is glued on a Plexiglass base, the *raquette*.

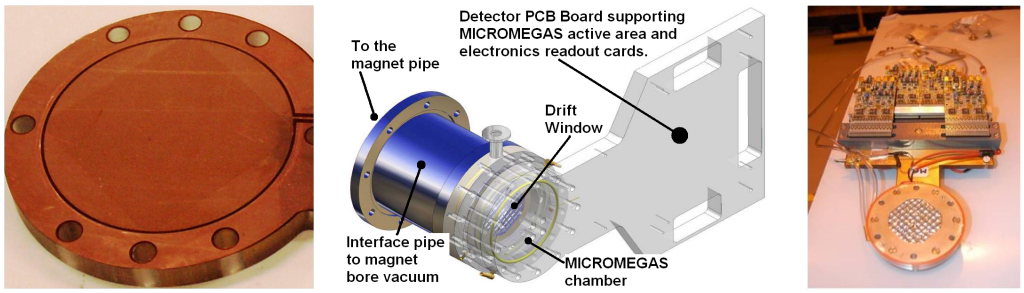

Figure 8.5: Left: Detail of the active area of a CAST micromegas (microbulk, ca. 2009). Middle: sketch of detector and connection to the magnet's cold-bore. Right: mounted detector with Gassiplex cards.

The rest of the chamber structure, with exception of the cathode, is made as well out of Plexiglass. The chamber has 2.5 (first designs) or 3 cm height (after 2007),

[1] Customary CAST notation: SSMM as sunset micromegas and SRMM as sunrise micromegas.
[2] The last example is the work summarized in chapter 9

whose ratio with the electrodes size allows to work without field shaper. On the top, the metallic cathode has a window for the connection with the magnet's bore, closed only with 4 μm of polypropylene (first designs) or 4 μm of mylar (after 2007). That foil has a deposition of aluminium in its inner side to assure the homogeneity of the drift potential along its surface. The window is glued to a metallic grid, the *strong-back*, in order to reinforce it because of the pressure difference between the chamber and the vacuum pipes. It is as thin as possible so as to improve the X-rays transmission. The chamber gas in an Ar/iC_4H_{10} mixture (between 2% and 5% iC_4H_{10} depending on the period) and is continuously renewed (2 l/h flow).

The strips signals are amplified and integrated with a Front-end Gassiplex card[199] controlled by a CAEN sequencer (V 551B) with two CRAM (V550) modules in a VME crate[200]. With such electronics a 10 bit value is available for each strip. Since the 2004 campaign the mesh pulse, always used as a trigger signal, is also recorded with a VME digitizing board, the MATACQ (MATrix for ACQuisition)[201] 12 bits dynamic range, at 1 GHz sampling frequency and an acquisition window of 2.5 μs per event. The acquired signals are described in section 8.3, see figure 8.15.

8.2.1.1 Early micromegas detectors (2003–2006).

The first micromegas detector, used during the 2003 campaign, was a classic one (see section 2.2), but already built by a second generation technique as the pillars were attached to the mesh. Both mesh and pillars were produced by etching of a Kapton-Copper foil, what produces a 50 μm gap. That gap is the most suitable for CAST gas conditions, which were Ar with 5% iC_4H_{10} at atmospheric pressure. Unfortunately the etching technique was not completely mastered then, and some residual copper on the Kapton pillars produced cross-talk between the strips, what severely affected its topological capabilities. The energy resolution was also affected being 16% FWHM from mesh pulses while 30% for the strips. At the beginning only the strips signals were read, up to the moment when an early version of the MATACQ board was installed. In fact, pulse shape analysis (PSA) was the main issue for discrimination during the rest of the campaign averaging a final background of $1.4 \times 10^{-4}\,\mathrm{keV}^{-1}\,\mathrm{cm}^{-2}\,\mathrm{s}^{-1}$from 2 to 8 keV.

The 2004 campaign micromegas' pillars were made of Kevlar and attached to the readout. An independently built electro-formed nickel mesh was tensed over a 100 μm amplification gap. The improvement of the strips signals (both energy resolutions were better than 20% FWHM) was complemented with the installation of the definitive MATACQ board (described above). These advances and the progress in analysis routines, with the possibility of combining mesh and strips information, led to near a factor 3 suppression of the background level: $5 \times 10^{-5}\,\mathrm{keV}^{-1}\,\mathrm{cm}^{-2}\,\mathrm{s}^{-1}$(2-8 keV). It must be kept in mind that those detectors worked without shielding; the final background spectra were dominated by a prominent copper peak (see figure 8.6). A complete description of CAST Phase I detectors is done in [205].

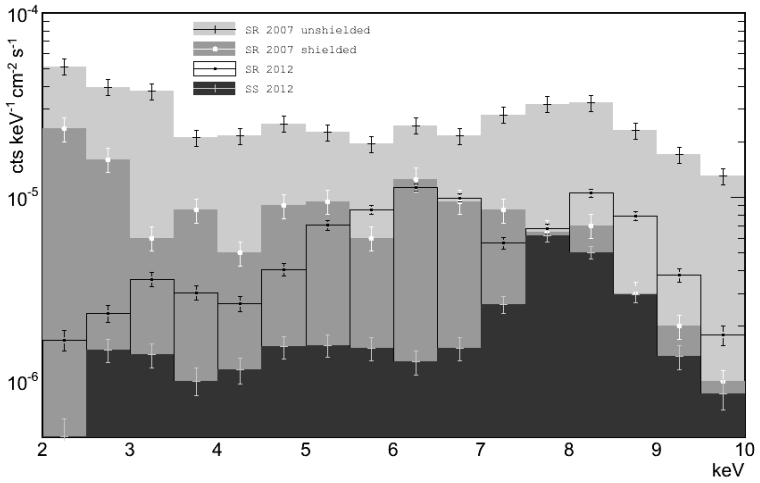

Figure 8.6: Evolution of CAST micromegas background spectra since 2007. The plotted spectra correspond to the following situations: First test of sunrise shielding (before and after installation) done using a classic micromegas. Background spectrum obtained in the same set-up during the Summer 2012. Improvements on detector signals and analysis allow to identify three peaks which are the main contribution to the background. The effect is more intense at low energies and the enhancement of the 8 keV copper fluorescence peak is an indication of improvement of software efficiency (see next section 8.3). Finally the Summer 2012 background spectrum registered in the sunset detector 1 after the application of the cosmic veto (see section 8.2.1.3).

8.2.1.2 The 2007 upgrade. New technologies and shielding (2008-2012).

As it was advanced, during the 2007 general upgrade of the experiment, the TPC detector was replaced in the sunset side with two new micromegas detectors; three of the four CAST detectors have been micromegas since then. However the micromegas group strategy was not conservative at all, more on the contrary up to four different strategies were undertaken in order to produce a significant step towards higher efficiency and lower background[198]:

- The new types of micromegas, both bulk and microbulk, were introduced in CAST. Even though the quality of the classic detectors was already very good, the robustness of the micromegas took a qualitative step which allowed the use of higher gains and so better performance. The detector readout was re-designed, as it is described with more detail in a dedicated subsection 8.2.2.

- The isobutane proportion of the chamber gas was decreased to so simplify the operation of the system to comply with the CERN's safety rules, since then they were 2.3% iC_4H_{10} in the sunrise and 2% in the sunset. Moreover the pressure was increased up to 1.4 bar to improve the quantum efficiency. This possibility is a direct consequence of the previous item, since the robustness

of the new micromegas allows the operation at high pressure (see section 5.1). The adaptation to the use of ^{3}He included the installation of a thicker window with strong-back between the magnet's bore and the detector's line and also an additional window to produce a differential pumping, which prevents the leak of the chamber gas to the magnet's bore. Today the loss of efficiency is mainly due to the windows transparency (see section 6.2.7.1).

- The sunrise docking place was lengthened so as to hold a X-ray optical telescope, i.e. a focusing device that can concentrate the signal in a detection area about 100 times smaller, therefore decreasing the relevant background rate by the same factor. The device was finally not installed because of its low efficiency, but the sunrise detector remains mounted after a 1.5 m length stainless steel pipe that connects it with the magnet bore. That powerful technique to improve the signal to background ratio is complementary with the rest of the strategies and has never been refused. Rather on the contrary, a new X-ray telescope is planned to be built for the 2013 upgrade.

- The installation of a shielding (figure 8.7). The sunrise shielding is a sort of compilation of shielding techniques against almost all the potential external background sources, even though the final design was strongly constrained by the available space that is shared with the CCD detector and its X-ray telescope. A main 2.5 cm thick layer of archaeological lead is shielded as well by an inner 5 mm thick layer of copper. An external polyethylene shielding was planned to moderate neutrons and a 1 mm thick layer of cadmium was thought as a neutrons absorber and so situated between the polyethylene and the lead. The first three layers were specifically built and enclosed in a cylindrical plexiglass box which, moreover, is flushed with nitrogen to avoid radon emanations. In the sunset side, both detectors shared a shielding composed of a common copper Faraday cage and a lead layer built of 5 cm thick bricks of clean lead. Because of set-up constrains and the use of standard lead bricks, the resulting shielding is not tight in some directions. Polyethylene bricks completed the shielding.

Aiming to evaluate separately the impacts of the shielding and the detectors evolution in the accumulated improvement, a direct comparison of the background taken by exactly the same detector before and after the installation of the sunrise shielding yielded a factor of 3 reduction[198]; while the global improvement with respect to 2006 is higher than a factor of 4. Besides, during the following campaigns the background levels went on decreasing down to another factor of 2 (see figures 8.3 and 8.6). This continuous improvement is related with the consolidation of the microbulk manufacturing technique and also with the development of the Multivariable analysis (MVA) discrimination routines for CAST (see section 8.3). To sum up: a factor of 3 reduction purely due to the shielding and near another 3 thanks to the use of better detectors together with more sophisticated analysis was obtained during 2006–2011.

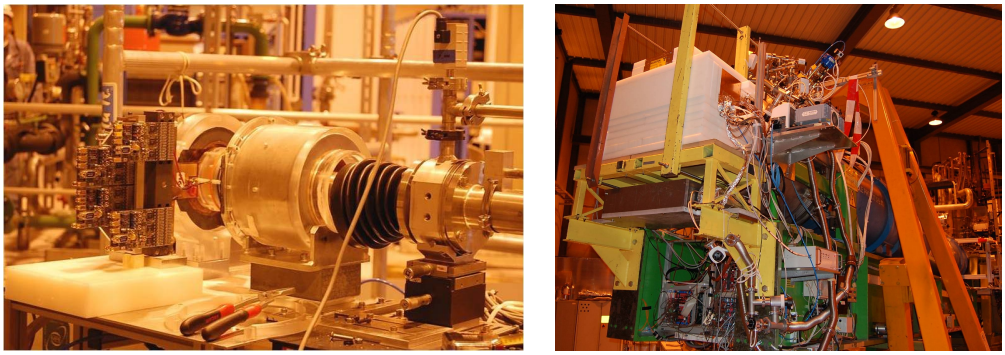

Figure 8.7: CAST micromegas shielding installation in 2007. Left: sunrise shielding just one step before being closed over the micromegas detector. The main opening for connection to magnet cold-bore is clearly visible, leaving place for installation of a X-ray telescope. The shielding was partially completed with a polyethylene layer as it can be seen in the (right) photo of the sunset side.

When comparing sunrise and sunset it looks like the sunset thicker shielding in some directions was somehow compensated by the much better closure of the sunrise, and the final results were quite similar: typical background values are 5–$7\times10^{-6}\,\mathrm{keV}^{-1}\,\mathrm{cm}^{-2}\,\mathrm{s}^{-1}$. We are always referring to the customary CAST range of interest (RoI): 2–7 keV. The typical final background spectra during this period showed the copper peak together with another shorter, but wider, peak around 6 keV, that is smaller in the sunset.

Regarding the new types of micromegas, the several bulk micromegas in operation in CAST yielded background levels almost as good as contemporary microbulks[3]: about $8\times10^{-6}\,\mathrm{keV}^{-1}\,\mathrm{cm}^{-2}\,\mathrm{s}^{-1}$while $7\times10^{-6}\,\mathrm{keV}^{-1}\,\mathrm{cm}^{-2}\,\mathrm{s}^{-1}$for microbulks[187] in 2008. It was reliability the criterion that finally made CAST opt for microbulks, since it seems that vibrations on CAST platform produced a slow deterioration of the bulks[4].

8.2.1.3 The 2012 sunset upgrade.

The last significant upgrade was carried out in 2012, before the Summer data-taking, and affected only the sunset detectors which where replaced and the shielding completely changed. The upgrade design obeyed two premises (largely discussed in the next chapters): the main contribution to the background was due to environmental γ flux and the 6 keV peak was a steel fluorescence originated in the vacuum pipes and the cathode. Therefore the goals were to increase the lead thickness and the shielding closure, avoid the steel fluorescence and improve the detector intrinsic

[3]However, it is very likely that bulk micromegas intrinsic radioactivity would has been a limitation for present CAST background levels and expectations.

[4]These days of very intense tests with the new detectors carried out in the own experiment are carefully related in [187].

radiopurity, otherwise the achievable improvement could be limited.

The copper innermost layer of the shielding was upgraded from 0.5 cm to 1 cm thickness, attenuating the natural γ from the lead (with energies between 72 and 87 keV) by a factor higher than 10^3. The polyethylene was removed to leave space available to extend the lead layer (now non archaeological) up to 10 cm thickness. Moreover many lead bricks were machined to assure better tightness than in the previous design, especially in the region where the electronics are plugged (the raquette's outlet) and around the connection to the magnet's cold-bore. This last unavoidable weak point has been minimized by inserting a 18 cm long pipe (see figure 8.8 left), which is also shielded with lead. Thus the detector is protected inside a deeper cavity (see figure 8.8 right).

The pipe and its interior surface are critical because the radiation originated there can freely access the detector via the X-ray window. Hence, all the stainless steel near the detector has been replaced with copper to prevent 5-7 keV X-ray fluorescences and improve the detector intrinsic radiopurity. That concerns the cathode, the gas connections to the chamber and the pipe itself. The latter is made out of copper and has 2 cm thickness. Near the detectors the pipe is reinforced with a 2 cm thick copper box which fits to the lead external shielding. In addition the pipe interior surface is covered by a Teflon coating to suppress the copper fluorescence.

The most spectacular effect of the upgrade was the disappearance of the 6 keV peak that has led to the level of $1.7\text{–}2.3\times10^{-6}\,\mathrm{keV}^{-1}\,\mathrm{cm}^{-2}\,\mathrm{s}^{-1}$(2–7 keV), that is to say, another reduction factor about 3 with respect to the SRMM value and about 4.5 with respect the previous SSMM. However it is thought (see chapter 10) that the potential of this new set-up, in terms of radiopurity and external γ screening, should allow further reduction.

For the Summer 2012 data-taking a cosmic muon veto was installed over the sunset (see figure 8.9). The time difference between the veto signal and the micromegas trigger is recorded and used to reject cosmic coincident events in off-line analysis. The veto was implemented using an available plastic scintillator which was mounted far from an optimum position because of incompatibilities between the scintillator dimensions and the present set-up.

The Monte Carlo computed geometrical coverage of the detectors by the veto is only 44% while the analysis of Summer data yields a 25% background reduction in both detectors in the 2–7 keV range (see figure 11.4), again the veto reduction is higher in the copper peak. Therefore the present best background level achieved in CAST by micromegas detectors is $1.3\text{–}1.7\times10^{-6}\,\mathrm{keV}^{-1}\,\mathrm{cm}^{-2}\,\mathrm{s}^{-1}$(2–7 keV).

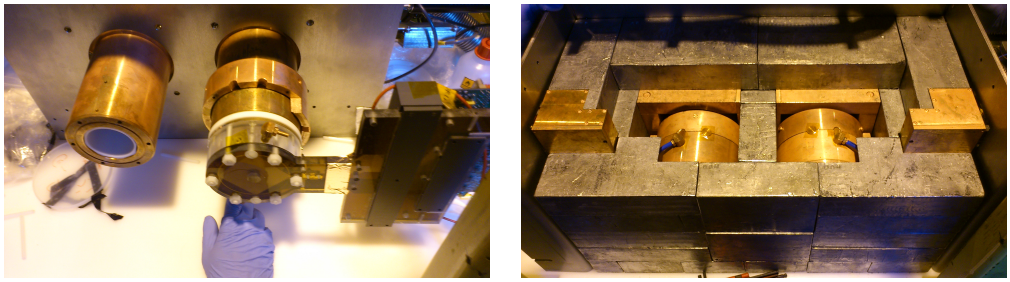

Figure 8.8: Left: early step during sunset 2012 installation. The auto-shielded copper pipe with an inner Teflon coating is visible in the left (Jura) bore; in the right bore (Airport) the detector installation using Teflon and Delrin screws, nuts and gaskets, the new copper gas connections and top piece of the new inner copper shielding which fits the pipe. Right: later step during shielding mounting process showing the careful design to adjust copper shielding to detectors (closing as much as possible every outlet), Faraday cage and lead layer. Note that not only detectors but also the pipe are shielded, thus the detectors' cavity can only be accessed thorough a long, strongly shielded and radiopure pipe.

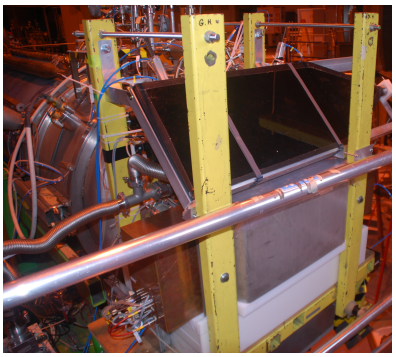

Figure 8.9: 2012 sunset final installation (see the Faraday cages backs with the electronic connections) showing the cosmic muon veto (plastic scintillator) over the shielding. The veto is mounted in 50° because of space availability with present vacuum system.

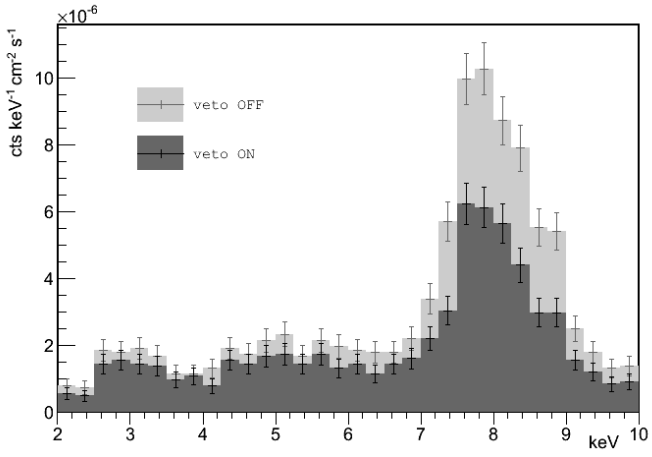

Figure 8.10: Background before and after the application of the cosmic veto.

8.2.2 The CAST micromegas readouts.

We are going to pay now special attention to the different readout designs used in CAST micromegas along the years. Apart from the crosstalk problem exposed in section 8.2.1.1, there was a fundamental difference between X and Y signals in early CAST micromegas detectors due to their readout design (see figure 8.11 left). One direction strips were directly drawn on the anode plane with 350 μm pitch, while for the orthogonal signals a series of unconnected pads had been provided. The pads were connected to the strips in a lower level by means of vias which consist of cylindrical holes filled with metal. Though the pads were wider than the surface strips to compensate the amount of surface charge collection, in practice pads signals had worse quality.

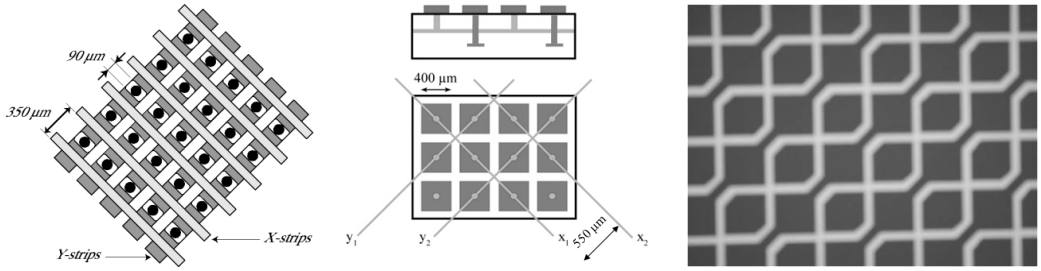

Figure 8.11: Left: classical CAST readout composed of strips and pads with vias (2002). Middle: pixel-like readout composed with three layers (2007). Right: pixel-like readout with only two layers (2009).

The experience from data analysis led to the idea that an anode pattern as homogeneous as possible would decrease the dispersion of the signal features by minimization of the dependency on the position of the signal generation process. Besides, a symmetric readout, with no significant difference between X and Y signal, would be useful for discrimination purposes. That concept came true with the 2007 detectors readout design (see figure 8.11 middle), which is essentially a pixel readout later reduced to a strips readout by means of two lower planes of orthogonal tracks. The pixels are connected to the tracks diagonally, that allows to conserve the compactness of the pixels but spacing the strips pitch. Thus, using a 550 μm pitch, the number of the lines was reduced to 106 covering the 36 cm^2 active area.

In microbulks the readout homogeneity goal is gone further as the mesh pattern is aligned with the anode layout. Every pixel was complemented with a kind of window with 3×3 holes with 30–40 μm diameter and 100 μm pitch (see figure 8.12 right). Taking this precaution the electrons crossing the mesh always find a perfectly defined anode below. The price to pay is a limited mesh transparency (see section 4.3 and figure 4.8), nevertheless CAST chambers work always in optimum gas conditions, so this should not be a practical limitation. In the bulk version the anode design was the same as it is shown in figure 8.13.

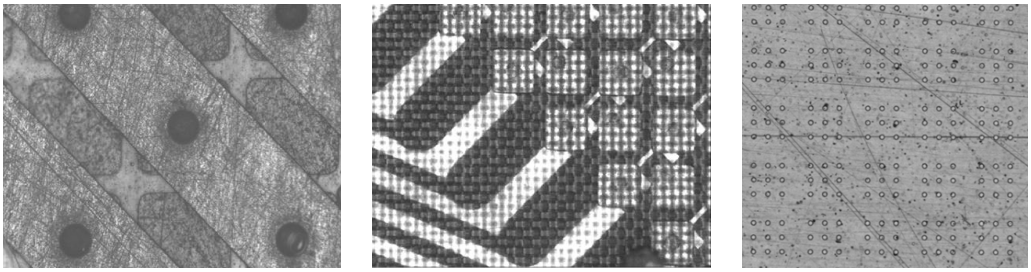

Figure 8.12: Left and middle: back and anode plane microscope views of 2007 pixel-like micromegas. Right: mesh pattern of the microbulk version with holes distribution correlated with pixels positions.

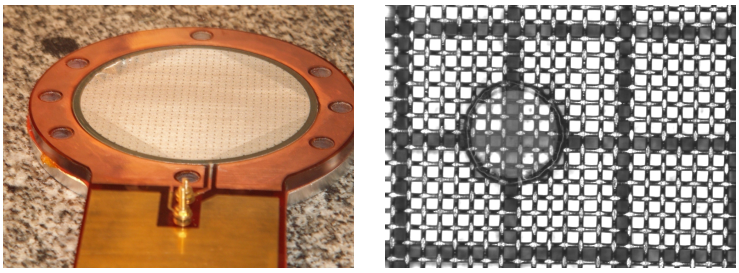

Figure 8.13: Left: bulk version with the stainless steel oven mesh over the same readout of figure 8.12 left and middle. The green vacrel pillars that catch the mesh are clearly visible. Right: detail at microscope of the oven mesh, showing one pillar on the pixelized readout.

The manufacturing process of such a pixelized-2D readout plus an amplification stage, *all in one*, was a milestone in the microbulk micromegas developments. It meant a demonstration of the state of the art in photo-lithography and kapton etching techniques (see figure 8.14).

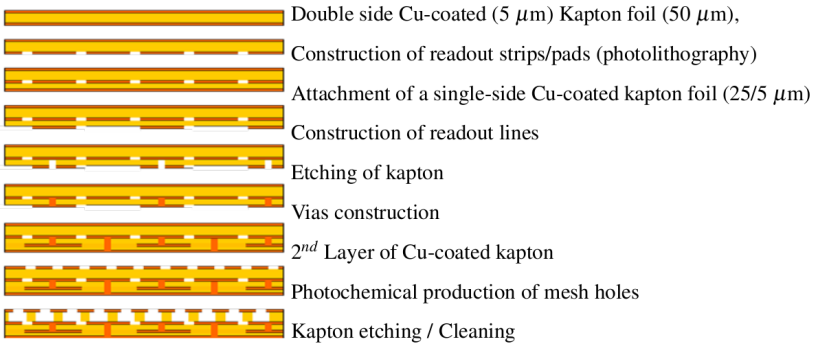

Figure 8.14: Sketch of a pixel-like three layers readout CAST microbulk manufacturation process. It is described in detail in [105].

In later CAST microbulks the three readout conductive layers (anode, pixels-strips X and strips Y) were reduced to only two by connecting half of the pixels in the anode layer itself by means of a narrow copper segment (see figure 8.11 right). Thus the manufacturing process is safer. Moreover the readout material has been reduced, so the potentially radiactive epoxy between layers and, particularly, one layer of copper which would contribute to the 8 keV peak.

As it was already explained in section 5.4, CAST micromegas readouts were used to study the radioactivity of micromegas planes by means of underground germanium spectroscopy[175]. The measurement of a complete 2007 CAST microbulk confirmed the new technique to produce complex but radiopure readouts.

8.3 The CAST data analysis.

The signal to background discrimination capabilities of the micromegas detectors represent their main advantage compared with solid state detectors, like the CCD. Maybe the most significant fact about this is that the CAST micromegas trigger rate is about 1 count/s, due mostly to cosmic muons which cannot be screened, while the final background, after off-line analysis, is of the order of fews counts/hour.

The discrimination is based on gathering the most useful and complete information from the event, that is determined by the drift in the chamber, the readout characteristics and the electronics response. All these aspects have evolved throughout CAST history, together with analysis routines. In CAST, the topological selection of the events means to find point-like events, since the photo-electron path induced by the X-ray with less than 7 keV is not long enough to generate a recognizable track after diffusion effects[5]. In these circumstances the key is wise definition of the parameters used for the event description that allows an precise detection of the deviations from the ideal targeted event. Minimizing the deviations certainly observed in X-ray events will be important to define an efficient criteria, that depends on the detector's performance (on its SNR, stability and homogeneity). The 6 keV events from a ^{55}Fe source (and sometimes the 3 keV events from the argon escape peak) are used as a standard for X-rays (axions) events.

The calibrations are taken daily and the definition of a X-ray signal is updated to incorporate any systematic effect that could affect the response of the detectors. At the same time, environmental parameters like the gas pressure, the flow, the temperature, are continuously monitored.

The off-line analysis can clearly be divided into two steps (though they are often confused): the *raw-data analysis* (section 8.3.1) and the *background discrimination* (section 8.3.2). The former involves the reduction of the raw-data, i.e. the mesh pulse shape and the two strips map (see figure 8.15), into a collection of simple

[5] Note the parallelism with the case studied in section 7.1. This is a situation like the one shown in figures 7.7 and 7.8 where, because of the CAST detectors actual diffusion coefficients, the γ events are still not distinguishable from nuclear recoils.

numbers which describe the event. The latter uses the already *digested* information to select the true X-ray events and reject the rest of the background.

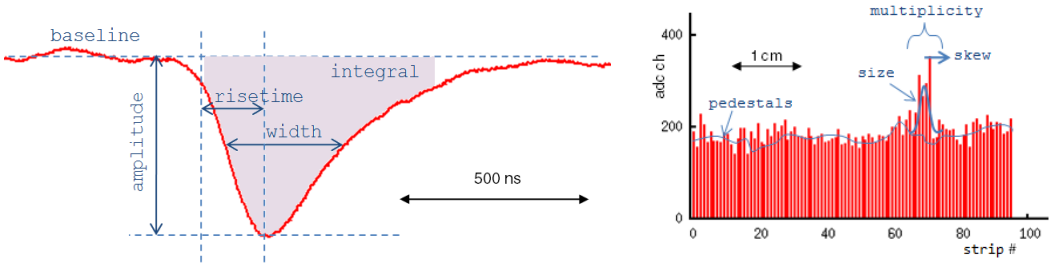

Figure 8.15: CAST raw-data (directly from acquisition on-line viewer screen-shot) from a ^{55}Fe calibration with a visual indication of the most important parameters determined by the CAST low level analysis. Left: mesh pulse. Right: one of the two strips axis.

There is no official CAST analysis package, but several alternative codes in constant evolution. However the data has generally been treated by two different analysis whose results are contrasted and, at present degree of development reached by analysis routines, found to be statistically compatible, only with the exception of some eventual systematic effects. Therefore, explaining in detail the CAST data-analysis is out of the scope of this thesis (other Ph. D. works have been devoted to CAST micromegas data analysis[202, 187, 203, 204]). We will just comment on the aspects that will be useful for the next chapters discussion; that includes a general view of the CAST analysis status.

8.3.1 CAST raw-data analysis.

In this section the low level analysis of CAST micromegas signals will be briefly commented. At this point, the mesh pulse and the two sets of strips signals are treated separately.

8.3.1.1 Mesh pulse analysis.

In the analysis of the mesh pulse the determination of the baseline is crucial as it affects the rest of the pulse parameters (see figure 8.15 left). The noise in the mesh signal has an effect on the rest of the parameters fundamentally from the uncertainty in the baseline determination. Depending on the analysis version some arithmetical smoothing or a Fourier treatment of the signal is performed. As the mesh pulse contains all the available temporal information, it is needed to record at least a time period as long as the maximum drift time to assure all the likely simultaneous interactions in the chamber to be registered, that is about 1–1.5 μs . Therefore about 1 μs of MATACQ card buffer is still available to record the baseline of each pulse.

The shaping time of the mesh signal amplifier must be selected regarding the compromise of being fast enough to be sensitive to the pulse shape while giving a good energy measurement. The typical pulse widths are of the order of 150–300 ns. In any case the time scale is given by the requirement of recording the maximum drift time. The temporal pulse parameters are computed by means of defining relative references respect with the pulse maximum. For instance the*risetime* is the time the pulse needed to rise from $x\%$ to $(1-x)\%$ of its maximum. In practice a longer range gives more resolution but is less robust against noise, therefore the criteria should be flexible and dependent on the SNR. The number and precise definitions of the observables vary with the analysis version, here [187] is followed and these are the definitions of the basic observables for the mesh pulse:

- *Pulse baseline:* Baseline voltage offset calculated with the first 100 pulse data points.
- *Pulse center:* Time at which the pulse reaches the maximum value.
- *Pulse amplitude:* The value at the *pulse center* after subtracting the *pulse baseline* value.
- *Pulse integral:* The pulse area enclosed between the *starting pulse time* and the *ending pulse time*. The starting and ending pulse times are defined when the pulse reaches 15% of the amplitude value to the left and the right of the *pulse center*.
- *Pulse mean center:* The addition of time values between the *pulse starting time* and the *pulse ending time* weighted with the pulse amplitude at the given times and normalized with the *pulse integral*.
- *Pulse risetime:* Time length between the *starting pulse time* and the time at which the pulse reaches 85% of the *pulse amplitude*.
- *Pulse width:* Time length between the points where the pulse reaches 50% of the *pulse amplitude*.

8.3.1.2 Strips signals analysis.

The strips analysis is carried out in three steps. First it must be decided which strips are fired one by one. In order to do that, a previous analysis is needed: the characterization of each strip *pedestal*. The pedestal is understood as not only the mean value in absence of signal for the strip, but also its typical variance. So a few samples (of the order of few thousand of events) are required to obtain the mean value and the standard deviation, σ. One special run should be taken, in absence of the radioactive source and using an internal fast trigger rate; however, in practice, it is observed that using the calibration run itself leads just to a small overestimation of the pedestals.

Once an amplitude has been determined for every strip the analysis continues searching for *clusters*, i.e. accumulation of fired strips related with compact ionization deposits (see figure 8.15 right). There can be accidentally no fired strips in the middle of a cluster, or isolated ones yielding high values. Therefore just the definition of a cluster is a complex task. In principle, only one interaction contained in the chamber is acceptable, however events with more than one cluster per axis could be considered as mono-cluster events if their relative or absolute weight (as the sum of the amplitudes of all the strips in the cluster) is very unbalanced. In that case one cluster could be considered as a fake cluster, due to an statistical fluctuation, crosstalk, etc. (see figure 8.16).

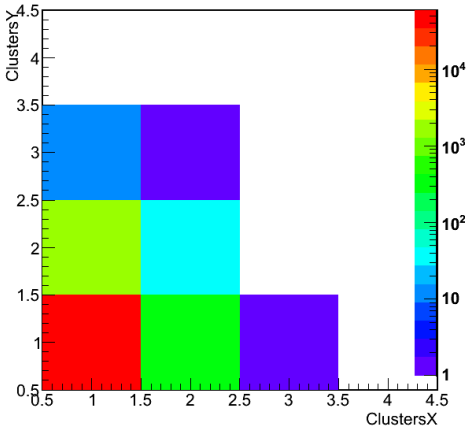

Figure 8.16: Identified clusters per event in X and Y axis in a ^{55}Fe calibration. The fact that events with two clusters only in one axis is much higher than events with two clusters found in both axis points to statistical fluctuation to have produced the secondary clusters, in that case they could be ignored. That can have an important effect in software efficiency for lower energy events.

In general the criterion must be flexible enough to be adapted to the detector performance; it could be stricter with very good detectors working at high gain, but it may need to be relaxed for noisy detectors or those presenting any geometrical defect.

The last step, with the clusters already identified, is to proceed with the description of the clusters themselves. Quoting again [187] the cluster's parameters are defined from their strips values $\hat{c}_i \equiv c_i - p_i$, with c_i the strip raw value and p_i the mean pedestal, as:

- *Cluster charge* $(\hat{c} = \sum_i \hat{c}_i)d$ *:* addition of the strips charge that define the cluster. Proportional to the number of electrons that generated the cluster, and to the ionization energy deposited by the originating process.
- *Cluster position* $(\mu = 1/\hat{c} \cdot \sum_i i \cdot \hat{c}_i)$*:* dtrip value weighted with the charge measured in each strip. This parameter describes the mean cluster position.
- *Cluster multiplicity:* describes the cluster size in terms of the number of strips that have been activated inside the cluster.
- *Cluster sigma* $\left(\sigma^2 = 1/\hat{c} \cdot \sum_i \hat{c}_i \, (i-\mu)^2\right)$*:* describes the cluster size weighted with the charge detected in each strip.

- *Cluster skew* $\left(\gamma = 1/\hat{c} \cdot \sum_i \hat{c}_i \left(\frac{i-\mu}{\sigma}\right)^3\right)$*:* describes the cluster asymmetry in terms of the third standardized moment. Skew values closer to zero mean a more symmetric cluster.

The selection of the events will start with analysed data where every event is described as a simple collection of parameters. Those modelled events are stored in light ROOT trees that allow an easy exploration and manipulation.

8.3.2 CAST background discrimination.

Although several versions of the selection analysis exist, there can be classified regarding two basic aspects of the discrimination algorithms: the way the discrimination criteria are applied and the way the energy dependence of the events is treated.

8.3.2.1 Regarding the application of the discrimination criteria.

The common idea relies on the definition of n *observables* from the descriptive parameters of the analysed data. Then to study their distribution from the calibration data in order to define an *acceptance volume* in the n-dimensional observables space, which will include the events that are most likely to be X-rays. The acceptance volume is built as big as needed to assure an estimated confidence for a true X-ray event to be found inside, that is denominated the analysis *software efficiency*, $\varepsilon_{\text{soft}}$; nevertheless the probability for any kind of background event to be rejected is, in principle, unknown. The performance of a discrimination criteria is evaluated according to the ratio, $\varepsilon_{\text{soft}}/\sqrt{b}$, where b is the resulting background level, which can be quantified only empirically after the application of the criteria.

The more straightforward implementation of the criteria is the ***Sequential Criteria Analysis*** **(SCA)** first used by Theopisti Dafni[202] in the analysis of the first CAST micromegas' data, and with Thomas Papaevangelou as the main supporter of later developments[6]. For each observable a tolerance range is defined from its distribution in calibration data (see figure 8.17). That defines an upper limit and a lower limit and a related software efficiency. The observable distribution can be considered to be gaussian and then the limits can be deduced from a fit as multiples of the standard deviation, but, in principle, the election is completely free. Then the several defined criteria are applied sequentially, as corresponds to independent observables, and the final software efficiency can be calculated only after the end of the sequence.

If correlation between parameters needs to be taken into account, combination of observables, as those related with the pulse shape (*risetime/width, amplitude/integral...*) or mesh and strips balance (*mesh amplitude/strips total charge*),

[6] For a recent reference see [203].

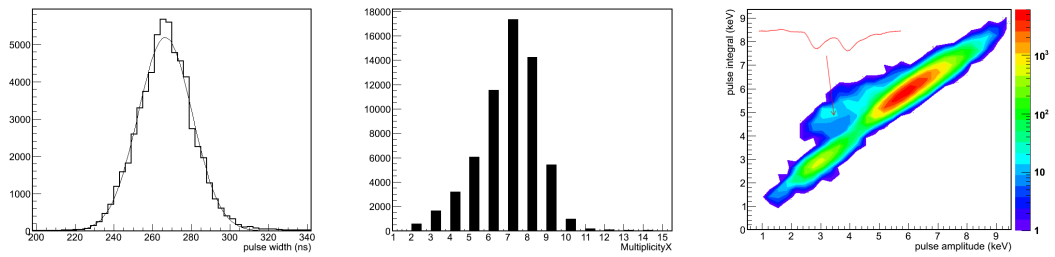

Figure 8.17: Examples of observables distributions which are practically gaussian (left: *pulse width*), not symmetric (center: partial *cluster multiplicity*) or strongly correlated (right: pulse amplitude vs pulse integral, with a detail showing the kind of event that escape to the general tendency). Distributions obtained from a ^{55}Fe calibration with M17 detector working with $\mathrm{HV}_{\mathrm{mesh}} = 315$ V.

can be directly used (see figure 8.18). However the expected ratio value can be reproduced by accident, so it is preferable to define a two dimensional criteria as an acceptance area drawn in the plane defined by the couple of observables. Again that area can be freely defined, and the present trend on SCA goes towards the definition of complex two dimensional criteria, often even as drawn by hand contours.

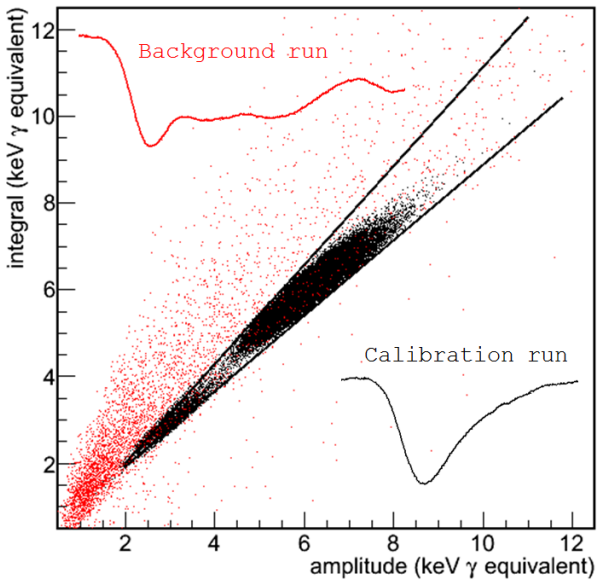

Figure 8.18: Demonstration of discrimination using the same observables couple of figure 8.17 right. The suggested two dimensional acceptance volume is represented with the two black lines. Note than the disperse population of background events deviates always in the same sense, as no longer integral/amplitude than point-like events can be expected.

In the ***Multivariate Analysis*** **(MVA)** a unique criteria is implemented in the n observables-dimensional space, dealing equally with all the observables. The MVA was introduced in CAST by Kostas Kousouris and reached its present development under the work of Javier Galán (which is carefully described in [187]). The theory is based in the definition of an n-dimensional generalized standard deviation from

the average X-ray event based on the mean values, μ_i, and standard deviations, σ_i, obtained for every observable individual distribution and the correlation matrix, V_{ij}, calculated between them. An event is represented as n x_i values for the n observables, and placed in the space as

$$X_i = \frac{1}{\sigma_i}(x_i - \mu_i) \tag{8.2}$$

what places the X-ray standard event in the origin of the space. Note that 8.2 is already taking into account the significant deviation observed for each observable, but also that it is assuming the observable distribution to be symmetric. The method goes further defining q, the significant deviation in units of the generalized n-dimensional standard deviation

$$q = \vec{X}^T \rho^{-1} \vec{X}; \qquad \rho_{ij} = \frac{1}{\sigma_i \sigma_j} V_{ij} \tag{8.3}$$

as the distance to the origin but measured according to the metric ρ_{ij}. In theory, if the observables distribution were strictly gaussian, the X-ray event *probability density function (pdf)* could be written

$$f(\vec{X}) = \frac{1}{(2\pi)^{n/2}|\rho|^{1/2}} \mathrm{e}^{-\frac{1}{2}q(\vec{X})} \tag{8.4}$$

and the MVA software efficiency could be expected to be 68% if the selection criteria was $q < 1$, 95% if $q < 2$, etc. However, in practice it is preferred to determine empirically the software efficiency using the calibration data when applying the q_L value that will be used to define the background rejection criterion.

It is remarkable that, if we focus only in one observable, its limits on the MVA criteria are not clearly defined, as it depends on the rest of observables values. It is needed to go to the n-dimensional space to be able to *draw* the acceptance volume frontier defined when $q = q_L$. That is an n-ellipsoid, but whose axis are rotated respect to those of the framework as consequence of the existing correlations between the observables. When changing q_L, therefore expanding or contracting the ellipsoid, in order to tune the software efficiency, we must be aware that we are extending the limits for each observable equally in both senses and at the same ratio (respect to their standard deviation) for every of them, assuming that all the distributions are symmetric and have the same pdf type.

Previously to the definition of the correlation matrix, some basic discrimination criteria are applied to make a preliminary selection of the more representative X-ray events. That is done applying a rough SCA. Even when the matrix reflects the correlation relationships, those more important are convenient to be included explicitly as any combination of basic observables. If desired one observable can be remarked by reformulating it so as to have a narrower pdf, for instance by using some power of it.

Finally a comparison between both analysis types will be commented. The main advantage of the SCA is the simplicity of the selection process and a clear definition of each independent selection criterion. The effect of each acceptance range can be quantified and adjusted (even by hand) depending on the particular case. The result is a robust analysis tool the user feels reasonably confident with. The generic mathematical formulation of the MVA makes easier the systematic study of observable combinations. The price to pay might be a less intuitive process to deal with, which can drive to some effects that will be commented just below. The different sets of observables that can be formed from the basic ones (that were defined in the previous section) were systematically numbered with an ID according to a rule explained in [187]. Not only the favourite one, but several sets of observables must be used every time to check that the result is not strongly dependent on the choice.

Since in the n-dimensional distance a combination of positions of several observables can compensate an important deviation in others, it can happen that events that show obvious deviations from a particular point of view are globally accepted (see figure 8.19). That is more likely to happen if the number of observables is high and, specially, if very similar observables are included, making the MVA deal with redundant information, an effect that is known as *statistical noise*. Whereas, in SCA, the addition of a new criterion can never produce the acceptance of an event otherwise rejected.

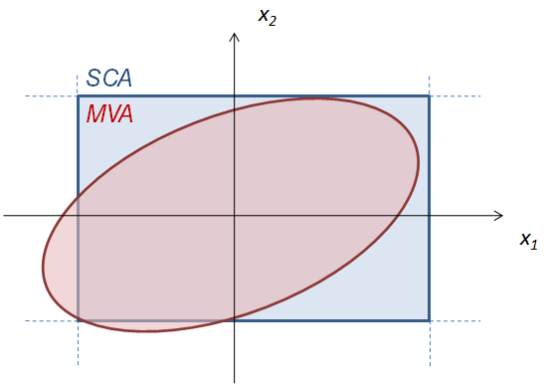

Figure 8.19: Sketch of the different ways the acceptance volume is defined in both types analysis for a couple of observables. It is graphically clear why MVA systematically yields higher rejection capabilities, but lower software efficiency; and also how some, in principle, unexpected regions of the observables space can be accepted.

It has been shown[187] that the final background was not improved with the inclusion of new observables, once the number of them in the combination is 6–8 (at least with the typical observables defined for CAST micromegas, see previous section). It is generally accepted that a basic efficient set of observables must include at least:

- A pulse time characteristic, which is a signature of the time amplifier (then disturbed by no point-like events), as its *risetime* or *width*.
- A pulse shape observable, which can show pulse deformations, like the ratios *risetime/width* or *amplitude/integral*.
- An observable related with the *cluster size*: as the strips multiplicity or any other definition of cluster size.
- A balance between both strips axis projections of the cluster.
- A balance between energy measurements through the mesh and the strips signals.

The observables related with the cluster shape are not very useful due to the SNR with present electronics and by the fact that they are highly affected by the diffusion during the drift. When using such a combination of observables both kind of analysis give similar results.

The analysis efficiency for events different than X-rays is unknown. In background spectra, spetially in the most recent ones in figure 8.6, show how the discrimination process enhances peaks which can be attributed to fluorescences. This fact is an eloquent proof of a satisfactory behaviour of the analysis. On the other hand, it means that an important part of the background events is composed of true X-ray events which cannot be rejected by analytical methods.

8.3.2.2 Regarding the treatment of the energy dependence.

Another relevant issue regards the observable's pdf dependence with energy. An ^{55}Fe source is used for calibrations (see figure 8.20), that gives a strong 6 keV peak inside the CAST RoI, though near the high energy extreme (see the expected axion's spectrum in figure 1.8), and also a scape peak at 3 keV (see section 3.2.1.1) about 20 times smaller. The baseline approach is to use only 6 keV events in order to define the discrimination criteria and later to use the 3 keV to estimate the software efficiency at lower energies. That yields a software efficiency that decreases with energy, a systematic effect that should be corrected. There have been proposed several strategies to face the problem.

There are two basic approaches: to avoid the energy dependence or to model it so as to correct it. To apply the first approach it is preferable to select observables with a soft energy dependence. In principle the *risetime*, for example, is a characteristic of the time amplifier which must be independent of the amplitude. Nevertheless that is only approximate if the detector has very good SNR. The only practical way is to use the escape peak to define the discrimination criteria. The 6 keV and 3 keV peaks must be mixed (in fact 3 keV events must be weighted to have a statistically relevant presence) in order to gather a group of representative X-ray events in the 3–6 keV energy range. Although there have always been doubts about the convenience

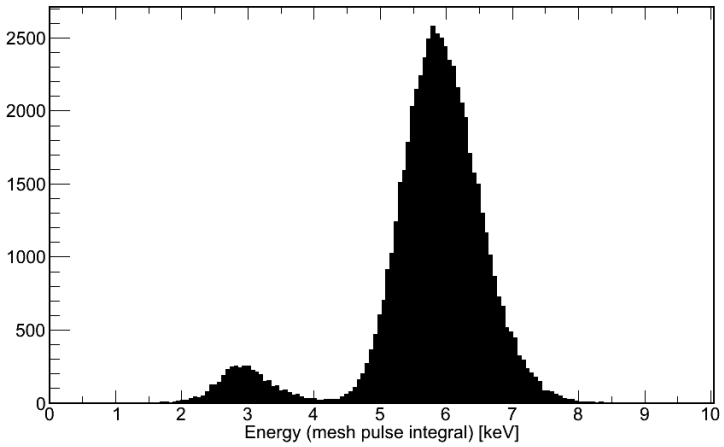

Figure 8.20: ^{55}Fe calibration spectrum taken with a CAST detector (M17).

of using the escape peak as a standard, because some effects can produce apparent 3 keV events which are not good ones, recent studies (see section 9.5) show that, after strict mono-cluster selection, the peak is composed almost exclusively by real X-ray events. That solution gets its primary purpose, the efficiency is actually constant in RoI (at least from 3 to 6 keV), however there is an obvious objection: the discrimination criteria are not optimized neither at 6 nor at 3 keV.

Ideally one can try to model the energy dependence that should be followed by the *good* observables' pdf and use the two peaks to adjust it, what would introduce a continuous energy dependence in the discrimination criteria. That approach was introduced by K. Kousouris for the MVA and so will be exposed in terms of q_L, but it could refer to any limit in units of σ applied in the SCA. The hypothesis is that the observables pdf is similar to that of the energy measurement itself, that is to say, the dispersion is basically statistical and limited by the number of primary charges. Being $q_L(E_0)$ the reference value obtained from the correlation matrix at the calibration peak energy $E_0 = 6\,\text{keV}$, q_L, seen as a function of the energy, could be defined as follows

$$q_L(E) = \left(\frac{E_0}{E}\right)^a q_L(E_0) \tag{8.5}$$

The exponential factor a should be expected to be $\frac{1}{2}$ in analogy with the degradation of the energy resolution with energy (see section 4.4.2.2), but it is left free so as to adjust a desired software efficiency at 3 keV. In practice a usually needs to be higher than the unity to yield an efficiency at 3 keV comparable to 6 keV. The homogeneity of MVA allows to naturally implement the energy dependence, however new symmetries are assumed by the model: the factor a is the same for every observable, the mean values have no energy dependence and the correction affects in the same ratio to all the directions. The possibility of intrusion of background

events in the accepted volume increases. For instance, if an observable has an energy dependence that makes the mean value to be lower (as it is the case of clusters strips multiplicity), (8.5) will drive to the extension of the acceptance volume to higher values of the multiplicity[7]. The approach of the energy correction of the observables' pdf, as it has been formulated here, works reasonably provided the detector shows good performance[8].

An intermediate approach could be the subdivision of the CAST RoI in two sub-ranges: a high energy range, where the discrimination criteria is defined with the 6 keV peak and a low energy range which would have the 3 keV peak as the reference. That solution has never been applied systematically because it would involve longer calibration runs in order to increment the escape peak statistics. It has the objection of producing an artificial frontier around 4.5 keV.

The progress in this issue should be boosted thanks to the recent installation at CERN of a new CAST micromegas test-bench to calibrate the detectors at different energies[203] (see more details in section 11.2).

8.4 Towards a better understanding of CAST background.

The transformation experimented by the sunrise spectrum between 2007 and 2012 (see the comparison in the figure 8.6) shows how the improvement in data analysis can help to have a more accurate picture of the background nature, in this case with a clear signature of a background dominated by fluorescence peaks. However, those will always be indirect hints that have to be interpreted. Our idea about a useful picture of the background must be based in a set of unequivocal cause-effect relationships, so the different contributions to the background can be evaluated. That allows to think in specific strategies.

The 2007 shielding aimed at a long list of potential background sources at the same time: external γ flux[9], neutrons, radon emanations. Though its efficacy was proven, several years later the specific importance of their contributions were still unknown. In contrast, the 2012 shielding were designed following well defined guidelines (section 8.2.1.3), the minimum required lead thickness was fixed to 10 cm while special cautions against Rn and neutrons were not considered. In order to get a justified intuition of the direction to follow, studies beyond the immediate CAST environment must be undertaken.

The next block of three chapters is a summary of the a research program which,

[7] This kind of cases are studied by means of simulations in section 9.5.

[8] The main objections indicated here seem not to be essential and could be considered in a future analysis upgrade.

[9] That was the main motivation for the shielding, inspired by the old TPC background dependence on its relative position to the dirty concrete wall in the CAST area. However such a position sensitivity had not been observed in the old micromegas detectors.

with the aim of improving the CAST detectors background, started in 2009 from the intuition that some environmental factors could have been limiting the final micromegas background. The (still not finished) program consists in two research lines which are independent, but complementary. The first one, the implementation of a Monte Carlo simulation of the CAST micromegas detectors (chapter 9) detailed enough so as to predict background levels after CAST analysis discrimination. And a second one, the construction of a set-up able to hold a CAST micromegas detector reproducing CAST conditions and to modify them so as to carry out specific tests (chapter 10). The simulations have the advantage of defining an unequivocal cause-effect relationship, but the impossibility of proving an undoubted plausibility. Many times, even if the cause-effect was perfectly described in the simulation, the cause itself is not known with the needed accuracy to yield precise predictions. On the other hand, with a test-bench one can directly influence the cause-effect channel, even if neither the cause nor the effect are previously known. If the detector properly works and the results are reproducible, the result is definitive. However many times the result is not easy to be interpreted. Therefore both lines have evolved in parallel though the results in each have influenced the development of the other.

Chapter 9

Simulations of the CAST micromegas background.

Contents

9.1 Simulation model description.

This chapter describes the simulation for the understanding of the background of present CAST micromegas detectors. The simulation relies on RESTSoft, indeed some of RESTSoft present features were developed for it. Therefore most of the simulations stages are just particular usages of the classes described in chapter 6. The GEANT4 program, that is the first stage describing the interaction of the radiation with the materials, is a particular version of the general RESTSoft GEANT4 application including a more detailed description of the micromegas chamber, the

geometry of the CAST sunrise set-up (see section 9.1.1) and a specific study of cases (see sections 6.2.6 and 9.2.3).

The main novelty of these simulations was the aim of taking into account the discrimination capabilities of CAST micromegas to determine the final background. Reproducing the electronic signals of the acquisition is the most reliable way to do it, thus the same analysis routines used with CAST real data could be applied to the simulated data. Not only the use of the RESTSoft routines for pulse generation, but also the simulation of the strips readout were needed and a specific event holder class, *TRestDaqCASTevent*, was implemented.

The process up to *TRestDaqCAST* event and the present degree of accuracy is reported in section 9.1.2. After that, an external program translates the data to the CAST raw data format, and then the common CAST analysis can deal with it as if it was delivered by the acquisition (the way it was described in the previous chapter). Doing that has the additional advantage that the simulations can be used to check the analysis working, a possibility that is shown in section 9.5.

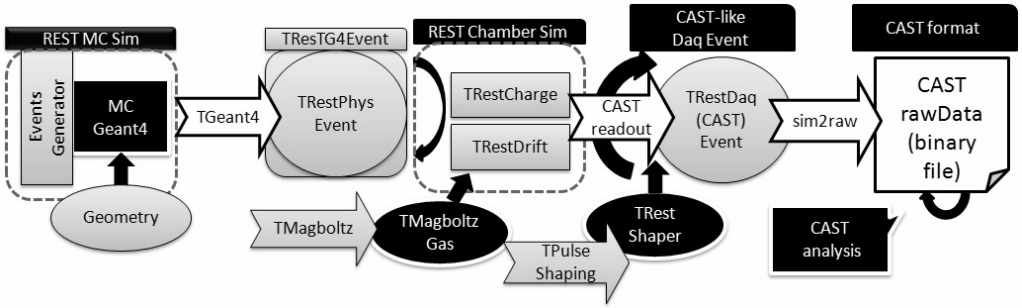

Figure 9.1: General sketch of the complete simulation chain. With a specific description of the sunrise set-up geometry, the usual simulation chain described in chapter 9 is used to produce *TRestPhysEvent*s which have drifted to the micromegas. Then a new event holder class, *TRestDaqCASTevent* has been implemented to produce and hold the DAQ-like data. The *sim2raw* program yields the data in the proper format. The three levels of data processing are accesible at every moment: *TRestG4Events* with the information rescued from the GEANT4 simulation (see section 6.7), *TRestDaqCASTEvents* (see section 9.1.2) with raw-data as it was generated (not subjected to analysis interpretation) and, finally, analysed events (see section 8.3.1), that the discrimination routines will consider.

The *micromegas plus set-up (geometry plus acquisition) model* is used in section 9.2 to compute the contribution of a particular background source, the environmental γ flux generated by natural radioactivity in the CAST area. The simulation of a γ flux from the simulation of single γ evaluates the response of the detector to that kind of events. Using these data a *high level* model is constructed which enables to compose a final background for a given environmental γ flux, without necessity of new simulations.

The actual CAST area environmental γ flux is studied in section 9.2.4. It is today known that the environmental γ flux is the dominant contribution to the background in set-ups with light shielding, up to the point that the simulation results provide results comparable with the actual sunrise background.

Therefore this kind of simulation is a clue to check also the *micromegas plus set-up model*. In fact an experimental cross-check with a radioactive source was carried out and is exposed in section 9.3. Once well established, the detector model can be applied to new background sources of increasing interest after the 2012 upgrade (see section 9.4).

9.1.1 Geometry.

The CAST sunrise set-up (SRMM) was used as the model of the geometry (see figure 9.2) since it represented the state of the art until Summer 2012, when the sunset set-up (SSMM) was upgraded. The geometry is reproduced in detail, though not exactly. Besides the shielding's layers and their respective thicknesses (which are sketched in figure 9.3 right), there is special interest in the materials that are directly exposed to the detector and in the imperfections of the detector's coverage by the shielding (like Polyethyene's shielding asymmetry) or outlets (like the front outlet of the shielding for the introduction of the vacuum system pipe).

The micromegas is essentially represented by a copper thickness that must contribute to the background fluorescence (see figure 9.4 left). However the structure of the cathode's window is precisely reproduced because of its importance for the detector quantum efficiency (see figure 9.4 right and section 6.2.7.1).

According to the same idea, the sunrise pipe that connects to the magnet's bore was reproduced with special precision, implementing all the connections between the vacuum system and the detector, even low density materials, that affect the coverage of the chamber's window. That includes the recently installed front shielding (drawn in pink in figure 9.2, see a photo in figure 9.44). The detector complete body (raquette) and Faraday cage as well, as they protect the second shielding's weak point: the raquette's neck.

Finally three virtual surfaces, which are not represented in the pictures, are present at the three main shielding's entrances in order to register the passage of external particles. One is inside the vacuum pipe at shielding's outermost level, but there is not any surface covering the complete shielding outlet which is slightly wider than the pipe diameter; a second one is the cathode's window itself and the last one is placed in the raquette's neck below the lead shielding.

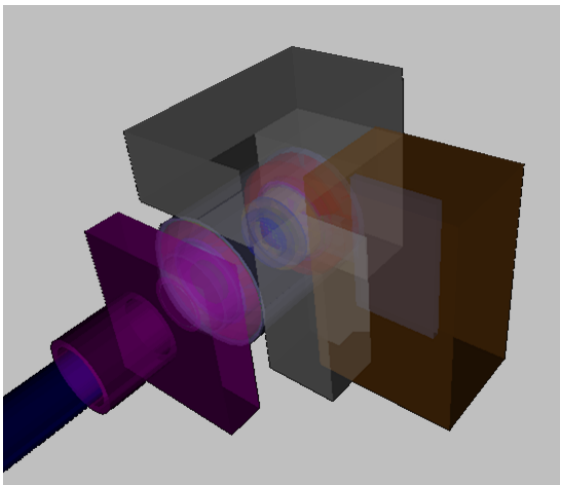

Figure 9.2: General view of the complete SRMM as implemented in GEANT4. Note the pipe to magnet partially shielded, the Faraday cage covering the detector's raquette and the polyethylene blocks.

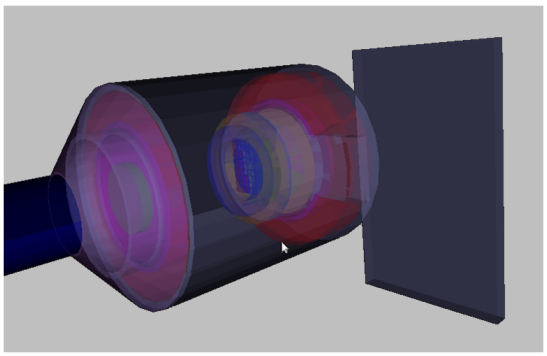

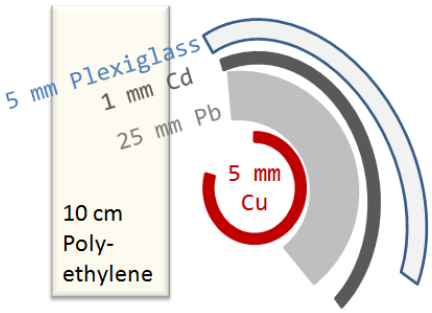

Figure 9.3: Left: GEANT4 SRMM geometry, detail of the shielding and pipe connection, to be compared with figure 8.7 left. Right: sketch of the shielding's layers.

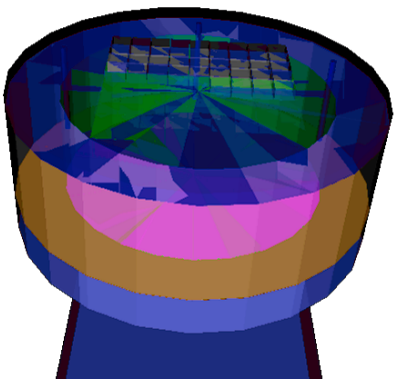

Figure 9.4: Left: GEANT4 geometry, detail of the detector. Right: sketch of the micromegas' layers.

9.1.2 Micromegas model.

Event generation and diffusion effects.

As it is shown in figure 9.1, the simulation follows the typical RESTSoft input-output chain scheme. The usual drift chamber simulation chain (see section 6.3.3) produces events like the ones represented in figures 9.6 and 9.8 left: charge distributions to which the diffusion effects have been added. The diffusion has been simulated according to the data obtained from Magboltz that is represented in figure 9.5, which corresponds to Ar/iC$_4$H$_{10}$ 98/2 at 1.4 bar and was evaluated at the drift electric field of 100 V/cm.

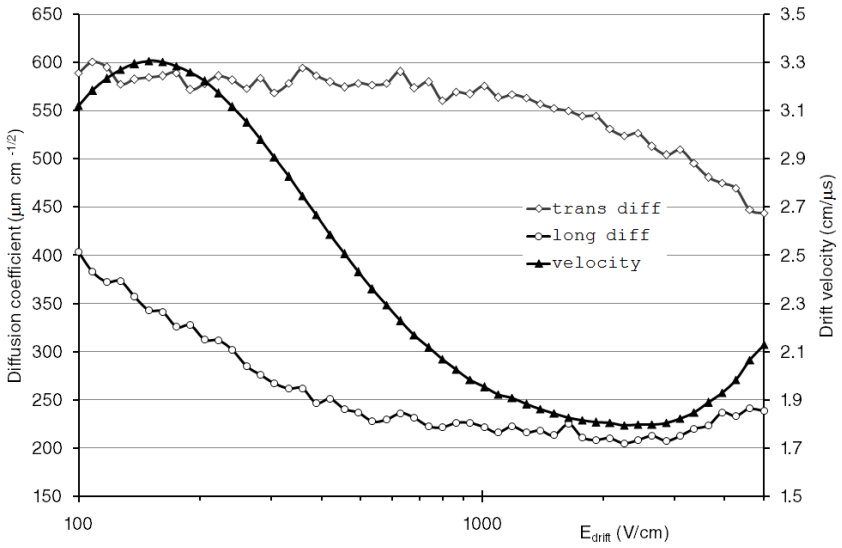

Figure 9.5: Gas properties as stored in the TMagboltzGas object used in the simulations. The CAST operation point is in the lowest drift field.

Drift and projection to the readout.

The charge distribution is projected into the three axis. The x and y axis (readout plane) are binned according to the readout pitch (figures 9.6 and 9.8 right) and the z with a short enough one, 5 ns, after calculation of the arrival time of each electron to the mesh according to the drift velocity (figures 9.7 and 9.9 left). That is the information stored in a *TRestDaqCASTevent*.

Amplification and transparency.

After the projection, the charges are amplified electron by electron. The avalanches are simulated using a single gaussian distribution (see section 6.3.4) since with an amount of primary charges around 75–227 and a mean strips multiplicity about 4-9 the number of avalanches contributing for each strip signal seems, in most of cases, big enough to justify that approximation (see figure 6.14).

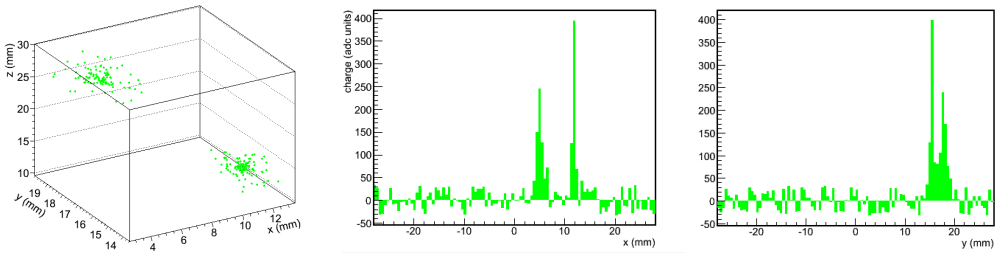

Figure 9.6: A double 3 keV photon event from a ^{55}Fe calibration. Left: charge distribution in the chamber, with diffusion effects Right: readout projections with strips noise addition.

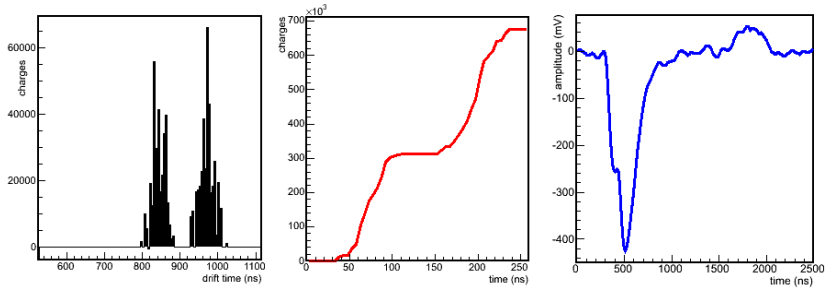

Figure 9.7: Mesh processing for the same event of figure 9.6, a double 3 keV photon. Left: temporal projection. Center: PA-like pulse. Right: time-amplifier pulse with noise.

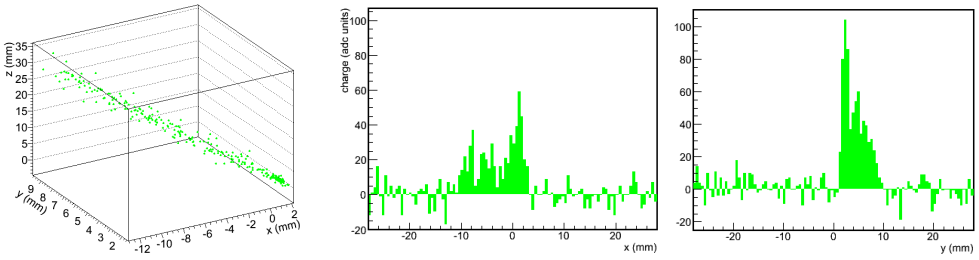

Figure 9.8: Charge distribution in the chamber (left) and readout projections (right), as in figure 9.6 for a high energy electron track crossing the chamber.

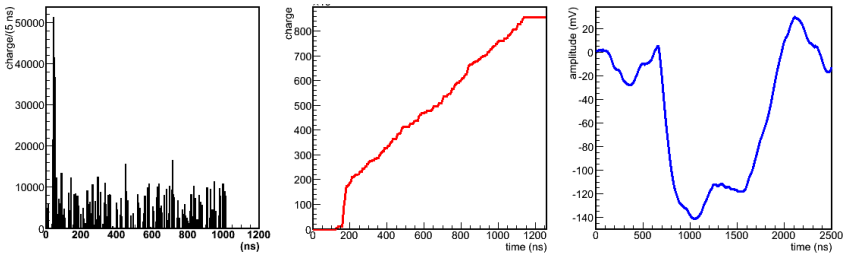

Figure 9.9: Mesh processing for the same event of for the same event of figure 9.8.

The avalanche is designed so as to produce a 12% FWHM peak at 6 keV; since the Fano factor for argon, $F = 0.2$, used in the primary charge generation, already limits the energy resolution to 7% FWHM, the total process yields $\Delta E = \sqrt{12^2 + 7^2} \simeq 14\%$ FWHM at 6 keV as the statistical limit for the micromegas (see figure 9.10 left). That selection surely overestimates the statistical variance during the amplification because smaller microbulk prototypes show about 11% total FWHM for ^{55}Fe calibrations in the same conditions (see section 4.4.3, in particular figures 4.22 and 4.23), a value that was justified regarding the statistics of the avalanche models in section 4.4.2.2. Therefore the degradation of the resolution must be mainly due to spacial inhomogeneities of the gain in larger CAST microbulks, which are not taken into account in these simulations. Regarding the mesh transparency, it is supposed to be fully transparent, as the CAST detector works inside the plateau.

Noise and electronic signals.

Up to this point the integral of the three signals (charge on x and y and time) is perfectly proportional. Three independent electronic gains can be configured for the mesh and the strips. However, for each strip signal an extra contribution is added to simulate the pedestal noise. These pedestals follow a gaussian distribution whose standard deviation can be independently defined for each strip.

The amplified charges are summed up as they are produced in the mesh (arrival time) to draw something similar to the pre-amplifier (PA) pulse (figures 9.7 and 9.9 center). That pulse is shifted, so the absolute z information is lost, to match with a certain pre-trigger period, as it is configured in the real DAQ to devote some time to define the pulse baseline.

The case of the strips signals will be discussed with some detail below, but for the mesh signal it relies on the usage of the *TRestShaper* class (see section 6.4). The *TRestShaper* is given the PA pulse which, after derivation and addition of a certain level of random noise, produces the input wave for the signal generator algorithm (figures 9.7 and 9.9 right).

9.1.2.1 Comparison with a real detector and tuning of the model.

The M17 detector, in operation in the LSC (see chapter 10), is chosen as the reference to compare with the simulated signals. This is a detector with an excellent performance. The goal is not the simulation to deliver the exact detector values, because they depend on the particular detector and settings, but to reproduce the general tendencies and correlations between observables[1], i.e. the detector's behaviour.

Regarding the mesh pulse.

The convolution mode of *TPulseShaper* (see section 6.4.2) is used; though it can give only a discrete number of risetime-width ratios, it was found that the 4-degree

[1] The observables we will refer to were defined in section 8.3.1.

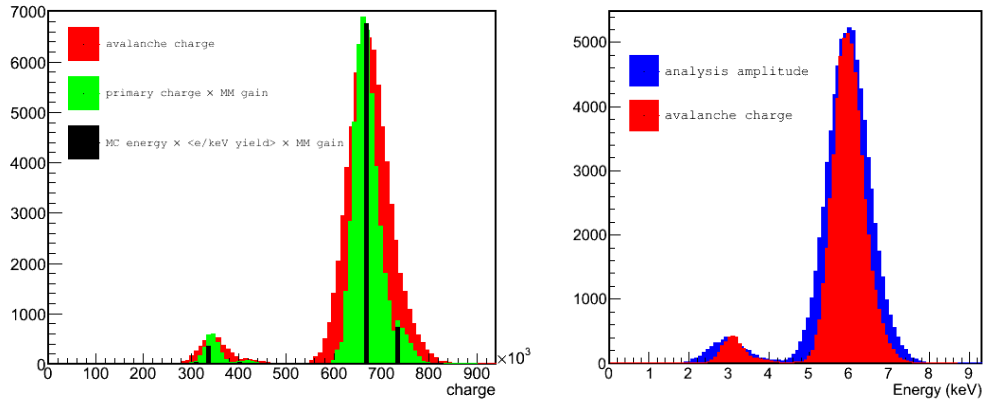

Figure 9.10: Contributions to the energy resolution for a ^{55}Fe spectrum. Left: effects of the successive chain transformations from the original energy lines, as registered by the GEANT4 application, in black; in green the status after the primary charge generation in the gas and, in red, the spectrum after the avalanche process in the micromegas. Right: Degradation of the spectrum (the same that was in red on the left) after noise addition to the mesh pulse and CAST analysis interpretation from the pulse amplitude. Note: the spectra have been renormalized for an easier comparison.

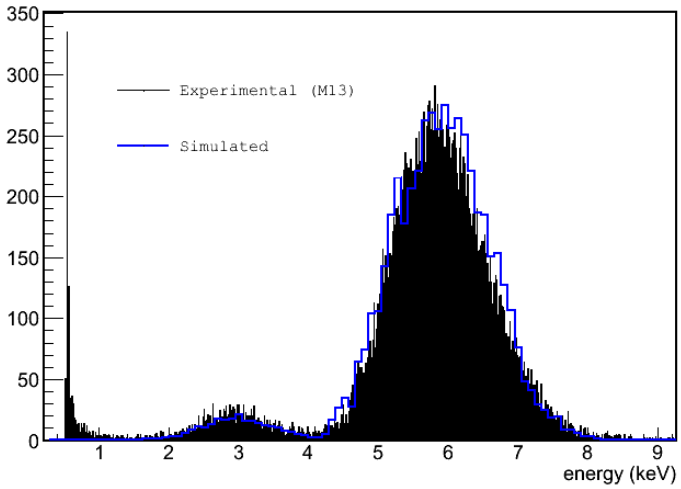

Figure 9.11: Comparison with an experimental CAST microbulk (M13) spectrum taken with a MCA (so reading the mesh pulse amplitude). The relative size of the photo-peak and the escape peak is a cross-check for the GEANT4 simulation, as it depends on the Physics and the detector's geometry.

unipolar delta-response adjusts quite well the M17's pulses shape as produced with the settings of the LSC DAQ (see table 9.1 and figure 9.12). The absolute values are reproduced using a peaking time of $t_p = 250$ ns. However the summary table

9.1 shows that the simulation is underestimating both the individual (regarding one unique observable) and relative (regarding the ratio or balance between two observables) variations.

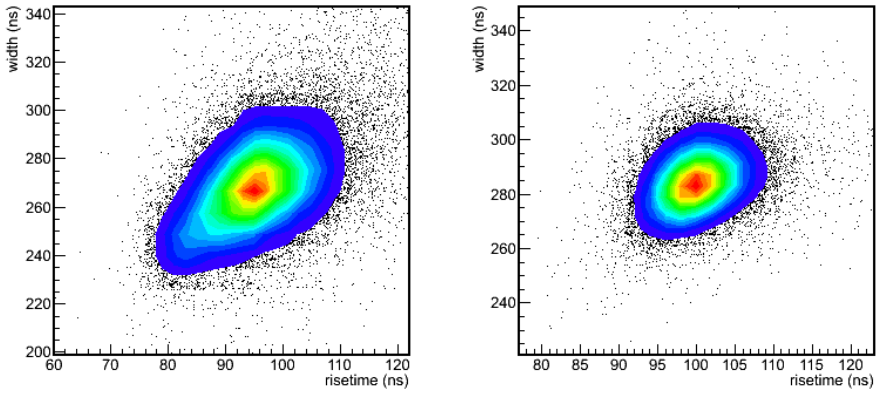

Figure 9.12: Experimental (left) and simulated (right) distributions for the main pulse shape parameters from a ^{55}Fe calibration. An ellipse with low eccentricity presents two observables softly correlated (for point-like events).

The effect of noise.

The most obvious cause of variation of the pulse shape parameters is the noise. However a increase of the signal to noise ratio (SNR) was checked to have a stronger effect on the energy resolution degradation than on the variance of the pulse shape values (that is a good sign for the CAST raw-data analysis robustness). A random noise amplitude ratio of 12% of the signal for a 6 keV pulse (i.e. a threshold around 0.75 keV, more or less coincident with the experimental one with the M17 at LSC), which has been used for the table 9.1, is the maximum one that does not produce an energy resolution worse than the real one. Besides the noise produces an error in the determination of the baseline level which propagates to both the rise and width estimations in the same sense (the lower the baseline level, the longer the times) yielding correlated variations.

The effect of the diffusion.

Another cause of pulse shape variations are the natural variations in the distributions of the arrival time of the charges to the mesh. Those depend mostly on the diffusion and then on the absolute position of the interaction. That is studied for a ^{55}Fe calibration from the window in figure 9.13[2].

We see from the plot on the left that most of the interactions are produced near the window, being 20.07 mm the average drift distance, z, in the 30 mm height

[2]This is an example of the usefulness of the availability of event descriptions at different processing levels.

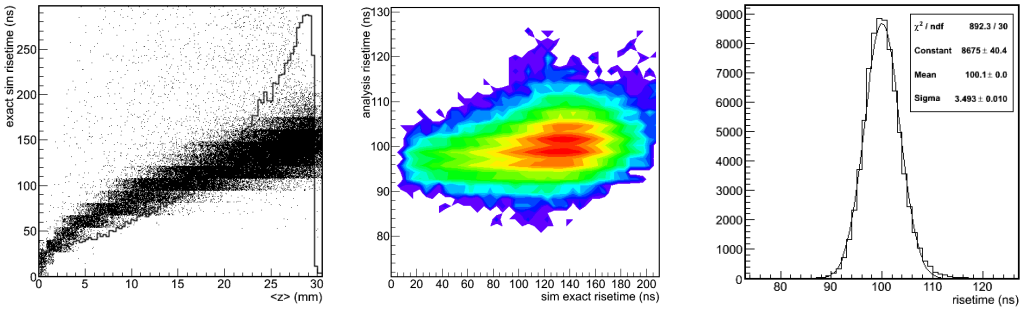

Figure 9.13: More distributions and relationships from a ^{55}Fe calibration. Left: *exact risetime* as a function of the drifted distance (z as the mean value from a fit to a gaussian function of the charge distribution) and histogram with the z distribution. Center: risetime as calculated by CAST raw-events analysis vs *exact risetime*. Right: total risetime distribution obtained with the CAST analysis.

chamber. The *exact risetime*, calculated as the difference between the mesh arrival time of the first and last electrons, goes with $\backsim \sqrt{z}$, as it is expected by construction. With 227 primary electrons on average we can relate this risetime with the σ from a gaussian fit of the distribution of the arrival times as $\approx 2 \times (3 \times \sigma)$. From the value of $\sigma_l \simeq 400\ \mu\text{m}\ /\text{s}^{1/2}$ taken from figure 9.5 and $v_{drift} \simeq 5\ \text{cm}/\mu\text{s}$ we have $\sigma \lesssim 25$ ns (when fitted to a gaussian, the charge distributions of figure 9.7 left yield $\sigma = 15$ ns). Therefore, for high z we are at the limit $\sigma \ll t_p$, i.e. $\sigma \lesssim t_p/10$, when the characteristic response function of the amplifier starts being affected by the temporal duration of the event (see figure 6.18 left).

In figure 9.13 in the middle can be observed how the analysis-deduced risetime is independent on the physical risetime up to the latter reaches ≈ 120 ns ($\sigma \approx 20\,\text{ns} \simeq t_p/12$), then the distribution becomes moderately growing with z [3]. Finally, because of the accumulation of events at high z and the dependence is soft, the risetime observable total distribution (i.e. summing up all the calibration events) is gaussian (figure 9.13 right).

Variations of the electronics response (a possibility).

Even though the paragraph above suggests that drift properties worse than the assumed by the simulation would have an effect in variations of the observables related with the pulse shape, that would be again correlated for risetime and width. Perhaps the only way to justify the non correlated variations would be the assumption that the electronics response is not perfectly stable and the introduction of

[3] Such a plot cannot be produced experimentally, nevertheless the straight line during most of the range is essential to assure no z dependence of the software efficiency and should be checked somehow, e.g. modifying the drift properties or using different energies for calibrations and then modifying the z distribution (see section 9.5.3, about the new CAST test-bench at CERN).

variations in the pulse shaping parameters for each pulse generation process. We note down this as a possibility of future improvements.

However we are going to consider acceptable the comparison done in the summary table 9.1 and the commented figures reasoning that *a too much stable pulse shaping could produce overestimated rejection capabilities for some background channels (electron and muon tracks, coincident photons ...) that produce bad pulse shapes, but the essential (unavoidable by analysis means) background, that composed of true mono-X ray events, must be well described.*

Regarding the strips signals.

Several possibilities have been implemented in *TRestDaqCASTevent*, that produces its own contents. The main features to be reproduced are the distribution of the observables that describe the event size (cluster multiplicity and sigma, see section 8.3.1), the differences between the x and y lectures, the energy resolution and some balances.

About the distribution of the charges x and y.

It must be remembered that using just a projection on both axis of the (already amplified) charges produces identical integrals in x and ys. There can be several causes that contribute to *the differentiation of the lectures of the charges of x and y axes*. The modern CAST microbulks mesh design (see section 8.2.2 and particularly figure 8.12) suggests an essential origin for a differentiation. The mesh pattern, composed of isolated holes groups over a *pixel* is conceived for a particular primary electron to produce an avalanche confined only on one pixel. According to Ramo's theorem (see section 4.5), if the signal is integrated (as the Gassiplex card does with the strips signals) finally only the electrons physically collected by the pixel will contribute to its associated signal amplitude. This option was implemented in *TRestDaqCASTevent*; then, given a final position for a primary charge after the drift, that is collected only by one strip and the simulated avalanche contributes only to the signal associated to this strip.

We will try an estimation of the deviation from zero in the charge balance, $B(ch) \equiv (ch_x - ch_y)/(ch_x + ch_y)$, due to the effect of the distribution of the primary charges between the x and y axes. The amount of electrons contributing to a strips axis from a ^{55}Fe X-ray follows a binomial distribution whose standard deviation is $\sigma = \sqrt{np(1-p)} \simeq 1/2\sqrt{227}$, since $n = 227$ primary electrons and $p = 1 - p = 1/2$. Note that the deviation in the difference is given by $2\times\sigma = \sqrt{227}$, since the deviation in one axis is followed by exactly the same deviation in the opposite sense in the other. Therefore the charge balance would be statistically limited to have a standard deviation about $\sqrt{227}/227 \simeq 7\%$. The experimental deviation for the M17 detector is 9% (see figure 9.15 and table 9.1).

About the size of the clusters.

Another differentiation factor between the x and y axes is the noise, which is added independently to each strip following a gaussian distribution around the pedestal value. The SNR also determines the analysis multiplicity from the original charge distribution projection on the readout axes (see figure 9.14 left). The multiplicity of the *TRestDaqCASTevent*, the *exact* multiplicity, i.e. determined by means of an ideal threshold, not affected by cross-talk nor other secondary effects, is a first reference, a kind of upper limit.

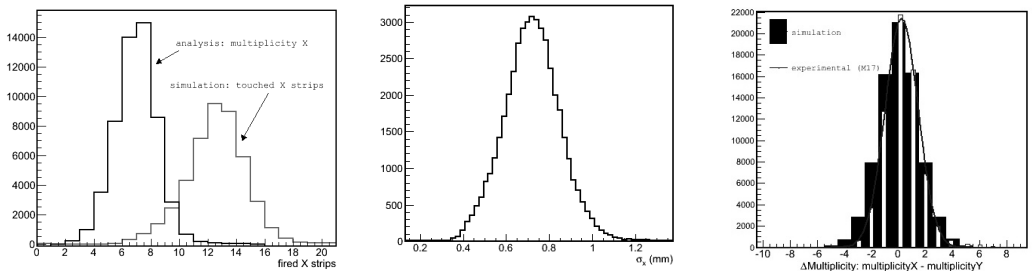

Figure 9.14: Left: *exact* multiplicities (no threshold, no noise) together with the probability distributions resulting from the CAST analysis. Center: one-dimensional cluster size σ_x. Right: experimental vs simulation multiplicities difference, the simulation slightly overestimates the difference.

Note that the *exact* multiplicity distribution is intrinsically asymmetric, as the final experimental distribution is (see figure 8.17 center). This asymmetry has the same origin shown for the risetime in figure 9.13 left, so it is due to a drift distance dependence of the observable; although, in this case, it is noticeable in the total distribution because the diffusion is more severe in the transversal direction. The same happens to the cluster size σ (see figure 9.14 center). That distribution has the advantage of being continuous and should be more robust, however, for detectors yielding low multiplicities, the distribution can be too close to zero, which can be origin of serious discrimination problems.

In contrast, the multiplicity difference, $M_x - M_y$ [4] (see figure 9.14 center) and the σ balance are gaussian distributions, like the charge balance. Note that the SNR of 1% of the 6 keV signal for every strip, that reproduces the proper multiplicity values (table 9.1), is already yielding an overestimated charge balance (figure 9.15 left); even though the charges were shared between all the strips. Although the differentiation about 7% due to the possible distribution of charges between strips that was explained before has not contributed here, the differentiation is already high.

[4] The multiplicity balance does not produce a good pdf because it is built from originally discrete pdf's composed of low numbers and then only a few values are repeated all the times.

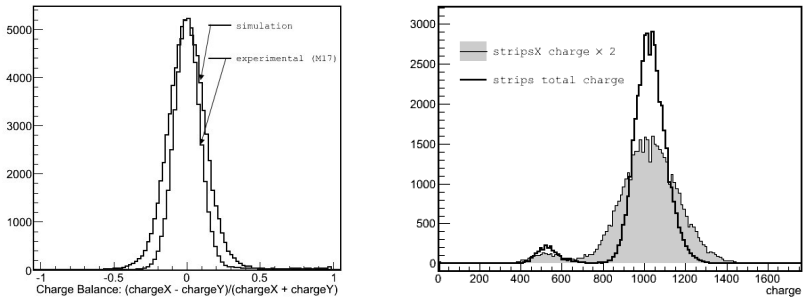

Figure 9.15: Left: experiment vs simulation charge balance. The simulated charge difference is only due to noise addition, however it overrates the reality. Right: partial (only one axis) and total (both axes summed) strips charge. The improvement is due to noise compensation (since the electronics statistics were shared).

Decreasing the noise produces a fast increase of the multiplicity and the decrease of the multiplicity difference. The noise addition seems necessary for reproducing the strips energy resolution. But the already mentioned SNR of 1% of the 6 keV is yielding a too good energy resolution final value (compared with the mesh). Additionally, it is thought that there can be cross-talk between neighbouring strips. That possibility has been implemented for adjacent strips with one or more iterations (then affecting to farther strips). Still such a process increases even more the multiplicity, but keeping the charge and multiplicity balances. Therefore it must be concluded that the charge balance of CAST microbulks is better than expected, regarding their energy resolution[5].

Thus we are going to accept the *noise as the only cause of differentiation between the lectures of the x and y axes, even though both the distribution of the primary charges and the cross-talk are well motivated*, because in practice that choice produces the most similar electronic signals and probability distributions of the CAST micromegas (see figure 9.16 and table 9.1). An increase in the balance tolerance will entail a strong negative impact on the discrimination capabilities.

Balances between mesh and strips signals.

Finally, a cross correlation is checked also graphically in figure 9.17. The most interesting thing is the accumulation of events around the region *(mesh amplitude, strips charge) = (3,6) keV*, which is present in both plots. The situation is very similar to that explained in figure 8.17.

[5]Some ideas to solve this paradox could be the introduction of some electronic attenuation of the signals or a discrete threshold for the gassiplex card to response combined with cross-talk; or the usage of a different noise distribution.

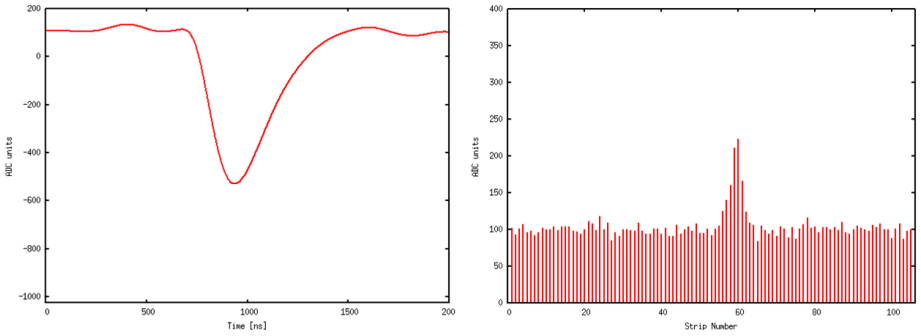

Figure 9.16: Mesh pulse and strips (x) signals for one 6 keV event, simulated with the settings justified in this section. To be compared with figure 8.15.

Observable	Experiment (M17)	Simulation
risetime [ns]	95 ± 7	100 ± 4
width [ns]	267 ± 15	284 ± 10
width/risetime	2.81 ± 0.20	2.85 ± 0.11
B(amplitude,integral)	$< 10^{-2} \pm 2.0 \cdot 10^{-2}$	$< 10^{-2} \pm 1.6 \cdot 10^{-2}$
Δ(multiplicity)	0.22 ± 1.3	$< 10^{-2} \pm 1.5$
B(σ_x, σ_y)	0.027 ± 0.13	$< 10^{-2} \pm 0.20$
B(charge$_x$,charge$_y$)	$< 10^{-2} \pm 0.09$	$< 10^{-2} \pm 0.13$
skew $\equiv \frac{1}{c}\sum_i c_i \left(\frac{i-\mu}{\sigma}\right)^3$	$< 10^{-2} \pm 0.28$	$< 10^{-2} \pm 0.29$
B(amplitude,charge)	$< 10^{-2} \pm 2.5 \cdot 10^{-2}$	$< 10^{-2} \pm 3 \cdot 10^{-2}$
B(integral,charge)	$< 10^{-2} \pm 1.5 \cdot 10^{-2}$	$< 10^{-2} \pm 4 \cdot 10^{-2}$

Table 9.1: Simulation experiment agreement summary table for gaussian pdf's. Mean values and standard deviations are given. B(x,y)≡ (x-y)/(x+y).

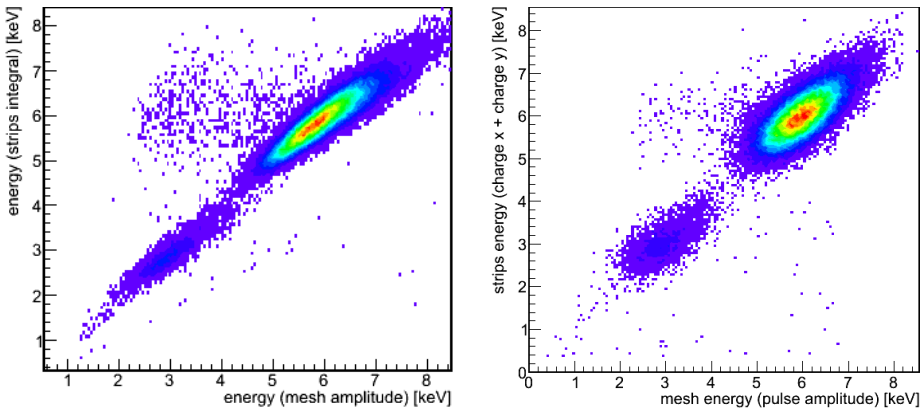

Figure 9.17: Strips and mesh pulse energy lectures during a ^{55}Fe calibration. Experimental with M17 CAST microbulk (left) and simulation (right).

9.1.2.2 Analysis tests.

Probably the best cross-check for the simulations is studying the effects of the application of CAST discrimination routines on simulated data. Besides, this leads to the opportunity of testing the physical meaning of the analysis selection.

We are going to pay some attention to a set of simulated events originated from 1460 keV γ, as those of ^{40}K. On the left of figure 9.18 the spectrum formed by the energies deposited in the CAST chamber is represented. These are ideal energy depositions as delivered by the GEANT4 simulation. The spectrum has a typical energy decreasing slope with a sharp rise around 6 keV.

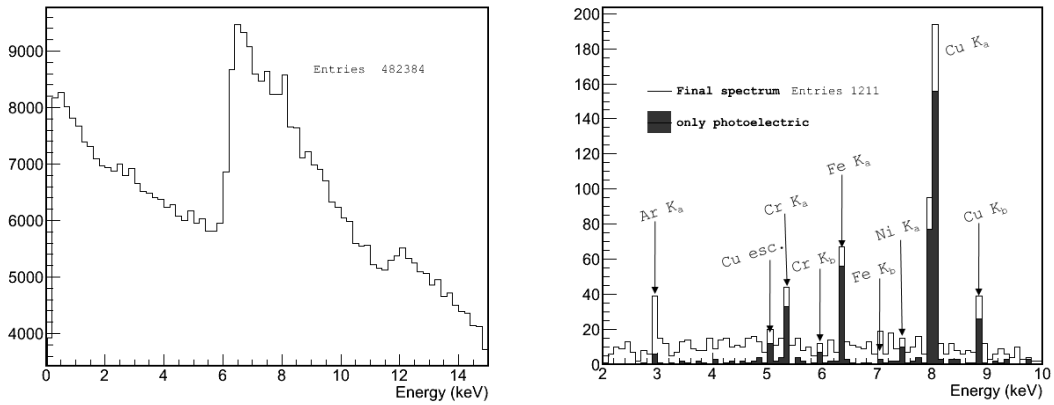

Figure 9.18: Simulated events from 1460 keV γ. Left: before discrimiation. Right: after discrimination using the set of observables (see section 8.3.1) with ID 2222 (section 9.2.1).

That shape has a simple explanation which is more easily understood in terms of the basic TPC event cases that were typified in section 6.2.6 (see table 9.2). More than 80% of the events are due to fast electrons that cross through the chamber as MIPs, thus the spectrum peaks about 7 keV, which is the corresponding energy deposition for a path of 3 cm length (see figure 3.5), i.e. the chamber height. Most of the electrons are due to interactions of the originally launched γ in the cathode and the readout. The electrons with directions other than vertical produce higher energy deposits, that produces the tail on the right of the peak; even a double track peak is rising around 12 keV.

That set of raw events are processed as explained in the previous section after they are ready for discrimination analysis. Once the selection routines have chosen a set of final events we can identify them again from the original set of TRestG4Events, and check their physical origin. The exact energy spectra for the events finally selected from the 1460 keV γ-induced set is drawn in figure 9.18 right. The shape has been reduced basically to a set of fluorescence lines (identified as produced by several set-up materials) over a flat base. When the events produced only by

Event type	Raw data	Final data
photoelectric	5.00%	38.73%
Compton effect	12.98%	48.39%
invading electron	82.02%	12.88%

Table 9.2: Basic study of cases for events originated by 1460 keV γ, before and after the application of MVA discrimination criteria (Observables set ID 2222).

photoelectric effect are drown it is clear that the analysis made a physical selection of these kind of events (see also table 9.2). From the initial 1529 photoelectric events in the raw set inside the range [2-10] keV, 1211 survived the cuts; that makes 79.2% acceptance for this event type, using MVA (section 8.3.2) configured to assure a 75% software efficiency. See section 9.5for a more detailed study.

Another cross-check is done by comparison of the results using different sets of observables with MVA. The group of observables sets (27 in total) which are used customary to analyse experimental data is applied to the same data above. All these sets are complete in the sense explained in section 8.3.2.1. Moreover, all the defined observables are included at least in one set. If one observable were failing in the simulation, the observables sets which contain it would lead to an anomaly in the final number of events after discrimination. Rather on the contrary, the final events distribution by all the observables sets is compact as it can be seen in figure 9.19. That is useful to estimate the systematic error associated to the election of a particular set. The same process is carried out with a set of events originated from much lower energy, only 100 keV γ. That has the purpose to check the same behaviour for events of a different nature, since practically all of them are fluorescences (see section 9.2.3).

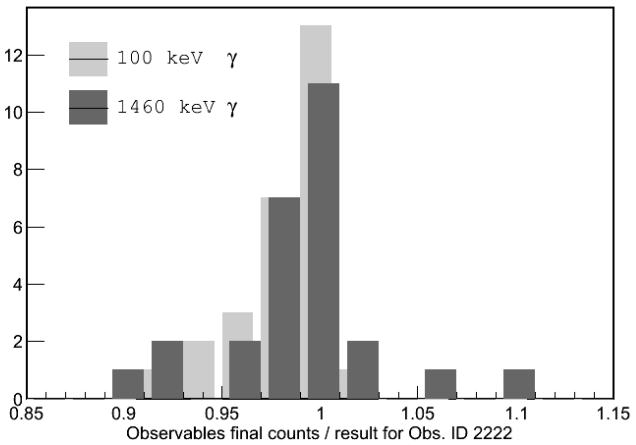

Figure 9.19: Final amount of events after application of MVA using 27 different sets of observables.

9.2 Simulation of the environmental γ flux contribution.

In this section the micromegas Monte Carlo model discussed in section 9.1 is used to study the contribution to CAST sunrise micromegas background by the environmental γ flux as consequence of the natural radioactivity of the materials of the area. The response of the whole set-up (composed of the detector plus its shielding) to external γ is evaluated in sections 9.2.2 and 9.2.3. Then the final calculation of the predicted final background is conditional upon a given environmental γ flux description. The estimation of the γ flux is an important source of uncertainty, though special measurements and analysis have been dedicated and are explained in section 9.2.4, before reporting the final results in section 9.2.5.

In principle the environmental γ flux is only one of the multiple background sources. However it was soon clear that it is the main one (at least until 2012 sunset upgrade), so much as it might be able to produce alone a partial contribution to the background comparable to the total one. This fact[6], and its strong dependency on the geometry implementation, made this kind of simulations extend in time and detail level, since entails the validation of the complete micromegas simulation model. Actually experimental measurements using a γ source have been carried out in the CAST area with the aim of testing the simulations (see section 9.3).

9.2.1 Methodology.

The environmental γ flux is simulated by launching γ in the GEANT4 application from a virtual sphere that surrounds the set-up geometry, homogeneously in the sphere surface and with isotropic directions. Different simulations runs are carried out for a set of discrete γ energies. These energies have been chosen to match the most intense emission lines from ^{232}Th, ^{238}U and ^{235}U decay chains, completed with the 511 keV peak, resulting on electron-positron annihilation, and a small set of low energy lines from 50 to 150 keV.

After the processing and analysis (as explained in section 9.1) of each γ line, the resulting *high level model* consists in a set of probabilities, spectra and related study of cases as functions of the initial energy of the γ.

- First, the probability of an event originated from an external γ of a given energy to generate a count which contributes to the final background (after the application of the discrimination criteria) inside the RoI; what we have called the *vulnerability* (see section 9.2.3).
- Second, the final spectrum generated from a simulation run for that discrete energy (also in section 9.2.3).
- Finally, the associated information that completes the picture of the final events group (see section 9.2.3).

[6] Lately proven experimentally, see next chapter.

All together represents our description of the nature of the background induced by environmental γ in the range from 50 to 2614 keV. For a given flux description (always considered as isotropic and homogeneous), the final background is built from the weighted (using the curve of the vulnerability dependence on energy) combination of spectra and other features. Contributions from γ with energies different than those characterized must be interpolated or approximated. That is done in section 9.2.5.

An important parameter for this kind of simulation, that is worth to comment, is the virtual sphere radius which has been set to 37.5 cm (centered in the origin where micromegas mesh is placed), what covers the complete shielding and Faraday cage up to the recently installed front shielding (see section 9.1.1). The pipe that connects the sunrise detector to the magnet bore is almost 1.5 m long, and its presence is important to understand the sunrise background origin. However that radius has obviously an strong effect in the GEANT4 computation time[7] and a compromise must be found. With this radius only the first few cm of unshielded pipe are contributing, but we would be sensitive to its effect in case it were relevant.

A ^{55}Fe calibration has been simulated as is done in the real set-up (from about 1 m distance from the pipe to the magnet's bore) in order to irradiate the detector in the same way. The analysis used is MVA using the observable set with ID 2222: width, charge balance, risetime/width, energy balance based on pulse height and strips charge, cluster size σ and clusters size balance; with 75% software efficiency for the 6 keV peak and using energy correction of the discrimination criteria (see section 8.3.2.2) so as to achieve 40% software efficiency for the 3 keV peak, as it has been done for real 2012 data.

9.2.2 The model: vulnerability and spectra.

9.2.2.1 Vulnerability curves.

Our first goal, the vulnerability curve as a function of the initially launched γ energy, is divided into two steps. The first step is the probability of the original single γ finally producing a count inside the 2-7 keV RoI and inside the projection of the magnet's bore area, that is the fiducial area for the analysis. This is named *raw vulnerability* and depends on the geometry and the detector quantum efficiency.

$$raw\ vulnerability \equiv \frac{raw\ counts\ in\ RoI\ and\ fiducial\ area}{launched\ \gamma} \tag{9.1}$$

Second, the probability of the count to be selected by the discrimination criteria, *acceptance* or the inverse of the *rejection power*; which regards essentially to the nature of the event.

[7] Actually each energy run is carried out in CERN's lxplus facility using hundreds, sometimes thousands, of computers during one or several days

$$acceptance \equiv \frac{final\ counts}{raw\ counts}\ \text{(in RoI and fiducial area)} \tag{9.2}$$

The obtained raw vulnerability curve is drawn in figure 9.20. The curve presents two fast falls that are moderated in the middle. Both falls are related with the probability of the original γ to go through two physical walls: the detector's shielding and the pipe's stainless steel thickness. Regarding the shielding, the γ energy is always low enough so as the shielding cannot be considered as transparent, however the mean free path in lead for the ^{208}Tl γ, $\lambda_{Pb}(2614\ \text{keV}) \approx 2$ cm, is actually near the shielding thickness. While the mean free path in iron equals the pipe thickness, 1.6 mm, approximately at the energy of 75 keV.

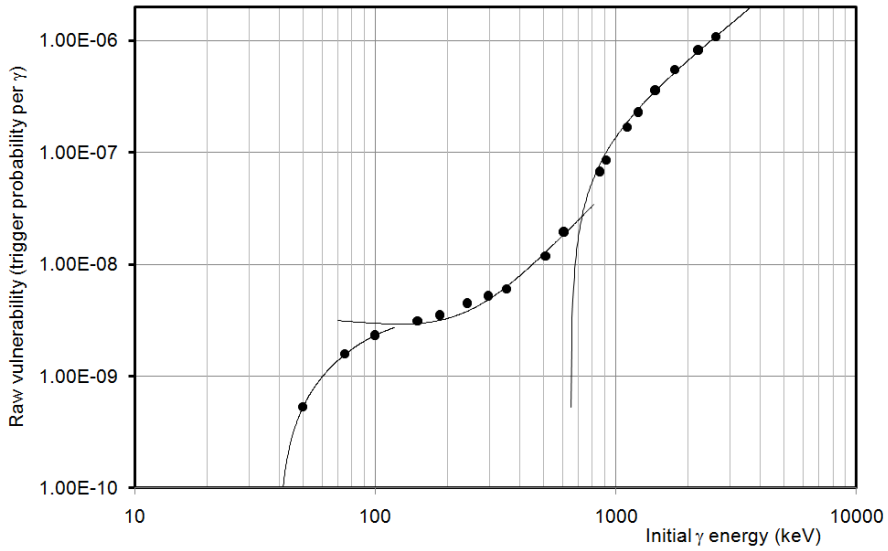

Figure 9.20: Raw vulnerability. The fits are drawn to empathize the three distinguishable ranges which are explained in the text.

Even when the event finally registered in the chamber can be only far related with the original γ, there is a clear tendency the acceptance, plotted in figure 9.21, that must be related with a change in the dominant event type (see the study of cases in next section 9.2.3).

There is a decrease of the rejection with energy, that becomes sharper at medium-low energies. It smooths the energy dependence of the final usable result (see figure 9.22):

$$fine\ vulnerability \equiv raw\ vulnerability \times analysis\ acceptance. \tag{9.3}$$

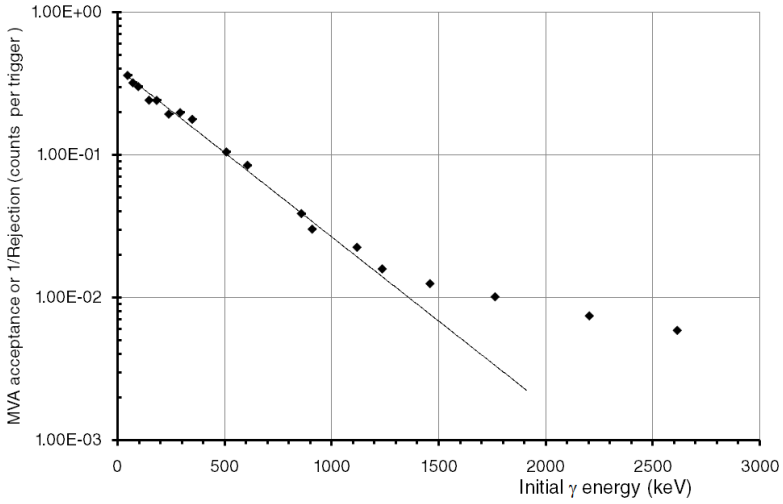

Figure 9.21: Final counts (after discrimination) per trigger (raw event registered in RoI and magnet's bore area). There is an exponential (fitted) rise at medium-low energies. Note that the rejection capabilities are reduced to only by a factor of 3 for low energy γ which are able reach the detector through the shielding.

The fine vulnerability curve is smooth enough to try a fit for extrapolation. That fit is done in three ranges (see the lines with different colors in figure 9.22), which are basically the same already detected for the raw vulnerability:

$$E < 170 \text{ keV}: \quad v \simeq (-1.155 \pm 0.28) \cdot 10^{-9} + (3.838 \pm 1.0) \cdot 10^{-12} E - (2.596 \pm 1.0) \cdot 10^{-13} E^2 + (5.964 \pm 3) \cdot 10^{-16} E^3 \quad (9.4)$$

$$170 \leqslant E \leqslant 900: \quad v \simeq (7.066 \pm 1.0) \cdot 10^{-10} + (2.374 \pm 5) \cdot 10^{-13} E + (2.075 \pm 0.5) \cdot 10^{-16} E^2 \quad (9.5)$$

$$E > 900 \text{ keV}: \quad v \simeq (-2.059 \pm 0.9) \cdot 10^{-10} + (6.117 \pm 1.2) \cdot 10^{-12} E - (1.115 \pm 0.4) \cdot 10^{-16} E^2 \quad (9.6)$$

9.2.2.2 Spectra.

Each point in figure 9.22 has an associated final spectrum produced by the CAST analysis. Only a few characteristic ones are shown in figure 9.23. They are enough to appreciate that a gradual evolution with the original γ energy also applies to the spectral shapes.

It looks like the copper fluorescence peak at 8 keV is always present, while a second peak around 6 keV, which clearly rises, is more notable at lower energies.

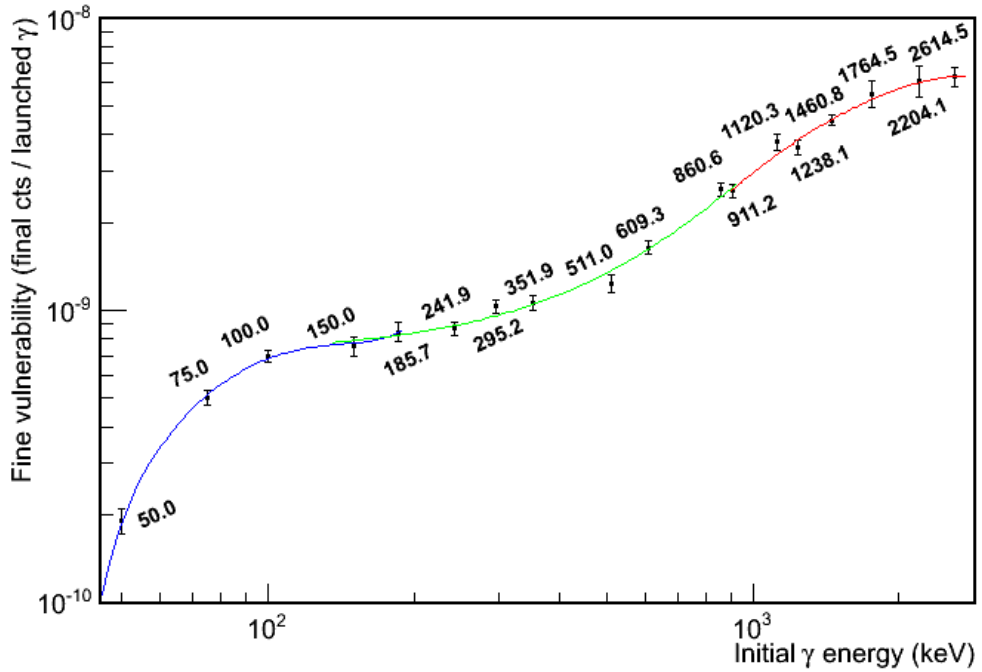

Figure 9.22: Fine vulnerability, or probability of an environmental γ producing a count in the final background in RoI and magnet's bore area. The labels point to the discrete energies for which the simulation has been performed and the three lines are the fits done for extrapolation. The bars report only statistical error at one σ.

The final relative weight between them will depend on the relative importance of the low energy γ. Equally, both are enhanced over a flat background level. The lower the γ energy, the relatively lower the flat level with respect to the peaks.

That completes the basic high level model. The progressive changes in the spectra shape allow to assimilate the contribution of near energies to any spectrum from the discrete collection. The values plotted in figure 9.22 give the specific importance of every count in the spectra and the fits (9.4) and the followings can be used for energies between the simulated ones.

9.2.3 The model: study of cases.

In this section we will discuss a qualitative description of the background. We will start again from a function of the external γ initial energy, to be able to later reconstruct the complete description from a combination of backgrounds associated to a given environmental flux. Besides the *basic chamber's study of cases* (see section 6.2.6) which divide them into photo-electric, Compton and electrons (see figure 9.24); a specific case labelling has been defined. The goal is to classify the events regarding the story which caused the chamber interaction relying on the CAST geometry, many times as a consequence of a secondary process.

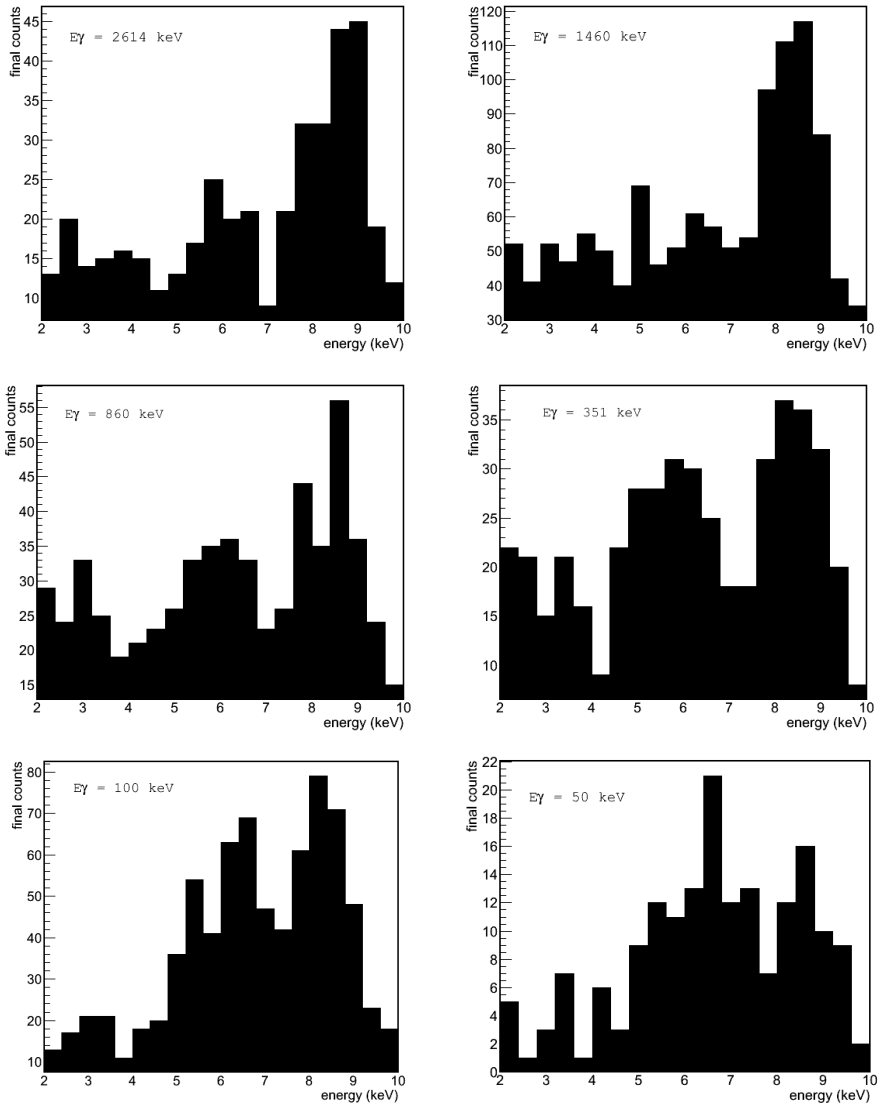

Figure 9.23: Final spectra obtained by CAST analysis for several of the simulation runs along the natural radiation energy range.

This *extended study of cases* is based on the identification of the following situations:

- Shielding Bremsstrahlung: an electron producing secondary photons by bremsstrahlung in the shielding layers (lead or copper).
- Magnet's bore pipe: any particle crossing the pipe interior at the level of the end of the lead shielding in direction to the detector. That label considers the contribution of the external (out of main shielding) piece of the pipe as a kind of attractor or antenna for γ, i.e., γ with initial different directions are

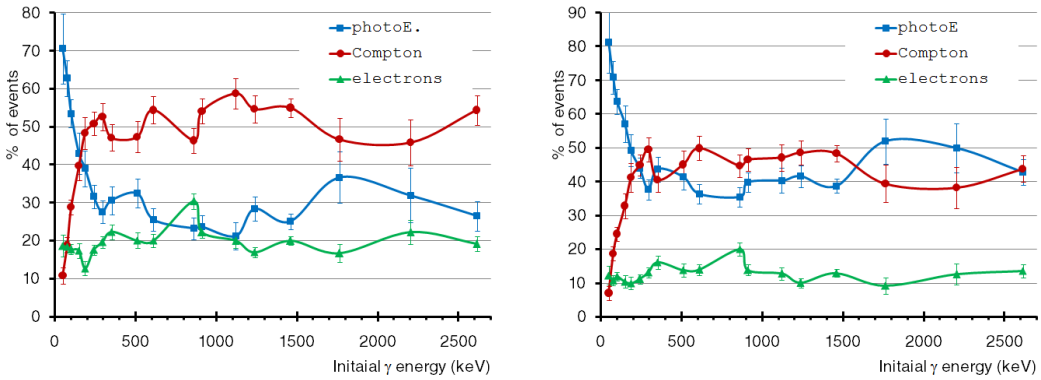

Figure 9.24: Basic cases statistics for events in the CAST RoI, [2–7] keV (left) and for the wider range [2-10] keV (right) where the copper peak is included. The bars report statistical error at one σ.

scattered by the pipe and go directly towards the detector through it. The copper front shielding over the external piece of pipe was already installed to minimize this effect.

- Cathode window: any particle crossing the mylar window and entering into the chamber.

- Detector raquette's neck: any particle crossing the plexiglass base (raquette) entering into the shielding cavity through the outlet for the raquette's neck between the micromegas and the gassiplex cards.

The percentage of final events associated to each case is summarized in figure 9.25.

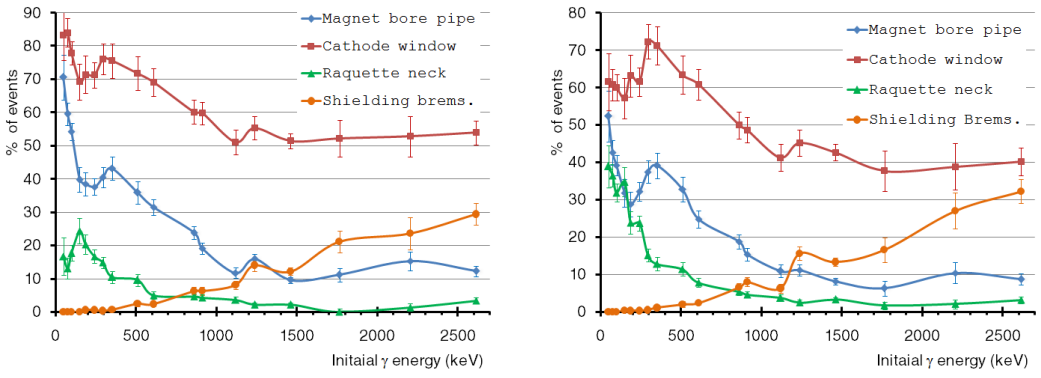

Figure 9.25: Extended study of cases for events in the CAST RoI, [2–7] keV (left) and [2-10] keV (right).

It is not assured that the action that activated one of these flags finally caused the event registered in the detector, but it is highly probable because of the simplicity of the simulation started by a single γ with very low probabilities to produce a trigger. In contrast to the basic chamber cases, these labels are not mutually exclusive (pipe and window are specially related) and not mandatory (events can be caused for none of these cases).

The graphics in figure 9.24 show that the relative proportions of the basic cases are near constant during most of the energy range, where photoelectric and Compton are the most important processes, being the Compton clearly dominant inside the CAST RoI since most of the photoelectric processes are related with the 8 keV copper fluorescence. There is a sharp change in the picture that starts around 300 keV, the photoelectric becoming dominant about 150 keV and finally producing most of the events. It can be seen in figure 9.26 how the Compton process produces basically a flat background in the RoI, while the photoelectric is strongly correlated with the fluorescence lines (see figure 9.27 and 9.18). Therefore a background presenting a peak signature in RoI must count with a relatively important contribution from low energy γ.

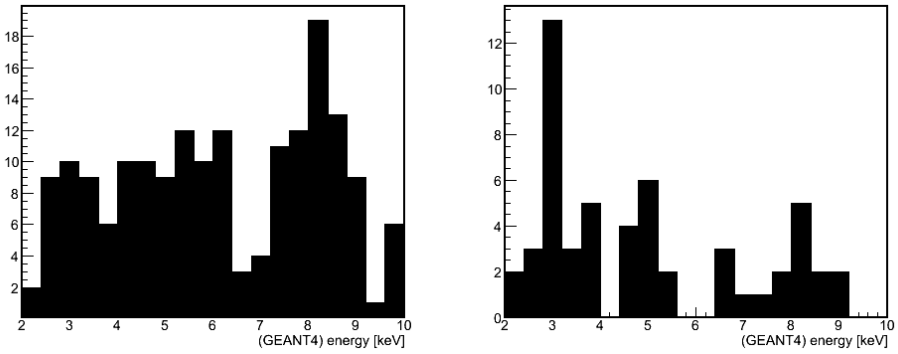

Figure 9.26: Partial final spectra of Compton and electron cases for the $E_\gamma = 2614$ keV run (see the total spectrum, the first one in figure 9.23). Left: Compton contribution (43.7% [2-10 keV]). Right: electrons contribution (13.5% [2-10 keV]).

It might be surprising to have a contribution from electrons, moreover almost constant with energy, passing the discrimination criteria. It can be seen as a border effect, because most of them are really photo-electrons produced in the cathode or the readout which burst into the chamber leaving a fraction of their energies. Besides, a fraction of them are related with true electron tracks which be taken as an X-ray event[8]. There are mechanisms that can produce this result, one of them is suggested by figure 9.26 right when it can be seen that they contribute to the 3 keV fluorescence peak.

[8]This point is interesting because is highly dependent on the detector and analysis performance and related with the contribution of cosmic muons. That topic is treated in section 9.5.

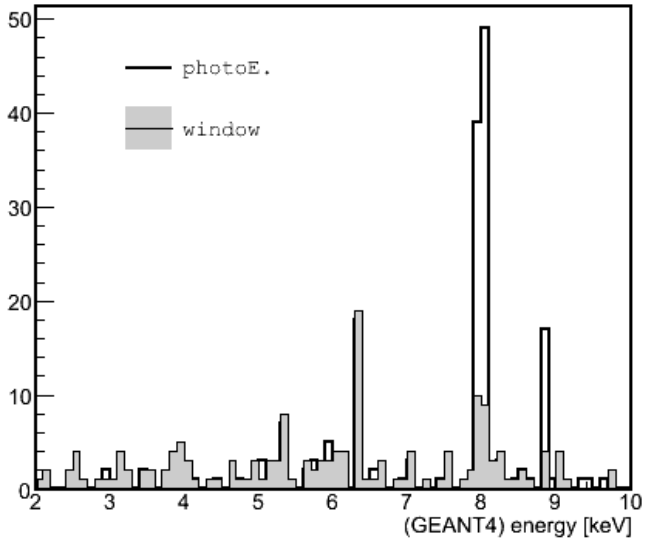

Figure 9.27: Partial final spectra for the $E_\gamma = 2614$ keV run selecting photoelectric (42.8% [2-10 keV]) and window (40.1% [2-10 keV]) events. Note the 6 keV peak matches, while the copper ones have other important contributions.

Regarding just the shape of the electron-induced final spectrum (see figure 9.26 right), it can be said their contribution is almost flat (excluding the 3 keV peak), but concentrated at low energies (the percentage of electrons contribution is double in RoI than in the wider range). It must be kept in mind that the energy measured by the analysis can notably differ from the ideal (GEANT4) deposited energy, being many times notably lower due to the particularities of the distribution of charges created by the electron along its track and the amplifier response. Because of that reason, events up to 15 keV energy deposited in the active volume are considered.

It is in the extended Study of cases picture where we find answers to the questions regarding figures 9.21 and 9.23. The change in the slope of the plot in figure 9.21, that means an alteration in the behaviour of the rejection capabilities, is clearly correlated with a replacement in the hierarchy of two contrary cases: the bremsstrahlung and pipe curves in figure 9.25 cross about 1250 keV. That is related with the high energy fall in the gross vulnerability (figure 9.20), and the medium energies semi-plateau which is due to the pipe channel to access the detector.

The bremsstrahlung, as a sort of photons-shower over the detector, reproduces basically a smaller version of the general background spectrum for high energy γ (see figure 9.28), with a strong copper peak; the pipe influence obviously tends to reinforce the fluorescences, specially those related with the stainless steel around 6 keV (that is more clearly seen in a lower energy γ induced spectrum, like the one studied in figure 9.29).

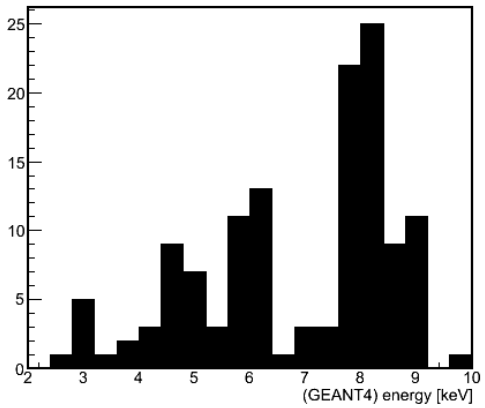

Figure 9.28: Partial final spectra for the $E_\gamma = 2614$ keV run selecting bremsstrahlung (32.1% [2-10 keV]) events.

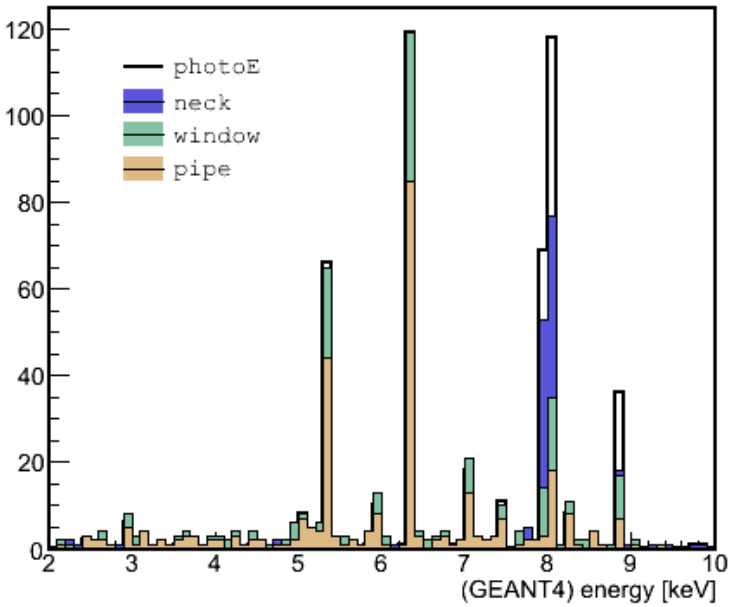

Figure 9.29: Partial final spectra for the $E_\gamma = 100$ keV run (see the total spectrum in figure 9.23) remarking photoelectric events (63.7% [2-10 keV]) and closely related secondary Casuistics. Note all the steel fluorescence events come from the window and the external pipe contribution. While the copper fluorescence has also an important contribution from the raquette.

Always more than half of the radiation came from the cathode window, what represents much more than its associated solid angle. This fact is not surprising as the window directly accessed from the shielding's outlet for the magnet's pipe, which is the most obvious weak point of the shielding and also a weak point of the

detector's structure. We see how its proportion rises below 1200 keV fundamentally because of the increase of the pipe contribution. It should be remarked that this is a contribution from the external piece of the pipe and the internal diameter of the pipe is smaller than that of the shielding outlet. Therefore, this contribution comes from external γ which were scattered by the pipe and then directed towards the detector through the window, despite the front shielding. Furthermore, they come from the same direction as the expected signal, so having similar distribution of the interaction positions as in calibrations; that is true for the x-y readout plane position (magnet's bore area), but also for the drifted distance, and makes any kind of discrimination based on z impossible.

Many of the scattered photons interact with the copper readout or have been produced by steel fluorescences in the pipe. The sharp increase of the photoelectric contribution (see figure 9.25), that happens around 200–300 keV, is related with the physical condition: $\lambda_{Fe} \sim 10 \times th$, being λ_{Fe} the mean free path of γ in iron and th the pipe thickness; i.e. when the γ do not just cross the pipe to the detector, but they start being more likely to interact with the pipe yielding fluorescence.

The increasing percentage of the pipe-window events as energy is lower is only decreased due to the presence of other access point through the shielding: the detector raquette's neck hole. This via seems to be preferred around 200 keV, despite its contribution being concentrated in the copper fluorescence out of the RoI (compare figures 9.25 right and left and confirm it in figure 9.29).

In conclusion, the typical high energy events (penetrating γ-radiation, Compton or bremsstrahlung) need for a rare chance to be accepted the discrimination criteria. In contrast, the low energy ones, specially events coming from the pipe, tend to mimic the calibration signals, reproducing the spatial and energy distributions, and that maximizes the analysis software efficiency.

9.2.4 The environmental γ flux in the CAST experimental area.

The model exposed in the previous section is just a rule to build a background using an environmental γ flux as input. The present section is dedicated to the measurement of the flux in the CAST area that leads to the configuration of the needed input. The environmental γ flux is subject to high uncertainties, nevertheless, which are transported to our final result. Besides, the deduction of the flux was done by a non standard procedure that is discussed in detail.

9.2.4.1 The necessity of a new γ flux measurements and a new approach for the flux interpretation.

The environmental γ background of the CAST experimental area had been measured in the past using germanium detectors[206]. The registered flux was used as an indirect measurement of the radioactivity of the walls of the CAST area. The most interesting conclusion for us from that study is the discovery of the fact that most of

the environmental γ radiation is originated in the walls, with a strong dependence on the different types of wall materials used in the CAST experimental area, being the concrete walls the most radioactive. As a consequence, the γ flux is neither homogeneous nor isotropic. However, trying an interpretation of those results as a γ flux is complex and risky. New flux measurements were carried out in the Summer of 2011[207].

The customary way a measured spectrum is interpreted as a flux is the following. The detector is firstly calibrated in *absolute efficiency* using a point-like radioactive source, whose activity is well known, situated at a given distance. The area of the different peaks generated by the source allows to make the translation to an equivalent homogeneous and isotropic flux. In figure 9.30 the 3×3 inches NaI(Tl) detector used for the measurements is shown together with the absolute efficiency curve which yields the relationship between a count in the detector and a γ crossing a 25 cm radius sphere centred on it.

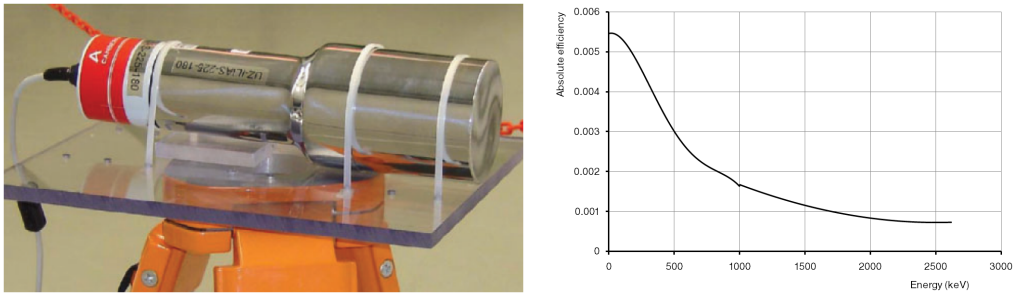

Figure 9.30: Left: picture of the NaI(Tl) detector, with photo-multiplier tube, in operation. Right: absolute efficiency curve deduced from the calibrations in efficiency at 25 cm distance[208]. It relates the counting rate with the flux taking into account geometric and quantum efficiency.

Then, for a later background measurement, the peaks are identified, weighted and translated into flux using the absolute efficiency curve. In the case a NaI detector, with much worse energy resolution than a germanium one, few peaks can be clearly identified, the rest of the peaks of the natural radioactivity chains can only be guessed by assuming the extra hypothesis that they are in secular equilibrium.

On the other hand, a simple GEANT4 simulation of the generation of the CAST area environmental radiation was performed for a piece of concrete wall (figure 9.31 left). Using the wall thickness, mass density and a homogeneous distribution of the decays in concrete (i.e. following the same assumptions the first CAST background measurements team had used to deduce the concrete radioactivity), 2614 keV γ from ^{208}Tl and 1460 keV γ from ^{40}K were launched inside the concrete wall. The resulting spectrum of γ escaping the wall, which can be seen in figure 9.31 right, shows that less of the 40% of the γ are in the peaks while the rest of them shape a continuum

which is decreasing with energy. The higher the auto-absorption, the lower the γ energy, but higher the relative weight of the continuum too. Moreover the spectrum shape obtained by this demonstration recalls the shape of experimental background measurements (see figure 9.35)[9].

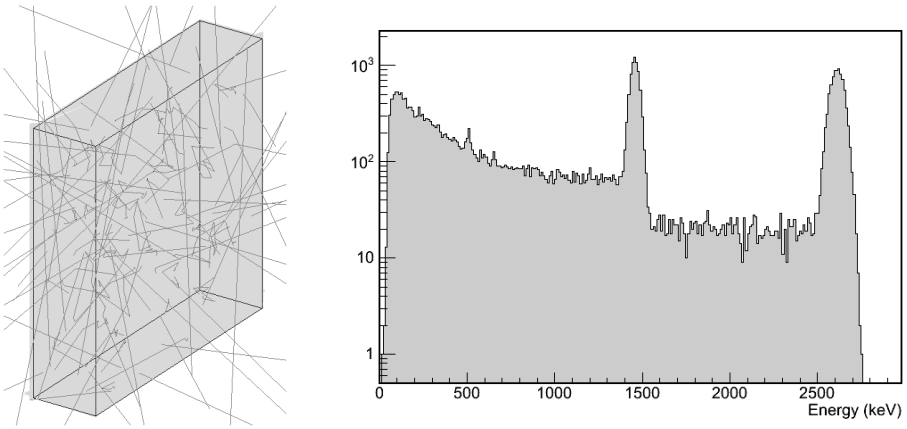

Figure 9.31: GEANT4 simulation of the generation of an environmental γ flux in the concrete walls. Left: Monte Carlo program screen-shot, showing how many of the rays are scattered by the wall itself. Right: obtained spectrum. It has been convoluted with a finite energy resolution for a more realistic view.

Consequently it was decided that, besides the flux related with peaks that are clearly identified in the background spectra, the counts which could not be justified as consequence of the detection of the peaks themselves, should be considered as real counts caused for a continuum γ flux.

A peak formation in a real detector's spectrum entails the production of a continuum because of Compton interactions (which are dominant in a big part of our energy range of interest, indeed) or due to energy lost by escaping of secondary γ or boundary effects. The experimentally determined absolute efficiency already accounts for all these effects together, but now we are interested in the energy distribution they yield. It has been developed a GEANT4 simulation of the NaI detector that was used to study this issue[209]. Direct comparisons with experimental calibrations (figure 9.32 for a ^{60}Co calibration) show a very good agreement in the shape

[9] Gloria Luzón has studied some spectra taken with a HPGe detector that had taken data unshielded at the LSC. This detector presents a very good energy resolution that allows to find many of the natural decay associated peaks. She found that the secular equilibrium hypothesis was not consistent with the peak areas; even worse, peaks which are consequence of the decay of the same isotope gave very different values. She has shown that there is an apparent loss of expected counts (related with higher energy peaks of the same isotope) as the energy gets lower, which seems to be systematic and can even be fitted with a simple parabola[210]. That could be an evidence that when the γ has been originated far from the detector (in contrast to the case when these detectors are used for measuring material samples) they can be scattered by obstacles in the area, which is more likely for lower energies.

of the induced continuum, particularly the rise of the Compton edge. In fact the real spectra present at low energies evidence of scattering produced by the intense radiation in massive materials nearby the detector (in particular a clear back-scattering peak).

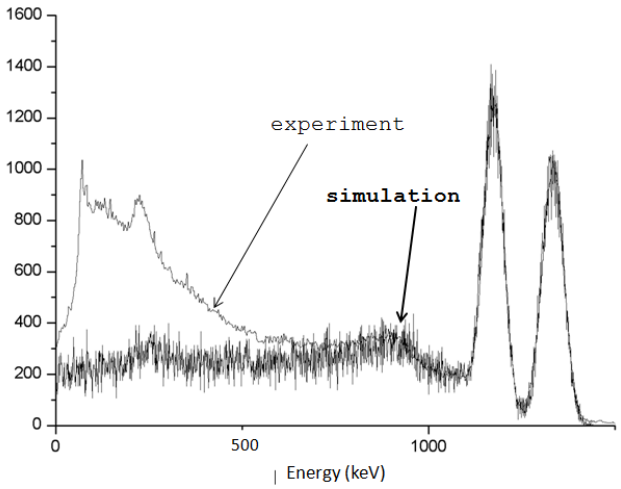

Figure 9.32: Simulated and experimental calibrations of the NaI detector with a ^{60}Co source. Simulation and comparison by E. Ruiz Chóliz.

Equivalent simulations have been done for relevant natural γ emissions, those related with the peaks identified in the experimental background spectrum (we focus in a measurement at SRMM platform) are plotted together in figure 9.33.

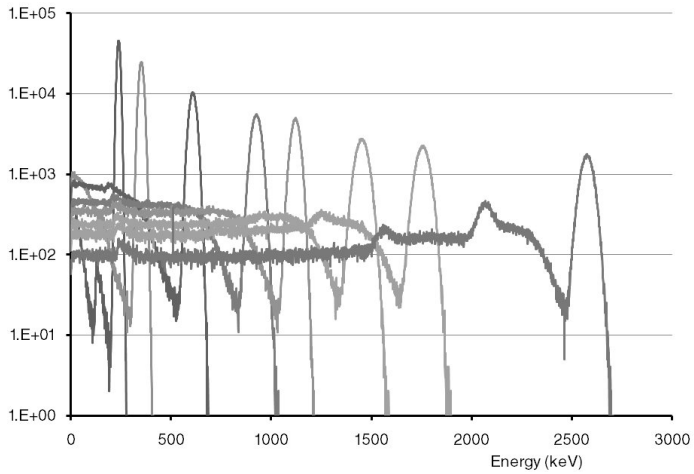

Figure 9.33: Simulated spectra produced by mono-energetic γ flux for the energies of detected peaks in the SRMM backgroun measurement. All of them have the same amount of total counts. Simulations performed by E. Ruiz.

The plot on the left of figure 9.34 shows the position of the detected peaks in the raw spectrum, in blue in figure 9.35, versus their expected energies; what also works as an energy calibration of the detector. These peaks are fitted and their areas are used to renormalise each simulated spectra of figure 9.33 which, when summed, produce the spectra in dark red in figure 9.35.

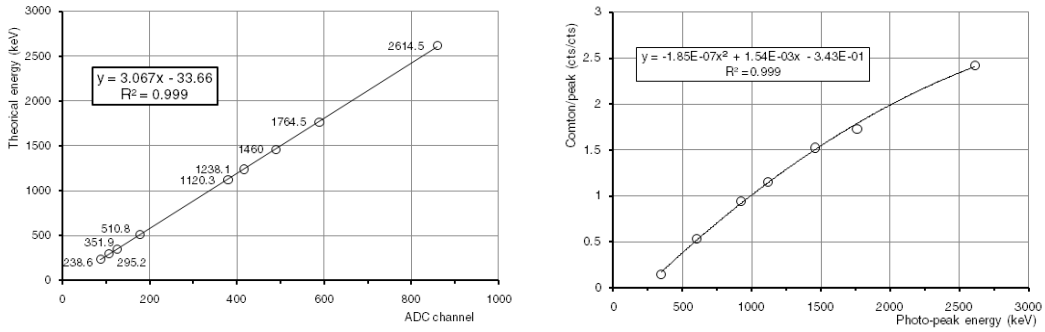

Figure 9.34: Left: energy calibration of the NaI detector based on the identification of natural decay peaks. Right: Ratio of the amount of counts in the photo-peak and in the Compton continuum for the spectra drawn in 9.33.

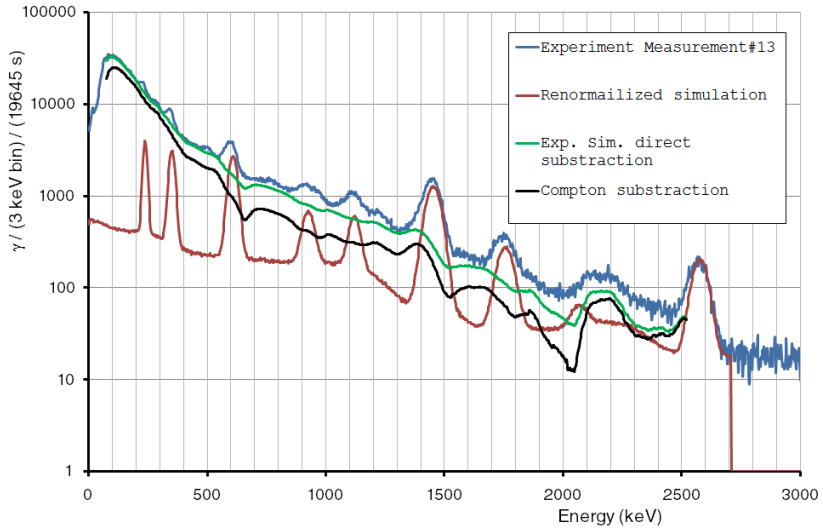

Figure 9.35: Experimental spectrum taken at SRMM platform and the successive stages along its process which is described in the text.

Thus these simulated spectra must contain all the counts that were originally produced by γ that really had the energy of any of the peaks. These γ have already been taken into account by the correction with the absolute efficiency curve of figure 9.30; but the subtraction of the combined simulation spectrum, plotted in green, manifests a large amount of counts that cannot be explained this way.

One additional comment might be necessary regarding the ^{232}Th chain 2204 keV peak, which is not very intense and difficult to be distinguished from the strong ^{208}Tl Compton peak showed in 9.33 in blue on the right. It has not been fitted as a peak and it seems to emerge more clearly after the ^{208}Tl Compton subtraction, but it is dealt with as part of the continuum flux.

There is still a fundamental problem to interpret the continuum because a big part of these counts can be consequence of partial depositions of higher energy γ. We rely again on the simulations spectra of figure 9.33 to produce the plot in figure 9.34 right from which a rule to evaluate effect is obtained. It looks like it would be a rough, but reasonable, approximation to consider these kind of spectra as the sum of a photo-peak plus a flat continuum starting at the Compton edge (3.22) with relative weight extracted from the fit in figure 9.34 right.

The process to reconstruct the original spectrum starts from the highest energy bin. The counts it contents are considered as properly registered γ, like an infinitesimal photo-peak, so the associated continuum is calculated and subtracted from the rest of the spectrum. Then the same is done for the remaining counts inside the following bin with slightly lower energy, and so on. The obtained spectrum is drawn in black in the graphic of figure 9.35 and, in principle, the absolute efficiency curve can be applied to deduce its related environmental γ flux, as it has been done in figure 9.36.

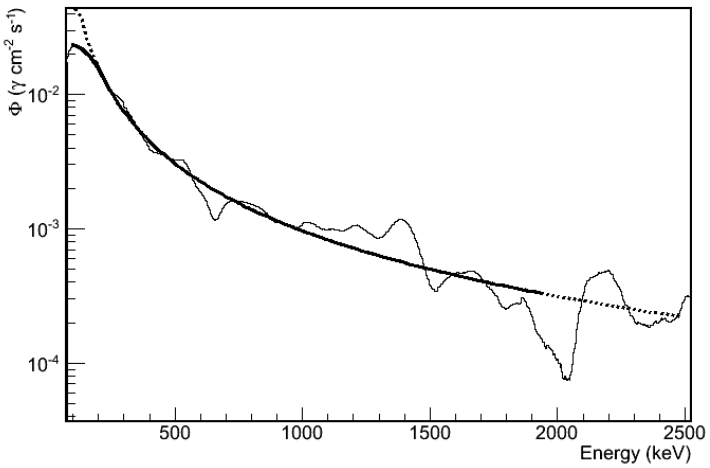

Figure 9.36: Extracted γ continuum flux after process and fit. The dashed line is an interpolation of the potential fit 9.8 beyond its range.

From the initial estimation the integrated flux $\int \Phi(E) \sim 0.5\,\gamma\,\mathrm{cm}^{-2}\mathrm{s}^{-1}$[207], including the hypothesis of secular equilibrium. Now we have found $\int \Phi(E) \simeq 0.37\,\gamma\,\mathrm{cm}^{-2}\mathrm{s}^{-1}$(from the peaks listed in table 9.3) $+ 2.19\,\gamma\,\mathrm{cm}^{-2}\mathrm{s}^{-1}$(from the continuum described in table 9.4). The final result is an histogram plotted in figure 9.36. Two approximative results can be useful for later calculations. First the fit

done in figure 9.36:

$$E < 210\text{keV}: \quad \Phi \simeq \quad 2.352 \cdot 10^{-2} \exp\left\{ \frac{(E[\text{keV}] - 85.17)^2}{3.167 \cdot 10^4} \right\} \tag{9.7}$$

$$E \geqslant 210\text{keV}: \quad \Phi \simeq \quad 48.70 \cdot (E[\text{keV}] - 36.51)^{-1.576} \tag{9.8}$$

And second, a reorganization in partial energy ranges around the simulated energies from section 9.2.2 done in table 9.4.

Peak energy keV	Φ $\gamma\,\text{cm}^{-2}\text{s}^{-1}$ $(\times 10^{-2})$
238.6	2.60
351.9	3.51
609.3	7.11
911.2	1.74
1120.3	2.48
1460.8	12.74
1764.5	3.33
2614.5	3.27

Table 9.3: Peaks identified in the background and their deduced flux.

9.2.5 Results.

At this point everything is ready to produce a simulation prediction for the environmental γ-induced background in the CAST sunrise detector. Two different predictions will be presented from two different reconstructions of the γ flux.

9.2.5.1 γ background using peaks and secular equilibrium.

Now the environmental γ flux will be deduced from the measurement of figure 9.35 considering the classical approach: evaluating the natural radioactive chains intensity in secular equilibrium. The most clearly visible peaks for each chain: ^{208}Tl peak at 2614 keV for the ^{232}Th chain, the ^{214}Bi 1764 keV peak for the ^{238}U chain and the ^{40}K peak at 1460 keV; are used to evaluate the activity of the full radioactive chain. Then an integrated flux about $0.5\,\gamma\,\text{cm}^{-2}\text{s}^{-1}$ is calculated[207].

The activity of the parent chain can be expressed as equivalent decays per unit area and time, which means that the flux associated to each γ is calculated by multiplying its relative intensity in the chain (emitted γ per parent decay). γ lines with intensities higher than 10^{-2} have been considered for the final background calculation. The table 9.5 shows the intensity of the chains and its contribution to the final background (plotted in figure 9.37), which has been calculated by application of the vulnerability simulated result or using the fit (9.4) and followings.

Simulated E keV	E_{start} keV	E_{end} keV	$\int \Phi$ $\gamma\,\mathrm{cm}^{-2}\mathrm{s}^{-1}$ $(\times 10^{-2})$	$\int \Phi / E_{range}$ $\gamma\,\mathrm{cm}^{-2}\mathrm{s}^{-1}\mathrm{keV}^{-1}$ $(\times 10^{-4})$
50.0	45.0	69.2	9.97	41.13
75.0	69.2	90.4	14.84	69.98
100.0	90.4	126.8	28.42	78.18
150.0	126.8	169.2	29.38	69.28
185.7	169.2	211.6	23.11	54.50
241.9	211.6	269.1	21.83	37.98
295.2	269.1	320.6	15.24	29.56
351.9	320.6	420.6	15.99	15.99
511.0	420.6	550.8	14.24	10.93
609.3	550.8	720.5	9.52	5.61
860.6	720.5	884.0	8.15	4.98
911.2	884.0	999.1	4.09	3.55
1120.3	999.1	1180.9	5.95	3.27
1238.1	1180.9	1299.0	3.87	3.28
1460.8	1299.0	1601.9	7.33	2.42
1764.5	1601.91	1950.2	3.80	1.09
2204.1	1950.2	2401.6	3.85	0.85
2614.5	2401.6	2550.0	1.23	0.83

Table 9.4: Extracted continuum environmental flux arranged in bins around the energies simulated in the construction of the environmental γ Monte Carlo model.

Chain parent	Equivalent activity $\mathrm{Bq\,cm}^{-2}$	Final induced background [2–7] keV $\mathrm{keV}^{-1}\,\mathrm{cm}^{-2}\,\mathrm{s}^{-1}(\times 10^{-7})$
^{238}U	0.2085	2.87
^{232}Th	0.0916	1.80
^{40}K	0.1274	1.99
Sum		6.66

Table 9.5: External γ-induced background by decay chain, considering them to be in secular equilibrium.

The result is far, nearly by one order of magnitude, from the experimental background level and has rather different spectrum shape (see figure 8.6). The main qualitative difference is the peak around 6 keV, which is dominant in the experimental spectrum while hardly noticeable in the simulated one. It has been seen in section 9.2.2 how this peak is due to the stainless steel fluorescences (the fluorescence origin is clear with GEANT4 ideal energy resolution) that produced in the pipe for the connection to the magnet's bore, and it is specially related with medium-low energy γ. Therefore the discussion in the previous section 9.2.4 about the presence

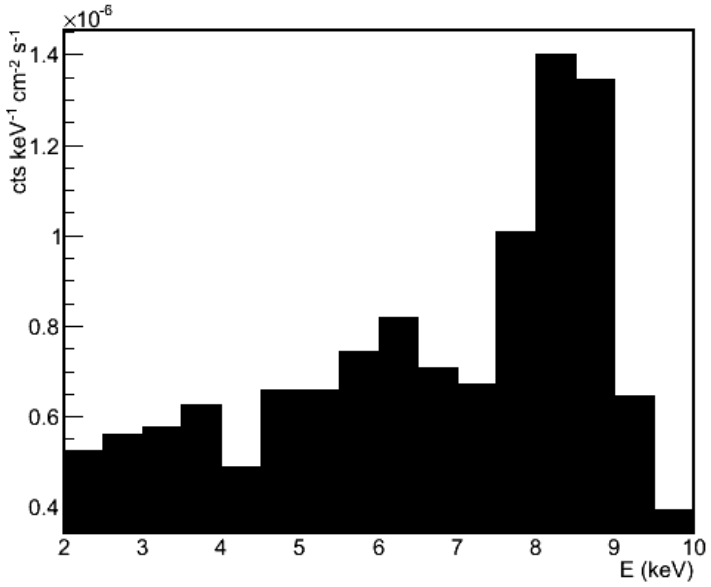

Figure 9.37: External γ-induced background spectrum by considering only the γ deduced for the main peaks direct measurement and the hypothesis of the natural chains to be in secular equilibrium.

of a medium-low energy γ continuum which has not been taken into account in this calculation becomes relevant.

9.2.5.2 γ background using peaks and continuum.

Now the final background will be build from the contribution of the flux associated to the individual peaks detected in the background measurement (see table 9.3) plus the contribution of the remaining continuum flux (see table 9.4) that was justified in the previous section 9.2.4. The cited tables are complemented with the values and fit of the vulnerability of section 9.2.2 to produce the following tables 9.6 and 9.7. In the same way the discrete spectra collection (see figure 9.23) is used to yield the final simulated background spectrum drawn in figure 9.38.

There are two alternative calculations summarized in table 9.7. The first one just takes values from table 9.4 and uses the directly obtained value from the simulation of the nominal energy associated to the bin. The second one makes use of the vulnerability fit for each little bin of the extracted continuum flux. The table shows that the flux and vulnerability curve are soft enough, and the simulated lines are dense enough so as there is not significant difference between both calculations.

The final background level in [2–7] keV RoI is $1.50\times10^{-6}\,\mathrm{keV}^{-1}\,\mathrm{cm}^{-2}\,\mathrm{s}^{-1}$with a clear 6 keV peak, but still relatively smaller than the experimental one. The Summer 2012 background is about $5.0\times10^{-6}\,\mathrm{keV}^{-1}\,\mathrm{cm}^{-2}\,\mathrm{s}^{-1}$in RoI, while tests made at surface with heavier shieldings (at least 5 cm of lead thickness) had led to the con-

Peak energy keV	vulnerability (bkg units)/flux ($\times 10^{-9}$)	induced background $\mathrm{keV}^{-1}\,\mathrm{cm}^{-2}\,\mathrm{s}^{-1}$
238.6	0.88	7.95×10^{-9}
351.9	1.05	1.27×10^{-8}
609.3	1.62	4.00×10^{-8}
911.2	2.59	1.56×10^{-8}
1120.3	3.39	2.92×10^{-8}
1460.8	4.50	1.99×10^{-7}
1764.5	5.26	6.09×10^{-8}
2614.5	6.31	7.17×10^{-8}

Table 9.6: Background contribution from peaks identified in the background measurement in the SRMM platform. Total background from the peaks $4.37\times10^{-7}\,\mathrm{keV}^{-1}\,\mathrm{cm}^{-2}\,\mathrm{s}^{-1}$.

Simulated E keV	Vulnerability(E_{sim}) (bkg units)/flux ($\times 10^{-9}$)	Bkg (rough calc.) $\mathrm{keV}^{-1}\,\mathrm{cm}^{-2}\,\mathrm{s}^{-1}$	Bkg (fine calc.) $\mathrm{keV}^{-1}\,\mathrm{cm}^{-2}\,\mathrm{s}^{-1}$
50.0	0.19	6.55×10^{-9}	1.35×10^{-8}
75.0	0.51	2.65×10^{-8}	2.93×10^{-8}
100.0	0.68	6.73×10^{-8}	7.03×10^{-8}
150.0	0.77	7.88×10^{-8}	7.88×10^{-8}
185.7	0.82	6.60×10^{-8}	6.64×10^{-8}
241.9	0.89	6.71×10^{-8}	6.69×10^{-8}
295.2	0.96	5.06×10^{-8}	5.06×10^{-8}
351.9	1.05	5.81×10^{-8}	5.95×10^{-8}
511.0	1.37	6.77×10^{-8}	6.49×10^{-8}
609.3	1.62	5.36×10^{-8}	5.51×10^{-8}
860.6	2.45	6.93×10^{-8}	6.31×10^{-8}
911.2	2.59	3.68×10^{-8}	3.88×10^{-8}
1120.3	3.39	7.01×10^{-8}	6.78×10^{-8}
1238.1	3.81	5.12×10^{-8}	5.11×10^{-8}
1460.8	4.50	1.14×10^{-7}	1.11×10^{-7}
1764.5	5.26	6.94×10^{-8}	6.88×10^{-8}
2204.1	6.01	8.03×10^{-8}	8.00×10^{-8}
2614.5	6.31	2.69×10^{-8}	2.66×10^{-8}
Sum		1.03×10^{-6}	1.06×10^{-6}

Table 9.7: Background contribution from the extracted continuum flux. *Rough calculation* refers to the direct use of the flux values of table 9.4 and the bin simulated energy multiplied by its vulnerability (second columnn). *Fine calculation* refers to the use of the proper vulnerability value from fits for energy bins as narrow as experimentally measured.

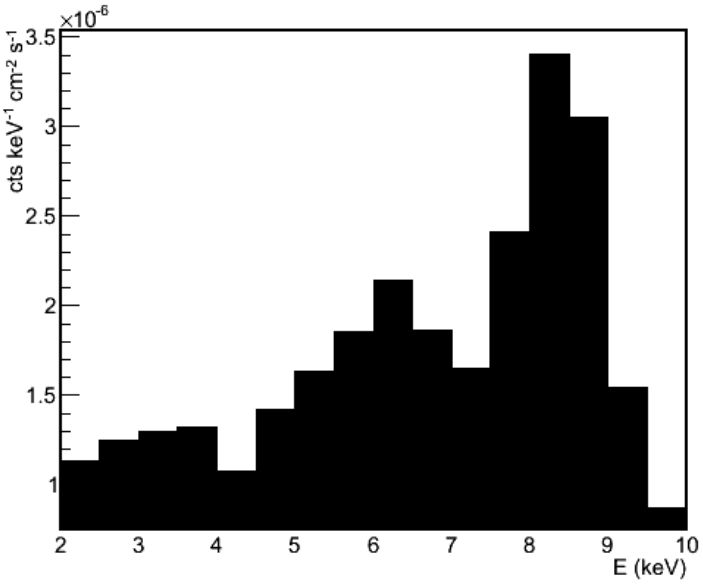

Figure 9.38: External γ-induced background spectrum by considering peaks plus extracted continuum.

clusion that about $2\times10^{-6}\,\mathrm{keV}^{-1}\,\mathrm{cm}^{-2}\,\mathrm{s}^{-1}$are contribution from cosmic rays, which is almost independent on the shielding thickness (see section 10.4). Therefore it could be said that simulation level agrees with reality by a factor 2, despite the clear underestimation of the 6 keV peak.

The total statistics of the cases study in figure 9.39 were obtained from all the events (from different γ energies) selected by the analysis. They were properly weighted according to the total background building rule that was summarized in the previous tables. It shows a balance of cases similar to the one of the medium-hight energy γ (see figure 9.24), though the final spectrum has a 6 keV peak which is the manifestation of the medium-low energy. The Compton effect is dominant, and sets the spectrum base (a kind of flat background), while photoelectric models the spectrum shape. The 6 keV peak is too small, that is the main reason the background level to be too low inside RoI. One can wonder whether the mechanism that produces such a big stainless steel fluorescence in the experimental background is understood from the simulations.

In figure 9.40 the cathode's window and, inside this group, the external pipe contribution to the final background of figure 9.38 are isolated. The figure 9.39 shows that more than one half of the final counts come through it (figure 9.39 right). In addition, the figure 9.40 demonstrates how a background that had larger contributions of the window and the pipe would have a great 6 keV peak as signature.

The spectrum obtained from the γ flux modelled as peaks plus continuum (in figure 9.38) seems to be halfway between the (continuum-less) spectrum of figure 9.37)

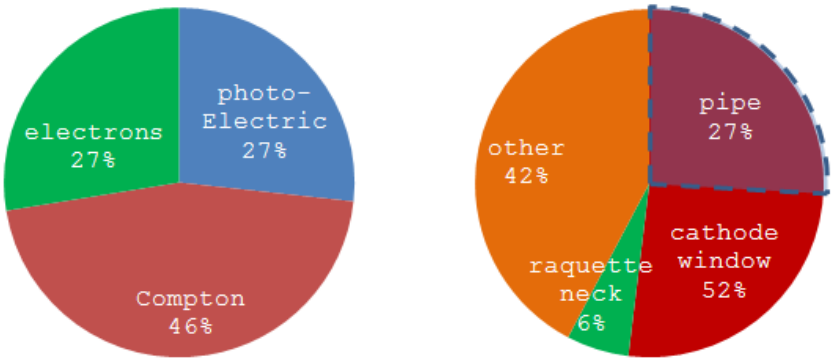

Figure 9.39: Study of cases on the final background inside RoI [2–7] keV. Left: basic study. Right: extended study. Note that *pipe* events are part of *window* events.

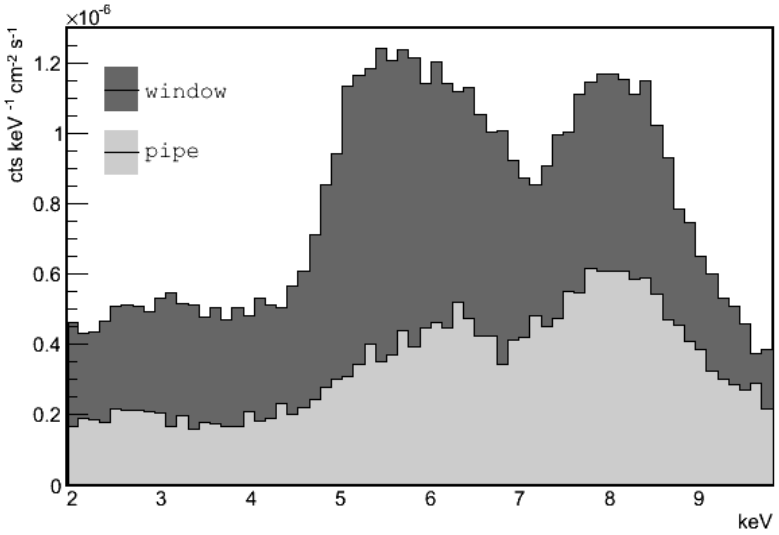

Figure 9.40: Contribution to the final spectrum through the cathode's window and the piece of pipe from detector to magnet's bore out of the shielding.

and the experimental one (figure 8.6), the latter being similar to the one of figure 9.40. Since the low energy γ increase the relative contribution of window events, in particular pipe events; a larger contribution of low energy γ would produce a simulated background more similar than the experimental one. The low energy continuum flux might have been underestimated, and/or the effects of the low energy γ on the background due to any limitation of the simulation.

The first possibility has to do with the flux measurements discussed in section 9.2.4. Certainly there are reasonable doubts about the efficiency at low energies of the NaI detector that was used to measure the background flux. There is no truly reliable calibration at energies below 250 keV, where the crystal encapsulation could

be an important limitation. The fit that uses a potential function describes well the continuum flux in a wide range of energies, but it is modified indeed about 250 keV. If it were extended at lower energies, as the dashed line in figure 9.36 suggests, the flux around 100 keV would increase more than a factor 5.

The second doubt regards our SRMM model, i.e. the way that set-up is affected by external γ (see section 9.2.2). Here the piece of pipe that is really included in the simulation (see the discussion at the end of 9.2.1) can be a relevant aspect because if the effective length of the pipe is too short, its contribution is smaller. Besides that, the simulation software efficiency is lower than the real one, particularly at very low energies, because of reasons that were already discussed in section 9.1.2.1, roughly that the simulated signals might be too noisy. That point is studied again in section 9.5.

In conclusion, the simulations explain a mechanism that can reproduce a spectrum shape similar to the experimental one (with a large 5–7 keV peak), that relies on the production of stainless steel fluorescences in the pipe mainly by low energy γ. There are clear hints that the simulations are underestimating the effects of this mechanism and it is likely as well that the flux of low energy γ has been underestimated by the measurements by a relevant factor. Therefore environmental γ can be expected to produce the most important contribution to the SRMM background, as it was checked lately by the tests reported in chapter 10. About 1/3 of the SRMM background has already been reproduced by the simulations; taking into account the mentioned limitations and tests, about 2/3 is a reasonable estimation of the total environmental γ contribution.

Since it is the dominant effect, a closer view is taken to the Compton events in figure 9.41, where the energy of the outgoing γ, after Compton scattering in the chamber, $E_{\gamma out}$, is plotted. That is again a weighted result for the final background from individual mono-energetic simulations.

Many of the energies of the initial γ energies are visible in the plot, corresponding to original γ that finally got access to the chamber and directly interacted in it. Note that the ΔE cannot be higher than 7 keV in order to produce an energy deposition inside the RoI, i.e. the γ energy before scattering plot is practically the same at this scale. However most of the Compton interactions are caused by secondary low energy γ. The mean escaping energy is 288 keV, though 61% (75%) of the events have $E_{\gamma out} < 200$ (< 300) keV.

In any case, what is clear from the simulations is that environmental γ contribution to the background can be prevented by means of an increase of the shielding thickness. There would still be *outlets* (pipe-window and raquette) interactions, which would become even more important if a thicker shielding were installed. Therefore a shielding upgrade will also have to procure a better coverage, as it was done for the 2012 Sunset upgrade that is described in section 8.2.1.3.

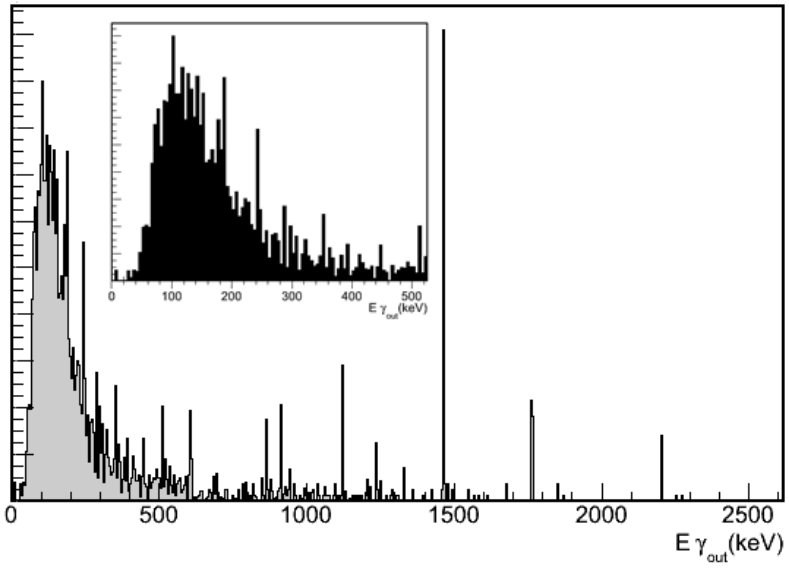

Figure 9.41: Energy spectrum of the outgoing γ, after Compton scattering in the chamber, for events that compose the final background.

9.2.5.3 Contribution of environmental Radon.

The environmental γ flux can be intensified by natural emanations of radon gas, even if the detector is protected by a nitrogen atmosphere. Although the radon contribution to the γ flux was actually measured together with the wall's one during the experimental background measurement, the radon concentration could produce important temporary variations that make the issue worth to be studied.

The approach in this section is similar to that of section 9.2.5.1; given a radon concentration, supposed to be homogeneous, the part of the ^{238}U chain that follows the ^{222}Rn decay is assumed to have the ^{222}Rn activity and the most intense γ emissions are considered. The problem to be faced is now geometric, related with the translation from a volumetric concentration to an equivalent flux, expressed in ^{222}Rn decays per unit time and surface (as we did in section 9.2.5.1), and it is represented in figure 9.42 left.

Let $\mathrm{d}N_\gamma$ be the rate of γ produced in a volume element $\mathrm{d}v$ situated at position $\vec{r}$, in our framework with origin in the center of the micromegas mesh. $\mathrm{d}v$ is placed out of the sphere S (see figure 9.42 left) with radius R_m where we want to calculate the γ flux. Then

$$\mathrm{d}N_\gamma = \rho_{Rn} \cdot I_\gamma \, \mathrm{d}v = \rho_{Rn} I_\gamma \, \mathrm{d}r \, r^2 \, \mathrm{d}\varphi \sin\theta \, \mathrm{d}\theta \tag{9.9}$$

with ρ_{Rn} the Radon concentration and I_γ the intensity of that particular γ emission. Then the possibility of an isotropically generated γ crossing S is the relative solid angle subtended by S as seen from $\vec{r}$. That solid angle is given by the following

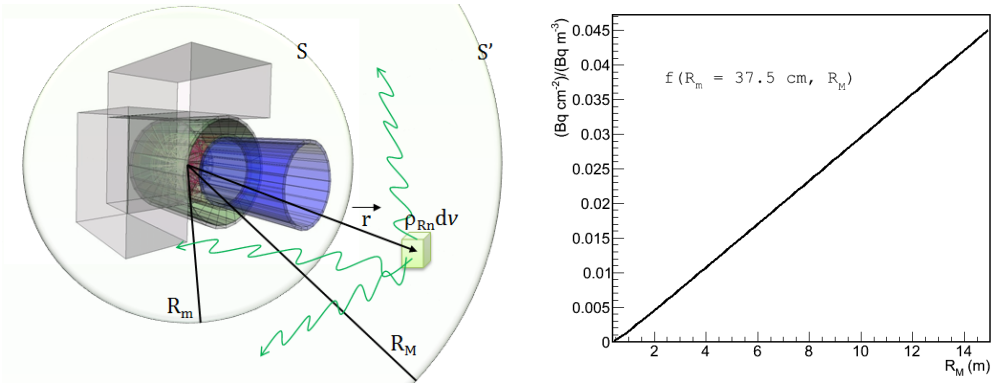

Figure 9.42: Geometrical factor needed to translate the volumetric concentration of an homogeneous radioactive source into a isotropic γ flux. Left: illustration of the calculation. Right: result for the virtual sphere used in the simulations as a function of the radius of the *framework-hall* sphere.

expression:

$$\Omega(r, R_m) = 2\pi \left[1 - \frac{r}{\sqrt{r^2 + R_m^2}}\right] \tag{9.10}$$

Thus the calculation we need to perform to deduce the flux crossing S, Φ_S, is

$$\Phi_S(R_m, R_M) = \frac{1}{4\pi R_m^2} \int_{S'-S} \mathrm{d}N_\gamma \frac{\Omega(r, R_m)}{4\pi} \tag{9.11}$$

where the integral is extended to the volume between the test sphere S and the bigger sphere S' with radius R_M. The result is

$$\Phi_S = \rho_{Rn} I_\gamma \cdot f(R_m, R_M) \tag{9.12}$$

with

$$f(R_m, R_M) = \frac{1}{6}\frac{1}{R_m^2}\left[r^3 - (r^2 + R_m^2)^{3/2} + 3R_m^2(r^2 + R_m^2)^{1/2}\right]_{R_m}^{R_M} \tag{9.13}$$

the geometrical factor, which is plotted in figure 9.42 right for $R_m = 37.5$ cm, as it is needed for a direct application of the high level γ model (see section 9.2.2). R_M should be of the order of the experimental hall dimensions, we have chosen 7 m, because SRMM are close to the walls in one direction. Then the equivalent ^{222}Rn activity is $1.8 \cdot 10^{-3}$ Bq/cm^2 for a concentration of 20 Bq/m^3 (typical values 5-20Bq/m^3), to compare with the values of table 9.5, specially with the ^{238}U equivalent activity, since there are practically the same γ. The contribution to the final

background is 1.2×10^{-10} keV^{-1}cm^{-2}s^{-1} per Bq/m^3. So 2.4×10^{-9} keV^{-1}cm^{-2}s^{-1} with 20 Bq/m^3.

In conclusion, the effect of radon concentration as intensification of the environmental γ flux at typical surface concentrations is negligible compared with current background levels. Although it could be significant, but always small, at underground environments, inside big halls and with concentration peaks of several hundreds of Bq/m^3. That issue should not be confused with the effect of ^{222}Rn, or its progeny, close to the micromegas chamber, where the high energy α-particles can produce an effect, as it is mentioned in section 9.4 and studied experimentally in section 10.3.2.2.

9.3 Experimental cross-check with a real γ source.

9.3.1 Motivations and goals of the tests.

Perhaps the high impact of low energy γ is the most remarkable aspect of the previously presented picture of CAST SRMM background due to the environmental γ flux. Such γ cannot, in principle, go through the detector shielding and they must access to the micromegas via an alternative way, which has to be the pipe that connects it to the magnet's bore. As it was explained, this soft radiation would reflect on the presence of fluorescence peaks in the background. An special signature would be the peak related with the stainless steel pipe, which certainly seems to be present in the experimental SRMM background spectra. This interpretation is important to be confirmed since it would imply that the accumulation of counts around 5–6 keV is due to real X-ray events and so it cannot be rejected relying on the performance of the detector and/or the analysis.

The experimental results with the replica of the SRMM set-up (see chapter 10) support this hypothesis because its spectra do not show the 5–6 keV peak and that set-up has not pipe outlet. However the high uncertainties in the low energy γ flux do not allow a precise quantitative evaluation of the effect in the simulations and, regarding its important qualitative consequences, a verification of this background channel was strongly motivated. The interest even increased after the installation of a shielding upgrade at the front of SRMM, specially thought to prevent γ intrusion by protecting the pipe region, which had not the expected effect[10].

With this aim a 122 kBq ^{57}Co source that emits 122 and 136 keV γ was placed in a set of strategic positions around the pipe region (see next section). This situation, where the background is almost absolutely dominated by a single well-known source, is ideal for a simulation cross-check. A direct evaluation of the effect on

[10] Due to background fluctuations during the second half of 2011, it was not possible to confirm a background reduction about 20% (internal communications, CAST 47th Collaboration Meeting, Jan 2012). However, later simulations of the new geometry and the tests explained in this section demonstrated that no further reduction could be expected.

the background of external controlled γ source would allow an immediate quantitative comparison between simulated and experimental data. Assuming the GEANT4 physics description to be correct, the divergences must be explained regarding only two aspects: an inexact description of the geometry or a different behavior of CAST analysis on simulated or real data (therefore that is a cross-check for the post-GEANT4 simulation chain); both cases of principal interest for the simulations development. First, the results for soft γ are highly dependent on the geometry details. Second, most of the soft γ-induced background is composed of 5–8 keV X-rays (stainless steel and copper fluorescences), and a good simulation performance for them has been already proven with simulated calibrations.

9.3.2 Methodology.

These tests were realized before the final simulation described in the previous chapter, since they (an other tests) provided hints to improve the simulations. Therefore some characteristics of the simulation are different than those described formerly.

- **Description of the ^{57}Co source**. The particles which are result of the cobalt electron capture are simulated one by one, i.e. one generated particle per simulated story. With this approximation we are neglecting the possibility of the coincidence of two interactions due to two different γ generated in the same decay, which is certainly tiny. In practice, the X-rays (which have energies lower than 15 keV) have no opportunity to produce an interaction in the chamber, we decided not to consider them for a faster simulation. In all the simulations summarized in the last section the complete source model (with exception of X-rays) has been used. The source activity has been considered to be 122 kBq, as measured by the CERN radioprotection personnel immediately after it was returned back. All the γ are started following an isotropic direction distribution. However the source is not isotropic due to auto-absorption. It was checked that an implementation of the source physical encapsulation was absolutely necessary to explain the experimental results[211]. The source holder plans were accurately followed: the source is not point-like but a circle, the metallic ring surrounding the source is specially relevant because it attenuates the γ flux in direction to the detector in several of the positions.

- All the **simulation settings** are as described in previous sections with the exception of the signal generation. For the mesh pulses the RCL model was used instead of the convolution algorithm, with parameters that best reproduced the M13 detector pulses ($\omega_C = 6.5$ and $\omega_L = 5.9$ MHz). The strips gain and noise was so that yield a relatively low mean multiplicity, especially for low energy X-rays (as it occurred with real M13 detector). To sum up, it could be said that a detector with a limited performance was being simulated, in the sense that the strips SNR was a bit pessimistic.

- The same **analysis** is used on both real and simulated data: MVA *without* energy correction. This analysis keeps the efficiency from 6 to 10 keV while

decreases it fast for energies below 5 keV, specially for the conditions of the simulation explained in the item above. So we can expect to reproduce basically the steel and copper fluorescence peaks and underestimate the background level at low energies. The set of observables used is Obs ID 2222 (the same we already used in previous section), but no strong dependence on Obs ID has been observed in analysis results.

- The **geometry** description used to obtain the following results is the same explained in the section 9.1. In fact this description was completed thanks to these tests to get the best agreement. The upgrades have always been based on real drawings focusing where the results seemed to require a more detailed description. Any change must be properly motivated, neglecting non essential aspects to keep simplicity. Most of the external light materials were added at this point when it was clear their relevance for low energy γ and some inaccuracies due to old plans were corrected.

9.3.3 Measurements plan and results

A brief description of the ^{57}Co source positions that were tested and their motivation will follow. The positions are described in cylindrical coordinates with origin in the center of the pipe at the end of the front shielding snout ($z \equiv$ distance, in mm, along the pipe, $\rho \equiv$ distance orthogonal to the pipe surface):

- *Position 0. ($z = 20$, $\rho = 1$).* The source is close to the copper snout (front shielding) end on the pipe. Distance to micromegas detector: ∼30 cm. Maximum exposition to the source with possibility of both direct interaction of γ with the micromegas and by means of pipe secondary interactions.

- *Position 1. ($z = 0$, $\rho = 80$).* The front shielding does not allow straight γ paths to the micromegas. Effect of pipe induced fluorescence with intense irradiation.

- *Position 2. ($z = 250$, $\rho = 250$).* Straight path of γ still not allowed, but the incident angles are changed and farther regions of the pipe are more intensely irradiated.

- *Position 3. ($z = -170$, $\rho = 111$).* Source on a bridge over the neck between the bulk and the front shielding. Source is attenuated with 1 mm thick aluminium foil to ∼60% of its γ flux intensity. No straight γ path is allowed, only the effect of low energy γ irradiation over this small piece of tube.

The result is presented in the figure 9.46. The background induced by the pipe outlet is concentrated in the fluorescence peaks. An study on the peaks origin is done in figure 9.45. The plot on the left shows the energy deposition in the chamber of the events simulated from position 0 versus the azimuth angle θ of the γ initial direction.

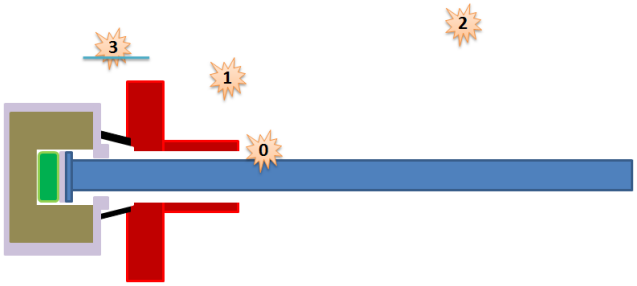

Figure 9.43: Sketch of ^{57}Co source positions.

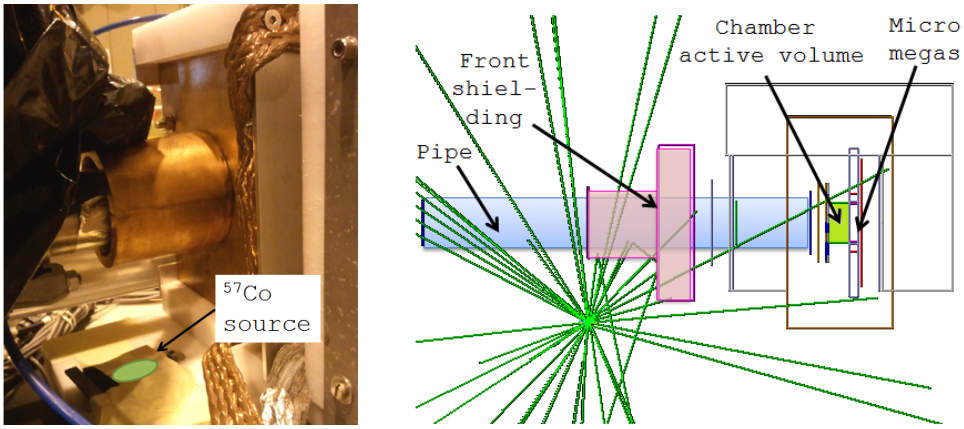

Figure 9.44: Experimental preparation of the measurement in position 1 (front pipe shielding clearly visible in the photograph) and its realization in the simulation.

It consists basically of a set of vertical lines, corresponding to the several fluorescence energies, and a horizontal line which is situated around the θ range that gives direct access to the micromegas. The counts are accumulated in the intersections

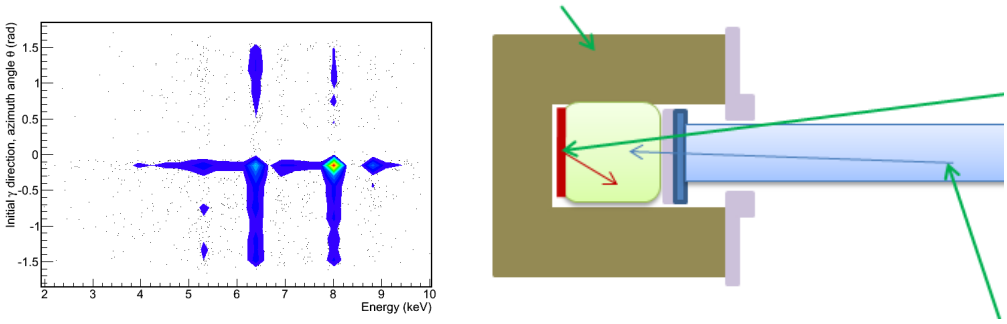

Figure 9.45: Left: exact (GEANT4 values) energy deposition versus initial azimuth angle from the simulation of the source position 0. Right: sketch to represent the typical events, ^{57}Co γ are drawn with green lines, 8 keV X-rays in red and steel fluorescences in blue.

of the lines, the biggest by far is related with the copper fluorescence peak at 8 keV which accumulates events that went directly to the micromegas like the one represented in the simple picture on the right. However, the steel fluorescence peak has even a bigger area, but must of its counts are dispersed along the θ axis and correspond to events like the second one, which has been drawn on the right. The most unfavoured θ are small ones in the opposite sense to the detector; curiously higher θ are preferred since they cross the pipe in a more oblique way increasing the scattering probabilities.

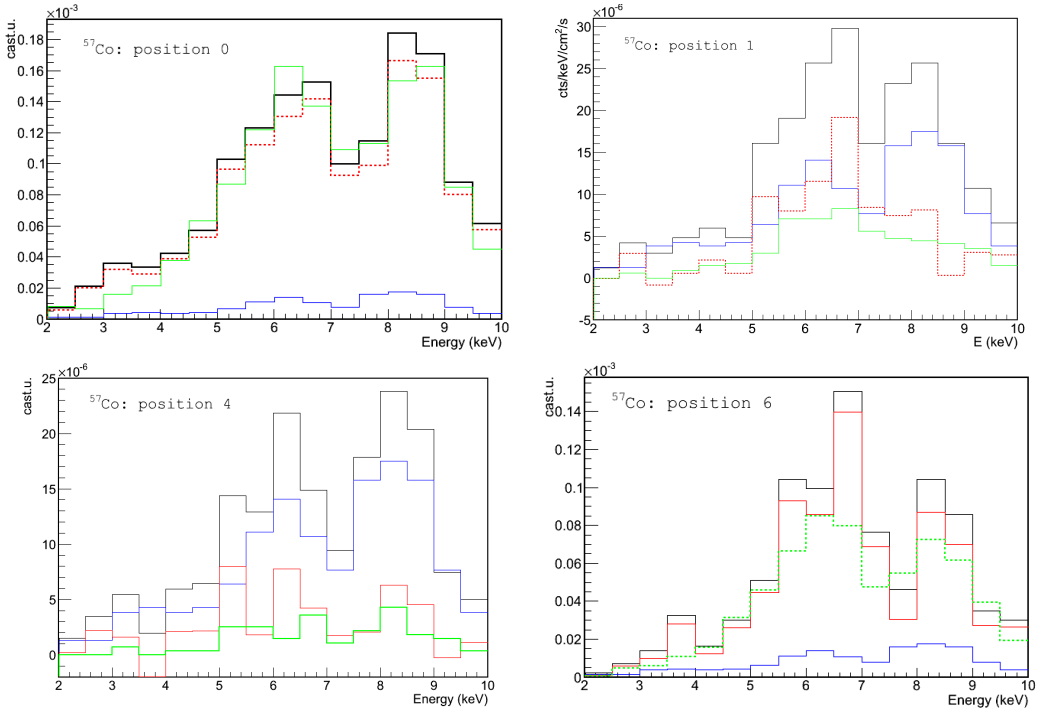

Figure 9.46: Experiment and simulation comparisons for the four source positions. The blue spectrum that is the detector's background in absence of the source (based on data-taking some days before the tests) is subtracted to the experimental spectrum, drawn with a black line, which is common for the four plots. Thus the experimental source contribution, drawn with a red dashed line, is obtained. The simulation spectrum is drawn in green. Details are given in the following table 9.8.

A very simple, but rather accurate, guideline on the interpretation of the low energy γ contribution through the pipe is that the copper fluorescence 8 keV peak is produced by γ which go directly to the chamber through the detector window, cross the gas and interact in the micromegas; while the steel fluorescence, 5–7 keV peak, is produced by irradiation of the pipe itself. Of course, γ can be scattered in the pipe and produce a copper fluorescence in the micromegas, but this channel is less likely in gammas below 150 keV. The balance between both peaks basically shows

	Pos	t(days)	rate(Hz)	2-10 keV	2-7 keV	7-10 keV
Bkg	—	5.32	0.7-0.8	8.1 ± 0.9	6.1 ± 1.0	11.4 ± 1.8
Meas.	0	4.19	0.9-1.0	90 ± 4	72 ± 4	120 ± 7
Subs.	0	4.19	0.1-0.3	82 ± 4	66 ± 4	108 ± 7
Sim.	0	3.75	0.16	83 ± 4	66 ± 4	111 ± 7
Meas.	1	3.80	0.7-0.8	13.3 ± 1.4	11.5 ± 1.7	16.4 ± 2.6
Subs.	1	3.80	0-0.1	5.3 ± 1.7	5.4 ± 2.0	5 ± 3
Sim.	1	7.72	0.01	3.4 ± 0.5	3.0 ± 0.6	4.0 ± 0.9
Meas.	2	4.59	0.7-0.8	10.8 ± 1.2	8.9 ± 1.3	14.0 ± 2.2
Subs.	2	4.59	0-0.1	2.7 ± 1.5	2.8 ± 1.7	2.6 ± 2.8
Sim.	2	6.36	0.01	1.4 ± 0.4	1.1 ± 0.4	1.9 ± 0.6
Meas.	3	0.98	0.7-0.8	55 ± 6	50 ± 7	64 ± 10
Subs.	3	0.98	0-0.1	47 ± 6	44 ± 7	53 ± 10
Sim.	3	3.78	0.10	40.0 ± 2.5	34.6 ± 2.9	49 ± 4

Table 9.8: Summary table: Nominal background, direct measurement, subtraction and simulation. Background levels expressed in $\times 10^{-6}\,\mathrm{keV}^{-1}\,\mathrm{cm}^{-2}\,\mathrm{s}^{-1}$. The trigger rate threshold for simulations was put to 1 keV.

the ratio between these two channels: the solid angle by the detector's window that is seen from the source (a path free of important obstacles) and the effect of the γ-irradiation of the pipe producing scattering and fluorescences. The agreement at low energies, below 4 keV, looks worse. It seems that the low software efficiency is exaggerated in simulated data. That must be corrected obtaining a realistic high gain detector producing clusters with higher multiplicities.

To sum up, the general performance of the simulations has been cross-checked; it has been shown that, providing the background origin to be well known, the detectors background can be reproduced, not only in shape, but also in absolute level. The SRMM model geometry was updated. The possibility of the soft environmental gammas being a channel through which background can be induced, especially in the 6 keV region, has been confirmed, even after the installation of the new front shielding. That helped to understand an apparent paradox (since the installation of the front-shielding did not lead to an important reduction of the background) and suggests that the shielding could still be upgraded for further background decrease. In fact, the last source position 6 emphasizes a weakness of the front shielding.

Perhaps a last comment is needed, because it might result surprising that a 122 kBq source has an influence comparable with a nominal background which is supposed to be produced by external γ. To start with, an important part of the nominal background is due to higher energy γ crossing the shielding. Besides, making some calculations can be helpful to demonstrate the importance of a diffuse, but homogeneous, environmental flux: a realistic γ flux around $1\,\gamma\,\mathrm{cm}^{-2}\mathrm{s}^{-1}$ when integrated along a 30 cm length piece of pipe gives about $600\,\gamma/\mathrm{s}^{-1}$ while the solid

angle subtended by pipe respect to the source in position 2 is about 1/1000, therefore $\sim 100\,\gamma s^{-1}$ reach the pipe.

9.4 Contaminations, radon, muons, etc.

The simulation of the background induced by external γ has been the main issue in the first phase of the study of CAST detectors background, that was focussed in a sunrise-like set-up with a relatively light shielding. These simulations have been also useful to check the whole simulation chain through studies like these explained in section 9.3 and 9.5.

Because of the completness and, later, also because the CAST set-ups evolution made other background sources relevant, new kinds of simulations are of our interest. Most of the required simulation upgrades are concentrated in the GEANT4 application, basically new event generation routines are needed and the presence of new particles may imply the addition of new Physics. The basic event model should be only minimally modified. Most of the new simulations are under development in collaboration with Javier G. Garza and already yielding the first results.

The role they play towards the understanding of the CAST detectors background will be better appreciated in the next chapters (10 and 11) where some preliminary results are shown. Just some milestones will be mentioned here:

- The contribution of the **internal radioactivity** from contamination present in the set-up materials does not imply the use of new particles in a different energy range, but the difficulty is in the generation of the primary vertex, or the origin of the simulation event (see section 6.2.4). The implementation is based in the *RadiactiveDecay* class of GEANT4 that follows the decay scheme of the isotopes. Thus consecutive decays are produced in the same simulated event. Special attention must be paid to the simulated time in order to distinguish between the decays that are practically simultaneous from these separated by significant time periods and manage with this information. The simulation of radon near the detector is just a particular case of this kind of simulation.

- A **cosmic muons** generator method has been implemented. It reproduces the muons flux at surface level, angular and energy distributions and μ^-/μ^+ ratio, according to the PDG's description.

- **Neutron** interactions in the CAST chamber should produce point-like interactions, since the nuclear recoil track is shorter thn an electron's one with equivalent energy. If a more detailed description of the interaction were required, GEANT4 could provide the vertex and initial energies and direction of the recoil to be simulated by SRIM and then imported by the RESTSoft simulation chain like in section 7.1.

9.5 Simulations and analysis.

The work summarized in this section follows the opposite philosophy than the previous ones. Instead of trying to reproduce real measurements to check the simulations plausibility and, particularly, the simulated signals and their analysis results; now ideal experiments will be simulated to learn about the analysis behaviour, i.e. how the analysis interacts with the different kind of events.

Our knowledge about the analysis software efficiency for CAST runs is limited to the distributions obtained from the main and escape peaks of the ^{55}Fe source, at 6 and 3 keV. Simulated efficiency curves for energies in the range [2–10] keV are studied in section 9.5.1 for several analysis types and parameters.

Our estimation of the software efficiency ε is based on the dispersion of the distribution of observables from X-rays calibrations, and it is expected to show a soft behaviour with the analysis parameters. However the suitable figure of merit is given by the ratio $\varepsilon/\sqrt{b}$, being b the background level, which depends on the efficiency of the discrimination with another event types different than X-rays, much more difficult to be studied experimentally. That is done in section 9.5.2.

The recent installation of a CAST detectors test-bench with the capability of performing calibrations at several energies brings the opportunity of a comparison with preliminary experimental results in section 9.5.3. The experimental results may suffer from a systematic error in case the diffusion in the chamber affects the analysis efficiency, as it seems to be. That would introduce a z position dependence of the software efficiency, a possibility that is briefly explored at the end of section.

This section is only a kind of appendix to the chapter's main body. The issues that are discussed here should be the matter of further study. Our aim is just pointing to a different usage of the simulations as a tool to improve the CAST detectors performance. The interplay with the new CAST detectors test-bench can be specially useful.

9.5.1 Obtaining of efficiency curves.

The simulated ^{55}Fe source is replaced by mono-energetic X-rays sources from 2 to 10 keV which irradiate the detector until 10^4 events are registered for being analysed. The ^{55}Fe calibration run (see report in section 9.1.2.1) is used to define the discrimination criteria then applied to the new X-rays runs. On the left of figure 9.47 the acceptance ratio is plotted for three different discrimination criteria (see section 8.3.2.1 for the definition of the different types of criteria). Two of the discrimination criteria relie in MVA analysis, but with a different choice of the set of observables; the observables set ID 3573 (customaryly used for data from the Canfranc Underground Laboratory set-up, see chapter 10) and the set ID 2222, that was used to produce the results of section 9.2. The third one uses a sequential

analysis routine[11]. In all the cases, the criteria have been defined regarding only the events in the main calibration peak, for which a 75% software efficiency has been asked, so the evolution of the curves shows how the observables distribution differs from the 6 keV standard.

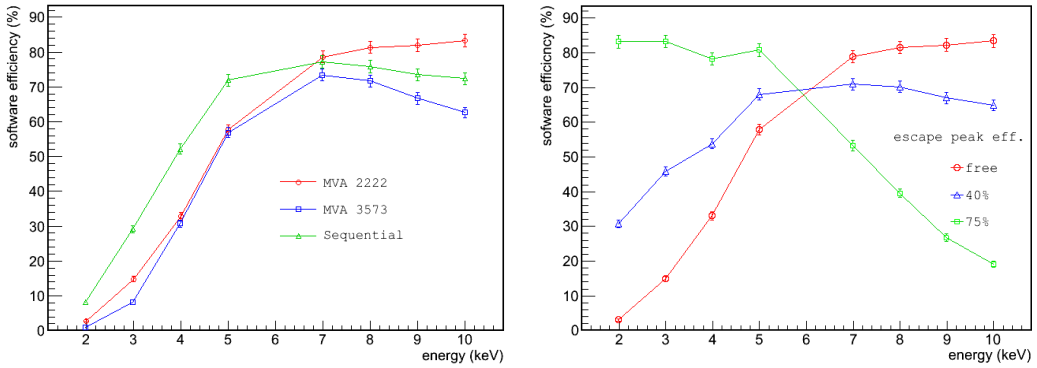

Figure 9.47: Software efficiency curves for simulated data. Left: without applying energy correction, comparing sequential analysis and multivariate analysis for two different set of observables. Right: effect of the energy correction so as to assure a given efficiency in the escape peak, all the curves are obtained with MVA and set ID 2222. *Free* means no energy correction. Note that 6 keV efficiency is set to 75% by the energy calibration for all the cases.

The three curves essentially agree. They show a kind of plateau at energies that are higher than the standard and a sharp decrease below this energy. The efficiency of the sequential analysis is clearly higher at low energy, what was expected from the systematic differences in the application of the criteria explained in section 8.3.2.1 and shown graphically in figure 8.19. The MVA results are more similar, specially at medium energies, since both sets are complete in the sense explained in section 8.3.2.1. The differences are not noticeable as energies are farther from the standard. The 3573 set gives systematically lower software efficiencies, a fact that could be explained because it contains several alternative definitions of cluster asymmetry and energy balance, what can cause statistical noise.

The most relevant feature is the asymmetry in the evolution of the high and low energy runes. When observables that are defined as absolute values (like the *multiplicity*) are considered, the software efficiency decrease slowly with energies higher than 6 keV. For the observables set ID 2222, that contains the *size* (that is less dependent on the signal strength than the multiplicity) and focuses more on the x and y balances, the software efficiency even increases with energy beyond the standard. That means that the increase of the photo-electron track[12] still does not

[11] Analysis version by J. A. García.

[12] In fact, in most of the cases a 10 keV event, for instance, is really composed of the sum of a 3 and a 7 keV electron tracks (see section 3.2.1.1), shorter than a 10 keV electron track.

imply a significant difference with the ideal target of the analysis, the point-like event, due to the diffusion effects.

In contrast, the fall of the software efficiency at low energies could be attributed to a deteriorated SNR. Such an explanation is directly applicable to the observables that are based in some of the energy definitions and their balances, but also true for the pulse features like the *risetime*, which is plotted in figure 9.48 left.

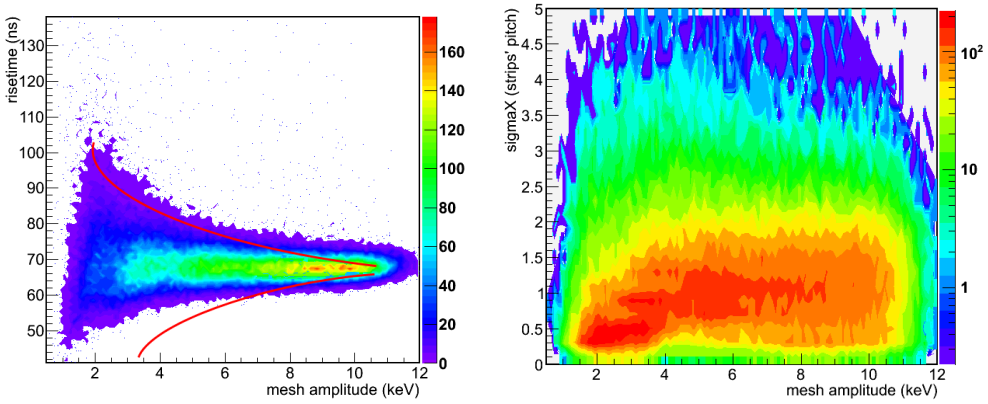

Figure 9.48: Observables distributions vs energy. Left: mesh pulse risetime. Red lines represent the acceptance region with energy correction. Right: size, as weighted multiplicity, for the x strips cluster.

This seems to confirm the suppositions done for the energy extension suggested in section 8.3.2.2 and expressed in the formula (8.5), which has been traditionally adopted by MVA analysis. At the plot of figure 9.48 left a line has been drawn that represents an energy correction of the acceptance region following the extension factor $(E_{6\ \mathrm{keV}}/E)^a$ with $a > 1$. The line fits well the rate with which the risetime distribution becomes wider at low energy, despite such an extension of the acceptance region (symmetry is assumed by the model) resulting clearly pessimistic for the deviations towards lower values of the risetime. This in not a grave problem in practice because the physical deviations of the mean risetime experimented by background events are towards higher times.

However other observables follow different patterns. The most evident case is the cluster size, defined simply as the *multiplicity* or as the charge weighted multiplicity size *sigma* (see definitions in section 8.3.1). Here the same degradation effects experimented by the mesh signal are more severe because the signal strength is shared among several strips which are registered by less sensitive electronics. The cluster size definition as *sigma* is less dependent on the strips signal strength, but still has a mean value that varies with energy (see figure 9.48 right).

Obviously trying to correct the deviation of the mean value by application of an extension factor, like in the risetime plot, is not a convenient strategy. In order to

apply the extension factor $(E_{6\ \mathrm{keV}}/E)^a$ to cover the events which moved down in size, a parameter a very high is needed. However that high a will produce a symmetric extension of acceptance area towards higher values. Even worse, according to the MVA formulation (see section 8.3.2.2) this enlarged factor a will be applied to the energy correction of all the observables since the a is a common factor that applies to the acceptance volume in the n observables-dimensional space.

The software efficiency curves produced by means of the application discrimination criteria using different a values for the extension of the acceptance volume are plotted on the right of figure 9.47. The a values that characterize the curves are those required to get an efficiency of 40% [13] and 75% [14] of the events of the escape peak in the calibration. It is remarkable the fact that the efficiency at 3 keV, calculated from simple X-ray events, is very close, always slightly better, than the efficiency that was calculated from the escape peak events. This suggests that using the escape peak to define discrimination criteria produce coherent results.

The tendency of the curve with the escape peak's efficiency left free (no energy extension applied, or $a = 0$) is practically inverted when 75% is asked trying to obtain a flat curve. At some point, near 6 keV in this case, the dispersion in the observables is practically not affected neither by the statistics nor the noise, and the energy correction becomes too strict. The fact that this curve is actually flat at low energies demonstrates that the extension formula, using just one parameter, gives a good description of the observables dispersion due to energy (at least towards one sense, regarding the plot on the left of figure fig:observablesEvolution). Therefore combining different a values for high and low energies any desired continuous efficiency curve might be produced. The effect the choice has on the final background is another issue that will be discussed in the next section. The fact that the figure of merit is $\varepsilon/\sqrt{b}$ must be kept in mind.

A final remark to end with: note that all the comments done in this section imply that the efficiency curves must be highly dependent on the detector performance, specially on the SNR, since we have invoked the SNR as the main cause of energy dependence that affects the analysis.

9.5.2 Effects on the background.

The same analysis settings that produced the software efficiency curves on the right of figure 9.47 are applied to the events of a simulated background run whose source is an isotropic flux of ^{208}Tl 2614 keV γ, like in section 9.2. The obtained final background spectra are plotted in figure 9.49.

The transformation suffered by the shapes of the spectra are understood from the efficiency curves. However the background level at low energies experiments

[13] As it is usually set for CAST SRMM. That efficiency curve is applicable to the results of section 9.2.

[14] As it is usually set for Canfranc Underground Lab analysis.

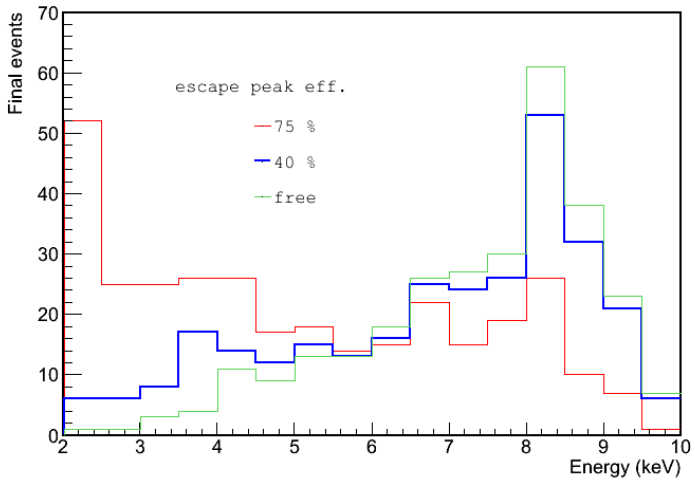

Figure 9.49: Final simulated background after applying MVA analyis with different energy corrections to a 2614 keV γ run.

a sharp increase at any point between 40% and 75%, and the copper fluorescence peak is reduced at the same time. That evolution completely changes the general spectrum shape and the physical interpretation one would make about the origin of the background. The nature of the background could change too; it can be asked whether the accumulation of low energy counts is really due to soft X-rays or to a different type of event that has been accepted in a higher proportion with the 75% settings.

The analysis of the event type (study of cases) that originated the final background (see section 9.2.3) shows that not X-rays, but electrons, which sum less than 20% of the final background without energy correction, become more than 40% when 75% software efficiency is guaranteed for the 3 keV escape peak.

The mechanisms by which electrons can fake X-rays are roughly classified in three types, from direct observation, in figure 9.50. All the events there represented passed the discrimination criteria configured for 75% efficiency. A first type (top) would consist of electrons that escape from the chambers solid pieces: the mesh and the cathode. These events are essentially indistinguishable from X-rays and their contribution to the final background decreases with the software efficiency as would be expected for X-rays too.

The second type (medium) contains events composed of a fast electron and a δ-ray. The minimum ionizing track of the father electron can hardly surpass the strips detection threshold; but when it suffers a knock-on collision, the secondary electron can be taken as a photoelectron. Only part of the events of this type accepted by the 75% MVA are rejected by the 40% MVA while most of them by the MVA without energy correction.

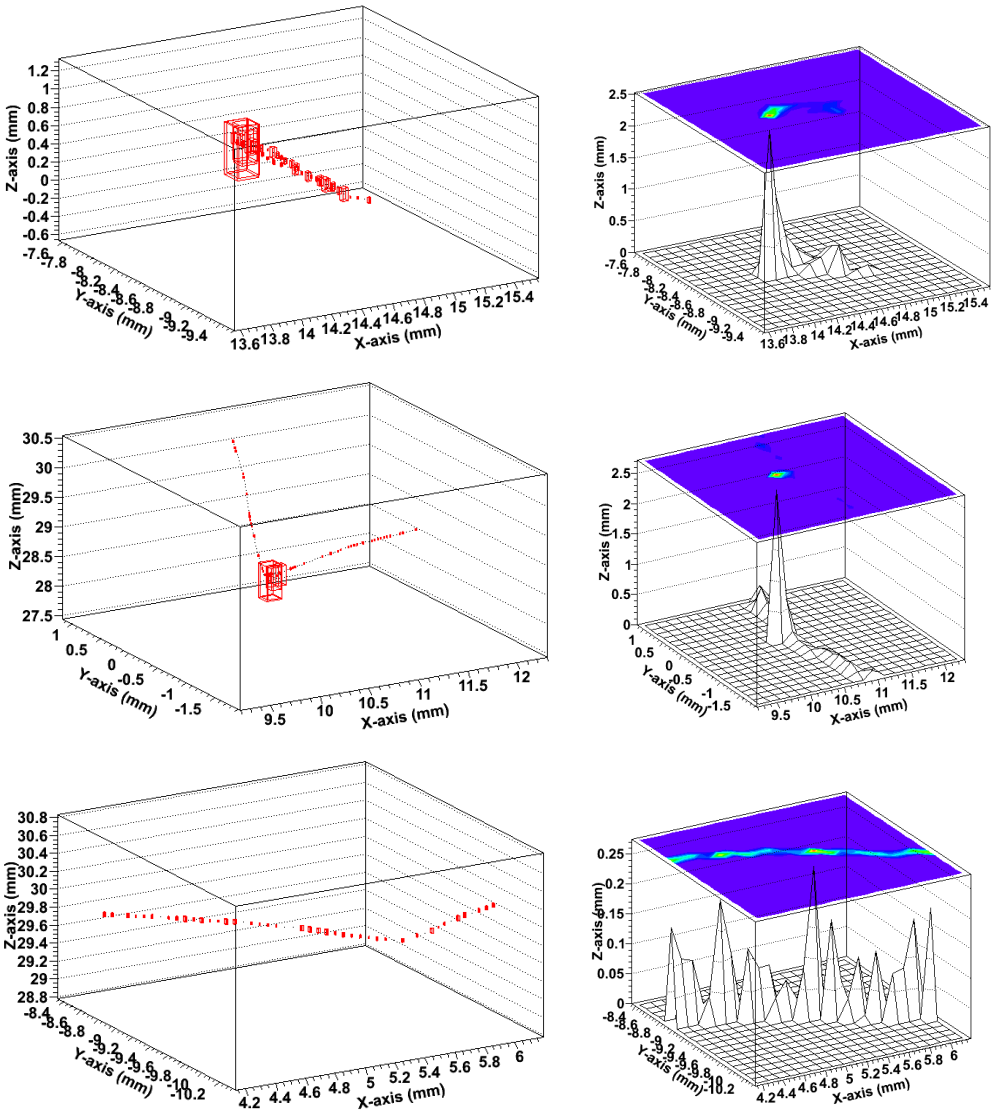

Figure 9.50: Electron events which are able to pass the discrimination criteria. Left: Simulation view in 3D, red boxes' size is proportional to the ionized charge. Right: readout projection. Top: photoelectron escaping from the mesh. Middle: MIP with a *delta*-ray. Bottom: horizontal fluctuating track.

A last type (bottom) can be produced when electrons which cross the chamber horizontally, thus the primary charge arrives to the mesh almost simultaneously and the mesh pulse looks acceptable. That kind of tracks generate small clusters by ionization fluctuations (a sudden change in the track direction is the most frequent mechanism). Most of these are rejected as cluster candidates by the analysis, but there is a possibility of one of them being accepted and the event can be taken as

mono-cluster if the rest of them were taken as accidental fluctuations. Of course these are very low energy clusters with bad x-y size balance and strips-mesh energy balance; however, as it was explained in section 8.3, the assumed deviations in some observables by the energy correction of the discrimination criteria can entail the acceptance of, in principle, unacceptable values for other observables. Practically the totality of these events are rejected already by the 40% MVA.

Regarding only the background levels and the detector sensitivity, the table 9.9 shows that, in practice, the situation does not change so dramatically. It suggests that it must be an optimum for the figure of merit $\varepsilon/\sqrt{b}$ between 40% and 75% software efficiency, just before events of the third type start being accepted.

MVA ε@3keV	$<\varepsilon>$ [2–7] keV	b [2–7] keV	$<\varepsilon>/\sqrt{b}$
free	43.6%	99 cts	4.38
40%	57.1%	132 cts	4.97
75%	75.5%	240 cts	4.87

Table 9.9: Analysis performance from the combination of figures 9.49 and 9.47.

The values of the table are just for guidance, they aim at a general behaviour by detectors and analysis. The mentioned optimization cannot be considered as applicable to every case, since both the efficiency curves as the background levels depend on the detector's performance. The capability to reject the electron tracks of the second and third types depends on having a SNR good enough so as to detect the minimum ionizing track. In addition the conclusions depend on the set-up and the present background sources. In an environment with cosmic rays crossing the detector as MIPs, for example, the background increase with software efficiency might be more severe.

Some hints that plausibility of the previous picture about the nature of the background and the interplay between the kind of events and the analysis and the performance of the detector can be found in experimental data. In figure 9.51 two backgrounds taken from different detectors in similar situations (CAST-like set-up, see chapter 10) are compared. While M10 is a detector with good general performance, M13 had a limited one, particularly a low gain. Both spectra have been produced by MVA at 75% software efficiency in the escape peak, however the one of M10 is similar to 40% spectrum of figure 9.49 while the one of M13 is similar to the simulated 75% spectrum in the same figure.

Three points can be concluded from this comparison:

- The plausibility of the efficiency curves and the explanation of the increase of the background by the simulations, from the likeness between the spectrum of M13 and the simulated one.

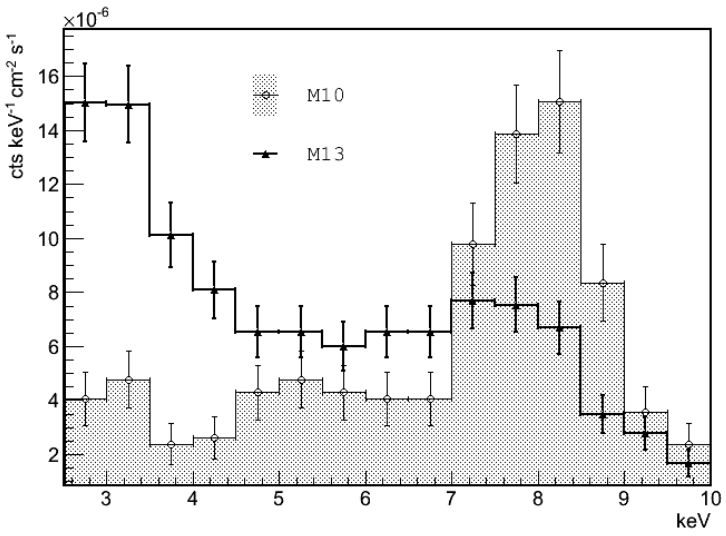

Figure 9.51: Background spectra by M10 (good performance) and M13 (limited gain and homogeneity problems) detectors. Both spectra have been obtained using MVA at 75% software efficiency in the escape peak.

- The sharp increase of the background by improving the software efficiency is avoidable with a good detector, and then the analysis energy extension is highly convenient and near flat efficiency curves should be possible, as is deduced from the behaviour of the background of M10.

- The detector reproduced by the simulation's electronic chain should be a detector with a bad performance from the SNR point of view, since it behaves like M13. Moreover the reasons we have found to explain the loss or efficiency in the simulations are related with a bad SNR. During the discussion of the parameter choice from the simulation in section 9.1.2, the SNR was seen to limit the energy resolution, though noise was needed to generate the observables dispersion. Other sources of variation should be considered, like a non ideal behaviour of the electronics that will allow a better SNR while higher dispersion in the simulated signals.

9.5.3 Comparison with experiment and some hints about diffusion.

The first tests done in the new CAST micromegas test-bench in Spring 2012[212] allow the calculation of the software efficiency for some X-rays energies produced by PIXE (Particle-Induced X-ray Emission). The experimental series is compared with the simulated one in figure 9.52 left; MVA, choosing observables set ID 3573, without energy correction was used to analyse both series. The behaviour is qualitatively similar, with remarkable flatness at high energies (note $\varepsilon \simeq 72\%$ at 8 keV starting with 75% at 6 keV) and the fall at low energies, which is less sharp in the experimental series (below 4 keV the software efficiency is much lower for simula-

tions). Keeping in mind that the detector used in the tests was the M18, later installed in the CAST sunset side, with an excellent performance, the comparison tends to confirm the conclusions extracted at the end of the previous section.

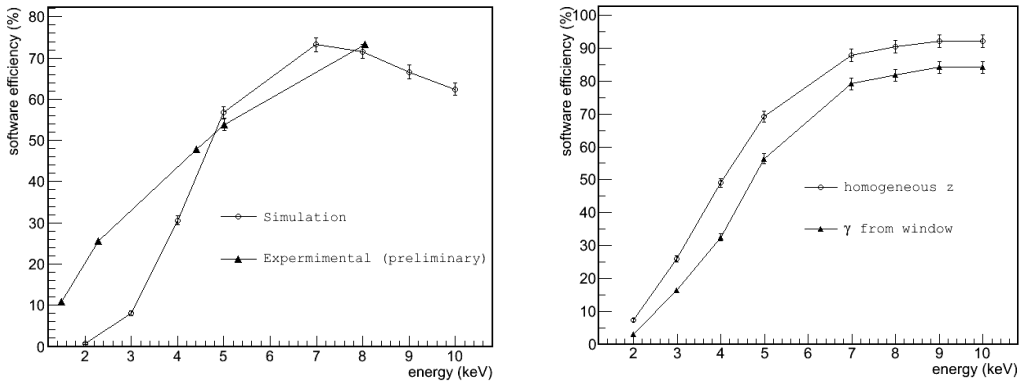

Figure 9.52: Comparison of efficiency curves with MVA observables set ID 3573 and no energy correction. Left: simulation vs experimental data. Right: Simulations of X-rays coming from the window or electrons (like X-rays forced to produce a photoelectron) with a homogeneous z distribution.

However the experimental data may be affected by a systematic error. While the X-rays that come from the PIXE beam face the detector from the calibration window in the front, the ^{55}Fe source has to be placed in the opposite site, and so the 6 keV X-rays enter into the chamber through a hole in its back. The main difference is an inversion of the z-distribution of the X-rays interactions in the chamber. The z-distributions for the simulated X-rays (facing the chamber from the window) are plotted in figure 9.53 left[15]. Thus the average drifted distance changes from near 2 cm, when calibrating through the window, to only about 1 cm if the calibration is done from the back.

The comparison with the distributions of observables obtained from customary calibrations (through the window) seems to point to a slight displacement of their distributions, particularly the one of the *risetime*. The figure 9.53 right shows the effect on the risetime distribution due to the z position that is produced after the convolution with the electronics response function.

Aiming to explore a possible dependence of the software efficiency on the z position, a set of electrons homogeneously distributed in the chamber is simulated,

[15]They are explained basically by the argon cross section plotted in figure 3.14 left. The presence of the argon fluorescence produces some apparent paradoxes like the fact that the drifted distance is practically the same at 6 keV than at 3 keV. Even for the 10 keV X-rays there is still a soft accumulation of events in the higher positions. Note that the irregularity of the z-distributions at energies lower than 6 keV rejects the possibility of the diffusion effects being the main cause of the software efficiency loss, since the latter is soft and continuous.

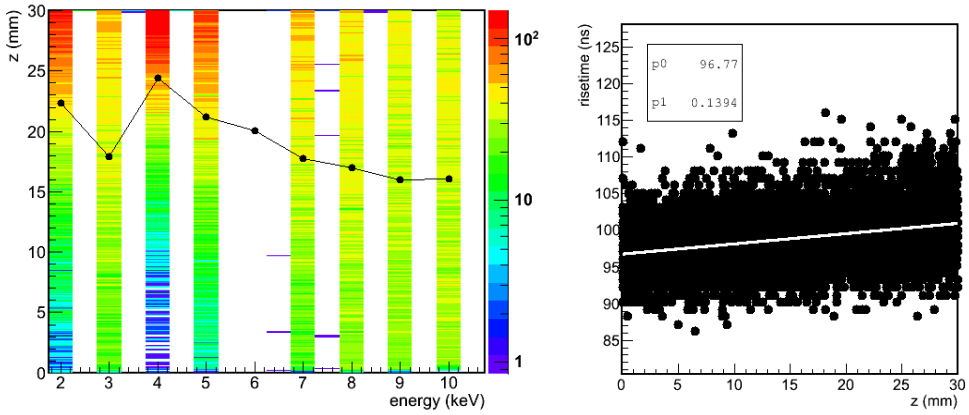

Figure 9.53: Left: z distribution for simulated X-rays coming from the calibration window. The 6 keV distribution was already plotted and studied with more detail in figure 9.13. The black dots mark the z average. Right: risetime values for 5 keV electrons homogeneously distributed in z. The white line is a linear fit whose parameters are in the legend.

just to generate events with a different drift time distribution. The analysis of the homogeneous series, using the usual ^{55}Fe calibration through the window, shows a systematic improvement with respect to the calibration-like X-rays (see figure 9.52 right). This could be interpreted as an slight increase of efficiency for the events with shorter drifted distance.

A graphical explanation can be found in figure 9.48 left, regarding the asymmetry of the distribution and the relationship with the selection area, which is actually symmetric. Even if the z distribution and the diffusion effects tends to disperse the observables distribution mainly towards higher values, the lower ones are well covered by the acceptance area. However there are natural limitations for the dispersion towards lower values: the finite track length, the amplifier maximum risetime, etc.

If future studies, combining simulation and experiments, confirmed that there is an increase of the observables distributions dispersion due to diffusion effects and, furthermore, that this systematic variation cannot help the analysis to select X-rays coming from the window (rather on the contrary), it would be convenient to improve the gas drift properties, for example with the addition of a small amount of CF_4.

Chapter 10

Surface and underground experimental tests of the CAST micromegas background.

Contents

The construction of a micromegas CAST-like set-up for experimental tests is a research line that is complementary with the simulations explained in the previous chapter. The goal is to detect or reject systematic effects caused by detector operation parameters or environmental variables and to evaluate the relative weight of the diverse background sources by modifying the detector environment or set-up. Specific tests are valid for confirming and evaluating the simulation predictions. The most relevant change is the installation of the set-up in an underground environment, which means a strong suppression of cosmic rays and so brings the possibility of testing thicker shieldings without secondary effects due to the interaction of high energetic ionizing particles in their mass budget.

Note: along the chapter references to "run numbers", RX, will be done. These runs are summarized in a table at the end of the chapter (section 10.5).

10.1 CAST-like test set-up. Acquisition and analysis.

The new set-up (figure 10.1) essentially reproduces the CAST sunrise one (SRMM) and was built in the University of Zaragoza. The light shielding is composed of a 2.5 cm thick lead layer with an internal shielding of 0.5 cm of copper. The two last copper-lead caps (top and bottom) are added after closing the Faraday cage, which encloses the detector and the front-end electronics. The cage is leak-tight and can be provided of a nitrogen flow which renew the inner volume typically 2-3 times per hour. The set-up has an automatic system for calibrations that uses a 6 keV X-rays ^{55}Fe source. The calibrator is installed in a rotating arm which, by means of a little electric motor placed outside the cage, can show the source to the detector or keep it screened by the internal lead walls. The set-up is completed with a CAST spare microbulk detector. A view of the set-up once completed, including an external CAST-like polyethylene shielding and the motor controller, can be seen in figure 10.3 left.

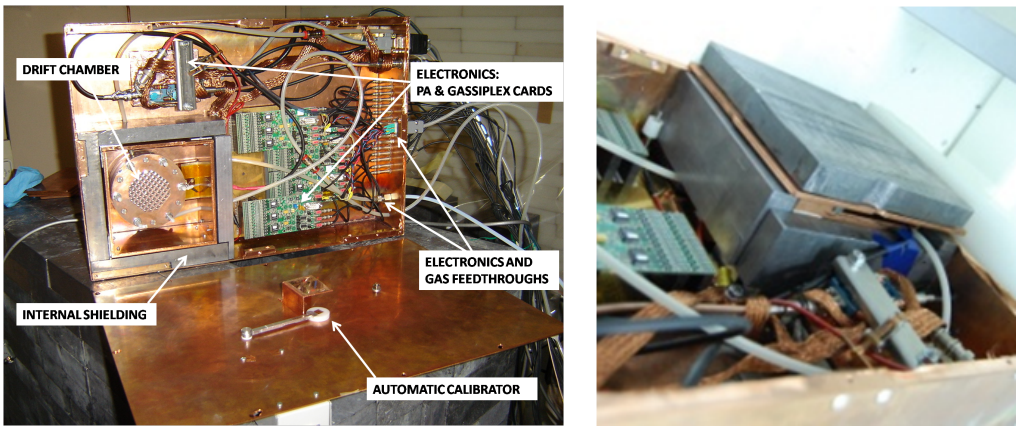

Figure 10.1: CAST sunrise replica for tests. Left: open Faraday cage. Right: illustration of the internal shielding when completed after Faraday cage is closed.

Regarding the acquisition, the CAST DAQ (see section 8.2) has also been reproduced. The Zaragoza's vesion is based in the same fundamental modules: CANBERRA 2004 PA, ORTEC 474 Timing amplifier and MATACQ card for the mesh pulse; Gassiplex cards and CRAM (V550) for the strips signals, so the information for analysis is the same[1].

The analysis used for the whole series of Zaragoza preliminary tests and Canfranc measurements is MVA with energy correction set to 75% efficiency at 3 keV, the same as for the calibration 6 keV peak, as was done for the CAST sunrise during 2007-

[1] The exact acquisition implementation is slightly different since the Sequencer module (V 551B) is replaced by the VME controller capabilities in a new version of the DAQ program written in pure C++ and due to J. Galán.

2009 campaigns. Procuring a high efficiency at low energies was aimed because of the interest in having the best sensibility for the underground background at very low energies. For tests carried out in different conditions the analysis settings will be specified.

A Slow Control system (SC) has been developed based in the general purpose National Intruments I/O device via USB[213], which has been connected a temperature and pressure sensors used to continuous monitoring of the room temperature and the micromegas chamber pressure. Also intensities associated to the drift and mesh voltages are read with nA precision, and the SC can send an inhibit signal that would switch off the power supply when considered convenient. The SC can be completed with an AlphaGUARD radon monitor[214] that, by means of extracting a continuous flow with a little pump, is able to record the radon concentration inside the Faraday cage.

Several existing differences with SRMM must be summarized. There is no cadmium layer in the test set-up and the lead of the internal shielding is not archaeological. Since there is no necessity of an outlet for connection to the magnet, the test set-up is basically closed in the 4π solid angle with exception of a narrow gap for the calibrator, the unavoidable outlet for the detector's raquette neck (also present in the sunrise) and a weaker zone in the join between the top an bottom layers with the rest of the shielding (that is easily appreciated in the photo of figure 10.1 right). While in the SRMM the immediate environment (with direct access to the chamber through the mylar window) is made of stainless steel, because there is the pipe to the magnet's bore; in the test set-up the chamber is open to the innermost cavity inside the shielding, all made of copper since its walls are composed of the internal layers of the shielding and part of the Faraday cage. This difference is emphasized by the fact that the cathode, which is the frame of the calibration window, was made of copper for most of the tests done at Zaragoza's test bench and at Canfranc Underground Laboratory. Furthermore, the contribution of a more radioactive cathode was measured lately and is reported in section 10.3.2.1.

10.2 Preliminary tests at surface.

During the commissioning of the new set-up at Zaragoza's lab, several tests were carried out with the goal of studying the dependence of the background on operational or environmental parameters. Despite the M13 microbulk detector used during that period had not the best performance and only a little range of operational parameters were allowed, its background level was comparable to CAST's[215] (Run reference, R0) and its evolution completely coherent[216].

The set of changes which had no influence on the detector background, with a CAST-like set-up (only the shielding described in the previous section) installed at surface (a report was given in [217]) were:

- Nitrogen flow interruption.

- Micromegas gain. Increased about a factor 2; provided there always was a good signal-to-noise-ratio (SNR).
- Variations in micromegas chamber pressure: 1.3–1.5 bar.
- Changes in timing-amplifier integration times: 50–100 ns.
- Upgrade of the external polyethylene shielding from 10 cm thickness and partial coverage to 20 cm thickness and 4π full coverage.
- Variability of environmental temperature: $\Delta T > 10^{\circ}$ C; it affects the gain stability, but not the background.

Only settings that degenerated seriously the detector performance had a response in the background level. The increase of the drift voltage to 1000 V, far from the transparency plateau of the micromegas, led to an increase of the background level higher than 50%. The level decreased again when the mesh voltage was increased, partially compensating the lost of gain and transparency. The hypothesis of the drift voltage itself to originate background events by generation of micro-sparks in the cathode was in this way rejected (up to the sensitivity of CAST-like background levels).

Many of these tests have been eventually reproduced underground in much more stable conditions and at lower background levels with the same result.

10.3 Underground operation.

Since 1985 the Canfranc Underground Laboratory (LSC)[218] is scenario for Rare Event Searches mainly carried out by the Nuclear Physics and Astroparticles group (LFNA) of the University of Zaragoza. The laboratory is situated at 2500 m.w.e. (meter water equivalent) under the Tobazo peak, in the point with larger rock overburden of the railway tunnel. Recently the laboratory was upgraded; though the first part of the tests explained here were still carried out in the facilities of the (now called) *old* lab.

The cosmic muons are known to be reduced by a factor of 10^{-4}[219] in the LSC. Then an installation of the set-up should imply an evaluation of cosmic rays contribution to the background. The complete scenario is not so simple, because the transfer to the LSC implies more differences. The environmental γ and neutron fluxes can vary notably, and the radon concentrations even orders of magnitude. Therefore we postpone that discussion until the next section 10.4. By the moment it is just commented that the direct transfer of the CAST-like set-up, equipped with the M13, from Zaragoza to Canfranc produced a very similar background level (see figure 10.2 comparing the runs R0 and R1), though the trigger rate was reduced from $\sim$1.0 Hz to $\sim$0.2 Hz. That fact confirms that cosmic muons produce most

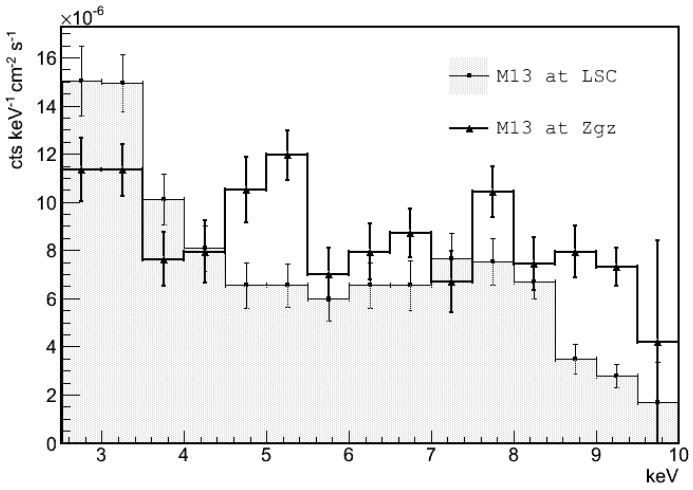

Figure 10.2: M13 background spectra taken at Zaragoza's test bench (R0) and at LSC (R1).

of the triggers and micromegas detectors to efficiently reject them. Undoubtedly cosmic muons were not the dominant contribution to the CAST background.

Besides, from the calculations exposed in section 9.2.5.3 it is deduced that environmental radon contribution would still be smaller or even negligible compared with γ. Regarding radon very close to the detector, it can be avoided by flushing nitrogen and its contribution will be evaluated in section 10.3.2.2. What is clear is that environmental γ flux and radon contributions can be practically blocked by a shielding upgrade and that contribution can be evaluated directly from a previous CAST-like underground reference, as it is done in the next section.

The LSC environment provides more advantages for this study: the stable environmental conditions reject possible systematic effects and the environmental γ radiation has been measured by the new laboratory characterization program[219].

10.3.1 Thicker shielding tests. Reaching set-up's limitations due to intrinsic radioactivity.

The measurement series summarized in this section have the goal of evaluating the relative weights from internal contamination and external radiation to the CAST background by making the CAST-like shielding evolve to an underground-like set-up. The M10 detector, a microbulk micromegas with better performance than the M13, comparable with detectors at work in the CAST experiment, is used until almost the end of the series. The detector is mounted with a copper cathode with the same strong-back mesh design and mylar thickness window used in CAST.

In two steps the original CAST-like set-up was surrounded by 20 cm of clean, but non archaeological, lead; first leaving the top with only the light shielding (R3) and

finally closing all the solid angle (see figure 10.3). The progressive decrease of the background confirms the cause is the improvement of the coverage (see figure 10.4).

Figure 10.3: Three different configurations of the external lead shielding: only CAST-like, i.e. 2.5 cm lead layer (the photo also shows the automatic calibrator external motor and electronic box and the feedthroughs used to extract the signals from the Faraday cage); 20 cm thick extra lead layer without closing the top of the lead castle, $5\pi/6$ coverage (the photo includes the electronics rack) and completing the external shielding, 4π coverage, (the photo shows the addition of a plastic box and the nitrogen dewar). All the configurations are provided of continuous nitrogen flow.

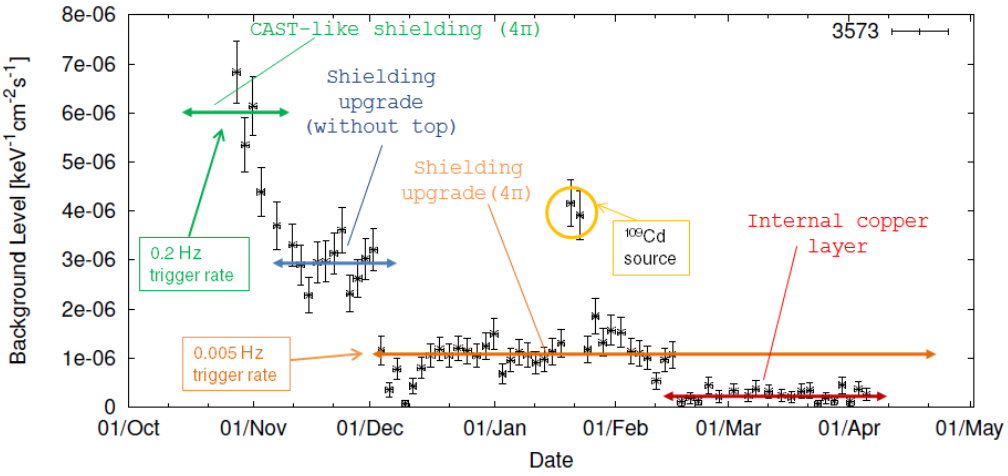

Figure 10.4: Evolution of the final background level (averaged from 2–9 keV, so including the copper fluorescence peak) of the M10 detector in the LSC along different set-up upgrades, from R2 and R3 to R4 and R5, including the period in between where probably a contamination of the Faraday cage limited the background. As a test done before the internal copper layer installation, the replacement of the ^{55}Fe source by a ^{109}Cd one during one week produced a background increase.

Consecutive increases of the lead layer drove to an important reduction of the background (a factor of 6) but a impressive fall of the trigger rate (a factor of $\sim$40). Then the interactions in the chamber had almost exclusively an external origin.

The spectra obtained during the first two phases of shielding completion shown a peak in the 5-6 keV region which remains independent of the external shielding (see plots in figure 10.5) and finally limits the background decrease to the level of 10^{-6}cts keV^{-1}cm^{-2}s^{-1}. The presence of such a peak introduced again the discussion about the origin of the 5-6 keV peak observed in CAST detectors. The simulations had explained the peak in CAST sunrise was produced by fluorescence of the stainless steel pipe (see chapter 9.2) and so it must have an external, but physical, origin no related with neither detector nor with analysis' systematics. Weeks of tests were devoted to understand the origin of the peak at LSC[220] until, finally, a 1.5 mm copper layer was inserted so as to close tighter the detector cavity (see figure 10.9), then the background dropped demonstrating its external origin. Since such a weak shielding could only block soft X-rays emissions the analysis performance remained out of doubt. The origin of the peak was attributed to a contamination of the Faraday cage inner surface.

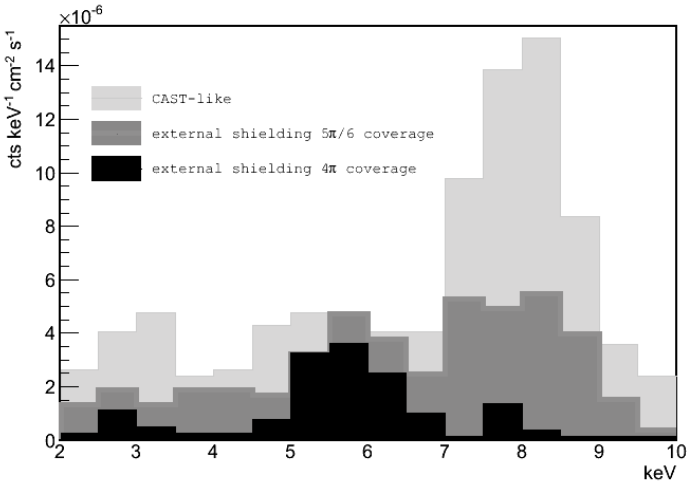

Figure 10.5: Evolution of background spectra with shielding upgrades. An existing 5–6 keV peak, that was almost not visible at CAST-like background level, became relevant after the first upgrade of the external shielding and it started dominating the background level once the external shielding was completed. The peak disappeared when a thin copper layer was used as is shown in figure 10.9.

10.3.1.1 Ultra-low background underground.

The addition of the thin copper layer led immediately to a sharp reduction of the background level (see last step in background progression plotted in figure 10.4) and a spectrum dominated by a copper fluorescence peak. The whole ultra-low background period (ULBP), contains R4+R5+R6+R7; see the spectrum in figure 10.7. The ULB was stable along almost six months of measurements, robust respect to electronic conditions and reproducible (see figure 10.6); it was twice interrupted

to perform two tests (R9 and R10, see next section 10.3.2) and recovered again. Besides some details are worth to be remarked and analysed.

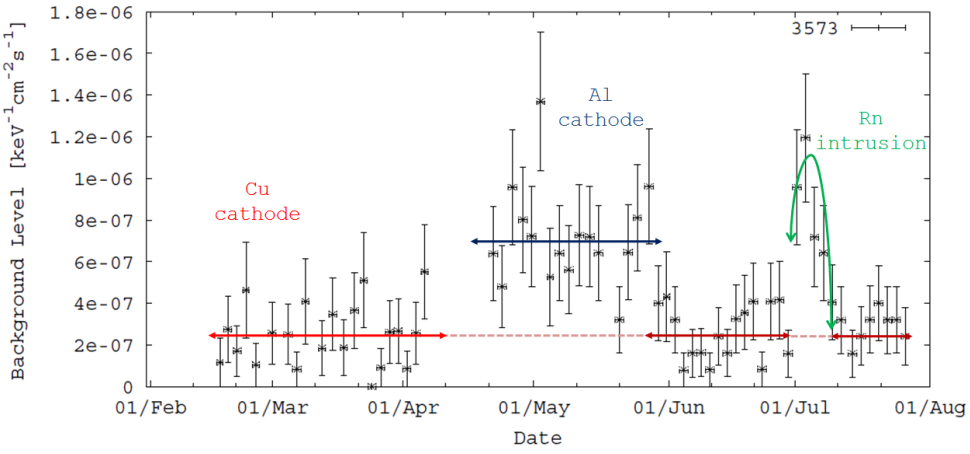

Figure 10.6: Background evolution during the ULBP (R4+R5+R6+R7) showing two rises due to the installation of an aluminium cathode (R9) and the interruption of the nitrogen flow (R10). The levels are averaged in the 2–9 keV range, including the copper peak.

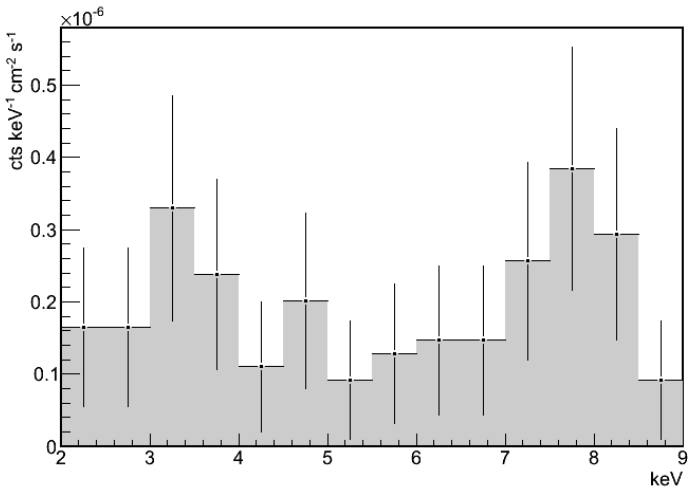

Figure 10.7: Global spectrum obtained during the three ULBP's (R4+R5, R6 and R7) showed in figure 10.6. It is mainly composed of copper and argon fluorescences.

When plotting the position in the readout plane of the final events one by one, two accumulation zones, or *hot spots*, clearly appeared in the *hit-map* (see figure 10.8 left). It is understood that they are not physical events but due to micro-sparks related with any kind of defect or trouble of the micromegas in these particular points. Nevertheless they accounted for 1/3 of the total amount of counts during the first partial ULBP (see 10.8 right) in such an small detection area. They were

rejected for the final background level calculation. In fact, after opening the chamber for the cathode replacement, they vanished. However, *it is very interesting for the understanding of the detector background limitations the fact that these micro-sparks events can evade the CAST discrimination criteria.*

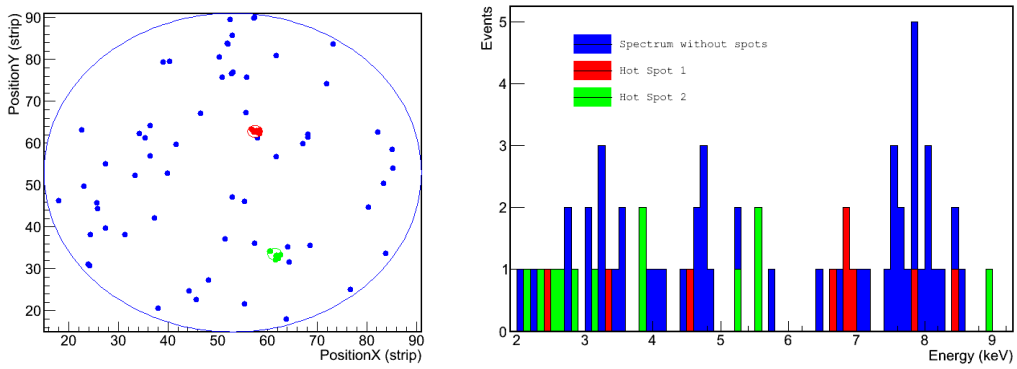

Figure 10.8: Partial results corresponding to the first ULBP. Left: events hit-map, where two accumulation zones (hot spots) are clearly detected. Right: background spectrum, the histogram distinguishes the events in the hot spots. These are distributed uniformly, while the rest of them tends to be accumulated in the copper fluorescence peak.

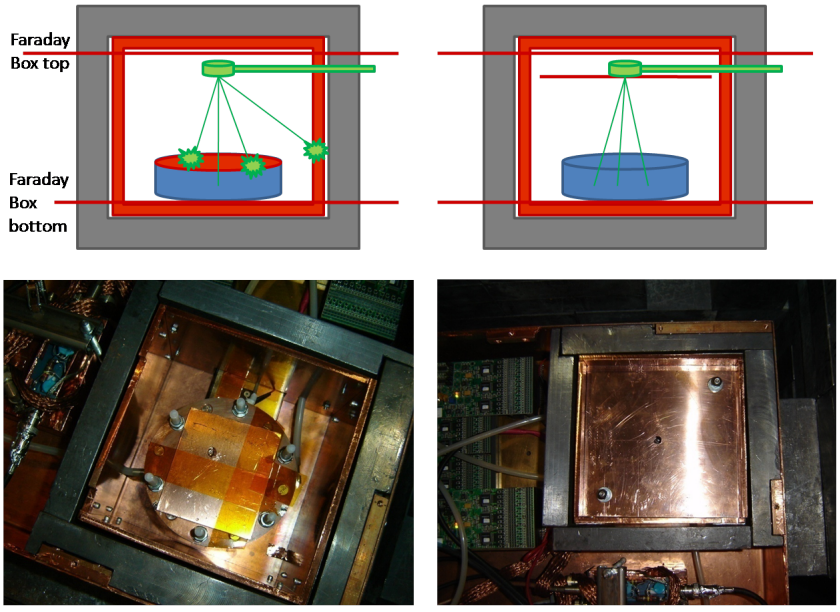

Figure 10.9: Two inner (inside the internal shielding) configurations. First (on the left) the ionization chamber is closed by a 1.5 mm thick copper layer. Second (on the right) the internal cavity is closed from its top. The first one was adopted only during the first weeks of the first ULBP, until March the 17th.

The mentioned thin copper layer was used to compare two different internal configurations, that divide the first partial ULBP into two periods, labelled R4 and R5. In a first configuration the copper layer was used to close the chamber's window, leaving a small hole for calibrations (R4, figure 10.9 left). In a second one the copper layer was moved up to the calibrator level, this way the calibrator gap was blocked and the Faraday cage top screened while the window is kept open to the interior of the inner shielding cavity (R5 and the following runs, figure 10.9 right). The second configuration has been adopted for the rest of the measurements.

A relatively larger copper peak found in the first configuration (see comparison in table 10.1) might be the unique difference between both internal configurations' background (taken with similar exposure, see the summary table 10.7). This is very interesting because both set-ups are not physically equivalent at all. That fact points to the idea that the radioactivity which causes the final background should be present in the detector itself. If the radioactivity were present, for instance in the lead walls, one would expect the interactions of γ emissions with the inner copper walls of the detector cavity to have an important contribution, because it has been shown that fluorescence are a very efficient via to produce final counts in this detector, since it is specialized in X-rays. However, when the copper layer closed the window, blocking the likely innermost shielding walls contribution, the effect on the background level was small[2].

	Cu layer on strong-back	Cu layer on top	All the ULBP
2-7 keV	1.5 ± 0.9	1.6 ± 0.9	1.5 ± 0.5
2-9 keV	1.8 ± 0.8	1.7 ± 0.8	1.7 ± 0.4

Table 10.1: Comparison between both internal configurations during the first ULBP. Final background levels expressed in $\times 10^{-7}\,\mathrm{keV}^{-1}\,\mathrm{cm}^{-2}\,\mathrm{s}^{-1}$and statistical errors as 2σ.

Besides, the copper peak seemed to be relatively higher in the first configuration, when the copper layer increases the copper surface directly exposed to the gas chamber. That geometry can be thought to be more favourable to the detection of copper fluorescence only if the exciting radiation is originated in the detector itself. *This is, in principle, an argument that reinforces the idea that the detector's intrinsic radioactivity is the main limitation for the background level evaluated in these tests.* However, the same reasoning stands for the radiation originated in the electronic components (gassiplex cards, etc.) that can reach the detector through the unshielded neck of the plexiglass base. Considering that case, *perhaps the background limitation is not put by the detector, but by the particular CAST-like set-up.* This is a sensible possibility to be explored in future tests (see chapter 11).

[2]Lately, the lead internal shielding was replaced by a copper one, 2.5 cm thick, and no background improvement was observed.

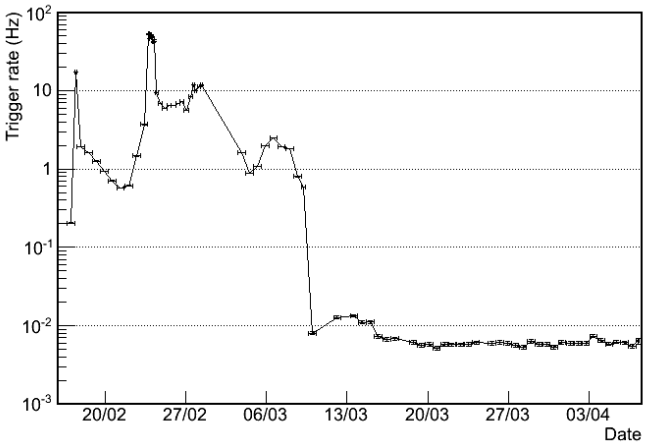

Figure 10.10: Evolution of the trigger rate during the first ULBP. Noise in the mesh line produced huge and variable increase of the trigger rate. The noise trouble is solved in March the 9th by the replacement of a damaged HV feedthrought of the Faraday cage; the background level kept stable.

Last, but not least, during the beginning of the ULBP the analysis had to deal with severe electronic noise conditions (see plot in figure 10.10). That fact motivated several changes in the electronic settings and micromegas gain. None of them affected sensibly the background level. When the noise was finally improved the trigger rate decreased to a stable 5×10^{-3} Hz, what was called *Ultra-Low Trigger Rate*, without reflection in the background level. This rate seems physical since a later improvement of the SNR, by means of a an increase of the integration time of the timing amplifier, in March the 24th had no effect. The same rate has been reproduced in all the later ULBP's when the noise conditions were good enough. A very brief analysis report about this period can be found in figure 10.11.

The table 10.2 summarizes the ULBPs and contains the final numbers. It might be noted a slow, but progressive, increase of the background level, though all the partial levels are compatible due to the few statistics. Such increase could be related with a slow degeneration of the M10 detector. Another possibility could be a progressive accumulation of radon progeny during the interruptions of nitrogen flow (mainly during the set-up interventions). Two arguments favorable to the radon accumulation hypothesis are that it looks like a faster increase in the 3rd ULBP, just after one week of radon intrusion in the detector environment; and the fact that the 2-7 keV averaged background increased respect to 2-9 keV, because a 3 keV peak is a kind of signature of radon induced background (see section 10.3.2.2).

	meas. time (days)	Bkg ([2-7] keV)	Bkg ([2-9] keV)
1st ULBP	41.41	1.5 ± 0.5	1.7 ± 0.4
2nd ULBP	25.86	2.0 ± 0.6	2.1 ± 0.6
3rd ULBP	19.65	2.8 ± 1.0	2.7 ± 0.8
Whole ULBP	86.92	1.9 ± 0.3	2.1 ± 0.3

Table 10.2: ULBP summary. Final background levels expressed in $10^{-7}\mathrm{keV}^{-1}\mathrm{cm}^{-2}\mathrm{s}^{-1}$ and statistical errors as 2σ.

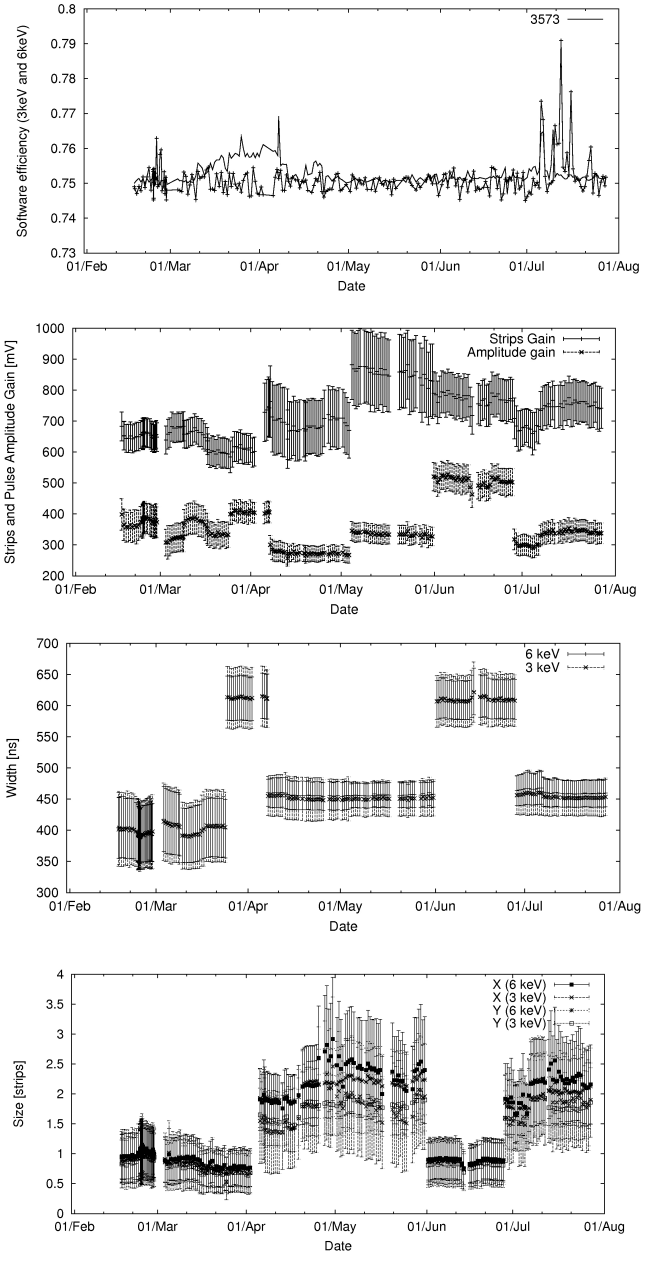

Figure 10.11: Evolution during the period of figure 10.6 of the software efficiencies (top), signal amplitudes (second plot) and some observables: mesh pulse's width and strips cluster's size (bottom). A 75% efficiencyiy for both 6 and 3 keV events could always be got. The gain plot reflects sharp changes of settings and conditions which are not correlated with the background steps, the latter are always explained only by physically relevant set-up changes. Mesh and strips correlated changes in gain are related with changes in mesh HV or gas. Changes that affect only to the mesh gain, are related with timing amplifier settings, clearly manifested in the pulse width evolution. At the middle of the third ULBP the timing amplifier integration time was again reduced without neither improving background level nor increasing the trigger rate. The cluster size is basically correlated with the strips gain, but also affected by the noise.

In any case, an upper limit about $2\times10^{-7}\,\mathrm{keV}^{-1}\,\mathrm{cm}^{-2}\,\mathrm{s}^{-1}$ *can be safely established for the background induced by the CAST microbulk detector intrinsic radioactivity, if using a copper cathode, even with a relatively big transparent window.*

10.3.1.2 Necessary lead thickness to reach the detector intrinsic limit.

Initially, the external shielding was upgraded to be thick enough so as to neglect any external γ flux influence. Once an intrinsic background limit estimation has been achieved, it is convenient to know which lead thickness is necessary to do it. The point is directly related with the feasibility of reproducing the strategy at surface, because of CAST platform weight and space limitations and, more fundamentally, cosmic rays likely interactions with the lead mass.

A first estimation could rely in a very naive calculation based in the attenuation suffered by the hardest natural radiation, the 2614 keV γ from ^{208}Tl. The mean free path of such a photons in lead is $\lambda \simeq 2.0$ cm; then the attenuation factor expected for a 2.5 cm shielding would be $\simeq 0.3$, which is rather coherent with the background decrease observed in the first installation of the shielding in CAST (see 8.2.1.2). Then, for an extra external shielding of 10 cm an additional attenuation of $\simeq 10^{-2}$, would be estimated; while the background has been reduced about 30 times from CAST-like level when installing the 20 cm thick lead shielding. Thus, being aware of the simplicity of such an estimation which does not have into account the secondary particles that can penetrate deeper in the shielding, it would be expected 10 cm to be enough to reproduce the same ULB level.

With the aim of confirming this fact, the external lead shielding was reduced to 10 cm in a series of measurements (R8) that started after the installation of our test bench in the Hall A of the new facilities. The M10 was replaced by the M17, with better performance. The M17 was mounted using the same copper cathode that had been recovered from M10, registering a background level of $(2.1 \pm 0.6)\times10^{-7}\,\mathrm{keV}^{-1}\,\mathrm{cm}^{-2}\,\mathrm{s}^{-1}$in [2-7] keV (see table 10.6 for more information) along an stable new ULBP (see figure10.12) and a spectrum (figure 10.13) very similar to that of the first ULBP.

The notable coincidence, in background level and also spectrum shape, with the results obtained by the M10 inside a 20 cm lead castle suggests that *the same intrinsic limit for the CAST-like set-up has been found with a different microbulk and only 10 cm of lead.* However it must be recognized the possibility of an accidental coincidence, due to the use of a thinner shielding but compensated by a better detector performance which cannot be completely rejected.

The robustness of the ULB level against the changing quality of the signals (see figures 10.11 and 10.6) *stands for the achieved level to be consequence of a physical contribution instead of being affected by any systematic effect.* In section 10.4 a progressive shielding upgrade is applied to the M17 (R14, R15 and, finally, R8), like it was done with M10 (see figure 10.4), which allows to understand the ULB

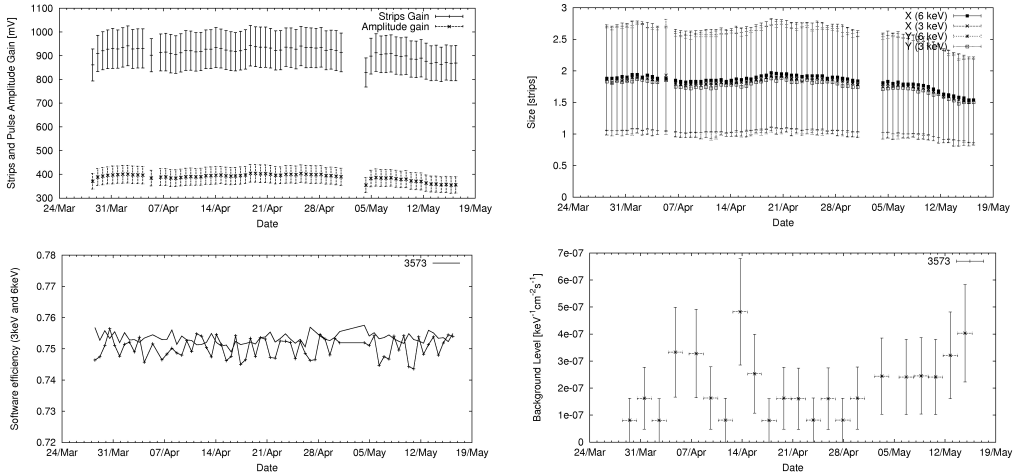

Figure 10.12: Stability and good gain of the M17 detector during the first ULBP in the new LSC Hall A (R8) with only 10 cm of lead thickness as external shielding. The higher gain increased the strips multiplicity from about 4 with the M10 to 7, but *size* observable remains more stable as a more accurate description of the real event dimensions.

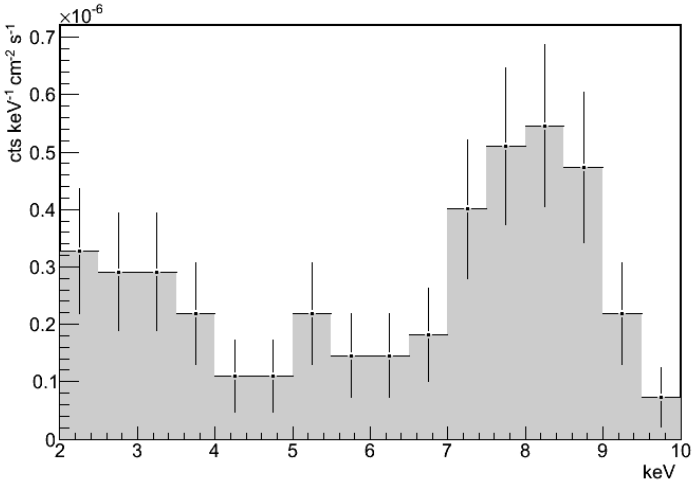

Figure 10.13: Spectrum taken by M17 with 10 cm thick external shielding (R8). To compare with that in figure 10.7.

level as a kind of saturation while the external influences are becoming negligible. *To consider a pragmatic conclusion: this ULB level,* $2\times10^{-7}\,\mathrm{keV}^{-1}\,\mathrm{cm}^{-2}\,\mathrm{s}^{-1}$*, can be achieved with a good detector, a radiopure cathode, an atmosphere clean of radon and a 10 cm thick lead shielding in absence of cosmic rays.*

10.3.2 Other contributions to the final achievable background: detector components and radon near the detector.

In previous section 10.3.1 we have talked about an *upper limit* for the background level imposed by the intrinsic CAST microbulk radiopurity; that is the suitable term since such measurements concern not only the micromegas but the whole detector, including chamber and accessories. The ULB implies a great sensitivity in order to evaluate the direct influence of radioactive pieces or other factors which can influence on the detector background. That has been the main research program of LSC set-up since the consolidation of the ULB in the new experimental hall. The effect of the two most obvious influences was already shown in figure 10.6 and are studied in detail in this section.

10.3.2.1 Aluminium cathode contribution.

Before starting the shielding upgrades the aluminium cathode, in principle the less radiopure piece of the chamber structure, had been replaced by a copper one. Once the first ULBP had been registered, the aluminium cathode was installed again with a double purpose: to evaluate its contribution and so as to create a perturbation to lately confirm the reproducibility of the ULB. The effect on the background is clearly visible in figure 10.6 (period in dark blue, R9), averaging the background reported in table 10.3.

	time (days)	Bkg ([2-7] keV)	Bkg ([2-9] keV)
Al cathode meas.	35.0	7.1 ± 1.2	7.2 ± 1.0
Difference with Cu meas.	—	5.2 ± 1.2	5.1 ± 1.0

Table 10.3: Final background levels during R9 expressed in $\times 10^{-7}\,\mathrm{keV}^{-1}\,\mathrm{cm}^{-2}\,\mathrm{s}^{-1}$and statistical errors as 2σ.

The background spectrum (see figure 10.14), when compared with the ULBP's one using a copper cathode, shows an increase of the copper fluorescence and a much more notable enhancement of the background in the low energy region. The trigger rate also increased up to 5×10^{-2} Hz, that is to say about one order of magnitude, what cannot be attributed at all to noise.

The aluminium cathode radioactivity was measured using a germanium detector in the LSC, finding the material to be relatively radiactive (see table 10.3.2.1). The result is not far from similar measurements done for aluminium, despite our cathode was specially dirty for the ^{238}U chain, which was found to be broken beyond ^{222}Rn. The high ^{238}U activity is deduced from the ^{234}Th value, which decays before the ^{222}Rn, so the radioactive origin cannot be attributed to radon accumulation due to long time exposure to high radon contributions in the old LSC.

The copper cathode was measured too with the same germanium detector. The limits obtained are much lower than the detected levels for the aluminium. It is

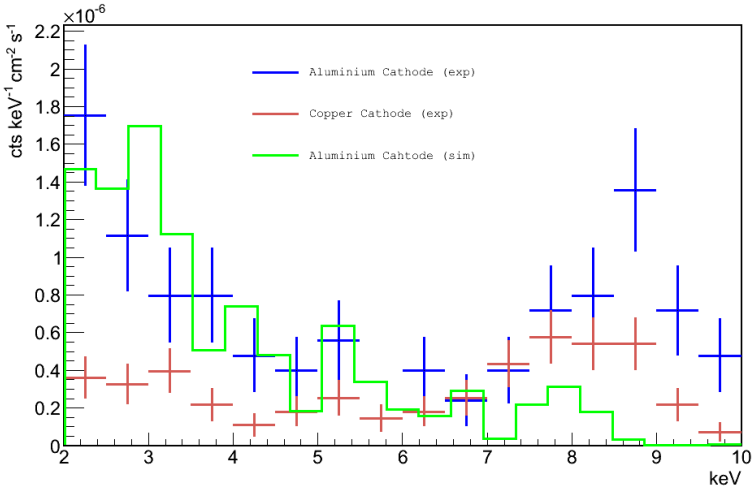

Figure 10.14: Experimental spectra collected with aluminium (R9) and copper cathode (old ULBP, R4-7) together with the simulated contribution from an aluminum cathode own radioactivity. Simulation and plot by J.G. Garza.

sample	units	^{238}U	^{232}Th	^{235}U
Al CAST cathode[222]	Bq/kg	30	0.42	0.49
Al measured at LSC[223]	Bq/kg	7-12	0.4-0.5	0.5-0.9
Cu CAST cathode[222]	mBq/kg	<27*	<22	<30
Luvata Cu[224]	μBq/kg	<12	<41	<91
Stainless Steel[223]	mBq/kg	10-70	10-70	3-60

Table 10.4: Radioactivity levels for common copper materials and direct measurements results. Note the units change.

interesting to note that such measurements include the mylar foil and, in particular, the glue used to join it. External measurements[3] of clean copper yield even much more restrictive limits for copper (which was the copper used for the sunset 2012 upgrade (8.2.1.3). *In consequence the copper cathode seems very unlikely to limit the* $\approx 2\times10^{-7}\,\mathrm{keV}^{-1}\,\mathrm{cm}^{-2}\,\mathrm{s}^{-1}$*present ULB level.*

Besides, most of cathodes which has been used in CAST were made neither of copper nor of aluminium, but stainless steel. There is certain diversity in the radioactivity measurements, but typical values are situated around the middle point between aluminium and copper. Therefore, *a stainless steel cathode can be expected to limit the ULB, while its contribution would be negligible at CAST-like levels.* This is exact whether regarding just the intrinsic radioactivity levels; however the possibility of stainless steel materials fluorescences in the range 5–7 keV could make our detector particularly sensitive to that material.

[3]Measured with GDMS (Glow Discharge Mass Spectroscopy).

The fact of having a clearly identified background source, whose cause and effect have been evaluated experimentally, means a great opportunity for reality and simulation comparison. The natural chains decays have been simulated[4] (see sections 6.2.4 and 9.1) according to the values in table 10.3.2.1 (until ^{222}Rn in the case of ^{238}U) yielding the background plotted in figure 10.14 together with the two experimental spectra. A big source of uncertainty come from the estimation of the ^{238}U chain activity.

Probably the most suitable comparison should be done with the subtraction of the copper's background from the aluminium's one, because, according to the former discussion, the ULB cannot be attributed to the copper cathode. Then an small copper fluorescence peak is expected and most of the background is concentrated in the low energy region. It seems that a simulated background caused by ^{238}U contamination of an aluminium cathode about tens of Bq/m^3 can explain the experimental background level and shape.

The most significant difference is the presence of a clear 3 keV peak in the simulated spectrum. It seems reasonable that superficial decays in the inner side of the cathode produce argon fluorescence in dead areas of the chamber that are later detected in the active volume. The case of the disagreement can be the assumption of a perfect parallel drift field by the simulation since the contrary (i.e. a drift field which was no perfect) could produce dead regions of the conversion volume. Although it is also possible that the energy resolution, degraded by gain variations along time, made not possible to distinguish the peak in practice.

That successful cross-check triggers a research line that relies in simulations and estimated radioactivity values to identify the causes of the observed ULB limit (see section 9.4).

10.3.2.2 Radon near the detector, background contribution and effects.

The nitrogen flow to the Faraday cage was interrupted during one week (see figure 10.6, period in dark green, R10). Besides the goal of the suppression of the radon contribution to the background, the nitrogen flow was considered necessary because it had been observed that radon decays close to the detector can induce sparks in the micromegas (see the sparking rate during nitrogen interruption in figure 10.15).

The mechanism is the following: ^{222}Rn progeny, as charged ions, can be trapped by the cathode window[5]. Later decays can bring a energetic α particle, above 5 MeV, prompting into the chamber, which is working with suitable gain to see X-rays, one thousand times less energetic. As a consequence the avalanche can produce a spark.

The radon progeny accumulated in the cathode window can induce background as well, what is shown in figure 10.15, where partial averaged background mea-

[4] Simulation by J. G. Garza.

[5] In fact, the same principle is being applied in a prototype of radon high sensitivity detector in the TREX-lab.

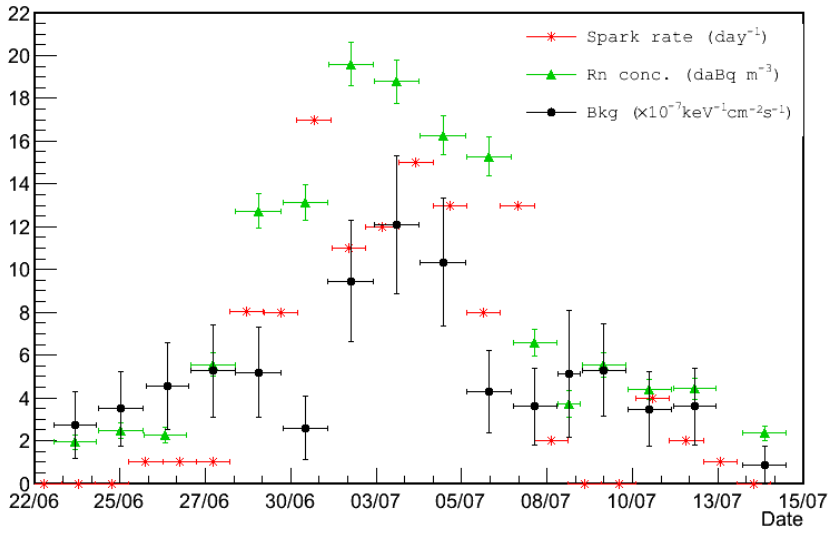

Figure 10.15: Radon concentration around R10 inside the detector's Faraday cage as were registered by the alphaGUARD detector and the effect on the micromegas background and sparks rate.

surements, sparks rate and radon concentration measured in the Faraday cage are clearly correlated. The radon concentration and background are directly contrasted in the plot of figure 10.16 left. The linear fit used to evaluate the radon contribution yields a base value of $(1.6 \pm 0.7)\times10^{-7}\,\mathrm{keV}^{-1}\,\mathrm{cm}^{-2}\,\mathrm{s}^{-1}$, compatible with the ULB level. From the fit slope the deduced radon influence is $(3.0 \pm 0.8) \times 10^{-9}\,\mathrm{keV}^{-1}\,\mathrm{cm}^{-2}\,\mathrm{s}^{-1}/(\mathrm{Bq\,m}^{-3})$.

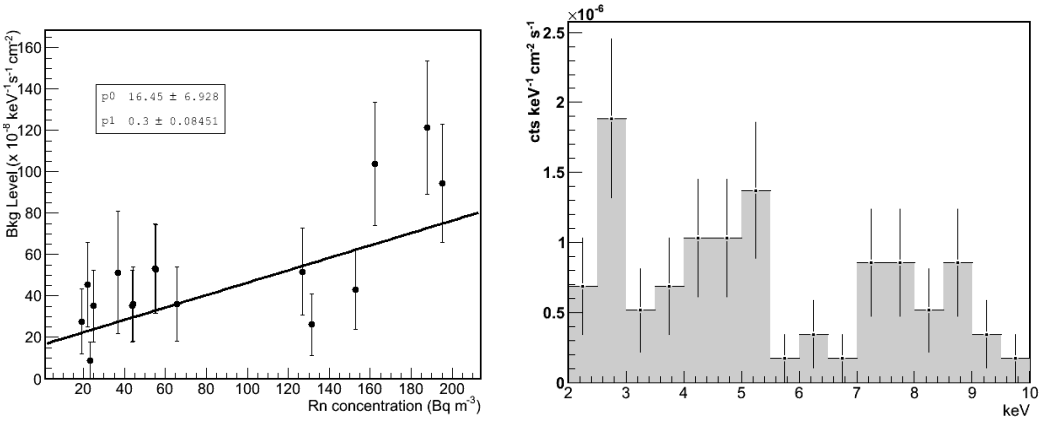

Figure 10.16: Left: Partial averaged background vs radon concentration during R10. The linear fit aims to estimate the value in absence of radon and its contribution. Right: background spectrum averaged during the radon intrusion period.

Therefore about 100 Bq m^{-3} are needed to have a contribution comparable to the ULB. Such a concentration is certainly possible for an underground lab (in the old LSC rooms concentration spikes of 800 Bq m^{-3} has been registered, typical values are 200-400 Bq m^{-3} and 80-100 Bq m^{-3} for the new Hall A) but not for a experimental hall at surface (CAST area typically registers 0-20 Bq m^{-3}). In conclusion, *this study definitely rejects the possibility of radon playing any significant role in the CAST detectors background at surface*, though the use of nitrogen flow is recommended for detector safety and stability.

Finally the background spectrum averaged during radon exposition days is plotted in figure 10.16 right. Its most relevant feature is what seems to be a strong 3 keV argon fluorescence, and the counts accumulation at low energies. The same shape has been detected more times when accidental radon intrusions had occurred. It reminds the aluminium cathode-induced spectrum (figure 10.14, what suggests such a peak could be a signature of a cathode contamination.

10.4 Surface vs underground and the cosmic rays contribution.

The cosmic rays, together with the necessity of an outlet for X-rays detection, are the most fundamental handicap for the reproduction of the underground background in a surface helioscope. However the cosmic rays effect on the CAST micromegas detectors background is subtle at the CAST levels that were achieved before the 2012 sunset upgrade, i.e. about $(5\text{-}7)\times10^{-6}\,\mathrm{keV}^{-1}\,\mathrm{cm}^{-2}\,\mathrm{s}^{-1}$. A first direct comparison between surface and underground backgrounds, using the M13 detector, yielded two completely compatible results (see figure 10.2). Unfortunately the M13 detector had not the best performance and its backgrounds show signs of dependence of the observable's distributions on the energy which surely affected to the software efficiency curve (see section 9.5, in particular figure 9.51). However, that is still the unique available direct comparison, i.e. using the same set-up, electronics and detector almost at the same time, up to date.

Undoubtedly CAST detectors had great discrimination capabilities for cosmic muons discrimination. The typical trigger rate is $\simeq 1$ Hz at surface, depending on the noise level and the threshold position. In Canfranc, with a CAST-like set-up, it is $\simeq 0.2$ Hz. That stands for comic muons as responsible of most of the interactions in the detector. The typical muon flux at surface can justify the difference, thus most of the interactions are due to cosmic muons crossing the chamber themselves.

The simulations have reported how high energy electron tracks can mimic X-ray signals (see 9.5.2, in particular figure 9.50), despite being very unlikely. The same must be expected for cosmic muons as MIPs, furthermore they cause approximately 4 times more triggers than electrons. Besides there is the contribution of muon-induced secondary events. The most obvious would be the generation of fluorescences in the immediate detector environment: pipe or cavity walls, cathode,

lead, etc.

However the simulation of cosmic muons is more complex than that of environmental γ, since it implies much higher energy particles and more Physics are involved, specially if we are interested in secondary events. It is not only that much more resources are consumed, but it is also more difficult to plan a cross-check of the results. The experimental approach can produce results easier (providing the availability of an underground lab); and that is the subject of this section.

10.4.1 Comparison of the backgrounds of one CAST detector in three locations.

The robustness of M10 microbulk detector have allowed the production of backgrounds in CAST-like set-ups in three different situations along more than four years, figure 10.17 and table 10.5 are a compilation. The oldest spectrum corresponds to the last period of the 2008 data-taking campaign, when the M10 was mounted in the sunrise side of the CAST magnet. The second one was registered at Canfranc old lab, using the CAST-like test set-up. For the most recent one, the CAST-like test set-up was moved to Zaragoza, and a new acquisition, based in T2K electronics and an oscilloscope (see section 5.5) was used[6]. A special electronic card was built for adapting the Gassiplex-like (SAMTEC) connectors to the T2K's (ERNIE), being the set-up able to read 192 of the 212 strips. However an interface program was written so as to reduce all the information gathered by the T2K electronics to only that the classic CAST acquisition can register. Thus data were written in CAST raw data format so as the CAST analysis routines can normally deal with them. The motivation is to perform direct comparison as independent on DAQ and analysis as possible.

set-up and date	run time (days)	Bkg (averaged [2-7] keV)
CAST sunrise (Fall 2008)	23.6	7.1 ± 0.4
Zaragoza (Nov 2011)	2.8	4.9 ± 1.0
LSC old lab (Nov 2010)	6.0	3.8 ± 0.6

Table 10.5: Attempt of evaluation of the effect of the set-up and environmental upgrades effect on M10 detector background from the spectra plotted in figure 10.17. The corresponding runs are R11, R2 and R12. Final background levels expressed in $\times 10^{-6}\,\mathrm{keV}^{-1}\,\mathrm{cm}^{-2}\,\mathrm{s}^{-1}$and statistical errors as 2σ.

The 2008 background (R11) has the typical CAST sunrise spectrum shape, with two comparable peaks at 6 and 8 keV. In comparison, Canfranc's background (R2) have a bigger 8 keV peak, but there is no 6 keV. Apart from this, the whole background level seems to be smaller below 7 keV. There are mainly two changes in the

[6]Nowadays the M10 detector is at work at the new Zaragoza T-REX lab in the CAST sunset replica set-up.

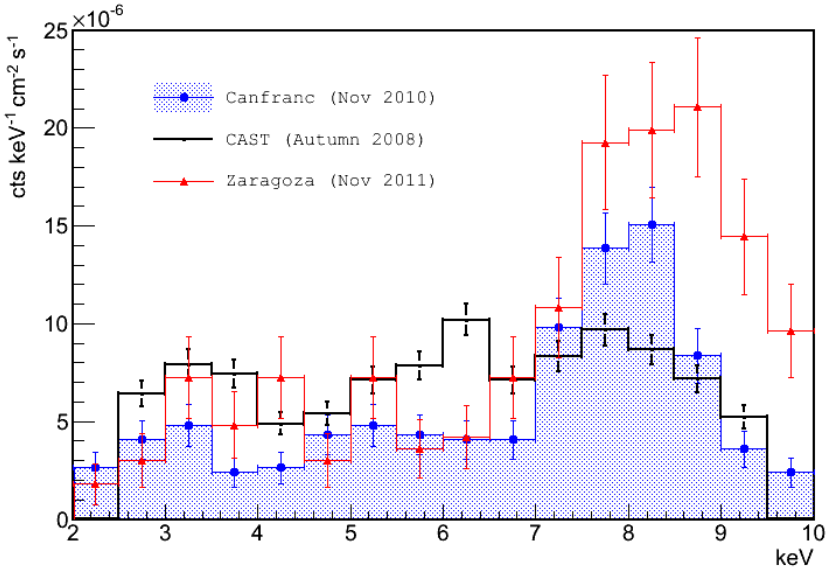

Figure 10.17: Three background spectra registered by the M10 microbulk detector: in CAST sunrise (R11) side and, with tests CAST-like set-up, underground (R2) and at surface (R12).

set-up to be considered in order to explain the background differences. The absence of the stainless steel cathode and pipe to magnet's bore in the test set-up explains the absence of the 6 keV peak in Canfranc, as the copper cathode and innermost copper walls of the detector's cavity of the test set-up explains the bigger 8 keV peak. Because of the 4π closure and the absence of the pipe in the test set-up, a sensible decrease of the background is expected; according to section 9.2, a reduction between 25% and 50% could be expected.

There are also environmental changes. To start with, the absence of the cosmic rays contribution. In addition, we must be aware that in the LSC the environmental γ flux is known to be more intense, perhaps twice than in the CAST area. Therefore a third background is added to the figure 10.5: R12 that represents the test set-up at surface (Zaragoza's lab). The new background level below 7 keV is similar to CAST, with the exception of the 6 keV peak. It is higher than in Canfranc at low energies, but similar at medium energies, with exception of a little 5 keV peak. Regarding the expected effect of the better closure in the 8 keV, it cannot be evaluated since the introduction of the detector in an environment made of copper compensates and exceeds the improvement. Precisely that copper fluorescence peak is notably higher than in Canfranc and explains the 5 keV peak as a escape peak. It is tempting to attribute the increase of the copper peak to the cosmic muons. On the other hand the copper cathode used for the particular LSC run had a different strong-back design, with lower optical transparency, which had an influence on the collection of external copper fluorescence induced X-rays.

Several conclusions can be drawn, basically from the comparison of the shape of the spectra. The 6 keV appears only in CAST set-ups, and can be attributed to stainless steel fluorescence. The underground background levels are systematically lower than at surface. The effect of cosmic-rays inducing fluorescences is suggested by comparison of Zaragoza's and Canfranc's spectra. The progression of table 10.5 looks coherent, it suggests that *the improvement of the tightness (pipe and shielding outlet being removed) led to an improvement of the background about 30%*, in agreement with the simulation estimation, and *a non negligible cosmic rays contribution about* $1\text{–}2\times10^{-6}\,\mathrm{keV}^{-1}\,\mathrm{cm}^{-2}\,\mathrm{s}^{-1}$ *which would be very dependent on the set-up*, since it seems closely related with the production of fluorescences.

Unfortunately a robust quantitative estimation of the cosmic contribution cannot be extracted from these data, since the particular set-up, environmental differences and the elapsed time between runs (the M10 suffered one severe intervention between each run) introduce systematic uncertainties of the same order of the effect.

Therefore, in order to determine the cosmic rays' contribution, a direct attempt of shielding upgrade at surface must be carried out, so as to have a signal to background improvement. Moreover, the cosmic rays' contribution may depend on the shielding thickness. That kind of tests are exposed in the next section.

10.4.2 Direct comparison of medium size shielding set-ups. Cosmics muons active veto.

Several set-ups with medium size shielding, about 5 cm lead, were performed at surface at Saclay's micromegas lab[225] and Zaragoza (like R13[221]) leading to a notable background decrease; the obtained backgrounds oscillate around $2\times10^{-6}\,\mathrm{keV}^{-1}\,\mathrm{cm}^{-2}\,\mathrm{s}^{-1}$. The surface runs were completed by the 2012 sunset upgrade (R16, see section 8.2.1.3), the first *heavy* ($>$ 5 cm thickness) shielding tested at surface.

These surface runs were complemented with a 5 cm external shielding set-up carried out in the LSC (R15) as part of the progression for the establishment of the ULB of the M17 detector[7] only with 10 cm of extra lead thickness (R8) (section 10.3.1.2), see figure 10.18 and table 10.6.

The direct comparison of both, surface and underground, set of runs done in figure 10.19 shows a clear saturation effect experimented by surface upgrades. On the other hand the underground values show a sharp decrease, that confirms the 10 cm thickness level as very close to be free of the external γ flux influence. This underground curve is corroborated by a set of simulations of several shielding thickness[226] which consider the external γ flux as the unique background source, so purely reflecting the screening effect of the shielding.

[7] For the M17 detector measurements the internal shielding (CAST-like) was made entirely in copper, so it is slightly lighter than for the M10 detector measurements. No clear background improvement was observed after the replacement of the internal lead with copper, using 10 cm

external shielding thickness	run time (days)	Bkg ([2-7] keV)	Bkg ([2-9] keV)
0 (only CAST-like)	6.0	67 ± 8	100 ± 9
5 cm	11.6	3.6 ± 1.4	4.8 ± 1.7
10 cm	43.1	2.1 ± 0.6	2.8 ± 0.5

Table 10.6: Progressive upgrade of the M17 shielding in the new LSC Hall A; the progression of runs is R14, R15, R8. The corresponding spectra can be found in figure 10.18. Final background levels expressed in $\times 10^{-7}\,\mathrm{keV}^{-1}\,\mathrm{cm}^{-2}\,\mathrm{s}^{-1}$ and statistical errors as 2σ.

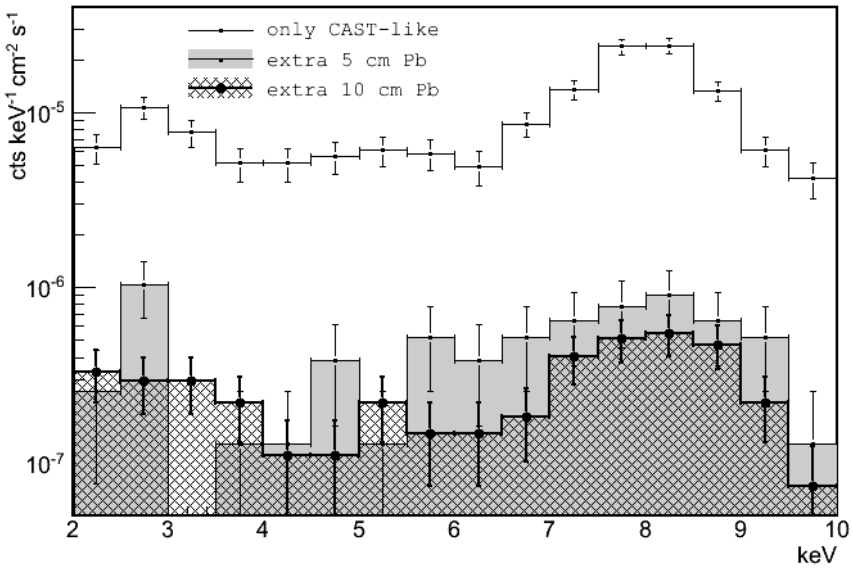

Figure 10.18: Progressive upgrade of the M17 shielding in the new LSC Hall A; the progression of runs is R14, R15, R8. The corresponding background levels can be found in table 10.6.

Some treatment of the simulation curve must be explained. Firstly the simulation points have been corrected by a common factor so as to match the first one, which is basically the one obtained in section 9.2, with the experimental value; thus trying to correct systematic errors due to simulation efficiency and other uncertainties. Finally the Canfranc's value for the intrinsic background level of the set-up (see 10.3.1), $\simeq 2 \times 10^{-7}\,\mathrm{keV}^{-1}\,\mathrm{cm}^{-2}\,\mathrm{s}^{-1}$, has been added to every point.

The simulation curve has been fitted to a combination of two exponential decays over a fixed ultimate background level. The two exponential decays constants try to broadly describe the different attenuation rates for the set of natural emission energies. It is remarkable the fact that the longer obtained attenuation constant corresponds to a mean free path of 6 cm, which is needed to explain the similarity,

external lead shielding.

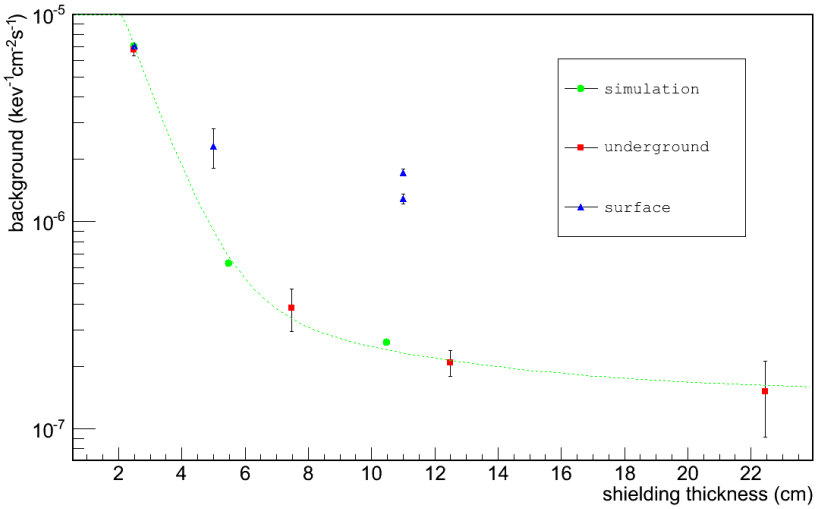

Figure 10.19: Underground vs surface. The improvement along the runs is exclusively due to external shielding upgrades. The red squares correspond to background measurements done in the LSC. The same strategy yields more modest results at surface (blue triangles). The difference should be attributed to cosmic rays. The thickest and lowest two points of the blue runs show the effect of the installation of a cosmic veto over CAST sunset detectors (see section 8.2.1.3). The green dots are simulation results used to draw the background decrease curve due to pure screening of environmental γ flux: the green line that is a fit of these points. The plot shows that this behaviour explains the underground runs.

but not coincidence, between the 5 and 10 cm results, that is three times the mean free path of ^{208}Tl 2614 keV γ, the most energetic of the natural radioactivity. This fact suggests that the estimation done at the beginning of section 10.3.1.2 was certainly naive and secondary radiation can notably extend the penetration of the radiation through the shielding. The simulations would be needed to estimate it. Therefore, perhaps an upgrade of the 10 cm shielding still may drive to a moderate improvement and should be considered in future.

To sum up, both set of values, *the simulations and the underground measurements, match and describe the background behaviour in absence of cosmic rays as a pure γ shielding effect. The disagreement with the surface series is notable and can only be attributed to the cosmic rays effect.* The good news are that *the cosmic rays contributions seems to be independent on the shielding thickness*, since no background increase is detected, at least up to 10 cm thickness.

A more direct proof should come from a set-up which also tests an strategy to avoid the cosmic muons: the installation of a plastic scintillator detector coupled to the acquisition used in Zaragoza's lab (see figure 10.20). The scintillator signal is recorded and time coincidences with the micromegas triggers can be checked off-line. Using the M10 detector with a 5 cm lead thickness (but

not very compact) the background detected in coincidence with the scintillator was $(3.0 \pm 0.6)\times10^{-6}\,\mathrm{keV}^{-1}\,\mathrm{cm}^{-2}\,\mathrm{s}^{-1}$, in 2 to 7 keV for a total background of $(5.0 \pm 0.8)\times10^{-6}\,\mathrm{keV}^{-1}\,\mathrm{cm}^{-2}\,\mathrm{s}^{-1}$[228]. It must be specified that the micromegas was mounted in *horizontal orientation*, i.e. with the micromegas' surface transversal to the upward direction, in contrast to CAST detectors set-ups and the rest of the tests, thus the flux of muons crossing the detector area is higher. *The muon-induced background accounted by the veto is of the same order than the surface background levels.* Moreover *the fact that it is higher than the one registered in vertical orientations, could be interpreted as a hint for the muons to cause directly the background, more likely than secondary radiation.*

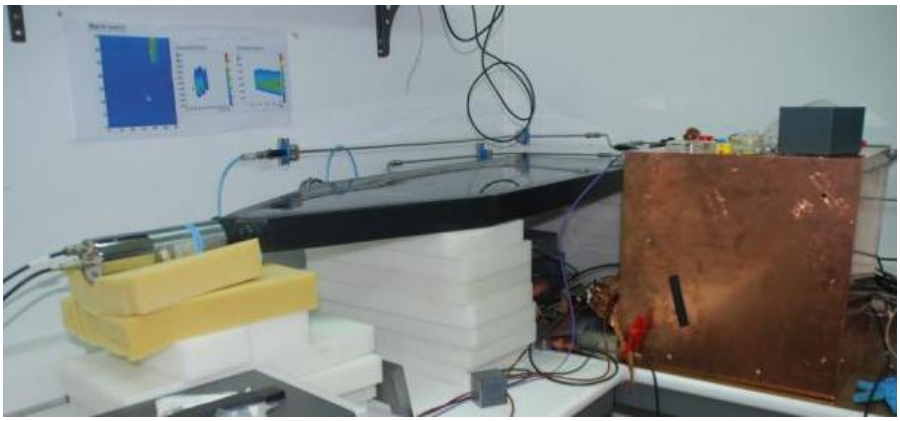

Figure 10.20: CAST-like set-up with plastic scintillator veto installed at Zaragoza's lab.

Once again, the CAST experiment itself was the first set-up proving an effective background reduction thanks to a new advance when a scintillator was added to the sunset set-up for the 2012 data-taking (see figure 8.9). Because of practical limitations the scintillator could be mounted so as to provide a 44% geometrical coverage for cosmic muons[8]. During the Summer 2012 campaign the veto got a 25% background reduction in both sunset detectors[227]. The averaged background, with and without cosmic veto, is plotted for one of them (sunset1) in figure (10.21). Thedr two background levels are also represented in figure 10.19 as the two thickest surface points. As it was already advanced by the spectrum comparisons of the previous section, the cosmic effect (and so the reduction) is more intense in the copper fluorescence peak.

A sunset set-up replica mounted in the Zaragoza's T-REX lab with a scintillator veto which has been calculated a geometrical coverage of 74% registered background values of $(1.8 \pm 0.3)/(1.18 \pm 0.28)\times10^{-6}\,\mathrm{keV}^{-1}\,\mathrm{cm}^{-2}\,\mathrm{s}^{-1}$with/without veto application, that is to say, a 36 ± 8 % reduction[229]. However, in this particular set-up the detector (again the M10) had been mounted with the same aluminium cathode

[8]Calculated from cosmic muons angular distribution at sea level without considering muons interactions (so straight trajectories and no secondary ones) and assuming a 100% efficiency for the veto.

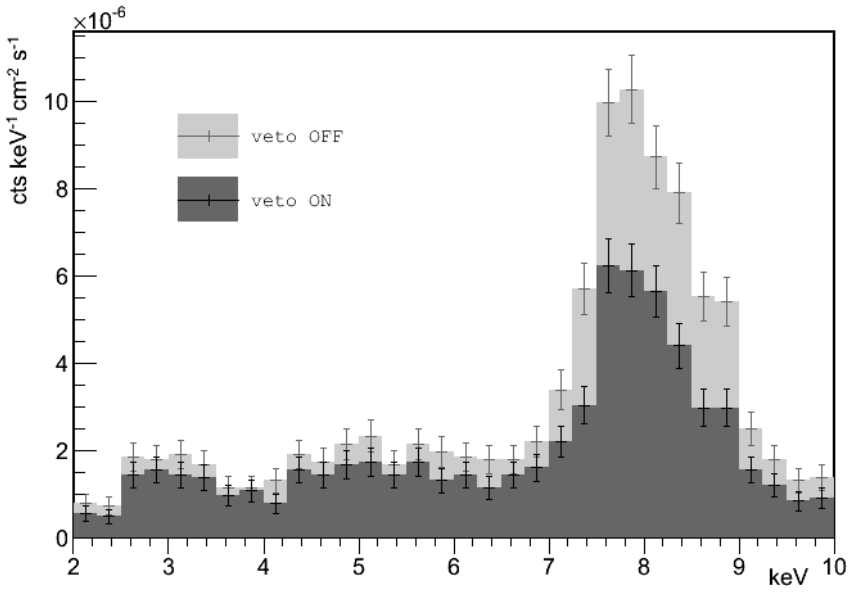

Figure 10.21: Background spectrum averaged by sunset detector 1 during the 2012 data-taking, with and without (R16) vetoing events in coincidence with the scintillator signal[227].

studied in section 10.3.2.1. The intrinsic background level for such a set-up was there evaluated to be $\simeq 7\times10^{-7}\,\mathrm{keV}^{-1}\,\mathrm{cm}^{-2}\,\mathrm{s}^{-1}$. Taking into account this floor level, unavoidable by means of the cosmic veto, the reduction experimented for the rest of the unexplained (but attributed to cosmic rays) background was really $\simeq 58\%$. In other words, the expected background for a geometrically equivalent set-up, but using a more radiopure copper cathode, should be about $7\times10^{-7}\times10^{-6}\,\mathrm{keV}^{-1}\,\mathrm{cm}^{-2}\,\mathrm{s}^{-1}$.

In conclusion, *the preliminary tests done with cosmic veto (including an official data-taking campaign of the CAST experiment) confirm the cosmic origin of one important part of background at surface for heavy shielded set-ups.* The clues point to the particular cosmic muons that directly cross the detector, or generate secondaries (as copper fluorescences) very close to it, to cause most of the background, because its contribution is almost independent of the detector shielding, but depends on the detector orientation. Therefore they should be strongly reduced by a cosmic veto, as the last test, with better geometrical coverage, has demonstrated.

10.5 Runs summary table.

R	Det.	Shd.	Lab	Bkg. [2-7] keV $\mathrm{keV}^{-1}\,\mathrm{cm}^{-2}\,\mathrm{s}^{-1}$	Exp. days	Comments
0	M13	C-l	Zgz	$\sim 9 \cdot 10^{-6}$	∼60	Systematic tests, see 10.2.
1	M13	C-l	LSC	$\sim 8 \cdot 10^{-6}$	15	
2	M10	C-l	LSC	$(3.8 \pm 0.6) \cdot 10^{-6}$	6.0	
3	M10	+20	LSC	$(2.4 \pm 0.2) \cdot 10^{-6}$	24.8	Closure, only $5/6 \cdot 4\pi$
4	M10	+20	LSC	$(1.5 \pm 0.9) \cdot 10^{-7}$	22.3	Window closed 5 mm Cu
5	M10	+20	LSC	$(1.6 \pm 0.6) \cdot 10^{-7}$	19.6	
6	M10	+20	LSC	$(2.0 \pm 0.6) \cdot 10^{-7}$	25.9	After cathode test
7	M10	+20	LSC	$(2.8 \pm 1.0) \cdot 10^{-7}$	19.7	After Rn intrusion
8	M17	+10	HA	$(2.1 \pm 0.6) \cdot 10^{-7}$	43.1	
9	M10	+20	LSC	$(7.1 \pm 1.2) \cdot 10^{-7}$	35.0	Al cathode
10	M10	+20	LSC	$\sim 1 \cdot 10^{-6}$	7	Variable Rn $\sim 200\,\mathrm{Bq/m^3}$
11	M10	SR	CAST	$(7.1 \pm 0.4) \cdot 10^{-6}$	23.6	2008 campaign
12	M10	C-l	Zgz	$(4.9 \pm 1.0) \cdot 10^{-6}$	2.8	T2K+Oscillo DAQ
13	M10	+2	Zgz	$(2.5 \pm 1.0) \cdot 10^{-6}$	4.9	T2K+Oscillo DAQ
14	M17	C-l	HA	$(6.7 \pm 0.8) \cdot 10^{-6}$	6.0	Cu shielding
15	M17	+5	HA	$(3.6 \pm 1.4) \cdot 10^{-7}$	11.6	
16	M19	SS	CAST	$(1.7 \pm 0.1) \cdot 10^{-6}$	92.3	2012 campaign

Table 10.7: Summary of runs with CAST microbulks. Runs are ordered as they appeared in the text. Tabled fields are: R (run reference number), Det. (detector name), Shld. (Shielding or set-up configuration), Lab (laboratory where the set-up was placed), background (with statistical errors as 2σ), Exp. (exposure time) and Comments. Keys for the configurations: C-l (CAST-like test set-up), +X (lead extra thickness in cm on C-l), SR (sunrise set-up, see section 8.2.1.2), SS (sunset set-up after 2012 upgrade, see section 8.2.1.3). Keys for places: Zgz (Zaragoza's chambers test bench), LSC (Canfranc *old* laboratory), HA (Canfranc new experimental Hall A), CAST (CAST experiment). The ULBP in the old LSC contains Runs 4-7. Runs 4 and 5 are also referred as the 1st ULPB, R6 as the 2nd ULBP (after test R9) and R7 as the 3rd ULPB (after test R10). R8 is also cited as the new ULBP in the new LSC. R14, R15 and R8 conform a shielding upgrade progression for the M17 detector; like R2, R3 and R4 for the M10.

Chapter 11

Conclusions and prospects from the study on the CAST micromegas background

Contents

In this chapter the conclusions deduced from the previous chapters will be briefly summarized. This is necessary since the three issues, operation in CAST, simulations and test benches, are interrelated. The study on the background in CAST micromegas along the past in chapter 8 remarked the basis that motivated the evolution of the detectors. These strategies are fundamentally the same which are now being applied to present and proposed developments. The simulation works summarized in chapter 9 were carried out with continuous feedback from the experimental tests of chapter 10. The first reliable test of the conclusions from the study was carried out in the CAST experiment itself (once again), when they were applied to the sunset upgrade in 2012 (section 8.2.1.3).

Most of the work, in particular the simulations, was focused on the sunrise set-up, which was the reference for the state of the art of micromegas background at low energies until the sunset upgrade in summer 2012. Therefore, in a first section the answers given for the initial basic questions, regarding the sunrise set-up, are summarized. These had been:

could the present (sunrise) background be improved with a better analysis performance? could small changes in detector, system or environmental parameters produce relevant impacts on the background?

is the present (sunrise) shielding the optimum one? which parts of it are really useful? can an upgrade produce further improvements?

is there an essential limitation, intrinsic to CAST detectors, to the background potential improvement?

the fundamental point that answers the rest was:

which are the main background sources?

At present, after the 2012 sunset upgrade, the level and nature of the CAST detectors' background have been completely changed; CAST sunset set-up is the new state of the art and the same questions must be addressed again. The CAST micromegas team has already undertaken new challenges, which try to exploit the same basic strategies. The conclusions from the new studies will need more time, but the inertia from the present understanding allows to make some estimations in the second section.

11.1 Answers from the background studies.

The background studies have focussed in the actual sunrise set-up in CAST (SRMM) or in the CAST-like set-up, the test-bench that was inspired by it. However some more general trends were also obtained and they will be valid for future reasoning. Therefore the background to explain has a level about (5-7)$\times 10^{-6}\,\mathrm{keV}^{-1}\,\mathrm{cm}^{-2}\,\mathrm{s}^{-1}$and the spectrum shape of figure 11.1 left, showing two peaks: one copper fluorescence at 8 keV and, probably, a stainless steel fluorescence around 5–7 keV.

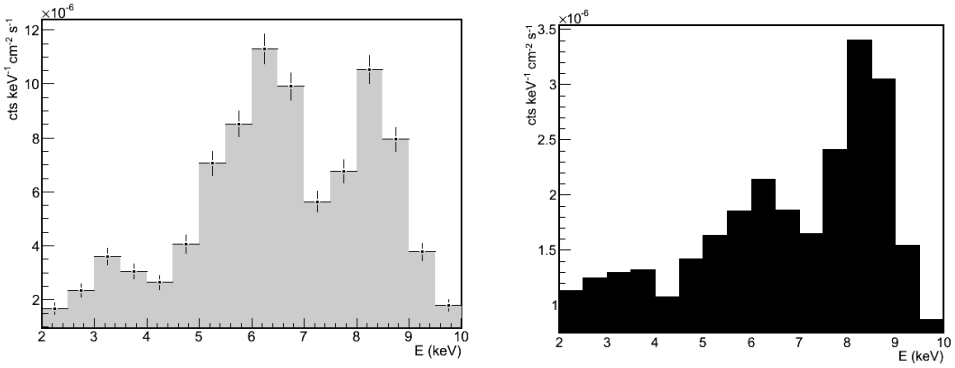

Figure 11.1: Left: Sunrise background spectrum averaged during the 2012 data-taking campaign[227]. Right: simulated background from environmental γ flux (see section 9.2).

11.1.1 About the dominant influence of the environmental γ flux.

From the simulations it is deduced that the environmental γ contribution is relevant, *they accounted for about 1/3 of the actual sunrise's background level* (see figure 11.1 right). Furthermore the simulations suggest this contribution to be higher since the spectrum shape, dominated by fluorescence peaks, points to a big impact of the fluorescences and the simulations show the way external γ can intensify this effect.

In *the simulated background a peak situated in the 5-7 keV range rises as a consequence of the stainless steel multiple fluorescence lines.* This peak is found to be mainly *a contribution of the medium-low energy γ which access the chamber via the outlet in the front of the shielding* and enter through the chamber's window, half of the times because they had previously interacted with the pipe that connects the micromegas to the magnet's bore.

However the simulated peak is small in absolute scale, when compared with the real one, and relatively small with respect to the simulated 8 keV copper fluorescence's peak. It is assumed that *such effect is underestimated by the simulation* because of several reasons: the big uncertainties in the low energy environmental γ flux, the fact that the pipe actual length is not completely considered in the simulation, and a worse software efficiency at very low energies for simulated data.

A scenario where there were more low energy γ and their vulnerability (probability of causing a final background count) was higher (for instance, because of a higher software efficiency) would produce a background very similar to the experimental one in level and spectrum's shape, only due to the environmental γ flux.

From the assumption of γ being mainly responsible of the peak and relying in results with thicker shieldings, *the weight of the environmental γ contribution to the sunrise background can be estimated around 2/3.* Besides the cosmic muons are also reasonable to produce additional stainless steel fluorescence when crossing the pipe.

Apart from that, *about 1/10 of the final γ-induced background would be due to* another outlet of the shielding: *the raquette's neck of the detector*, through which the electronic signals are extracted. In this case, they mainly contribute to the copper fluorescence peak at 8 keV.

Therefore an increase of the pure screening of external γ, i.e. basically an increase of the shielding's lead thickness, has a high background improvement potential. However, the minimization of the outlets and the prevention of the fluorescences are mandatory too. All that, of course, if no secondary effects due to interaction with cosmic rays rise and the set-up's intrinsic radioactivity does not prevent it.

The experimental tests are coherent with the simulation picture. In particular, the sunset 2012 upgrade followed the simulation guidelines and the background was reduced more than a factor 3 only by the passive shielding. Moreover the 5-7 keV peak vanished after the replacement of the stainless steel cathode and the introduction of a copper pipe that minimizes the shielding outlet and situated the

stainless steel vacuum pipes far from the detector. Furthermore, *the shielding measures against neutrons have no effect at sunrise level and radon contribution has been evaluated to be negligible at surface.*

11.1.2 About the contribution of cosmic rays.

The tests carried out at *surface* yield different results those *underground* with equivalent shieldings whey the lead thickness is increased (see figure 11.2), the *disagreement revealing the effect of the cosmic rays.* The background decrease is more modest at surface and saturates between 5 and 10 cm of lead thickness at 2012 sunset level, i.e. $\sim$(1-2)$\times 10^{-6}\,\mathrm{keV}^{-1}\,\mathrm{cm}^{-2}\,\mathrm{s}^{-1}$.

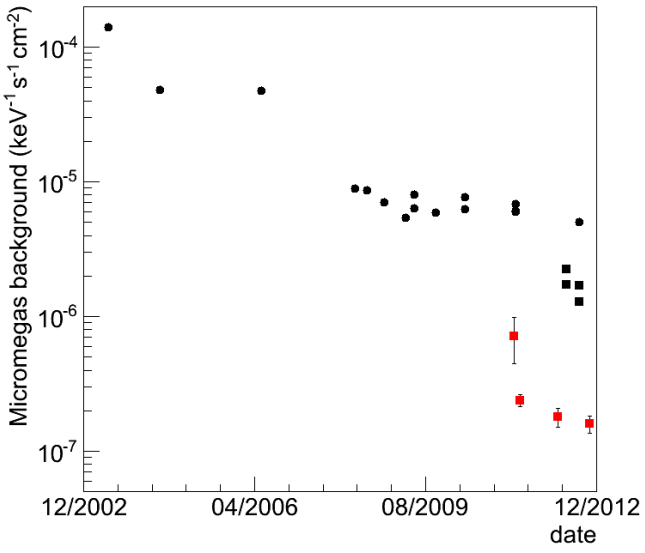

Figure 11.2: History of CAST detectors background including Canfranc values. The black series are the CAST levels during true data-taking campaigns (explained in detail in section 8.2.1), in particular the squares correspond to 2012 sunset levels. The red series are LSC results using heavy shielding. The first improvement was due to the replacement of the aluminium cathode with a copper one. The last two points obtained with only 10 cm lead thickness.

The cosmic rays interactions with the shielding do not seem to increase the background with the lead thickness, at least up to 10 cm, i.e. a thicker shielding does not entail the generation of secondary radiation in it that finally affects the background. There are hints (see section 10.4.2) from which *the muon-induced background seems to be dependent on the detector orientation.*

The cosmic muons tend to increase the fluorescence copper peak, which is generated by interaction with the most immediate detector environment: the readout and the cathode. The cosmic rays must be also responsible of part of the stainless steel fluorescence registered in the sunrise background, what could be a complementary explanation of why the γ simulation only is not able to reproduce the peak's actual size.

On the other hand *the simulations have shown that fast electrons*, above hundreds of keVs, *can mimic X-rays signals*, for instance when δ-rays or secondary argon

fluorescences occur. In these cases, the possibility of a correct interpretation is highly dependent on the analysis settings and the detector's performance, specially the strips SNR. This kind of events contribute with 1/4 to the background produced by the γ simulation. *The same mechanism could be applied to muons* as they are also MIPs.

The facts explained above suggest that *the interactions of the cosmic rays which produce the final background are not due to complex processes happening in the shielding's mass budget, rather they occur near the detector. Then a cosmic veto should significantly reduce their contribution* and its efficiency could be estimated essentially regarding the coverage of the detector's chambers. The limit for this reduction, besides the veto practical efficiency, depends on the contribution of background sources of different nature (see next sections). The tests done up to now, including the sunset data-taking during Summer 2012, reported background decreases not far from the geometrical coverage calculated for the scintillator veto in that way.

11.1.3 About the the set-up's intrinsic radioactivity.

The underground tests found *an intrinsic limit for the tests set-up*, a sunrise replica, using a copper cathode and placed together with the electronics inside a Faraday cage, about $2{\times}10^{-7}\,\mathrm{keV}^{-1}\,\mathrm{cm}^{-2}\,\mathrm{s}^{-1}$, so *near 30 times lower than the sunrise level* (see figure 11.2). This limit is thought to be intrinsic to the basic set-up and not related with the lead mass of the extra shielding, even though it is not archaeological, since blocking the chamber's window has no detectable effect on the background (see section 10.3.1.1) and ^{210}Pb decays or bremsstrahlung would be expected to produce fluorescence in the copper inner walls surrounding the detector. *Lead walls of 10 cm thickness are needed to reach this* level, and the dependence with the thickness agrees with the one expected from simulations that consider only the screening of an external γ flux and a fixed floor level.

11.1.4 About the nature of the background events.

According to the simulation picture of the environmental γ flux-induced background, which is thought to be dominant (about 2/3 of the total sunrise's background) is composed of 1/2 of Compton interactions, which produce a flat spectrum. A fraction of 1/4 of the events where electrons directly interact with the gas, some of them just consequence of photoelectric effects in the cathode or the mesh while others are fast electrons crossing the chamber. Finally about 1/4 of photoelectric interactions accumulated in the fluorescence peaks, that accounts only the stainless steel peak since the copper one is beyond the CAST RoI. The latter type of events should be more significant in reality, because of the reasons that were explained in section 11.1.1, as it is clear from the comparison of spectra in figure 11.1.

The contribution from cosmic muons must be composed of an important part of induced fluorescence events, in the stainless steel peak and in the copper escape

peak at 5 keV, and other part of direct muons' tracks, similar to the electron events from γ.

As consequence most of the final background events are true mono-cluster photon events: all the photo-electric events, like fluorescences, and the Compton events, which are also due to single interactions. They sum *roughly 2/3 of the total background events*, which *cannot be rejected by the analysis*. The remaining 1/3 might be rejected by an optimized detector and analysis.

11.1.5 About the influence of the detector parameters and other systematics.

Last but not least, the different background levels achieved in the tests seem to be well defined for the set-up essential geometry and materials and to be reproducible. Nor detector performance (once acceptable), neither environmental or electronic parameters, neither analysis version had relevant impact in the background level.

To sum up, simulations and tests agree in the following rought picture of the sunrise background. About 2/3 is produced by external γ, half of them due to the stainless steel fluorescence. The remaining 1/3 is due to cosmic muons, again part of them contributing to the steel peak. Intrinsic radioactivity, radon or other background sources are negligible at this level.

11.2 Prospects for next CAST background improvements.

The recently confirmed background picture, that was the initial goal of this work, becomes a secondary issue. Today the status of the art for micromegas background at low energies has moved to the sunset side of the CAST magnet, after the 2012 upgrade. A new background picture must be drawn. Only the conclusions or tools that are applicable to the new scenario are useful, e.g. the micromegas Monte Carlo model. The new Zaragoza's test set-up is now a sunset replica (see figure 11.3 left), built at the same time than the actual sunset set-up following the same careful guidelines regarding materials and cleaning; it is currently installed in the T-REX lab. The sunrise set-up replica, which inspired the old tests set-up, is still in operation in the LSC.

Two are the main references available for valuing the new scenario: the underground level $\sim 2{\times}10^{-7}\,\mathrm{keV}^{-1}\,\mathrm{cm}^{-2}\,\mathrm{s}^{-1}$and the sunset level during the 2012 campaign $\sim 10^{-6}\,\mathrm{keV}^{-1}\,\mathrm{cm}^{-2}\,\mathrm{s}^{-1}$(see figure 11.4). Additional information comes from the background reductions obtained by the different cosmic veto essays. Therefore, in the new picture roughly 1/5, or less, of the background is intrinsic to the detector. We considered it might be lower because the detector's own radioactivity could have

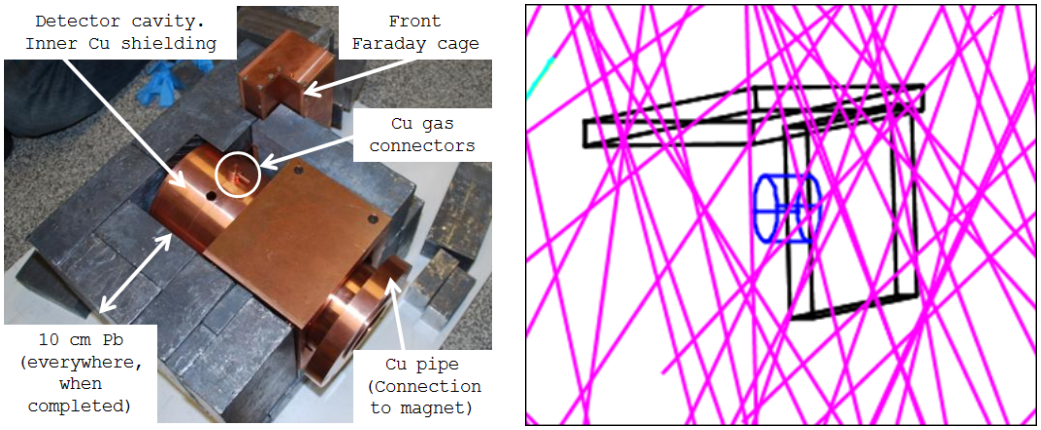

Figure 11.3: Left: mono-detector sunset replica in an intermediate montage stage. Right: ray-tracking simulation of cosmic muons rain over one CAST detector partially covered by a preliminary veto design. Computed coverage for the set-up: 95%.

been reduced since the sunset detectors already incorporated radiopurity improvements which have not been tested yet in the LSC. The rest of the background is attributed to cosmic rays. Although the mechanism that produces the final events is not completely known (apart from the fluorescence peaks), the muons passing near the detector are thought to produce the main contribution. New ideas have been conceived in order to answer one more time to the same questions we did for the sunrise.

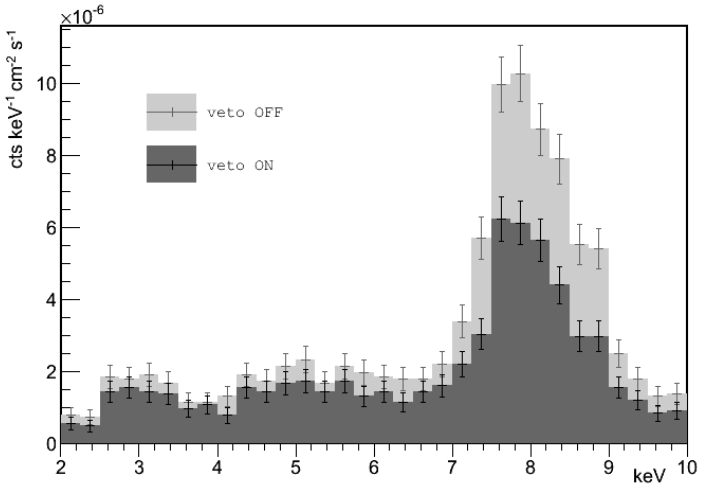

Figure 11.4: Sunset micromegas background accumulated during the summer 2012 data-taking campaign by detector 1, before and after applying the cosmic rays veto[227].

11.2.1 About a future shielding upgrade.

Is the present (sunset) shielding the optimum one? which parts of it are really useful? can an upgrade produce further improvements?

The most obvious step is the implementation of a high efficient cosmic veto. A new events generator method for the Monte Carlo (see **??**) has been written to emulate the cosmic muons energy and angular distribution. Up to know it is being used to evaluate the geometrical coverage of preliminary veto designs for the 2013 upgrade (see figure 11.3 right). If no other fundamental limitation arises, the LSC levels will, in principle, be reproducible at surface with a perfect cosmic veto.

One limitation that makes a difference between sunset and LSC set-ups is the presence of outlets in the shielding of the CAST set-ups. We have quantitative indications of the weight of the contribution of the shielding's outlets to the sunrise's background. From simulations they are about 1/2 of the total γ-induced background and concentrates in the stainless steel fluorescence peak. It is expected that muons contributed in a similar way. All the counts in that peak can be assumed to be produced via the shielding's main outlet in the front-side. So they represent roughly 1/2 of the total sunrise background, which is actualy higher than the present sunset background.

On the other hand, great efforts have been devoted to minimize the effect of the outlets. The front outlet solid angle has been decreased by the introduction of the copper pipe in the new sunset. Preliminary simulation tests suggest the outlet's influence on environmental isotropic γ flux induced background to be very small[226]. In any way, testing that hypothesis is very easy with the sunset replica (see figure 11.3) just by trying to shield the outlet.

Moreover the main channel to produce background events via the front outlet, the stainless steel fluorescence, has been strongly suppressed thanks to the replacement of steel with copper which, in addition, has been internally shielded with a teflon coating. In fact, the peak is not found in Summer 2012 spectrum (see figure 11.4). Furthermore, the new pipe is radiopure. It must also be remembered that the sunrise set-up was particularly vulnerable to this effect due to the long stainless steel pipe; the old sunset set-up, before 2012, already produced background spectra with a smaller stainless steel fluorescence peak.

The possible use of a X-ray optics focussing device coupled to the micromegas to improve the signal to background ratio, would allow further minimization of the oultet because the chamber's window could be significantly reduced.

Regarding the second shielding outlet for the extraction of the micromegas' signals, the Monte Carlo simulations evaluated its contribution to be $\sim$1/10 of the sunrise background, that is about 1/2 of the sunset level. However the solid angle of this outlet has also been strongly reduced due the extension of the lead shielding from 2.5 to 10 cm thickness. The problem has been already considered for the new detectors design[227](expected for 2013 sunrise upgrade) where this outlet is

removed of the shielding because a the new detector's raquette is made of copper, thus fully integrated in the innermost shielding.

Other kind of upgrades, like a new shielding against neutrons, may be suggested by the underground study of the LSC's level. If this level was demonstrated to be lower, a further increase of the lead thickness could be proposed.

11.2.2 About the intrinsic background level of the detector and the radiopurity.

Is there an essential limit, intrinsic to CAST detectors, to the background potential improvement?

The LSC's ULB level is not definitely attributed to the microbulk radioactivity yet. Actually preliminary simulations of the radioactivity of the microbulk readout and other less fundamental detector pieces[230] yield background values $<5\times10^{-8}$ keV^{-1} cm^{-2} s^{-1}. The sunrise-like tests set-up, still at LSC, is sequentially replacing the non radiopure pieces of the detector: teflon nuts and washers instead of steel ones, copper gas connectors replacing brass ones and teflon o-rings to close the chamber avoiding viton; the internal lead shielding replaced with a copper one, and the copper cathode cleaned with acid etching. These improvements are already included in the previously mentioned new detector design, to be used in the sunrise side in 2013. Finally the microbulk itself can be replaced by other technologies, still under development, like *cuflon* (copper and teflon foils)-based manufacturing.

Some precautions were adopted in advance in the sunset set-up: thicker copper walls and copper gas connectors. In addition all the copper pieces follow typical ultra-low background cleaning techniques, including acid etching.

The ULB level can be determined not by the detector's material budget, but by the particular set-up's design. The CAST detector used still has a raquette whose neck which cannot be completely shielded. Despite the upgrade of the external walls thickness, the internal shielding remains the same to shield the radioactivity generated by the electronic elements in the other side of the Faraday cage. Their contribution could have became now the limiting factor. The internal shielding can be upgraded and/or the electronics moved farther by means of flat and flexible cables. That is already done in the new sunset-like tests set-up that uses T2K electronics which are connected with long flat cables. This set-up will be mounted in the LSC.

11.2.3 About the nature of the background, analysis and electronics upgrades.

Firstly, it does not seem likely that sparks or any kind of rare noise are systematically limiting the background, since the background levels (always taken with good SNR) look almost independent on detector status and conditions. Another possibility is that the underground environment itself would mean a limitation, for example due

to neutrons flux. The LSC set-up is planned to be provided with a shielding against neutrons.

could the present (sunset) background be improved with a better analysis performance? could small changes in detector, system or environmental parameters produce relevant impacts on the background?

While the answer to the same question in the previous section (regarding the sunrise) was that basically it was not possible; now (regarding the sunset), if the background, even after the application of a realistic cosmic veto, is still dominated by muon events, the new answer is: probably yes. The lessons learnt from γ simulations about the fast electrons contributing to the final background could surely be applied to muons as both are MIPs. The focus of the simulations has moved from γ to muons. The kind of events they can generate must be systematically studied and the most potentially dangerous cases identified.

Several R&D lines and expected upgrades are already intended to improve signal quality and analysis. In section 8.2.2 was generically asserted that the homogenization of signals and the increase the available information had led to the discrimination improvements. That idea regarded, until now, the X-Y strips's signals equivalence. The new upgrades aim at the readout plane's signals and the third dimension, i.e. the time signal[1]. There is still a kind of extra dimension where to generalize the analysis: the event energy.

11.2.3.1 The electronics upgrade: possibilities for a T2K-based DAQ.

In the new detectors' design[227] the readout remains essentially the same, the main upgrade comes from the chamber structure, which is provided with a field shaper and metallic walls. Such structure should improve the drift field homogeneity. Besides, the adoption of the T2K electronics means the upgrade of CAST detectors from a 2D readout with an additional fast time signal to a true TPC (see figure 11.5). This fact brings, at least the following possibilities:

- *to apply pulse shape analysis to every strip signal.* The know-how accumulated from mesh pulse analysis could be transfered to the strips.
- *to achieve a better SNR.* Thanks to the new electronics features, but also due individual pulse analysis that allows to subtract the instantaneous baseline to each pulse, instead of applying an averaged pedestal. According to the simulations a sensitive enough evaluation of the strength of the strips signals is the key parameter *to reject MIP tracks*, because the fundamental difficulty is, in most of cases, the identification of the weak ionization path of a MIP.
- *to improve energy resolution and lower the energy threshold.* The pulse shape analysis applied to the strips signals has an advantage with respect to the mesh

[1] Some hints about the convenience of this kind of upgrade were already noted in section 7.1.2 from an apparently different context.

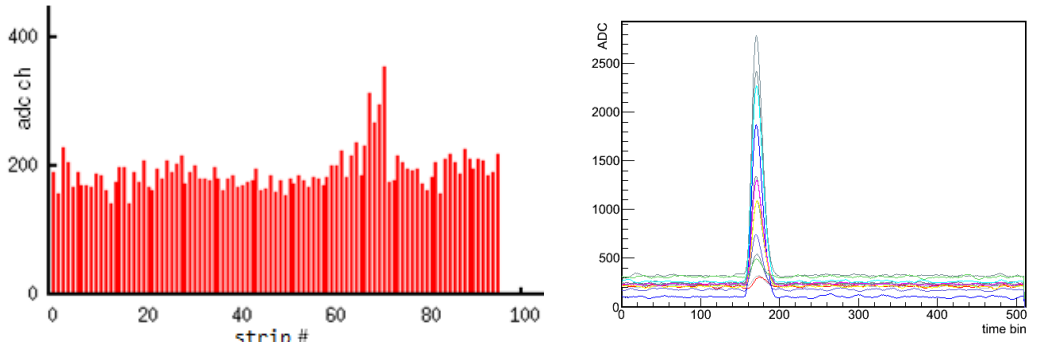

Figure 11.5: Strips signals upgrade. ^{55}Fe 6 keV X-ray signals in a CAST micromegas as seen by the classic Gassiplex card (left) and the T2K electronics (right).

one: the electric capacity of the strips is much lower and so the noise. The strips signals should become the main reference for the energy determination.

- a further specialisation of the mesh signal. Thanks to their new time capabilities, the strips signals alone are enough to reject most of the events that before needed the mesh signal analysis. In particular, multi-cluster events aligned in the z direction or vertical tracks can be easily rejected using only the information from the strips. There is no more the necessity to record the whole chamber drift time for the mesh signal, then *the mesh signal could be even faster*. There is no more sense in integrating the mesh signal, entailing primary information sacrifice, since the valid reference for the energy will be given by the strips. The preamplifier pulse could be directly analysed, which will deliver a better time information.

- In section 9.5.3 it was shown that diffusion of primary electrons in the gas is already affecting the shape of the signals. That would be more evident if the signals become faster, in particular if the preamplifier pulse is recorded. The application of more sensible discrimination routines could be limited by the diffusion or, perhaps, even a sort of z-dependent analysis could be developed. Regarding to the *diffusion properties, new gas mixtures* (e.g. the addition of CF_4), could be tested for powering these possibilities.

11.2.3.2 The possibility of an energy-dependence analysis characterization of the detectors.

It was already suggested in sections 8.3 and 9.5 how the study of the energy dependence of the observables could improve, more than the discrimination power, the relationship between signal detection efficiency and background. The precise determination of the efficiency versus energy curve is one of the most crucial works still pending for the CAST micromegas detectors and would enhance the reliability of

CAST results. The CAST micromgas team has started a tests-bench at CERN[203] provided with an electron beam which, by means of PIXE (particle induced X-rays emission) can generate several emission lines depending on the selection of a target material: 1.49 keV (Al), 2.12 keV (Au), 2.29 keV (Mo), 4.41 keV (Ti) and 8.05, 8.9 keV (Cu). Note these lines are complementary with the typical CAST calibration at 5.9, 6.2 and 3 keV (^{55}Fe). There is also the possibility of using the ^{241}Am alphas to produce the PIXE in a simpler set-up.

In conclusion, to answer again *the same questions, the same strategies*, that brought CAST detector here, can be invoked. They are still not exhausted, rather on the contrary they are expected to bring shortly a new step down. In order fulfil the expectations of the new proposed axion helioscope IAXO background levels of the order or $10^{-7}\times10^{-7}\,\mathrm{keV}^{-1}\,\mathrm{cm}^{-2}\,\mathrm{s}^{-1}$or even less are demanded, depending on the different (realistic or optimistic) considered scenarios[193]. We will try a very rough estimation. The present LSC level, $2\times10^{-7}\,\mathrm{keV}^{-1}\,\mathrm{cm}^{-2}\,\mathrm{s}^{-1}$could be reduced to $1\times10^{-7}\,\mathrm{keV}^{-1}\,\mathrm{cm}^{-2}\,\mathrm{s}^{-1}$, with the adoption of the radiopurity precautions already installed in the SSMM. Assuming that the rest of the background is due to cosmic muons and interpolating the performance of the cosmic muon veto from the tests already done, it could be estimated that the background levels in CAST will be around $2\text{–}6\times10^{-7}\,\mathrm{keV}^{-1}\,\mathrm{cm}^{-2}\,\mathrm{s}^{-1}$already for the 2013 campaign.

Chapter 12

Summary and conclusions.

The Rare Event Searches is a heterogeneous field from the point of view of their physical motivations; $\beta\beta0\nu$ decay experiments, direct detection of WIMPs as well as axions and other WISPs (candidates for the DM, but also motivated by other questions from Particle Physics) were considered in chapter 1. The field is rather defined by the requirements of these experiments, essentially a very sensitive detector with low background which is usually operated in underground laboratories.

The availability of a rich description of the event registered by the detector is a powerful tool for the discrimination of the signal from the background. That is a goal that makes the rare event searches experiments evolve to become more sophisticated, in order to produce more information about the event by means of applying pulse shape analysis, segmenting their sensitive volumes, the specialization of different active zones, combining different signals, etc.

The topological description of the interaction that can be delivered by a gaseous TPC, that includes the ionization path and $\mathrm{d}E/\mathrm{d}x$ along it, is a useful source of information about the event. That is particularly clear for the $\beta\beta0\nu$ decay, where the complete reconstruction of the ionization path would allow to identify the decay events that are composed of two electrons with a common vertex. Regarding the DM searches, there can be several approaches. Beyond some energy threshold, the nuclear recoils induced by the collisions with WIMPs or neutrons can be discriminated from γ/β events since the electron's tracks are longer and less straight than nuclear recoils. If the nuclear recoils were be fully reconstructed, deducing their initial direction (and, perhaps, sense), the directional signature of DM could be invoked to claim a positive signal. Even with more modest topological capabilities, a TPC can discriminate nuclear recoils and X-rays from higher energy β, muons, α, besides with good noise rejection and avoiding border effects down to low energy thresholds, surely below the keV. This latter kind of operation is suitable also for X-rays detectors of helioscopes, where WISP into photon conversion is produced.

The generic requirements for a gaseous TPC that is intended for rare event searches are the following. Very good *imaging*, that requires both good drift properties of the chamber and a good performance of the readout, probably with high granularity. The readout must yield also high *gain* so as to allow a low energy threshold (that is a main goal for DM) and a correct reconstruction of the ionization paths of MIPs (which can be essential for imaging of electrons or for discrimination of β and muons). In order to increase the detector's *efficiency*, many times operation at high pressure is required. This can be needed to increase the detector's quantum

efficiency for γ and X-rays or in order to contain high energy tracks or to have an effective self-shielding to detect secondary interactions or avoid border effects. *Radiopurity* must be guaranteed for the detector, starting from the readout itself, to the whole chamber structure, including the gas. The *source/target-equal-to-detector approach*, very common in rare event searches, can impose the *operation with particular gases*. If a light readout is also required (to combine signals or in order to reconstruct the absolute position of the event) that may imply *operation without quencher*. In this case, the requirements are also strong for the *supporting gas system* and further constrictions apply to the material selection for the chamber. In addition these properties must be *scalable*, large TPCs will be needed to increase the source/target mass. That applies also to the *readout and* their *electronics*, which will have to be more compact (integration in cards), fast (usage of ASICs, optical links) and multiplied (low consuming, multiplexing). Last, but not least, *stability and reliability* during long time data-taking are needed. In the particular case of $\beta\beta0\nu$ decay experiments, very good energy resolution is also demanded.

Such requirements could be fulfilled by TPCs because they are equipped with MPGDs, which were introduced in chapter 2. This work focussed in micromegas that stand out on stable high gain, fast signals, spatial resolution and robustness. Chapters 3, 4 and 5 were intended to be an ordered exposition on micromegas phenomenology. Since that is still a recent technology (in particular the bulk and microbulk types of micromegas) many of the presented experiments and characterization efforts are original. The text had always present the particularities of rare event searches. The questions addressed above were proven, addresed or, at least, the state of the R&D was reported.

The paths of low energy electrons were characterized by means of GEANT4 Monte Carlo simulations, and the results were compared with customary estimations. They are useful to estimate the strength of the signals in the micromegas, depending on the chamber and readout design parameters (gas type and pressure, readout pitch). They are also interesting to deduce if the length of the path can have an influence in the signals, so as they would be seen as different than point-like events for discrimination purposes.

The much shorter paths of ions, of primary interest for directional DM searches, were studied as well using SRIM simulations. After giving a general view, the study focused in argon nuclei as WIMP target. The role of secondary recoils produced by elastic collisions seemed to be important, more complex simulations being required. It was shown how a collision followed by a secondary recoil can suddenly change the direction of the primary recoil. Besides they influence, and can even invert, the expected Bragg curve, making more difficult the event reconstruction. Moreover, according to our conclusions, the variable number of collisions would work as an additional degradation of the energy resolution for ion recoils, with relevant effects for low energy signals. It was presented a fast review on recent efforts on this issue from theory and simulations to experiments inside CYGNUS groups. Its conclusions,

together with ours (also presented in CYGNUS), seem to be rather pessimistic, since the head-tail effect (invoked to deduce the sense of the recoil) is not clear for ions heavier than helium below 100 keV, while, at the same time, identifying the former piece of the path seems important for a precise reconstruction of the initial direction.

The signals in microbulk micromegas from X-rays and α-particle events have been systematically compared to conclude that there is no significant difference or quench-like effect; the ratio of the intensity of the α signal was always at least 96% of the X-ray signal taken in the same conditions. Firstly, the W-value should be very similar; then recombination does not affect to α, if the drift field is intense enough (over 150 V/cm in Ar/iC_4H_{10} 98/2), and the transparency of the mesh behaves equally.

The drift properties of typical gas mixtures have been discussed from plots generated with Magboltz for reference. The transparency of the mesh, an specific issue to micromegas, has been described in detail. The transparency curve has been defined, parametrized and discussed for different mesh types, and related with their geometrical layout. In particular the diffusion properties of the gas have been proven to influence the mesh transparency.

A step by step procedure has been explained to generate the result of avalanches in micromegas using customary models, starting from either the gain curve of the micromegas or the Townsend coefficient dependence on the electric field of the gas. The gain curves have been studied for bulk and microbulk micromegas using different gas mixtures and conditions. The effect of several quencher gases where explored, in particular for bulk micromegas, with special attention to the highest part of the gain curve. It was shown that different quencher gases bring different properties that can be combined or balanced in ternary mixtures. Isobutane brings stability that allows very high gain at relatively low amplification fields; CO_2 inhibits the over-exponential behaviour of the gain curve at high gain, what produces a better energy resolution that does not degrade at high gains; CF_4 contributes to the enhancement of the drift properties which also reflects in the mesh transparency. Many of these tests were carried out for the first time with this technology.

Three series of microbulk prototypes were characterized, contributing to the progressive refinement of the technology. An energy resolution of 11.0% FWHM at 6 keV (world record for a MPGD) with Ar/iC_4HC_{10} 95/5 at atmospheric pressure was registered, with only small deviations for most of the rest of the microbulks. Furthermore a 100 cm^2 microbulk with a pixelized readout was tested and instrumented, reconstructing three dimensional α tracks and yielding a performance, in gain an energy resolution, that was not far from that of the small prototypes.

The microbulk prototypes were also tested at high pressure. The maximum achievable gain decreases with pressure, roughly exponentially, however gains comfortably above 10^3 were registered with Ar/iC_4H_{10} 99/1 at 10 bar. The energy resolution degrades with pressure progressively, but slowly. Operation with pure noble gases, argon and xenon, was also tested. Gain over 10^2 was obtained for

pure xenon at 4 bar, which is not allowed by other MPGDs. The energy resolution measurements were encouraging towards $\beta\beta0\nu$ decay prospects, 2.5% FWHM in pure xenon at 4 bar for 5.5 MeV α, despite systematic limitations. The importance of the supporting gas system was put in value, confirming significant improvements with the selection of the construction materials, accumulating benefits from cleaning procedures as pumping and bake-out, the usage of filters and recirculation.

Germanium spectroscopy measurements on two microbulk samples and raw materials have been reported. They showed micromegas to be a radiopure readout in terms of activity per unit area, even when compared with PMT readouts specifically designed for rare event searches. Hints were found also that the manufacturing process of microbulk could be further optimized from the radioactive point of view.

A library and some programs have been developed to adapt the T2K electronics for the T-REX researchers as a general purpose electronics for micromegas detectors with imaging capabilities. The data are dealt according to the T-REX customary philosophy and way of working and the library has been provided with simple analysis tools.

A big part of the work has been devoted to the development of libraries and programs for generic Monte Carlo simulations on low energy TPCs. The package was called *RESTsoft* (Software for Rare Event Searches with TPCs) and is presented in chapter 6, also in a guide-like style. It includes a versatile GEANT4 application optimized for the simulation of gases in the low energy region. The nature of these kind of interactions, as they are simulated by GEANT4, is discussed with certain detail through several simulation tests. Two examples of works that were carried out with the RESTsoft GEANT4 application were discussed. The calculation of the CAST micromegas detectors quantum efficiency for X-rays and the reproduction of a γ spectrum in an high pressure xenon TPC, that allowed its proper interpretation.

Further libraries were written to simulate the specific processes of TPCs and micromegas (primary charge generation, drift processes, implementation of the readout, generation of the electronic signals, i.e *the TPC simulation chain*) and associated tools for information management and interpretation of the results. The T2Kelectronics library is linked to RESTsoft by means of a *bridge* class due a common conception of the ideal TPC physical event. The classes the RESTsoft library contains can be combined to write complex programs to develop an specific simulation followed by analysis at different levels.

Two examples of these complete programs were shown in chapter 7. In the first example the case for a non directional dark matter TPC is studied. Several observables related with the event size and shape were explored in order to estimate the possibility of discriminating nuclear recoils from γ/β events. It was shown that a full three dimensional reconstruction of the events, yielded by a pixelized readout, is a considerable advantage. The simulation of a feasible chamber prototype with 10 cm height and a gas with diffusion coefficient $\sigma = 100\,\mu\text{m cm}^{-1/2}$ produced a γ/β rejection power about $1/10^5$ for energies above 20 keVee (electron equivalent) using

discrimination criteria applied sequentially that accept about 90% of the simulated nuclear recoils. A possible figure of merit for the chamber design (choice of gas and chamber's height) was pointed out by the maximization of the target active mass, i.e. where the γ/β events are efficiently rejected. For Ar/CF_4 mixtures at atmospheric pressure the optimum was found around a proportion of 70/30 and a height about 1 m. A very similar mixture, Ar/CF_4 75/25, was tested with a bulk micromegas achieving good performance in gain, energy resolution and transparency. The second example is a demonstration of the discrimination power expected for a high pressure xenon TPC for $\beta\beta0\nu$ decay and a preliminary study of the nature of the most dangerous background events.

The role micromegas detectors have played in the CAST experiment was reviewed in chapter 8. The detectors were described in detail, in particular the last microbulk versions. The strategies followed to improve the background more than a factor of 50, since the beginning of the experiment to 2011 (typical background level 5-7$\times10^{-6}$ keV^{-1} cm^{-2} s^{-1}[2–7] keV), were carefully discussed: discrimination power, that relies on an outstanding micromegas performance (specially since the introduction of the microbulk technology), a DAQ that provides signals from mesh and anode strips, and a sophisticated analysis; selection of low activity materials for the detector construction and the use of passive shielding. The specific contribution of each one were tried to be evaluated, and they were critically commented on, in particular, the analysis and shielding design. The latter was upgraded in 2012 achieving a factor 5–4 of improvement in the background level (1.3–1.7$\times10^{-6}$ keV^{-1} cm^{-2} s^{-1}[2–7] keV).

To provide more precise guidelines aiming to continue and accelerate the encouraging evolution of micromegas backgound in CAST and to deliver prospects for IAXO, a less contemplative study on the micromegas background must be intended, regarding the contribution of the different background sources and the nature of the final background events. That was undertaken in chapters 9 (simulations) and 10 (test-bench). RESTsoft was used to implement a complete simulation chain, from the GEANT4 interactions to the production of CAST raw-data files. The geometry of the CAST sunrise set-up was implemented since it had the lowest background until the 2012 sunset upgrade. A set of γ measurements in the CAST experimental area were specifically devoted to this activity. The deduction of an environmental γ flux in the area was justified and used as input for the simulations. The obtained background contribution from the environmental γ has a similar magnitude than the experimental one ($\sim 1/3$ was obtained, $\sim 1/3$–$2/3$ was estimated) and its study showed how γ can produce its typical shape with a strong contribution of a stainless steel fluorescence.

The micromegas Monte Carlo model was tested *in situ* with a ^{57}Co γ-source of $\simeq 100$ keV with an excellent agreement. The model is available for new simulations concerning different background sources. This model can be used also as a tool for a better understanding of the background events-analysis interplay, and some facts

about that issue were shown. In particular some observations demonstrated the importance of the detector strips SNR for the rejection of MIPs, what pointed out that cosmic muons could be a relevant background source.

Underground operation of CAST detector with a heavy shielding (at least 10 cm lead thickness) an a copper cathode produced a background ~ 30 times lower than CAST sunrise's background, $\sim 2{\times}10^{-7}\,\mathrm{keV}^{-1}\,\mathrm{cm}^{-2}\,\mathrm{s}^{-1}$. This background was stable and reproducible. The contribution of radon near the detector was also evaluated to be $(3.0 \pm 0.8) \times 10^{-9}\,\mathrm{keV}^{-1}\,\mathrm{cm}^{-2}\,\mathrm{s}^{-1}/(\mathrm{Bq\,m}^{-3})$, which is negligible at surface. Such a background level was not reproducible at surface with heavy shielding, a fact that was attributed to the cosmic rays contribution. This point was confirmed when the efficiency of the usage of a cosmic veto was proven.

The success of the sunset 2012 upgrade has been the first application/confirmation of the conclusions from these studies. The shielding was upgraded to a leak tight 10 cm lead shielding, avoiding the stainless steel and using a copper cathode and the background level obtained was $1.3\text{–}1.7{\times}10^{-6}\,\mathrm{keV}^{-1}\,\mathrm{cm}^{-2}\,\mathrm{s}^{-1}$(4–5 times lower than sunrise). That result included a 25% reduction by a preliminary cosmic veto that provides the detectors with $\sim$44% geometric coverage for cosmic muons. The conclusions and prospects deducible from simulations and experimental tests were summed up in chapter 11.

In conclusion, the prospects to the application of micromegas to rare event searchers are encouraging for the three main issues that were proposed. To start with, the state-of-the-art micromegas has been measured to be radiopure. Some steps towards scaling the readout areas up have been taken with good results. These bigger and more complex readout are efficiently instrumented with the T2K electronics. They are currently being extensively used for T-REX activities: NEXT1-MM TPC, the new CAST DAQ, a high sensitive radon detector prototype with imaging capabilities, the future T-REX-DM chamber.

The tests on the different aspects of the micromegas operation that are demanded by rare event searches (high pressure, particular mixtures, absence of quench, light detection) produced encouraging results. The R&D continues on these directions, and the usage of Penning mixtures is one of the most promising possibilities.

The RESTsoft package is already a useful tool used in T-REX to understand and/or conceive small experiments and ambitious projects. In particular, the simulation of CAST detectors, where a high level of detail was demanded, has yielded a varied set of comparisons with reality that help to validate and improve the code. The results produced by CAST simulations, but also by simulations on $\beta\beta0\nu$ decay and dark matter discrimination power of a TPC with micromegas, are encouraging.

The impressive progression of the background of CAST micromegas detectors may be the most significant milestone. There has been an important advance in the understanding of the background nature, the potential of the different applied strategies and the way the detector performance and the analysis methods interact with

the different kinds of background events. It can be assured that this progression, which have improved more than two orders of magnitude from the first micromegas installation, will not stop in the present sunset background level, and the future IAXO helioscope will be provided with more sensitive micromegas detectors.

The ultra-low background obtained in the LSC (which is only an upper bound, probably no a real limit for the micromegas) is one of the facts that support this assertion. But its significance goes beyond the application to helioscopes. It demonstrates the possibility of registering ultra-low background below 10 keV with a low energy threshold (below the keV seems to be feasible), what motivates the T-REX-DM project, that follows a CAST-like approach.

Chapter 13

Resumen y conclusiones.

La Física de Sucesos Poco Probables es un campo heterogéneo desde el punto de vista de las cuestiones de la física que motivan los experimentos englobados en este área. En este trabajo se han considerado los experimentos de identificación de la desintegración doble beta sin neutrinos ($\beta\beta0\nu$), perteneciente a la física nuclear; y la detección directa de WIMPs y también de axiones o, más genéricamente, WISPs, todos ellos candidatos a formar parte de la materia oscura (DM), pero también motivados por diversos problemas de la física de partículas. El campo está pues mejor definido por la serie de requerimientos y técnicas comunes a estos experimentos que están esencialmente basados en un detector muy sensible, caracterizado por un fondo muy bajo y que típicamente necesita ser operado en un laboratorio subterráneo.

El disponer de una descripción de los eventos registrados en el detector, tan rica como sea posible, es una herramienta útil para discriminar la señal buscada del fondo. Éste es uno de los objetivos que están marcando la evolución de los experimentos de física de sucesos poco probables, los cuales tienen tendencia a la sofisticación, pues es necesaria para conseguir una información más completa del evento registrado por medio del estudio de la evolución temporal de la señal (análisis de la forma de los pulsos), de dividir su volumen activo en detectores independientes, de la especialización de las diferentes zonas del detector para obtener información complementaria, de la combinación de señales de diferente naturaleza, etc. La otra tendencia es inevitablemente el aumento de su tamaño para exponer una masa mayor que sirva de blanco (detección directa) o fuente ($\beta\beta0\nu$).

La descripción de la topología del evento que puede proporcionar una cámara de proyección temporal (TPC) gaseosa es una fuente muy útil de información que consiste en la marca de ionización trazada por las partículas cargadas, incluyendo la intensidad con que esta ionización se produce por unidad de longitud. La utilidad de esta información es especialmente obvia para el caso de un experimento de desintegración $\beta\beta0\nu$, ya que la desintegración da lugar a eventos que responden a una clara descripción en términos topólogicos: la de dos electrones cuyas trayectorias parten de un vértice común, además el tramo final de ambas trayectorias se caracteriza por un aumento de la intensidad de la ionización. Una TPC podría reconocer este patrón y seleccionar los eventos correctos. En cuanto a la detección directa de WIMPs, existen varios enfoques que podrían funcionar, incluso coexistir, en distintos rangos de energía. Por encima de un cierto umbral de energía los retrocesos nucleares producidos por las colisiones de los núcleos del gas con WIMPs o neutrones podrían distinguirse de eventos γ/β porque las trayectorias trazadas por

los electrones son más largas y menos rectas. Si además (probablemente a partir de un umbral de energía mayor) la trayectoria del retroceso nuclear pudiese reconstruirse con precisión suficiente como para permitir deducir su dirección inicial (a ser posible, también el sentido), se podría recurrir a la huella de direccionalidad que se espera de las señales inducidas por WIMPs que formaran parte de un halo galáctico. Esto reforzaría definitivamente una identificación positiva de detección de materia oscura. Incluso con capacidades de reconstrucción topológica mucho más modestas una TPC que no pudiera distinguir los retrocesos nucleares de rayos X, si podría discriminar eventos producidos por electrones con mayores energías, muones, partículas α, además proporcionando un muy buen filtrado de ruido electrónico y evitando efectos de borde. Todo ello hasta umbrales de energía probablemente bajo el keV y con una alta eficiencia en la identificación positiva. Este último modo de operación es apropiado para los detectores de rayos X que se utilizan en helioscopios, donde son producidos por la conversión Primakoff de axiones y WISPs. Estos tres campos de acción y el interés de la aplicación de TPCs en cada uno de ellos se presentaron en el capítulo 1.

Los requerimientos que podrían definirse genéricamente para una TPC aplicada a física de sucesos poco probables serían los siguientes. Obviamente, la capacidad de reconstruir la *topología* del evento con un buen nivel de detalle, esto exige unas buenas propiedades de deriva para conservar la traza de ionización original y un alto rendimiento por parte del plano de lectura, que deberá constar de un diseño segmentado, probablemente con unidades del orden de mm ó sub-mm. Será esencial para el plano de lectura funcionar con una *ganancia* alta, bien para obtener un umbral bajo (fundamental para detección de DM) o con el fin de reconstruir correctamente las trazas de partículas mínimamente ionizantes (lo que puede ser crítico para interpretar la topología de electrones, pero también para discriminarlos, junto con los muones cósmicos). Para incrementar la *eficiencia* de la TPC, muchas veces es ventajoso operar a alta presión. Esto aumenta la eficiencia cuántica del volumen de gas para la detección de γ, pero también puede requerirse para contener las trayectorias completas de partículas ionizantes de energías altas o ser conveniente para obtener un eficiente efecto de auto-blindaje por parte del propio gas y para protegerse de los efectos de borde. La *radiopureza* debe garantizarse para el detector completo, comenzando por el plano de lectura, pero los criterios en la selección de materiales y procesos de baja actividad afectarán al diseño de la cámara y al propio gas. La estrategia de *identicación de fuente/blanco con el detector* mismo, es muy común en física de sucesos poco probables y puede imponer el *uso de un gas determinado* o rentringir seriamente la elección. Si se quiere combinar con la detección de luz para aumentar la información sobre la naturaleza de la interacción o para habilitar la capacidad de reconstruir la posición absoluta de la misma, probablemente esto implique la *operación sin gas quencher*, habituales aditivos que afectan profundamente a las propiedades de la cámara. En tal caso los requisitos serían también exigentes para el *sistema de gas auxiliar* y nuevos criterios se aplicarían para la elección de materiales. Además, todas estas propiedades exigidas deben ser *escal-*

ables, es decir, han de mantenerse cuando TPCs más grandes se construyan para incrementar la masa de blanco/fuente. Una ventaja de las TPCs es que las cámaras pueden crecer de forma bastante natural, el aumento de la complejidad es absorbida principalmente por el plano de lectura y su *electrónica*. Ésta última deberá tender a ser compacta (integrada en tarjetas), permitir un rápido procesado y transmisión de una cantidad creciente de datos (uso de ASICs y fibra óptica) y multiplicarse fácilmente (bajo consumo, multiplexado de señales). Por último, pero sin dejar de ser un aspecto esencial, el detector debe acreditar *estabilidad y fiabilidad* durante largos periodos de toma de datos. En el caso partícular de una TPC para desintegración $\beta\beta0\nu$, una muy buena *resolución en energía* es primordial.

Existe la posibilidad de cumplir con todos estos requisitos gracias a que las TPCs modernas están equipadas con MPGDs (estructuras del orden de micras para la amplificación de electrones en gases que se utilizan como planos de lectura), una breve introducción de los cuales se hace en el capítulo 2. De todos ellos, este trabajo se ha centrado en micromegas que sobresalen por su rendimiento, en particular por el mantenimiento de altas ganancias con estabilidad, la generación de señales rápidas, la integración del ánodo que posibilita una muy buena resolución espacial y la robustez de su estructura. A lo largo de los capítulos 3, 4 y 5 se ha pretendido hacer una exposición ordenada de la fenomenología de los detectores micromegas, en la que se han tenido siempre presentes las particularidades del contexto de la física de sucesos poco probables, con la idea de crear una referencia práctica. Dada la juventud de esta tecnología (especialmente las versiones bulk y microbulk) muchas de las pruebas y observaciones incluídas para ilustración de sus propiedades son originales. Se han tratado de probar las cuestiones que se planteaban en el párrafo anterior o, al menos, de responder comentando el estado de la investigación y desarrollo sobre los puntos abiertos.

Las trayectorias de los electrones de baja energía se caracterizaron por medio de simulaciones de Monte Carlo y los resultados se compararon con cálculos frecuentemente propuestos en la literatura. Estos datos resultan útiles para estimar la cantidad de carga que puede esperarse en la micromegas en función del diseño de la cámara, las condiciones del gas y la segmentación del plano del ánodo. También puede resultar interesantes para deducir el punto en el que la longitud de la trayectoria comenzará a influir en la forma de las señales, de manera que deje de poder considerarse como un evento puntual, lo que debe considerarse por los algoritmos de discriminación.

Las trayectorias, mucho más cortas, de los iones, de un interés inmediato para búsquedas direccionales de DM, se estudiaron a su vez utilizando SRIM para las simulaciones. Después de dar algunas conclusiones generales, el estudio se centró en los retrocesos nucleares de argon, usado como blanco para los WIMPs. El papel jugado por las colisiones con otros núcleos que dan lugar a retrocesos secundarios pareció ser relevante, por lo que se necesitarían simulaciones algo más complejas que los contemplaran. Se vio que, además de que una de estas colisiones puede modificar

bruscamente la dirección del retroceso principal, la presencia de los retrocesos secundarios puede cambiar profundamente, hasta llegar a invertir, la curva de Bragg, lo que dificulta notablemente la tarea de reconstrucción. Además, de acuerdo con nuestras simulaciones, el número variable de colisiones secundarias sufridas supondría un mecanismo adicional de degradación de la resolución de la energía para retrocesos secundarios, que tendría efectos notables para señales de baja energía. Se han recogido algunos de los diversos esfuerzos recientes en esta materia, todos realizados en la órbita de CYGNUS, y que han abarcado formulaciones teóricas, bastantes simulaciones y algún resultado experimental. Las conclusiones que nos parece poder extraer del conjunto, incluyendo las nuestras (también presentadas en CYGNUS) se nos antojan algo pesimistas porque no parece claro que el efecto cabeza-cola (la decisión del sentido de la trayectoria basada en la curva de Bragg) pueda utilizarse eficazmente para iones más pesados que el helio con energías menores de 100 keV, mientras que el hecho de encontrar el extremo inicial de la trayectoria parece un punto de partida necesario para poder reconstruir la direción inicial con precisión.

Se compararon sistemáticamente las señales producidas por rayos X y partículas α en microbulk micromegas para no encontrar ninguna diferencia práctica entre ellas, nada parecido a un efecto de *quench*; la intensidad de las señales α fue, en todo caso, al menos un 96% de la generada por rayos X. Esto significa, para empezar, que los valores W son muy similares, la recombinación no afectaba a las trazas mucho más densas de las α en cuanto el campo de deriva superaba los 150 V/cm (en Ar/iC_4H_{10} 98/2) y la transparencia de la *mesh* (el electrodo-rejilla que da paso a la región de amplificación de la micromegas) mostraba una evolución idéntica con el campo de deriva.

Se han analizado las propiedas de deriva de varias mezclas arquetipo a través de los gráficos generados por el programa Magboltz, que se han mostrado con detalle para servir de referencia. La curva de transparencia de la mesh, por ser un aspecto específico de micromegas, se ha definido, parametrizado y discutido con especial ahínco, relacionándose con el diseño geométrico de la mesh. En particular se han proporcionado pruebas de que las propiedades de difusión del gas tienen una influencia no pequeña en la transparencia.

Se ha explicado un procedimiento paso a paso para generar la producción final de carga de avalanchas en micromegas, apoyándose en los modelos habituales y a partir de la curva de ganancia de la micromegas o de la dependencia del coeficiente de Townsend del gas con el campo eléctrico. Las curvas de ganancia de micromegas, bulk y microbulk, se han estudiado probando varias mezclas gaseosas en diferentes condiciones. Con bulk micromegas se exploró la utilización de varios quenchers, poniendo una atención especial a la parte final, más alta, de la curva de ganancia. Se comprobó que los distintos quenchers proporcionan diferentes propiedades a la mezcla que pueden combinarse o compensarse hasta cierto punto utilizando mezclas ternarias. Se ha visto que el isobutano dota al gas de estabilidad, lo que permite alcanzar ganancias más altas, además con campos de amplificación relativamente ba-

jos. El CO_2 inhibe el comportamiento sobre-exponencial que las curvas de ganancia tienden a mostrar cuando la ganancia es muy alta, lo que, se ha comprobado, va unido a un deterioro de la resolución en energía; de modo que las mezclas con CO_2 exhiben una mejor resolución en energías que no se deteriora apenas con la ganancia. El CF_4 se añade para mejorar las propiedades de deriva, lo que se refleja también en una mejora de la transparencia de la mesh. Muchas de estas observaciones se hacían por primera vez para esta tecnología.

Tres conjuntos de prototipos microbulk, que fueron fabricados sucesivamente, se caracterizaron contribuyendo así al progreso de está técnica. Un espectro con una resolución de un 11.0% FWHM (anchura a media altura) se registró para rayos X de 6 keV en Ar/iC_4H_{10} 95/5 a presión atmosférica, lo que supone un record mundial para MPGDs. La mayoría del resto de las microbulk caracterizadas fueron peores sólo por pequeñas desviaciones respecto de este valor. Además se testeó un prototipo pixelizado de 100 cm^2 de área activa, en el cual se pudieron reconstruir trazas tridimensionales de partículas α y que mostró un rendimiento, en cuanto a ganancia y resolución, no muy alejado del de las versiones más pequeñas.

Los prototipos de microbulk se probaron con gas a alta presión. Se ha visto que la ganancia máxima alcanzable decrece, aproximadamente de forma exponencial, con la presión; sin embargo ganancias sobradamente por encima de 10^3 pudieron lograrse utilizando Ar/iC_4H_{10} 99/1 en todos los casos, al menos hasta 10 bar. La resolución en energía también se deteriora con el aumento de la presión, pero lo hace despacio y con tendencia a estabilizarse. Se probó también la operación con los gases nobles puros, argon y xenon. Con xenon puro, los prototipos microbulk registraron una ganancia superior a 10^2 a 4 bar para una α de 5.5 MeV, algo que parece no estar al alcance de otros MPGDs. Los resultados en resolución fueron también alentadores para la perspectiva del $\beta\beta0\nu$, obteniéndose un 2.5% FWHM para las mismas condiciones, pese a constatar algunas limitaciones sistemáticas. Se ha puesto en valor la importancia del sistema de gas auxiliar, y se han confirmado mejoras significativas gracias a la selección de materiales, una mejora acumulativa por el uso sistemático y combinado del bombeo y el baqueado (calefactado del sistema para fomentar la expulsión de gases), el uso de filtros y la recirculación del gas.

Se han descrito las medidas de espectrometría con germanio realizadas con dos muestras de microbulk micromegas, así como algunos de sus materiales primarios. Los resultados mostraron que se trata de un plano de lectura radiopuro en términos de activad por unidad de área, incluso cuando se compara con PMTs específicamente diseñados para experimentos de física de sucesos poco probables. También se hallaron indicios de que el proceso de manufactura de las microbulk podría optimizarse desde este nuevo punto de vista mejorando aún más la radiopureza.

Una librería y algunos programas fueron escritos para adaptar la electrónica del experimento T2K a los intereses de T-REX, donde se adopta como electrónica de propósito general para TPCs con capacidades de reconstrucción topológica. De esta

manera los datos se tratan de acuerdo con la filosofía de T-REX y se integran en sus procedimientos habituales. Se ha dotado a la librería de funcionalidades básicas, herramientas sencillas de análisis y visualización que han sido frecuentemente utilizadas en el trabajo de laboratorio de T-REX.

Gran parte del trabajo se ha invertido en el desarrollo de librerias genéricas y programas para simulación Monte Carlo de eventos de baja energía en TPCs. El paquete, llamado RESTsoft (software para física de sucesos poco probables con TPCs), se presentó en el capítulo 6, también tratando de conseguir un estilo de "guía de usuario". Incluye una versátil aplicación de GEANT4 optimizada para la simulación de gases en la región de baja energía. La naturaleza de este tipo de interaccioes, tal GEANT4 las simula, en particular la ionización por parte de electrones, se discutió con cierto detalle a través de varios ejemplos utilizados como tests. Dos ejemplos de trabajos realizados con la aplicación GEANT4 de RESTsoft fueron presentados. El cálculo de la eficiencia cuántica de un detector micromegas de CAST y la reproducción, para su correcta interpretación, de un espectro producido con una fuente γ en una cámara de xenon a alta presión.

Se han desarrollado librerías para continuar la simulación con los procesos específicos de TPCs y micromegas (generación de carga primaria, procesos de deriva, implementación del plano de lectura, generación de pulsos electrónicos; todo en serie se denominó la *cadena de simulación de una TPC*) junto a herramientas para la administración de datos e interpretación de los resultados. La librería *T2Kelectronics* está conectada naturalmente con RESTsoft, auxiliada por una *clase puente*, gracias al concepto común sobre el típico evento físico registrado en una TPC. Las clases del paquete RESTsoft pueden combinarse para escribir programas complejos que desarrollen una simulación específica y analísis a distintos niveles de la cadena de transformaciones.

Dos ejemplos de este tipo de programas de simulación más complejos se presentaron en el capítulo 7. El primero se usó para abordar el caso de una TPC no direccional para búsqueda de DM. Se exploraron algunas definiciones para el tamaño del evento que utilizar como observables para la discriminación de retrocesos nucleares frente a eventos γ/β. Se puso de manifiesto que una reconstrucción completa en tres dimensiones, producida por un plano de lectura pixelizado, conlleva ventajas considerables. Se simuló un prototipo completo de una cámara bastante viable de 10 cm de altura y llena de un gas con coeficiente de difusión $\sigma = 100\,\mu\text{m cm}^{-1/2}$, este detector fue capaz de desarrollar un poder de rechazo de eventos γ/β de alrededor de $1/10^5$ para energías por encima de los 20 keVee (electrón equivalente), utilizando criterios de discriminación aplicados secuencialmente, los cuales aceptaban sobre el 90% de los retrocesos nucleares simulados en la misma cámara. Se estudió una posible figura de mérito para el diseño de la cámara (la elección del gas y su altura) que maximizase la *masa activa*, siendo ésta la perteneciente al núcleo blanco que está encerrada en el volumen en el cual los eventos γ/β son eficazmente rechazados. Aplicándolo a mezclas de Ar/CF_4 se concluyó que el óptimo se encontraría entorno

a la proporción 70/30 con una cámara de aproximadamente 1 m de altura. Una mezcla muy similar a la propuesta, Ar/CF_4 75/25, se testeó con una micromegas tipo bulk, observándose un buen rendimiento en ganancia, transparencia y resolución en energía. En un segundo ejemplo se hizó una demostración de las capacidades de discriminación de una TPC de alta presión para desintegración $\beta\beta0\nu$. En un estudio preliminar se mostró la naturaleza de los eventos más peligrosos para el fondo del experimento.

El papel, de creciente importancia, que los detectores micromegas han jugado en la historia del experimento CAST fue analizado en el capítulo 8. Se describió a los detectores con detalle, espacialmente las últimas versiones basadas en la tecnología microbulk. Se discutió cuáles han sido las estrategias que han permitido mejorar el fondo de las micromegas más de un factor 50 desde la instalación del primer detector hasta 2011 (nivel típico de fondo $5\text{–}7\times10^{-6}\,\mathrm{keV}^{-1}\,\mathrm{cm}^{-2}\,\mathrm{s}^{-1}$[2–7] keV): la capacidad discriminativa, que se fundamenta en un rendimiento extraordinario de las micromegas (sobretodo después de la introducción de las microbulk), un sistema de adquisición que combina el pulso generado en la mesh y las señales de las strips en que está segmentado el ánodo, y un sofisticado análisis; la selección de materiales radiopuros para la construcción del detector y el uso de blindajes pasivos contra la radiación ambiental. Se ha intentado evaluar cual ha sido la contribución específica de cada estrategia, y han sido comentadas con afán de crítica constructiva, especialmente el diseño del blindaje y algunos aspectos de las rutinas de discriminación. Precisamente el blindaje fue mejorado en 2012 consiguiendo un descenso del nivel de fondo en un factor 5–4 ($1.3\text{–}1.7\times10^{-6}\,\mathrm{keV}^{-1}\,\mathrm{cm}^{-2}\,\mathrm{s}^{-1}$[2–7] keV).

Con el objetivo de concretar las líneas maestras para revitalizar la alentadora progresión de los fondos obtenidos por las micromegas en CAST y proyectar predicciones razonables para IAXO (el helioscopio que lo sucederá), debía emprenderse un estudio menos contemplativo, que atendiese a la importancia relativa de las diferentes fuentes que contribuyen al fondo así como a la naturaleza de los eventos que finalmente lo componen. Esto se llevó a cabo en los trabajos comprendidos en los capítulos 9 (simulaciones) y 10 (tests experimentales). Se utilizó RESTsoft para componer una completa cadena de simulaciones desde las interacciones de GEANT4 hasta la producción de datos en el mismo formato en el que lo hace la adquisición de CAST. La geometría del montaje *sunrise* se tomó como modelo porque esta disposición obtenía el fondo más bajo, hasta la remodelación del *sunset* ya en verano de 2012. Una serie de medidas de γ se dedicó a caracterizar la actividad en el área experimental de CAST. Se justificó el uso de un flujo ambiental γ como punto de partida para las simulaciones, deducido a partir de estas medidas. La contribución obtenida para el flujo ambiental γ es del mismo orden que el fondo experimental total ($\sim$1/3 fue obtenido directamente, $\sim$1/3–2/3 se estima apoyándonos en más observaciones). Además, el estudio detallado de la simulación mostró como este tipo de radiación produce la típica forma del espectro experimental global, con una importante contribución proveniente de la fluorescencia del acero inoxidable.

El modelo planteado para las micromegas se testeó *in situ* utilizando una fuente de ^{57}Co que emité γ con energías entorno a los 100 keV, obteniéndose un excelente acuerdo simulación-estimación experimental. El modelo queda así establecido y disponible para la evaluacion de la contribución de distintas fuentes potenciales de fondo. Otro uso que podría darse al modelo sería el de herramienta para explorar la interrelación entre los diferentes tipos de eventos del fondo y el análisis. Algunas tendencias fueron ya indicadas en un primer tanteo para demostrar esta posibilidad. En particular algunas observaciones han puesto de manifiesto la importancia de una buena relación señal-ruido en las señales de las strips para rechazar MIPs, lo que se entendió como una advertencia de que los muones cósmicos podían ser una fuente relevante de fondo, ligada al rendimiento del detector.

Los tests realizados en el Laboratorio Subterráneo de Canfranc con detectores CAST con blindajes pesados (de al menos 10 cm de espesor de plomo) y un cátodo de cobre, dieron lugar a un fondo $\sim$ 30 veces más bajo que el del montaje *sunrise* de CAST (record hasta entoces), $\simeq 2{\times}10^{-7}\,\mathrm{keV}^{-1}\,\mathrm{cm}^{-2}\,\mathrm{s}^{-1}$. Este nivel se ha mostrado estable y reproducible. También se evaluó la contribución del radon cerca del detector como $(3.0 \pm 0.8) \times 10^{-9}\,\mathrm{keV}^{-1}\,\mathrm{cm}^{-2}\,\mathrm{s}^{-1}/(\mathrm{Bq\,m}^{-3})$, lo cual produciría efectos despreciables en superficie. El nivel de ultrabajo fondo no fue reproducible al instalar blindajes pesados en superficie, lo que fue atribuído a la acción de los rayos cósmicos. Este hecho se confirmó cuando se pudo probar que la instalación de un veto cósmico producía una eficiente reducción del fondo.

El éxito de la remodelación del montaje del *sunset* en 2012 ha supuesto la primera aplicación/confirmación de las conclusiones obtenidas de estos estudios, así como la realización de un test de indubitable valor añadido. El blindaje fue ampliado hasta un diseño más hermético de 10 cm de grosor de plomo, evitando el uso de acero inoxidable que fue reemplazado por cobre (en especial el cátodo del detector). Los antiguos blindajes exteriores de polietileno y cadmio fueron, al contrario, desestimados. Con esta configuración los detectores promediaron un fondo de 1.3–$1.7{\times}10^{-6}\,\mathrm{keV}^{-1}\,\mathrm{cm}^{-2}\,\mathrm{s}^{-1}$(5–4 veces menor que el del *sunrise*) durante la campaña de verano de 2012, incluyendo un 25% de reducción extra debida a un veto cósmico cuya instalación provisional procuraba tan sólo un 44% de covertura geométrica de los muones cósmicos. Las conclusiones y predicciones que pueden deducirse de la combinación de los hechos e indicios acumulados por ambos estudios (simulaciones y tests experimentales) se expusieron en el capítulo 11.

Concluyendo, las perspectivas para la aplicación de micromegas son prometedoras para los tres objetivos de física de sucesos poco probables que nos propusimos. Para empezar, la tecnología micromegas más brillante en su rendimiento, se ha confirmadio radiopura. Se han dado varios pasos hacia su escalado para conseguir planos de lectura de áreas mayores, con buenos resultados. Estos planos de lectura, además de mayores también más complejos, se leen eficazmente con la electrónica T2K, más compacta y que proporciona más información. Actualmente está siendo utilizada extensivamente en las actividades de T-REX: la TPC de alta presión NEXT-1-MM, la

nueva adquisición de CAST, un detector de alta sensibilidad de radón con capacidad de reconstruir las trazas α, la futura cámara T-REX-DM.

También han dado resultados alentadores los tests realizados con micromegas sobre algunos aspectos de su operación requeridos por algunos escenarios de la física de sucesos poco probables: alta presión, uso de algunas mezclas en particular (incluyendo gases nobles puros), detección de luz. La investigación y el desarrollo continuán en estas direcciones, siendo el uso de mezclas Penning una de las soluciones más prometedoras.

El paquete de librerías RESTsoft se muestra ya como una herramienta útil usada en T-REX para la comprensión y/o la concepción de pequeños experimentos o proyectos más ambiciosos. La simulación de los detectores CAST, en particular, ha tenido que alcanzar un alto nivel de detalle en el cual se han realizado un conjunto de comparaciones con el experimento que son valiosas para validar y mejorar el código. Los resultados producidos por las simulaciones de CAST, junto con las simulaciones sobre el poder de discriminación de una TPC para la desintegración $\beta\beta0\nu$ y la detección directa de DM son muy alentadores.

La impresionante progresión del fondo de los detectores micromegas en CAST es, quizá, el resultado más significativo de las posibilidades de la aplicación de esta tecnología en física de sucesos poco probables. Se han hecho avances importantes en la comprensión de la naturaleza de su fondo y, por tanto, en la determinación potencial de las distintas estragegias aplicadas para reducirlo y el modo en que el rendimiento del detector y las rutinas de discriminación se interrelacionan con los distintipos tipos de eventos del fondo. Puede asegurarse que la evolución del fondo, que ha mejorado en más de dos órdenes de magnitud desde que la primera micromegas fue instalada en CAST, no se detendrá en el presente nivel, y que el futuro helioscopio IAXO contará con detectores micromegas más sensibles.

El nivel de fondo tan bajo obtenido en el Laboratorio Subterráneo de Canfranc (el cual representa probablemente tan sólo una cota superior, y no una limitación realmente impuesta por la micromegas) es uno de los hechos que apoyan la última afirmación. Sin embargo, su relevancia va más allá de la aplicación de micromegas en helioscopios. Se ha demostrado la posibilidad de registrar fondos muy bajos bajo 10 keV con un umbral en energías también muy bajo (conseguirlo bajo el keV se antoja bastante inmediato), esto ha motivado el enfoque actual del proyecto T-REX-DM, cuyo prototipo sigue una línea tipo CAST.

Bibliography

[1] I.G. Irastorza *et al.*, Status of R&D on Micromegas for Rare Event Searches: The T-REX project, Proceedings of the Third International Conference on Directional Detection of Dark Matter (CYGNUS 2011), *EAS Pub. Ser.* **53** (2012) 147-154. 1, 143

[2] H.V. Klapdor-Kleingrothaus, Sixty Years of Double Beta Decay: From Nuclear Physics to Beyond Standard Model Particle Physics, *World Scientific* (2001). 3

[3] F.T. Avignone III, G.S. King III and Yu G. Zdesenko, Next generation double-beta decay experiments: metrics for their evaluation, *New J. Phys.* **7** (2005) 6. 3

[4] A. Gouvea, On Determining the Neutrino Mass, FNAL Theory Seminar, March 30, 2006. 3

[5] N. Fatemi-Ghomi, Mearurement of the Double Beta Decay Half-life of ^{150}Nd and Search for neutrinoless Decay Modes with the NEMO3 Detector, PhD Thesis, Univerity of Manchester, 2009. 3

[6] P. Vogel, Neutrinoless double beta decay, (2008) `arXiv:hep-ph/0611243`. 4

[7] C.E. Aalseth *et al.*, Neutrinoless double beta decay of ^{76}Ge: first results from the International Germanium Experiment (IGEX) with six isotopically enriched detectors, *Phys. Rev. C* **59** (1999) 2108. 4

[8] M. Gunther *et al.*, Heidelberg-Moscow $\beta\beta$ experiment with ^{76}Ge: full setup with five detectors, *Phys. Rev. D* **55** (1997) 54. 4

[9] H. Klapdor-Kleingrothaus *et al.*, First Evidence for Lepton Number Violation and of the Majorana Character of Neutrinos, *Modern Physics Letters A* **16** (2002) 092007. 4

[10] The Majorana Collaboration, White Paper on the Majorana Zero-Neutrino Double-Beta Decay Experiment, (2003) *Preprint* arXiv:nucl-ex/0311013. 4

[11] I. Abt *et al.*, GERDA Letter of Intent, A new ^{76}Ge Double Beta Decay Experiment a LNGS, (2004) *Preprint* arXiv:hep-ex/0404039. 4

[12] C. Arnaboldi *et al.*, CUORE: a cryogenic underground observatory for rare events, *Nucl. Instrum. Meth. A* **518** (2004) 775. 4

[13] EXO collaboration, Search for Neutrinoless Double-Beta Decay in 136Xe with EXO-200, *Phys. Rev. Lett.* **109** (2012) 032505. 5

[14] EXO collaboration, Observation of Two-Neutrino Double-Beta Decay in Xe-136 with EXO-200, *Phys. Rev. Lett.* **107** (2011) 212501. 5

[15] KamLAND-Zen Collaboration, Measurement of the double-beta decay half-life of 136 Xe with the KamLAND-Zen experiment, *Phys. Rev. C* **85**, 045504 (2012). 5

[16] A.S. Barabash *et al.*, NEMO3 and SuperNEMO double beta decay experiments, *J. Phys. Conf. Ser.* **39** (2006) 347. 5

[17] R. Luescher *et al.*, Search for $\beta\beta$ decay in ^{136}Xe: new results form the Gotthard experiment *Phys. Lett. B* **434** (1998) 407. 5

[18] F.J. Iguaz, Development of a Time Projection Chamber prototype with Micromegas technology for the search of the Double Beta Decay of ^{136}Xe, PhD Thesis, Universidad de Zaragoza, (2010) `http://zaguan.unizar.es/record/5731`. 6, 65, 95, 97, 99, 154

[19] L. Seguí, Pattern Recognition in a High Pressure Time Projection Chamber prototype with a Micromegas readout for the ^{136}Xe double beta decay, PhD Thesis, Universidad de Zaragoza (2013). 6, 97, 99, 109, 154

[20] NEXT collaboration, NEXT, a HPGXe TPC for neutrinoless double beta decay searches, Letter of Intent to the LSC Scientific Committee, *Preprint* arXiv:[hep-ex] 0907.4054 (2009). 6

[21] K. Pushkin, R&D for the EXO-GAS experiment to search for neutrinoless double beta decay, poster presented i the 12th Pisa Meeting on Advanced Detectors, May 2012. 6

[22] G. Bertone, D. Hooper and J. Silk, Particle dark matter: evidence, candidates and constrains, *Physics Reports* **405** (2005) 279-390. 6, 8

[23] E. Komatsu *et al.*, Seven-Year Wilkinson Microwave Anisotropy Probe (WMAP) Observations: Cosmological Interpretation, *Astrophys. J. Suppl.* 192:18 (2011). 6

[24] S. Perlmutter (Supernova Cosmology Project), Supernovae, Dark Energy, and the Accelerating Universe, *Physics Today*, April 2003. 6, 7

[25] S.W. Allen, A.E. Evrard, A.B. Mantz, Cosmological Parameters from Observations of Galaxy Clusters, *ARA&A* (2011) **49**:409-470. `arXiv:1103.4829`. 6

[26] `http://www.rssd.esa.int/index.php?project=planck` 6

[27] Plank collaboration, Planck 2013 results. I. Overview of products and scientific results, `arXiv:1303.5062`. 6

[28] Plank collaboration, Planck 2013 results. XVI. Cosmological parameters, `arXiv:1303.5076`. 6

[29] T.A. Porter, R.P. Johnson and P.W. Graham, Dark Matter Searches with Astroparticle Data, *Annu. Rev. Astro. Astrophys.* **49** (2011) 155-194. 7

[30] D. Clowe *et al.*, A Direct Empirical Proof of the Existence of Dark Matter, *Astrophys. J.* (2006) 648:L109-13. 7

[31] J.L. Feng, Dark Matter Candidates from Particle Physics and Methods of Detection, *Annu. Rev. Astro. Astrophys* **48** (2010) 495-545. 8

[32] A. Morales *et al.*, Improved constraints on WIMPs from the International Germanium Experiment IGEX *Phys. Lett. B* 532:8-14, (2002). 8

[33] I.G. Irastorza, Physics at Underground Laboratories: Direct Detection of Dark Matter, (2009) `arXiv:0911.2855`. 8

[34] R. Lang and W. Seidel, Search for dark matter with CRESST. *New Journal of Physics*, 11(105017):1-26, (2009). 8

[35] E. García *et al.*. High performance scintillating bolometers in the search for WIMPs: ROSEBUD Experiment. *Proceedings of the Sixth International Workshop on he Identification of Dark Matter (IDM)*, (2006) 302-307 . 8

[36] CDMS Collaboration, Search for annual modulation in low-energy CDMS-II data, (2012), `arXiv:1203.1309` 8

[37] V. Sanglard, EDELWEISS-II Dark Matter Search: status and first results. *TAUP09 proceedings* (2009). `arXiv:0912.1196`. 8

[38] D. Akimov *et al.*, WIMP-nucleon cross-section results from the second science run of ZEPLIN-III, *Phys. Lett. B* 709: 14 (2012). 9

[39] E. Aprile *et al.*(XENON Collaboration), The XENON100 Dark Matter Experiment, (2011) `arXiv.org:1107.2155`. 9

[40] LUX Collaboration, The Large Underground Xenon (LUX) Experiment, *Nucl. Instr. and Meth. A* **704** (2013) 111-126. 9

[41] ArDM Collaboration, The ArDM exeriment, *Acta Phys. Polon. B* 41:1441-1446, (2010). 9

[42] R. Bernabei *et al.*, DAMA/LIBRA results and perspectives *J. of Physics: Conf. Ser.* **375** (2012) 012002. 9

[43] J. Amaré *et al.*, Dark matter searches with NaI scintillators in the Canfranc undergroud laboratory: ANAIS experiment. *J. Phys. Conf. Ser., 39:123-125 (2006).* 9, 118

[44] E. Aprile *et al.*, Dark Matter Results from 225 Live Days of XENON100 Data, *Phys. Rev. Lett.* **109** (2012) 181301. 10

[45] M.C. Smith *et al.*, The RAVE survey: constraining the local galactic escape speed, *Mon. Not. R. Astron. Soc.* **379** 755 (2007). 10

[46] B. Morgan, A.M. Green and N.J.C. Spooner, Directional statistics for realistic weakly interacting massive particle direct detection experiments, *Phys. Rev. D* **71**, 103507 (2005). 10, 11

[47] G.J. Alner *et al.*, The DRIFT-II Dark Matter detector: Design and commisioning, *Nucl. Instr. and Meth. A* **555** 173-183(2005). 11, 65

[48] H. Nishimura *et al.*, A Direction-Sensitive Dark Matter Search Experiment (NEWAGE) *J. Phys. Soc. Jpn.* **78** (2009) Suppl. A 218-220. 11

[49] J.B.R. Battat *et al.*, DMTPC: Dark matter detection with directional sensitivity, *PoS IDM2010* (2011) 042. 11

[50] D. Santos *et al.*, MIMAC: A micro-tpc matrix for directional detection of dark matter, *J. Phys.: Conf. Ser.* **309** 012014 (2011). 11, 23

[51] S. Ahlen *et al.*(developed in CYGNUS 2009) The case for a directional dark matter detector and the status of current experimental efforts, *IJMPA* **25** 1 (2010). 11

[52] C.E. Aalseth *et al.*, Search for an Annual Modulation in a P-type Point Contact Germanium Dark Matter Detector, *Phys. Rev. Lett.* **107** (2011) 141301. 12

[53] A.V. Belikov, J.F. Gunion, D. Hooper and T.M.P. Tait, CoGeNT, DAMA, and light neutralino dark matter, *Phys. Lett. B* **705** (2011) 82-86. 12

[54] D. Hooper and C. Kelso, Implications of CoGeNT's new result for dark matter, *Phys. Rev. D* **84**, 083001 (2011). 12

[55] G. 't Hooft, Symmetry Breaking through Bell-Jackiw Anomalies, *Phys. Rev. Lett.*, **3** (1976) 37(1):8. 12

[56] S. Weinberg, The U(1) problem. *Phys. Rev. D*, **2** (1975) 14(12):3432-3450. 12

[57] C.A. Baker *et al.*, Improved experimental limit on the electric dipole moment of the neutron, *Phys. Rev. Lett.* **97** (2006) 131801. 13

[58] H.Y. Cheng, The Strong CP Problem Revisited, *Phys. Rept.* **158** (1988) 1. 13

[59] R.D. Peccei and H.R. Quinn, CP Conservation in the Presence of Instantons, *Phys. Rev. Lett.* **38** (1977) 1440-1443. 13

[60] R.D. Peccei and H.R. Quinn, Constraints imposed by cp conservation in the presence of instantons, *Phys. Rev. D.* **16** (1977) 1791-1797. 13

[61] S. Weinberg, A New Light Boson?, *Phys. Rev. Lett.* **40** (1978) 223-226. 13

[62] F. Wilczek, Problem of Strong P and T Invariance in the Presence of Instantons, *Phys. Rev. Lett.* **40** (1978) 279-282. 13

[63] P. Sikivie, Experimental Tests of the "Invisible" Axion, *Phys. Rev. Lett.* **51** (1983) 1415. 13, 15, 17

[64] M.S. Turner, Windows on the Axion, *Phys. Rept.* **197** (1990) 67-97. 13

[65] J. Jaeckel and A. Ringwald, The Low-Energy Frontier of Particle Physics, *Annual review of Nuclear and Particle Science* **60** (2010) 405-437. 13

[66] M. roncadelli, a. De Angelis and O. Mansutti, Evidence for a new light boson from cosmological gamma-ray propagation?, *AIP Conf. Proc.* **1018** (2008) 147-156, `arXiv:0901.4085`. 13

[67] M. Simet, D. Hooper and P.D. Serpico, The Milky Way as a Kiloparsec-Scale Axionscope, *Phys. Rev. D* **77** (2008) 063001. 13

[68] G.W. Pettinari and R. Crittenden, On the Evidence for Axion-like Particles form Active Galactic Nuclei, *Phys. Rev. D* **80** (2010) 083502. 13

[69] N. Bassan, . Mirizzi and M. Roncadelli, Axion-like article effects on the polarization of cosmic high-energy gamma sources, *JCAP* **1005** (2010) 010. 13

[70] G.G. Raffelt, Axion constraints from white dwarf cooling times, *Phys. Lett B* **166** (1986) 402. 14

[71] J. Isern, E. García-Berro, S. Torres and S. Catalán, Axions and the white dwarf luminosity function, *J. Phys. Conf. Ser.* **172** (2009) 012005. 14

[72] J. Isern, E. García-Berro, L. Althaus and A. Corsico, Axions and the pulsation periods of variable white dwarfs revisited, *astron. Astrophys.* **512** (2010) no. A86 86. 14

[73] B. Holdom, Two U(1)'s and Epsilon Charge Shifts, *Phys. Lett. B* **166** (1986) 196. 14

[74] S. Davidson and M.E. Peskin, Astrophysical bounds on milicharged particles in models with a paraphoton, *Phys. Rev. D* **49** (1994) 2114-2117. 14

[75] S.M. Carrol, Quintassence and the rest of the world, *Phys. Rev. Lett. 81* (1998) 3067-3070. 14

[76] P. Brax and K. Zioutas, Solar Chameleons, *Phys. Rev. D* **82** (2010) 043007. 14

[77] S Hannestad, A. Mirizzi, G.G. Raffelt and Y.Y. Wong, Neutrino an axion hot dark matter bounds after WMAP-7, *JCAP* **1008** (2010) 001. 14

[78] P. Sikivie, Axion cosmology, *Lect. Notes Phys.* **741** (2008) 19-50. 14

[79] O. Wantz and E.P.S. Shellard, Axion Cosmology Revisited, *Phys. Rev. D* **82** (2010) 123508. 14

[80] L. Visinelly, Axions in Cold Dark Matter and Inflation Models, Ph.D. Thesis (2011) University of Utah, `arXiv:1111.5281`. 14

[81] P. Arias *et al.*, WISPy Cold Dark Matter, (2012) `arXiv:1201.5902`. 15

[82] J. Redondo and A. Ringwald, Light shining through walls, *Contemp. PHys.* **52** (2011) 211-236. 15

[83] J.N. Bahcall, W.F. Huebner, S.H: Lubow, P.D. Parker and R.K. Ultich , Standard Solar Models and the Uncertainties in Predicted Capture Rates of Solar Neutrinos, *Phys. Rev. Lett.* **54** (1981) 767. 15

[84] J.N. Bahcall and M.H. Pinsonneault, What do we (not) know theoretically about solar neutrino fluxes?, *Phys. Rev. Lett.* 92(12):121301 (2004). 15

[85] K. van Bibber, P.M. McIntyre, D.E. Morris and G.G. Raffelt, Design for a practical laboratory detector for solar axions, *Phys. Rev. D* **39** (1989) 2089. 17

[86] I.G. Irastorza *et al.*, Towards a new generation axion helioscope, *JCAP* **1106** 013. 16, 17

[87] G.G. Raffelt, Astrophysical axion bounds, *Lect. Notes Phys.*, 741:51-71 (2008). 16

[88] I.G. Irastorza *et al.*, The International Axion Observatory (IAXO), Proceedings of the 7th Patras Workshop on Axions, WIMPs and WISPs, Mykonos, Greece, 2011. `arXiv:1201.3849`. 17, 161, 282

[89] H. Geiger, E. Rutherford, An Electrical Method of counting the Number of α-Particles from Radio-Active Substances, *Proc. Royal. Soc. A* **81** (1908) 141. 19

[90] G. Charpak *et al.*, The use of multiwire proportional counters to select and localize charged particles, *Nucl. Instrum. Meth.* **62** (1968) 262. 19

[91] D.R. Nygren, A Time Projection Chamber-1975, PEP1975 proceedings **198** (1975). 20

[92] D.R. Nygren and J.N. Marx, The Time Projection Chamber, *Physics Today* **31**,46 (1978). 20

[93] J. Derré *et al.*, Statial resolution in Micromegas detectors, *Nucl. Instrum. and Meth. A* **459** (2001) 523-531. s

[94] Y. Giomataris, P. Rebougeard, J.P. Robert and G. Charpak, MICROMEGAS, a multipurpose gaseous detector, *Nucl. Instr. and Meth. A* **376** (1996) 26-36. 20

[95] A. Oed, Position-sensitive detector with microstrip anode for electron multiplication with gases, *Nucl. Instrum. meth. A* **263** (1988) 351. 20, 22

[96] S.F. Biagi and T.J. Jones, The microdot gas avalanche chamber: an investigation of new geometries.*Nucl. Instr. and Meth. A* **361** (1995) 72. 20

[97] F. Sauli, GEM: A new concept for electron amplification in gas detectors, *Nucl. Instrum. Meth. A* **386** (1997) 531. 20

[98] R. Bellazzini *et al.*, The WELL detector, *Nucl. Instrum. Meth. A* **423** (1999) 125-134. 20

[99] M. Bouianov *et al.*, Performance and applications of a μ-TPC, *Nucl. Instrum. Meth. A* **535** (2004) 236. 20

[100] A. Delbart *et al.*New developments of Micromegas detector, *Nucl. Instrum. Meth. A* **461** (2001) 84-87. 20

21, 48, 87

[101] Y. Giomataris *et al.*, MICROMEGAS in a bulk, *Nucl. Instr. and Meth. A* **560** (2006) 405-408. 23

[102] T. Alexopoulos *et al.*, Development of large size Micromegas detector for the upgrade of the ATLAS muon system, *Nucl. Instrum. Methods A* **617** (2010) 161-165. 23

[103] T2K Collaboration, Time projection chambers for the T2K near detectors, *Nucl. Instrum. Meth. A* **637**, 25 (2011). 23

[104] F.J. Iguaz *et al.*, Micromegas detector developments for Dark Matter directional detection with MIMAC, *JINST* **6** P07002.

[105] S. Andriamonje *et al.*, Development and performance of Microbulk Micromegas detectors, (2010) *JINST* **5** P02001. 24, 171

[106] F.J. Iguaz *et al.*, New developments in Micromegas Microbulk detectors, *Phys.Procedia* **37** (2012) 448-455.

[107] T. Dafni, on behalf of the NEXT Collaboration, Micromegas planes for the neutrinoless double beta decay search with NEXT, *J. Phys.: Conf. Ser* **309** (2011) 012009. 25, 109, 126, 128

[108] M. Chefdeville *et al.*, An electron-multiplying 'Micromegas' grid made in silicon wafer post-processing technology, *Nuclear Inst. and Meth, A* **556** (2006) 490-494. 25

[109] J.L. Visschers *et al.*, Direct readout of gaseous detectors with tiled CMOS circuits,*Nuclear Inst. and Meth, A* **572** (2007) 203-204. 25

[110] X. Llopart, M. Campbell, R. Dinapoli, D. San Segundo and E. Pernigotti, MediPix2, a 64k pixel read-out with 55 μm square elements working in single photon counting mode, *IEEE Trans. Nucl. Sci.* **49** (2002) 2279-83. 25

[111] X. Llopart, R. Ballabriga, M. Campbell, L. Tlustos and W. Wong, Timepix, a 65k programmable pixel readout chip for arrival time, energy and/or photon counting measurements, *Nuclear Inst. and Meth, A* **581** (2007) 485-494. 25

[112] M. Chefdeville. Development of Micromegas-like gaseous detectors using a pixel readout chip as collecting anode, Ph. D. Thesis, University of Amsterdam, 2009. `http://eprints.eemcs.utwente.nl/15374/` 25, 49, 58, 72, 73

[113] M. Ziegler, P. Sievers and U. Straumann, A triple GEM detector with two-dimensional readout, *Nuclear Inst. and Meth, A* **477** (2001) 260-263. 27

[114] A. Breskin *et al.*, A concise review on THGEM detectors, *Nuclear Inst. and Meth, A* **598** (2009) 107-111. 27

[115] W.R. Leo, Techniques for Nuclear and Particle Physics Experiments,Springer-Verlag Berlin Heidelberg, 1994. 30, 33, 46, 56, 130

[116] W. Blum, W. Riegler and L. Rolandi, Particle detection with Drift Chambers (Second Edition), Springer-Verlag Berlin Heidelberg, 2008. 30, 32, 60, 62, 63, 65, 78, 114, 139

[117] Wikipedia enciclopedy, Helmut Paul (2006). 31

[118] K. Nakamura *et al.(PDG)*, JP G **37**, 075021 (2010) and 2011 partial update for the 2012 edition `(pdg.lbl.gov)` 31, 33, 34, 37, 53

[119] Wikipedia enciclopedy, Helmut Paul (2007). 32

[120] V.A. Chechin and V.K. Ermilova, *The ionization-loss distribution at very small absorber thicknesses*, Nucl. Instrum. Methods **136**, 551 (1976). 33

[121] U. Fano, Penetration of protons, alpha particles and mesons, *Ann. Rev. Nucl. Sc.* **13**, 1 (1963). 34

[122] E.J. Kobetich and R. Katz, *Phys. Rev* **170** (1968) 391. 35

[123] `http://physics.nist.gov/PhysRefData/Star/Text/method.html` 36

[124] J. Linhard *et al.*, *Mat.-Phys. Medd.* 33 **10**, (1963)

[125] J. Lindhard, M. Scharff and H. E. Schiott, *Mat.-Phys. Medd.* 33, **14** (1963). 38, 42

[126] J.F. Ziegler, *Historical Review on The Stopping and Range of Ions in Matter* `http://www.srim.org/SRIM/History/HISTORY.htm` 38, 39

[127] J. F. Ziegler, *et al*, *Stopping and Ranges of Ions in Matter* series Pergamon Press, New York (1978-1984). 39

[128] `http://www.srim.org` 39

[129] P. Majewski *et al.*, Simulations of the Nuclear Recoil Head-Tail Signature in Gases Relevant to Directional Dark Matter Searches, *Astr. Ph.*, 35, **5** (2010) 284. 40, 44, 45

[130] J.D Lewin and P.F. Smith, Review of mathematis, numerical factors, and corrections for dark matter experiments based on elastic nuclear recoil, *Astr. Ph.*, (1996) 6:87. 41, 43, 51

[131] A. Hitachi, Quenching factor and electronic LET in gas at low energy, Proceedings of the 3rd Symposium on Large TPCs for Low Energy Rare event Detection, *J. Phys. Conf. Ser.* **65** (2007) 012013. 42, 44

[132] J.A. Phipps, J.W. Boring and R.A. Lowry, (1964) *Phys. Rev.* 135, A.36 42

[133] A. Tomás, F.J. Iguaz and I.G. Irastorza, talk given in the First Workshop on Directional Detection of Dark Matter (CYGNUS 2007). `http://www.hep.shef.ac.uk/conferences/cygnus2007/talks/zaragoza.pdf` 42, 44, 45

[134] J. Billard, F. Mayet and D. Santos, Three-dimensional track reconstruction for directional Dark Matter detection. *JCAP* 04 (2012) 006 44, 45

[135] D. Dujmic *et al.* (DMTPC Collaboration) *Astr. Ph.*, 30:58, (2008). 44

[136] D. Dujmic *et al.* (DMTPC Collaboration), Observation of the "head-tail" effect in nuclear recoils of low-energy neutrons, *Nucl. Instrum. Meth. A* 584:327 (2008). 44

[137] G.F. Knoll. Radiation detection and measurement. John Wiley and Sons, 3rd edition 2000. 46

[138] M.J. Berger *et al.*, XCOM: Photon Cross Sections Database. `http://www.nist.gov/pml/data/xcom/index.cfm` 46, 47, 125, 126

[139] S.Y.F. Chu, L.P. Ekstrom and R.B. Firestone. The Lund/LBNL Nuclear Data Search, `http://nucleardata.nuclear.lu.se/nucleardata/toi` 47

[140] G. Jungman, M. Kamionkowski and K. Griest. Supersymmertric dark matter. *Phys. Rep.,* 267:198-373, 1996. 51

[141] Evaluated Nuclear Data File (ENDF) Retrieval & Plotting. `http://www.nndc.bnl.gov/sigma` 52

[142] I.G. Irastorza, Un telescopio subterráneo de axiones y WIMPs como instrumento de investigación astrofísica y detector de Materia Oscura, Universidad de Zaragoza, 2001. 52

[143] S. Cebrián. Estudio del fondo radioactivo en experimentos subterráneos de búsqueda de sucesos poco probables: CUORE y ANAIS, PhD Thesis, Universidad de Zaragoza, 2002. 52, 113, 118

[144] M. Martínez. Diseño de un prototipo para un experimento de detección directa de materia oscura mediante modulación anual con centelleadores de ioduro de sodio, PhD Thesis, Universidad de Zaragoza, 2006. 52, 113, 118

[145] D.H. Perkins. Introduction to High Energy Physics, Cambridge University Press, 4th edition (2000). 53

[146] Y.S. Tsai, *Rev. Mod. Phys.* **46**, 815 (1974). 53

[147] F. Sauli, Principles of operation of Multiwire Proportional and Drift Chambers, CERN Yellow Reports 77-09, (1977). 56

[148] D. Combecher, *Proceedings of the 3rd Symposium on Neutron Dosimetry in Biology and Medicine*, ed. by G. Burger and H.G.Elbert (1977) **97**. 56

[149] N. Palladino and B. Sadoulet, Nuclear Instrum. Methods **128**, 323 (1975). 60

[150] S.F. Biagi, Montecarlo simulation of electron drift and diffusion in counting gases under the influence of electric and magnetic fields, *Nucl. Instrum. Meth. A* **421** (1999) 234. Program and cross sections available in `http://www.cern.ch/magboltz` 60, 62, 132

[151] J. Townsend, Electrons in gases (Hutchinson, London, 1947). 60

[152] C.J. Martoff *et al.*, Low Pressure Negative Ion TPC for Dark Matter, *Nucl. Instr. and Meth. A* **440** 355(2000). 65

[153] Y. Giomataris, P. Rebourgeard, J.P. Robert and G. Charpak, MICROMEGAS: A high-granularity position-sensitive gaseous detector for high particle-flux environments, *Nucl. Instrum. Meth. A* **376** (1996) 29. 67

[154] F.J. Iguaz, E. Ferrer-Ribas, A. Giganon and I. Giomataris, Characterization of microbulk detectors in argon- and neon-based mixtures. arXiv:1201.301. 73

[155] S. Cebrián *et al.*, Micromegas readouts for double beta decay searches, *JCAP* **10** (2010) 010. 74, 98, 99

[156] S. Cebrián *et al.*, Micromegas-TPC operation at high pressure in xenon-trimethylaminte mixtures, (2012). Preprint arXiv:1210.3287. 75

[157] M.E. Rose and S.A. Korff, An Investigation of the Properties of Proportional Counters, *Phys. Rev.* **59** 850-9 (1941) . 75

[158] W. Diethorn, A methan proportional counter system for natural radiocarbon measurements, UASEC Report NY06628 (1956). 76

[159] Y. Giomataris, Development and prospects of the new gaseous detector 'Micromegas', *Nucl. Instr. and Meth. A* **419** (1998) 239-252. 76, 77

[160] M. Chefdeville *et al.*, Pulse height fluctuations of integrated Micromegas detectors, *Nucl. Instr. and Meth. A* **591** (2008) 147-150. 77

[161] T. Dafni *et al.*, Energy resolution of alpha particles in a Micromegas detector at high pressure, *Nucl. Instrum. Meth. A* **608** (2009) 259. 77, 95, 96, 97, 98

[162] W. Legler, The influence of the relaxation of the electron energy distribution on the statistics of electron avalanches, *Brit. J. Appl. Phys.* **18** (1967). 79, 80

[163] J. Byrne, Statistics of the electron multiplication process in proportional counters, *Proc. R. Soc. Edinburgh*, **XVI A 33** (1962). 79

[164] J. Derré *et al.*, Fast signals and single electron detection with a MICROMEGAS photodetector, *Nucl. Instrum. Meth. A* **449** 314-321 (2000). 79, 91, 97

[165] G.D. Alkhazov, Statistics of electron avalanches and ultimate resolution of proportional counters, *Nucl. Instrum. Methods* **89**, 155 (1970). 80

[166] T. Alexopoulos *et al.*, Micromegas study for the sLHC environments, *JINST* **5** P02001 (2010). 88

[167] S. Ramo, Currents induced in electron motion, *Proc. IRE* **27**, 584 (1939). 90

[168] J. Dolbeau *et al.*, The solar neutrino HELLAZ project, *Nucl. Phys. Proc. Suppl.* **138** (2005) 94.

[169] A. Tomás *et al.*, Development of Micromegas for neutrinoless double beta decay searches, 2009 *JINST* **4** P11016. 94, 95, 104

[170] S. Cebrián *et al.*, Micromegas-TPC operation at high pressure in xenon-trimethylamine mixtures, 2013 *JINST* **8** P01012. 95, 99, 100

[171] C. Balan *et al.*, Micromegas operation in high pressure xenon: charge and scintillation readout, 2011 *JINST* **6** P02006. 97, 98, 100

[172] B. Ramsey and P. Agrawal, Xenon- based Penning mixtures for proportional counters, *Nucl. Instrum. Meth. A* **278** (1989) 576. 99

[173] C.A.N. Conde and A.J.P.L. Policarpo, *Nucl. Instr & Meth.* **53** (1967) 7-12. 100

[174] D. Nygren, Can the intrinsic energy resolution in xenon be surpassed?, *J. Phys.: Conf. Ser.* **309** (2011) 012006. 100

[175] S. Cebrián *et al.*, Radiopurity of micromegas readout planes, *Astroparticle Physics* **34** (2011) 354-359. 101, 172

[176] E. Aprile, The XENON100 Dark Matter Experiment at LNGS: Status and Sensibility, *J. Phys: Conf. Ser.* **203** (2010) 012005. 102

[177] T2K Collaboration, The T2K experiment, arXiv:1106.1238. 102

[178] D. Calvet *et al.*, AFTER, an ASIC for the Readout of the Large T2K Time Projection Chambers, *Nuc. Science, IEEE Trans. on* **55** 3 (2008) 1744-1752. 102

[179] SAMTEC, GFZ-30-03-G-10-AD. 105, 106

[180] LeCroy WR6050. 108

[181] ROOT team, ROOT framework for data processing, `root.cern.ch` 112

[182] S. Agostinelli *et al.*, GEANT4 - a simulation toolkit, *Nucl. Instrum. Meth. A* **506** (2003) 250-303 113

[183] J. Allison *et al.*, GEANT4 developments and applications, *IEEE Transcations on Nuclear Science* **53** (2006) 270. 113

[184] GEANT4 Collaboration, Application Developer's Guide, `http://geant4.cern.ch` 114

[185] O.A. Pokratenko *et al.*, Event Generator DECAY4 for simulation of double beta processes and decays of radiactive nuclei, *Phys. At. Nucl.* **63** (2000) 1282-1287. 120

[186] CLHEP - A Class Library for High Energy Physics, `http://proj-clhep.web.cern.ch` 120

[187] J. Galán, Probing eV-mass scale Axions with a Micromegas Detector in the CAST experiment, PhD Thesis, Universidad de Zaragoza, 2011. 2011 *JINST* TH **003**. 138, 161, 167, 173, 174, 175, 177, 179

[188] J. Billard, F. Mayet and D. Santos, Low energy electron/recoil discrimination for directional Dark Matter detection, *JCAP* 07 (2012) 020. 153

[189] S. Andriamonje *et al.*(CAST collaboration), An improved limit on the axion-photon coupling from the CAST experiment, *J. Cosmol. Astropart. Phys* 04 (2007) **10**. 159

[190] E. Arik *et al.*, (CAST collaboration), Proving eV-scale axions with CAST, *J. Cosmol. Astropart. Phys* 02 (2009) **008**. 161

[191] M. Arik *et al.*, (CAST collaboration), Search for Sub-eV Mass Solar Axions by the CERN Axion Solar Telescope with ^{3}He Buffer Gas, *Phy. Rev. Let.*, **107** 26 (2011) . 161

[192] CAST collaboration, CAST final results with ^{3}He Buffer Gas, in preparation (2013). 161

[193] I.G. Irastorza *et al.*, The International Axion Observatory (IAXO), Proceedings of the 7th Patras Workshop on Axions, WIMPs and WISPs, Mykonos, Greece, 2011. `arXiv:1201.3849`. 17, 161, 282

[194] D. Kang, Search for solar axions with the CCD Detector at CAST (CERN Axion Solar Telescope). PhD thesis Albert-Ludwings-universität, **36**, 2007. 161

[195] D. Autiero *et al.*, The CAST time projection chamber. *New Journal of Physics*, 9(6):171, 2007, **48** 163

[196] G. Luzón *et al.*, Background studies and shielding effects for the tpc detector of the CAST experiment, *New Journal of Physics*, 9(7):208, 2007, **49** 163

[197] S. Cebrián *et al.*, Background study for the pn-CCD detector of CERN Axion Solar Telescope, *Astroparticle Physics*, **48** 28:205-215 (2007). 163

[198] J. Galán *et al.*, New Micromegas detectors in the CAST experiment,*NIM A* **604**, 15 (2009). 161, 165, 166

[199] J.C. Santiard *et al.*, Presented at the 6th Pisa Meeting on Advanced Detectors (1994) *CERNECP-94-17*. 164

[200] T. Geralis , G. Fanourakis, Y. Giomataris and K. Zachariadou, The data acquisition of the Micromegas detector for the CAST experiment, *IEEE Nucl. Sci. Symp. Conf.* (2003) **5** 3455-99. 164

[201] D. Breton, E. Delagnes and M. Houry, Very high dynamic range and high sampling rate VME digitizing boards for physics experiments, *IEEE Trans. Nucl. Sci.* (2005) **52** 2853. 164

[202] T. Dafni. A Search for Solar axions with the MICROMEGAS Detector in CAST. PhD thesis, Technischen Universität Darmstadt, 2005. **36, 54, 108**. 173, 176

[203] T. Vafeiadis, Contribution to the search for solar axions in the CAST experiment, PhD thesis, Aristotle University of Thessaloniki (2012), to be published. 173, 176, 182, 282

[204] C. Yildiz, PhD thesis, Dogus University, Istanbul (2013), in preparation. 173

[205] P. Abbon *et al.*, The Micromegas detector of the CAST experiment, *New Journal of Physics* **9** (2007) 170. 164

[206] Dumond Gerard, Background Measurement for CAST experiment, Technical Note,CERN-SC-2004-027-RP-TN. 211

[207] T. Dafni *et al.*, Background Measurement at the CAST experiment, CAST internal note (2012). 212, 216, 217

[208] A. Rodríguez, internal communication (2012). 212

[209] E. Ruiz Chóliz, Detección directa de materia oscura en el Laboratorio Subterráneo de Canfranc, TAD in the F'sica Atómica, Molecular y Nuclear Area of the University of Zaragoza (2012). 213

[210] G. Luz'on, internal communication (2012). 213

[211] A. Tomás, Brief report on simulations about ^{57}Co source tests in SRMM, CAST internal note, Feb 2012. 227

[212] T. Vafeiadis, talk given in the 48th CAST Collaboration Meeting (Patras, May 2012). 240

[213] NI USB-6008, `http://sine.ni.com/nips/cds/view/p/lang/es/nid/201986` 245

[214] `http://www.genitron.de/products/alpha_slides.html` 245

[215] A. Tomás, CAST Microbulk Micromegas in the Canfranc Underground Laboratory, Proceedings of the 2nd International Conference on Technology and Instrumentation in Particle Physics (TIPP 2011), *Physics Procedia* **37** (2012) 478-482. 245

[216] J. Galán, talk given in the 41st CAST Collaboration Meeting (CERN, Feb 2010). 245

[217] A. Tomás, talk given in the 42nd CAST Collaboration Meeting (CERN, Jun 2010). 245

[218] LSC website, `http://www.lsc-canfranc.es` 246

[219] G. Luzón et al. Characterization of the Canfranc Underground Laboratory: status and future plans. *Proceedings of the International Conference in the Identification of Dark Matter (IDM2006)*, pp 514-519. 246, 247

[220] A. Tomás, talk given in the 43rd CAST Collaboration Meeting (CERN, Jan 2011). 249

[221] J.A. García, talk given in the 47th CAST Collaboration Meeting (CERN, Jan 2012). 264

[222] S. Cebrián and D.C Herrera, private communication. 258

[223] ILIAS radiopurity data base `http://radiopurity.in2p3.fr` 258

[224] Taken from NEXT experiment radiopurity data base. 258

[225] F.J. Iguaz *et al.*, CAST internal document (Jan 2011). 264

[226] J.G. Garza, talk given in the 47th CAST Collaboration Meeting (CERN, Jan 2012). 264, 278

[227] Th. Papaevangelou for the CAST Collaboration, 2012 Status report of the CAST Experiment and Running in 2013-2014, CERN-SPSC-2012-028. 267, 268, 272, 277, 278, 280

[228] J.A. García, talk given in the 48th CAST Collaboration Meeting (Patras, May 2012). 267

[229] A. Diago, talk given in the 49th CAST Collaboration Meeting (CERN, Sep 2012). 267

[230] J.G. Garza, talk given in the 50th CAST Collaboration Meeting (CERN, Feb 2013). 279